SELF-ASSEMBLY OF STRUCTURALLY DIVERSE PHOSPHOMOLYBDATES: SYNTHESIS, STRUCTURE AND PROPERTIES

Submitted to University of Calicut

in partial fulfillment of the requirements

for the Degree of

Doctor of Philosophy in

Chemistry

By

JISHA JOSEPH

Under the guidance of

Dr. JENCY THOMAS

RESEARCH AND POST GRADUTE DEPARTMENT OF CHEMISTRY

ST. THOMAS COLLEGE (AUTONOMOUS)

THRISSUR, KERALA-680001

DECEMBER 2020

7-12-2020

CERTIFICATE

This is to certify that the thesis entitled *"**Self-Assembly of Structurally Diverse Phosphomolybdates: Synthesis, Structure and Properties**"* is an authentic record of research work carried out by Jisha Joseph under my supervision in partial fulfillment of the requirements for the degree of Doctor of Philosophy, in Chemistry of University of Calicut and further that no part thereof has been presented before for any other degree.

Dr. Jency Thomas

(Supervising Teacher)

DECLARATION

I hereby declare that the thesis entitled "**Self-Assembly of Structurally Diverse Phosphomolybdates: Synthesis, Structure and Properties**", submitted to the University of Calicut in partial fulfillment of the requirements for the award of the Degree of Doctor of Philosophy in Chemistry is a bonafide research work done by me under the supervision and guidance of Dr. Jency Thomas, Assistant Professor, Research & PG Department of Chemistry, St. Thomas College (Autonomous), Thrissur, Kerala.

I further declare that this thesis has not previously formed the basis of any degree, diploma or any other similar title.

Jisha Joseph

ACKNOWLEDGEMENT

Dedicated to,

Sacred Heart CMC Province
Mananthavady
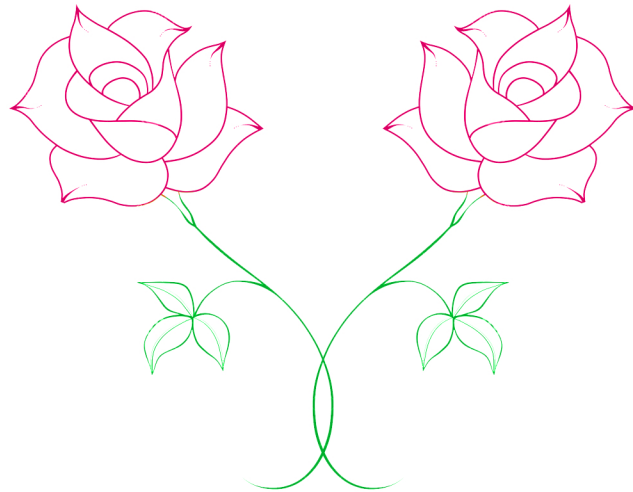
*As we express our gratitude,
we must never forget that
the highest appreciation is not
words, but to live by them.*

John F Kennedy

PREFACE

Phosphomolybdate (PMO) is an important sub-class of Polyoxometalates (POMs). This phosphorous and molybdenum containing heteropolyanions comprise of a distinguished family with versatile structural features and promising applications. The counter cations of these anionic clusters can be metal ions, metal complexes or protonated organic moieties. The Phosphomolybdates are widely classified into various types. Among these, Strandberg-type $\{P_2Mo_5O_{23}\}^{6-}$, Keggin-type $\{PMo_{12}O_{40}\}^{3-}$, Wells Dawson-type $\{P_2Mo_{18}O_{62}\}^{6-}$ and as fully reduced cluster $\{P_4Mo_6O_{31}\}^{12-}$ are the predominant types. Since they are supramolecular materials they can self-assemble into tuneable size and shape with varying dimensionality. In this thesis, seven novel Strandberg-type PMOs and one copper based Keggin-type solid have been reported along with their characterization and related physico-chemical properties. Ammonium Phosphomolybdate (APM) which is a Keggin-type PMO was synthesized along with its two composites with polyaniline and poly (N-methylaniline), namely APM/PAni and APM/PNMAni respectively. APM was found to be a good ion-exchanger to remove cationic dye-stuffs from its aqueous solution with high efficiency and appreciable reusability. The Cr(VI) removal efficiency of APM and its composites have been investigated and APM/PNMAni was observed as a good candidate for the same.

Two synthetic methods have been used in the thesis namely, solvent evaporation technique and hydrothermal technique. In the first method, P and Mo precursors along with organic moiety and metal chlorides were taken in the form of clear aqueous solution and kept undisturbed for the self-assembly process. The slow evaporation of the solution at room temperature resulted in crystallization of PMO based solids. In the second method, a hydrothermal bomb was used; which is a sealed Teflon container. The reaction

was carried out under autogenous pressure and the precursors were added along with water. A temperature range from 100-180ºC was selected for a time span of 3 days. The slow cooling of the apparatus was allowed for the crystallization of solids.

The thesis is divided into seven chapters. Chapter I comprises of a brief introduction to the work, giving emphasis to the synthetic routes, different classes of PMOs based on their structural features and properties along with their important applications. A literature survey on the research carried out in this area for the past decade was carried out and systematically tabulated.

In chapter II, two new Strandberg cluster (referred to as $\{P_2Mo_5\}$) based PMOs namely, $\{H-2a3mp\}_5[\{PO_3(OH)\}\{PO_4\}Mo_5O_{15}]$, and $\{H-2a4mp\}_5[\{PO_3(OH)\}\{PO_4\}Mo_5O_{15}]$. $6H_2O$ were synthesized *via* solvent evaporation technique using 2-amino-3-methylpyridine (2a3mp) and 2-amino-4-methylpyridine (2a4mp) respectively. These solids formed a supramolecular framework stabilized by hydrogen bonding interaction between cluster anions and organic moieties. CH…π interactions between the organic moieties reinforced the crystal packing. The electrochemical behaviour of the synthesized solids was explored by means of three electrode system using 1 mM $K_4[Fe(CN)_6]$ in 0.1 M KCl as supporting electrolyte. In addition, the optical band gaps of the solids were also calculated using ultraviolet-diffused reflectance spectroscopy data. Cyclic voltammogram of both the solids showed reversible waves corresponding to Mo^{VI}/Mo^V electron process. The optical band gap energies of the solids showed slight difference on account of their difference in the nature of the ligands.

In chapter III, self-assembly of molybdate and phosphate precursors in the presence of zinc ions and organic ligands *viz.* benzimidazole (*bimi*), 4-aminopyridine (*4-ap*) and pyrazole (*pz*), has been carried out under hydrothermal condition. The crystallization of

Strandberg cluster based solids {H$bimi$}$_5$[HP$_2$Mo$_5$O$_{23}$].5H$_2$O, {H$bimi$}$_6$[P$_2$Mo$_5$O$_{23}$].H$_2$O, {4-Hap}$_4$[H$_2$P$_2$Mo$_5$O$_{23}$].2H$_2$O, {4-Hap}$_5$[HP$_2$Mo$_5$O$_{23}$] and {Hpz}$_6${Zn(pz)$_4$(H$_2$O)$_2$} [{Zn(pz)$_2$P$_2$Mo$_5$O$_{23}$}$_2$].8H$_2$O was observed. The chapter highlights the structural differences in the supramolecular isomers; and the effect of supramolecular isomerism and nature of ligands on the optical band gap energies (E$_g$) of the synthesized solids.

In chapter IV, an attempt was made to crystallize phosphorous and molybdenum precursors in the presence of MCl$_2$.xH$_2$O (M = Co, Ni, Cu and Zn) with pyrazole to form PMO solids of varying dimensionality. The solids obtained were: {Hpz}$_6${Zn(pz)$_4$(H$_2$O)$_2$}[{Zn(pz)$_2$P$_2$Mo$_5$O$_{23}$}$_2$].8H$_2$O, [{Cu(pz)$_4$}$_2$ {H$_2$P$_2$Mo$_5$O$_{23}$}].H$_2$O, {Ni(pz)$_4$}[{Ni(pz)$_4$}$_2${H$_2$P$_2$Mo$_5$O$_{23}$}]$_2$ [{Ni(pz)$_4$}{Ni(pz)$_4$ (H$_2$O)} {HP$_2$Mo$_5$O$_{23}$}]$_2$. 14H$_2$O, [Ni(pz)$_4$Cl$_2$], {pz}$_2$[{Co(pz)$_4$}$_5$ {P$_2$Mo$_5$O$_{23}$}$_2$].6H$_2$O and [{Cu(pz)$_2$}$_4$ {CuMo$_{12}$O$_{38}$(OH)$_2$}].8H$_2$O. Among these, the last solid is a rare example of copper based Keggin cluster. Except for this solid, which was synthesized using hydrothermal method; all other solids were obtained via solvent evaporation method. The magnetic properties of the solids were investigated using Guoy Balance.

In chapter V, synthesis, characterization and dye removal efficiency of ammonium phosphomolybdate (APM) which is a Keggin-type solid has been discussed. It was concluded that APM could be effectively used as an ion-exchanger to remove cationic dye-stuffs from aqueous solution. The dyes used for investigation were methylene blue, malachite green, methyl red and eosin. The influence of parameters such as nature of light, amount of APM, contact time and pH on dye removal efficiency was investigated.

In chapter VI, the synthesis and characterization of two composites of APM with polyaniline and poly (N-methylaniline), namely APM/PAni and APM/PNMAni respectively have been summarised. The difference in band gap energy in APM upon the

formation of the composite was investigated, and the capacity of these composites in the removal of hexavalent chromium from aqueous solution was explored. It was concluded that APM/PNMAni could effectively reduce harmful Cr(VI) to environmentally benign Cr(III).

Chapter VII concludes the entire work and emphasizes the future scopes of PMO based hybrid solids.

LIST OF ABBREVIATIONS

1. APM — Ammonium phosphomolybdate

2. APM/PAni — Ammonium phosphomolybdate/polyaniline composite

3. APM/PNMAni — Ammonium phosphomolybdate/poly(N-methylaniline) composite

4. APS — Ammonium persulphate

5. BET — Brunauer-Emmett-Teller

6. BVS — Bond valence sum

7. CTAB — Cetyl trimethyl ammonium bromide

8. CV — Cyclic voltammetry

9. DDW — Double distilled water

10. DMF — Dimethyl formamide

11. DMSO — Dimethyl sulphoxide

12. DPC — Diphenyl carbazide

13. EDAX — Energy dispersive X-ray spectroscopy

14. EY — Eosin

15. FESEM — Field emission scanning electron microscope

16. FTIR — Fourier Transform Infrared

17. GCE — Glassy carbon electrode

18. JCPDS — Joint committee on powder diffraction standards

19. MB — Methylene blue

20. MG — Malachite green

21. MR — Methyl red

22. ORTEP	Oak ridge thermal ellipsoid plot
23. PAN	Polyacrylonitrile
24. PAni	Polyaniline
25. PMA	Phosphomolybdic acid
26. PMMA	Polymethylmathacrylate
27. PMO	Phosphomolybdate
28. PNMAni	Poly(N-methylaniline)
29. $\{P_2Mo_5\}$	$\{P_2Mo_5O_{23}\}^{6-}$
30. $\{PMo_{12}\}$	$\{PMo_{12}O_{40}\}^{3-}$
31. $\{P_4Mo_6\}$	$\{P_4Mo_6O_{31}\}^{12-}$
32. POM	Polyoxometalates
33. PXRD	Powder X-ray diffraction
34. rGO	Reduced graphene oxide
35. SEM	Scanning electron microscopy
36. TGA	Thermogravimetric analysis
37. TMC	Transition metal complex
38. UV-DRS	Ultraviolet-Diffused reflectance spectroscopy
39. UV-Vis	Ultraviolet-visible
40. 2a3mp	2-amino-3-methylpyridine
41. 2a4mp	2-amino-4-methylpyridine
42. bimi	Benzimidazole
43. 4-ap	4-aminopyridine
44. pz	Pyrazole

ABSTRACT

Polyoxometalate (POM) is an important class of early transition metal-oxygen clusters with plenteous intrinsic structures and widespread applications. Phosphomolybdate (PMO), a prominent sub-class of POMs, has been attracting the attention of researchers on account of their versatile building blocks and controllable architectures. Supramolecular self-assembly is a powerful tool to create PMO solids with attracting properties. Important factors affecting the self-assembly process are nature of organic moiety, temperature, pH of the medium and nature of metal ions. Owing to the controllable external factors, the self-assembly can lead to the formation of supramolecular aggregates with varying size and dimensionality such as one dimensional chain, two dimensional sheets and three dimensional networks. Moreover, nitrogen donor ligands and their pH related nature play a vital role in the crystal engineering. They have the capability to form complex with metal centres or undergo protonation. Recently a new trend of designing composite materials of PMOs with suitable substances like polymers has been observed.

In this thesis, various novel PMOs with varying structure and dimensionality have been synthesized. The characterization of the synthesized solids was done successfully by single crystal X-ray diffraction, powder X-ray diffraction, fourier transform infrared spectroscopy and thermo gravimetric analysis. The behavior and dynamics of these solids on account of their non-bonding interactions involved in the self-assembly process and affecting factors have been illustrated. Some predominant properties of the synthesized solids like optical band gap energy, magnetic properties and electrochemical properties were investigated. Ammonium phosphomolybdate (APM), a member of Keggin-type PMO was synthesized and characterized. Its ability to remove cationic dye-stuffs from aqueous solutions was explored. Two unique composites of APM with

polyaniline and poly(N-methylaniline) *viz*. APM/PAni and APM/PNMAni were synthesized and characterized. Moreover, APM/PNMAni composite was found as a good candidate to reduce environmental pollutant Cr(VI) to Cr(III) from contaminated aqueous solution.

TABLE OF CONTENT

CONTENTS		Page No.

Chapter IV   **Metal pyrazole complex incorporated PMO cluster based solids**   **113-143**

Publications and Conference presentations

LIST OF TABLES

CHAPTER IV: METAL PYRAZOLE COMPLEX INCORPORATED PMO CLUSTER BASED SOLIDS

CHAPTER V: REMOVAL OF CATIONIC DYES FROM WATER USING APM

CHAPTER VI: INVESTIGATIONS USING COMPOSITES BASED ON APM

LIST OF FIGURES

LIST OF SCHEMES

CHAPTER I

Introduction and
Review of literature

Summary

Soft-chemistry routes provide favorable conditions for self-assembly of phosphomolybdates (PMOs) with peculiar properties. This chapter gives a brief outline on the various synthetic methodologies to design structurally diverse PMOs and major types of PMO cluster anions with their versatile structural features. Based on their self-assembly pattern they have been broadly classified into four distinct classes. Class I consists of PMO clusters covalently linked by transition metal complexes (TMCs) extending into multi-dimensions. Class II comprises of discrete PMO clusters with TMCs as counter cations. Class III includes PMO clusters derivatized by TMCs and Class IV comprises of coordination polymers in which PMO clusters have been incorporated. In addition, the important structural features of PMOs have been explained in a nutshell. PMOs have a wide range of applications, of which biomedicinal, catalytic, electrochemical and magnetic properties have been discussed.

I.1 Introduction

Polyoxometalates (POMs) are a prime class of oxo-bridged early transition metals in high oxidation states (such as Mo^V, Mo^{VI}, W^{VI}, V^V, Ta^V and Nb^V) [1,2]. These metal-oxygen anion clusters have contributed a lot towards the rapid development of inorganic chemistry in the past decades on account of their structural diversity and potential applications in fields of research such as medicine, catalysis, magnetism, photochemistry and redox chemistry [3-7]. The first POM, $\{PMo_{12}O_{40}\}^{3-}$ was reported by Berzelius in 1826 and later Keggin solved the structure of related anion $\{PW_{12}O_{40}\}^{3-}$ [8,9]. The POMs are broadly classified as isopolyanions with general formula of $\{M_nO_{(4n-m)}\}^{(2n-m)-}$ in which there are no heteroatoms present within the framework and heteropolyanions which include one or more heteroatoms within their frameworks with general formula of $\{X_xM_nO_m\}^{y-}$, where $X = B^{III}$, Si^{IV}, Ge^{IV}, P^V, $As^{III/V}$, Sb^{III}, Bi^{III}, Se^{IV} or Te^{IV} and $M = V^V$, Nb^V, Ta^V, Mo^{VI}, Mo^V, or W^{VI} (refer Scheme I.1).

Among the different heteropolyanion clusters, phosphorous and molybdenum containing clusters namely phosphomolybdates (PMOs) comprise of a distinguished family with versatile structural features and promising applications. The counter cations of phosphomolybdate anions can be (i) metal ions like Na^+, K^+ Ca^{2+} and Cu^{2+} (ii) metal complexes and (iii) organic cations [10-15]. Formation of these types of crystalline solids is a self-assembly process. Being supramolecular materials, they can self-assemble into aggregates with multiple dimensionalities. There are a number of examples for 1-D, 2-D and 3-D networks of phosphomolybdates in the literature [16-18]. Intermolecular interactions like hydrogen bonding, π-π stacking and electrostatic interactions play a vital role in stabilizing the supramolecular assembly [19-21]. Although many researchers have been

exploring these solids, crystal engineering of PMO cluster anion based solids faces challenges including critical control of parameters such as pH and solubility of reactants. For example, Yan *et. al.* have explained the importance of pH of solution in the formation of PMO solids $(C_6H_{18}N_2)_2[H_2P_2Mo_5O_{23}].2H_2O$ and $(C_6H_{18}N_2)_{4.5}[H_3P_2Mo_5O_{23}].6H_2O$ which were synthesized using the same organic amine but at different pH levels [22]. Moreover, the crystallization of organic-inorganic hybrid PMO solids is a very complicated process due to unpredictable behavior of PMOs, metal ions and ligands during self-assembly which poses the problem of predicting the structure and composition of the final products [23]. Therefore, in the present work, a systematic synthesis of PMO cluster based solids was carried out using soft-chemistry routes to evaluate the role of parameters such as pH, nature of organic ligand and its concentration. Further, the structure elucidation of the synthesized solids was carried out and their properties were investigated.
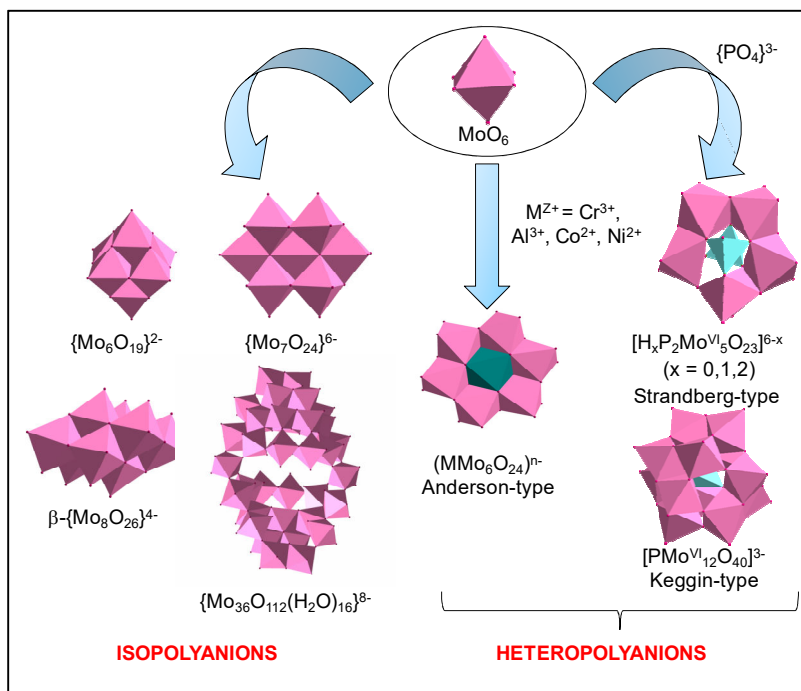
Scheme I.1. Scheme showing a few examples of isopolyanions and heteropolyanions of molybdenum.

I.2. Types of PMO clusters

POMs exhibit a large variety of clusters of varying sizes, shapes and composition. Based on their various topologies and intriguing frameworks different types of POM clusters have been reported in literature. Keggin, Anderson, Wells Dawson, Strandberg, and Silverton-type building blocks being the predominate ones in this area. Among these POMs, PMOs crystallize mainly as Strandberg-type $\{P_2Mo_5O_{23}\}^{6-}$, Keggin-type $\{PMo_{12}O_{40}\}^{3-}$, Wells Dawson-type $\{P_2Mo_{18}O_{62}\}^{6-}$ and as fully reduced cluster $\{P_4Mo_6O_{31}\}^{12-}$. Therefore, a brief discussion on the above mentioned cluster anions is given below.

I.2.1. Strandberg-type cluster $\{P_2Mo_5O_{23}\}^{6-}$

Diphosphopentamolybdate (VI) was first characterized by Strandberg in 1973 [24]. Relatively smaller size and higher electron density of the cluster anion favor the high coordination ability of the cluster anion. Strandberg-type of POMs are the first heteropolyanions in which organic groups are covalently bonded to a phosphorous heteroatom that allow a number of chemical reactions to take place in the intra-crystalline region [25]. As reported by Thomas *et. al.* $\{P_2Mo_5O_{23}\}^{6-}$ (abbreviated as $\{P_2Mo_5\}$ hence forth) is composed of "five distorted MoO_6 octahedra with two capped PO_4 tetrahedra. A pentagonal ring is formed by five MoO_6 octahedra by sharing edges and corners, which in turn is connected to two PO_4 tetrahedra to each side of the ring sharing three oxygen atoms with different MoO_6 units" [26]. Phosphorous atoms share three oxo groups with Mo ring where one exhibits μ_2-bridging linking one Mo site and phosphorous; while the other two exhibit μ_3- bridging linking two Mo sites and phosphorous (as shown in Figure I.1). The Mo-O distance can be divided into three distinct types: (i) short Mo-O terminal bonds of distance

1.689(3)-1.717(3)Å (ii) medium Mo-O bonds which link two Mo atoms of distance 1.897(3)-1.963(3)Å (iii) longer Mo-O bonds which link Mo and P atoms of distance 2.199(3)-2.417(4) Å [22,27]. This type of cluster forms reasonably stable anions in aqueous solution when a soluble molybdate source is acidified with phosphoric acid over a wide range of pH [28]. $[H_xP_2Mo_5O_{23}]^{(6-x)-}$ (x = 0,1,2) has been considered as an anionic building unit in the supramolecular assembly. The two extrusive $\{PO_4\}^{3-}$ groups enable coordination to bridging units and help in extending dimensionality [29]. The phosphorous heteroatom in Strandberg cluster can be inorganic phosphorous or organophosphine. Till date, several Strandberg-type POMs based on organophosphine $\{RPO_3H_2\}$ where R = $-C_6H_4CO_2H$, $-(CH_2)_nPO_3H_2$ (n = 2-6,9), $-(CH_2)_nCO_2H$ (n = 1,2), $-C_6H_5$, $-CH_2CH_3$, $-CH_3$ have been reported [30-32].

I.2.2. Keggin-type cluster $\{PMo_{12}O_{40}\}^{3-}$

Classical Keggin-type cluster anion (abbreviated as $\{PMo_{12}\}$ hence forth) consists of a central $\{PO_4\}$ tetrahedron surrounded by four vertex sharing $\{Mo_3O_{13}\}$ trimers which comprised of three $\{MoO_6\}$ octahedras linked in a triangular arrangement by sharing edges. The entire unit takes on a close-knit cage-type arrangement and is known as α-Keggin structure. By rotating one, two, three or all the four (Mo_3O_{13}) groups by 60° around the C_3 axis, stereoisomers (β-, γ-, δ- and ε- respectively) can be obtained [33]. Among these isomers, the α-isomer is the one which is widely studied structure with a stable framework (Figure I.2). The P-O bond lengths are in the range of 1.471(15)-1.609(16) Å. Mo-Ot (terminal), Mo-Oc (central) and Mo-Ob (bridge) bond lengths are in the ranges 1.646(5)-1.667(5) Å, 2.405(7)-2.518(7) Å, and 1.900(6)-1.993(6) Å respectively [34].
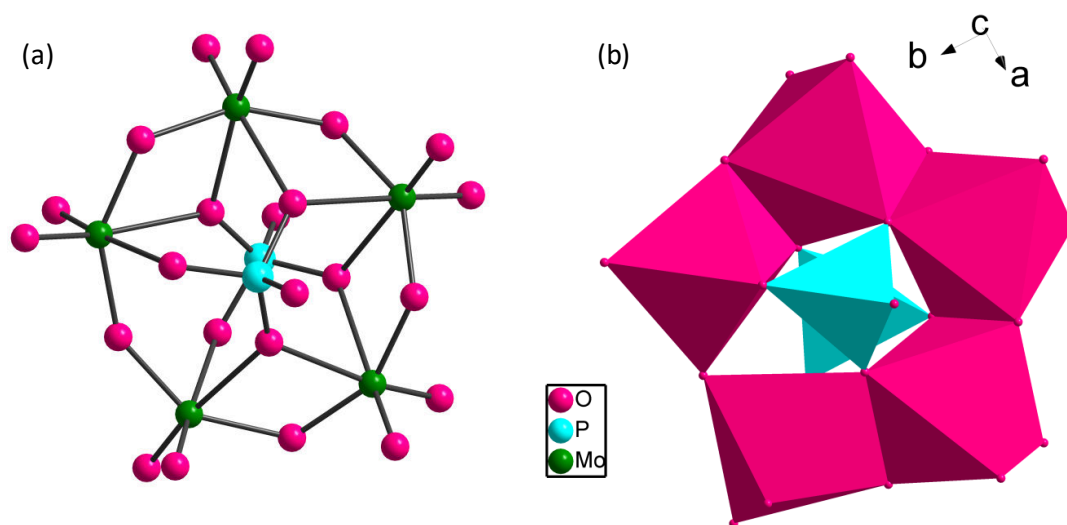
Figure I.1. (a) Ball-and-stick (b) polyhedral view of Strandberg-type anion.
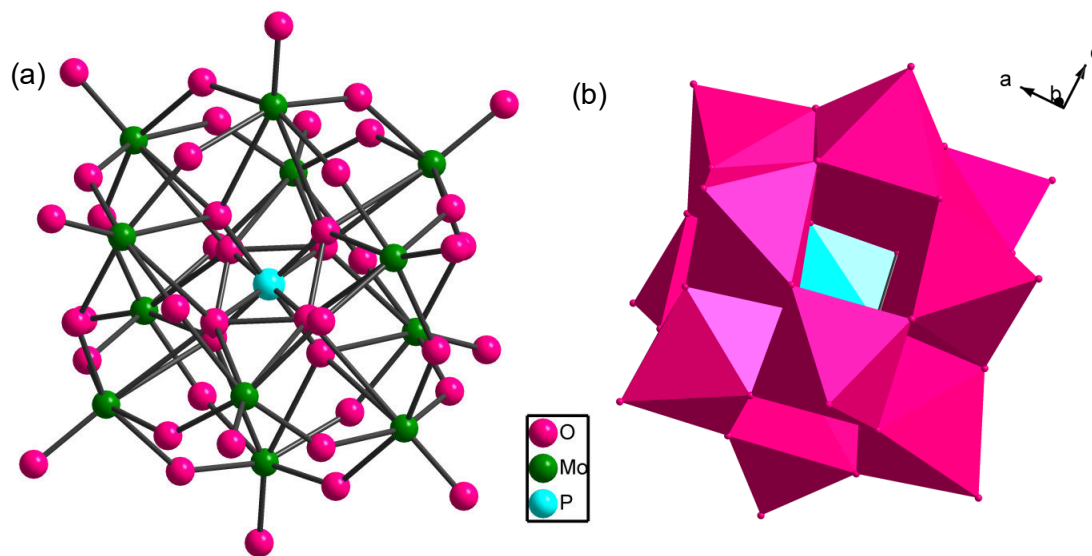
Figure I.2. (a) Ball-and-stick (b) polyhedral view of α-Keggin anion.

I.2.3. Wells Dawson-type cluster {$P_2Mo_{18}O_{62}$}$^{6-}$

Wells Dawson-type polyanion consists of 18 terminal and 36 μ_2-bridging oxygen atoms. There are eighteen MoO_6 octahedras present which exhibits two distinct structural types; six 'cap octhedras' which are divided into subsets of three and twelve 'belt octahedras' grouped

into two subsets of six as shown in Figure I.3 [35]. Six possible isomers are identified in Dawson structure, α, β, γ, α*, β* and γ*. The β isomer is obtained as result of rotation around the symmetry axis C_3 of the α structure by $\pi/3$. The symmetry of the molecule is lost and the Dawson structure is divided into two equivalent parts and attains a C_{3v} symmetry. The isomer γ is obtained by the second rotation of α isomer, around the symmetry axis C_3 by $\pi/3$ which leads to the symmetry plane. The isomers α*, β* and γ* are formed by the similar rotations of α, β and γ in the presence of an inversion centre [36].

I.2.4. Fully reduced cluster $\{P_4Mo_6O_{31}\}^{12-}$

In $\{P_4Mo_6O_{31}\}^{12-}$ (abbreviated as $\{P_4Mo_6\}$ hence forth) cluster anion, all the six Mo atoms are in +5 oxidation state. Six edge sharing MoO_6 octahedras form a ring decorated by four PO_4 tetrahedra. Three such tetrahedras are present in the ring and the fourth one at the midpoint. The central PO_4 tetrahedron furnishes three μ_3- O bridging the six molybdenum atoms; while the three peripheral PO_4 groups connect two molybdenum atoms by two oxygen atoms. In the presence of suitable organic ligands and at high temperature under hydrothermal conditions $\{P_4Mo_6\}$ forms as a competitive phase with $\{P_2Mo_5\}$ [37]. All the Mo(VI) ions which are in d^0 electronic configurations are transferred into d^1 Mo(V) ions. Unlike $\{P_2Mo_5\}$, fully reduced type PMOs requires a suitable metal ion (Fe^{2+}, Zn^{2+}, Mn^{2+}, Co^{2+}, Ni^{2+}, Cd^{2+}, Cu^{2+} and Na^+) for further stabilization [38] and the entire structure attains an hourglass-type dimer $\{M(P_4Mo_6O_{31})_2\}$ (refer Figure I.4).
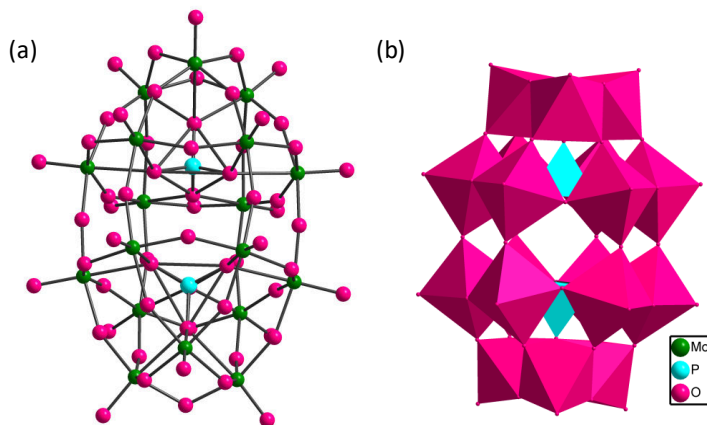
Figure I.3. (a) Ball-and-stick (b) polyhedral view of Wells Dawson-type anion.
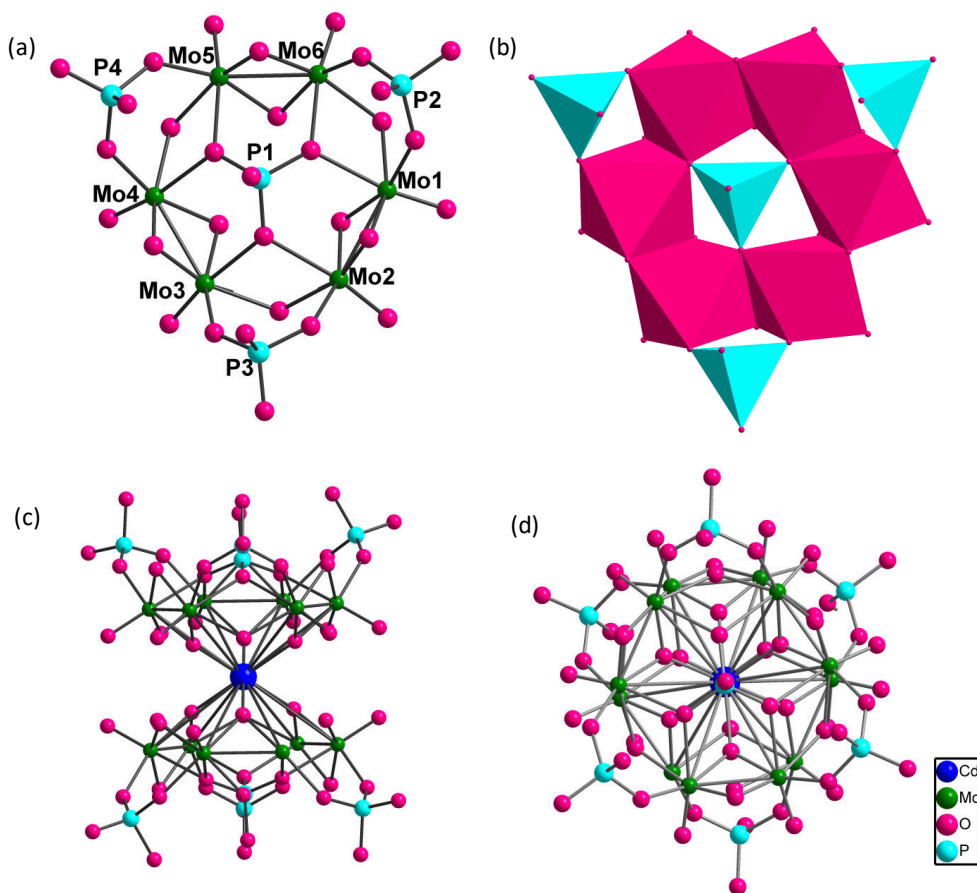
Figure I.4. (a) Ball-and-stick representation of top view of basic structural unit of $\{P_4Mo_6O_{31}\}^{12-}$ (b) polyhedral view of $\{P_4Mo_6O_{31}\}^{12-}$. (c) Side view and (d) top view of hourglass-type $\{M(P_4Mo_6O_{31})_2\}$.

I.3. Classification of PMO cluster based solids

The self-assembly of the basic structural unit PMO, organic ligands, metal ion and/or metal complex results in structural diversity including zero dimensional (0-D) species, one dimensional (1-D) chain, two dimensional (2-D) layer and three dimensional (3-D) framework. On the basis of their self-assembly pattern, PMO cluster based solids can be broadly classified as follows.

Class I: Solids in which PMO clusters are covalently linked to transition metal complexes (TMCs) extending into multi-dimensions.

Class II: Solids having discrete PMO clusters with TMCs as counter cations.

Class III: Solids in which PMO clusters are derivatized by TMCs to form either discrete or extended structures.

Class IV: Coordination polymers incorporated PMOs.

A brief explanation about each class is given below.

I.3.1. Class I

In this class the PMO cluster anion is covalently linked to TMCs extending the dimensionality into 1-D chains, 2-D sheets or 3-D frameworks. Strandberg-type cluster $\{P_2Mo_5O_{23}\}^{6-}$ contribute substantial amount of structures to this class as compared to other cluster anions. Class I solids reported in the literature during the last decade with TMCs of Ni^{2+}, Co^{2+}, Cu^{2+} and Zn^{2+} have been summarized in Table I.1. One of the examples of Class I solids is discussed herein. $[H_3O]_2[Cu_2(Pyim)_2(H_2O)_3][P_2Mo_5O_{23}].6H_2O$ (where $Pyim$ = 2-(2′-pyridyl)-imidazole) reported by Hu *et. al.* [39] was synthesized under hydrothermal condition. The structure consists of $\{P_2Mo_5O_{23}\}^{6-}$ anion, two Cu^{2+} ions with different

coordination modes, two *Pyim* ligands, three coordinated water molecules and eight lattice water molecules. Cu(1) ion is five coordinated by two O atoms from two $\{P_2Mo_5O_{23}\}^{6-}$ clusters, two N atoms from one *Pyim* ligand and one O atom from a coordinated water molecule. The Cu(2) ion is six coordinated by two O atoms from two $\{P_2Mo_5O_{23}\}^{6-}$ anions, two N atoms from one *Pyim* ligand and two O atoms from two coordinated water molecules. It is interesting that each $\{P_2Mo_5O_{23}\}^{6-}$ cluster as a tetradentate inorganic ligand, connected by two Cu(1) and two Cu(2) complexes to form a 1-D infinite chain (refer Figure I.5).
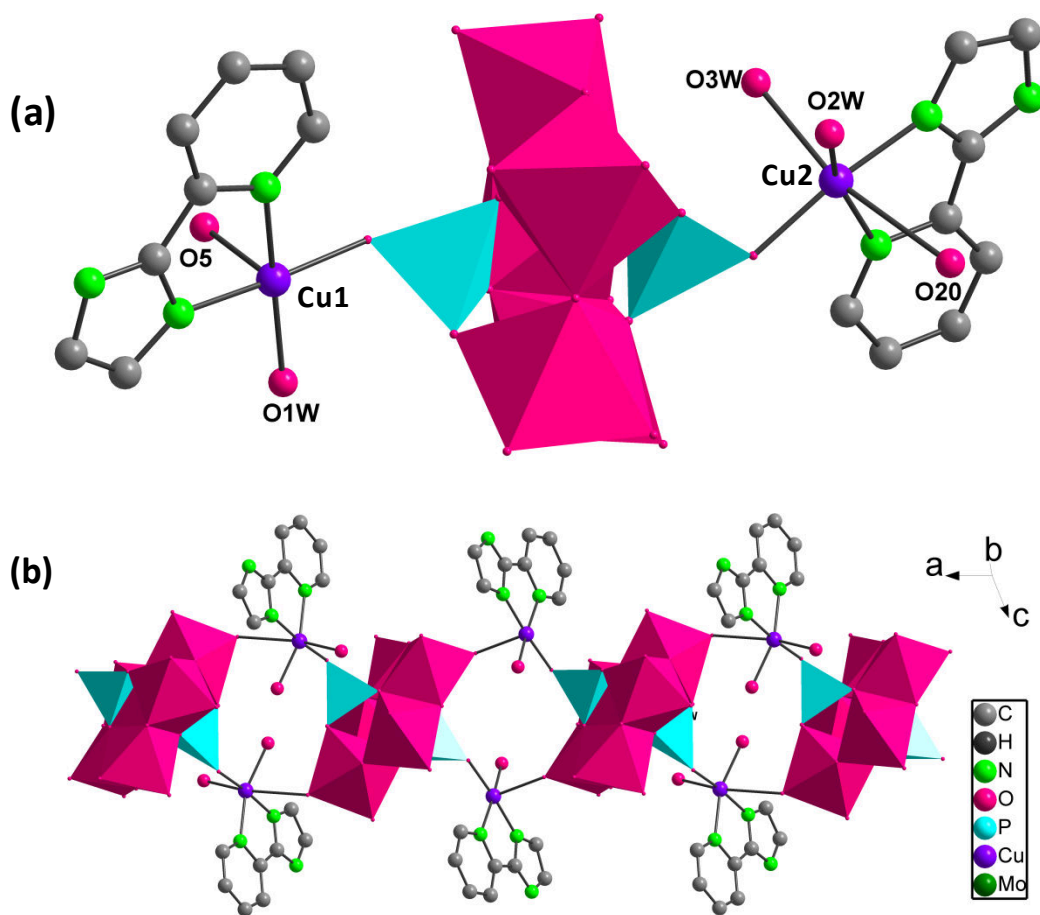
Figure I.5. (a) Figure showing coordination of $\{P_2Mo_5O_{23}\}^{6-}$ cluster anion with Cu(1) and Cu(2). (b) 1-D chain in $[H_3O]_2[Cu_2(Pyim)_2(H_2O)_3][P_2Mo_5O_{23}]\cdot 6H_2O$. The hydrogen atoms and lattice water molecules have been removed for clarity.

Table I.1 Class I solids wherein PMO clusters are covalently linked to TMCs extending into multi-dimensions.

Sl No	Solid	Cluster	Structure description	Dimens-ionality	Ref.
1	$(pz)_2[\{Co(pz)_4\}_5\{P_2Mo_5O_{23}\}_2].6H_2O$ (pz = pyrazole)	$\{P_2Mo_5\}$	Two Co-Pyrazole complex units covalently link $\{P_2Mo_5\}$ clusters to form 2-D sheets and the third Co-pz complex unit connects the sheet to form a double sheet	2-D	[26]
2	$(pz)\{Ni(pz)_4(H_2O)_2\}[\{Ni(pz)_4\}_5\{P_2Mo_5O_{23}\}_2].2H_2O$ (pz = pyrazole)	$\{P_2Mo_5\}$	Two Ni-pz complex units covalently link $\{P_2Mo_5\}$ cluster into 2-D sheets and third Ni-pz complex unit connects the sheets to form a double sheet	2-D	[26]
3	$\{Cu(pz)_4(H_2O)_2\}[\{Cu(pz)_4\}\{Cu(pz)_4(H_2O)\}\{P_2Mo_5O_{23}\}].2H_2O$ (pz = pyrazole)	$\{P_2Mo_5\}$	Two asymmetric octahedral Cu-pz complexes link $\{P_2Mo_5\}$ clusters into a double chain which is capped by a third octahedral Cu-pz complex unit. A fourth complex unit occurs in between the chains as a counter cation	2-D	[26]
4	$(pz)[\{Zn(pz)_3\}_3\{P_2Mo_5O_{23}\}].2H_2O$ (pz = pyrazole)	$\{P_2Mo_5\}$	$\{P_2Mo_5\}$ cluster is linked to four trigonal pyramidal Zn units $\{Zn(py)_3O_2\}$ and one tetrahedral $\{Zn(py)_3O\}$ unit to form a 3-D framework	3-D	[26]
5	$Na_8[\{Cu(H_2O)_4\}(HP_2Mo_5O_{23})_2].8H_2O$	$\{P_2Mo_5\}$	$[P_2Mo_5O_{23}]^{6-}$ cluster is connected by $\{Cu(H_2O)_4\}$ linkers to form 1-D wave-like chain	1-D	[29]
6	$Na_8[\{Co(H_2O)_4\}(HP_2Mo_5O_{23})_2].6H_2O$	$\{P_2Mo_5\}$	$[P_2Mo_5O_{23}]^{6-}$ cluster is connected by $\{Co(H_2O)_4\}$ linkers to form 1-D wave-like chain	1-D	[29]
7	$[H_3O]_2[Cu_2(Pyim)_2(H_2O)_3][P_2Mo_5O_{23}].6H_2O$ ($Pyim$ = 2-(2′-pyridyl)-imidazole)	$\{P_2Mo_5\}$	$\{P_2Mo_5O_{23}\}^{6-}$ clusters connected by copper complexes to generate one dimensional chain	1-D	[39]
8	$[Cu_3(Pyim)_3(H_2O)_4]$	$\{P_2Mo_5\}$	$\{P_2Mo_5O_{23}\}^{6-}$ clusters	1-D	[39]

	$[P_2Mo_5O_{23}]$.$7H_2O$ (*Pyim* = 2-(2′-pyridyl)-imidazole)		connected by copper complexes to generate one dimensional chain		
9	$(Himi)[\{Cu(imi)_4\}_2 (HP_2Mo_5O_{23})].3H_2O$ (*imi* = imidazole)	$\{P_2Mo_5\}$	Cu-O coordination mediates the formation of a 2D sheet with $(Himi)^+$ and water molecules in the cavities of the 2-D sheet	2-D	[40]
10	$[\{Cu(pz)_4\}_2 \{H_2P_2Mo_5O_{23}\}].H_2O$ (*pz* = pyrazole)	$\{P_2Mo_5\}$	$\{P_2Mo_5\}$ clusters with copper pyrazole complex to give a 3-D framework	3-D	[40]
11	$H_2[\{Cu(HL)(H_2O)\}_2 (P_2Mo_5O_{23})].5H_2O$ (H*L* = 2-acetylpyrazine thiosemicarbazone)	$\{P_2Mo_5\}$	Each Cu(II) is coordinated by one S atom and two N atoms of the ligand, O atom of the water molecule and one O_t atom of the cluster anion	3-D	[41]
12	$(C_5H_7N_2)_6[Cu(H_2O)_3 HP_2Mo_5O_{23}]_2.4H_2O$ (2-aminopyridine)	$\{P_2Mo_5\}$	Two bridging Cu(II) atoms link two adjacent P_2Mo_5 polyanions to give a centrosymmetric dimer $Cu_2(P_2Mo_5)_2$. The cluster is stabilized by O-H…O bonding	3-D	[42]
13	$[Cu(bim)_2]_2\{[Cu(bim)_2]_2 [PMo_9Mo_3O_{40}]\}$ (*bim* = benzimidazole)	$\{PMo_{12}\}$	The reduced Keggin PMo_{12} cluster is covalently bonded to two capping $[Cu^{II}(bim)_2]^{2+}$ fragments via its eight surface bridging oxygen atoms on two $\{Mo_4O_4\}$ faces or pits in the opposite positions	3-D	[43]
14	$[Cu(mim)_2]_4[PMo_{11}MoO_{40}].H_2O$ (*mim* = 2-methylimidazole)	$\{PMo_{12}\}$	Every $[Cu^I(mim)_2]_4 [PMo^{VI}_{11}Mo^VO_{40}]$ unit is connected with four adjacent ones to form a tetrahedral structure	3-D	[43]
15	$[Cu(en)(enH)]_2[P_2Mo_5O_{23}].3H_2O$ (*en* =ethylenediamine)	$\{P_2Mo_5\}$	Each $[P_2Mo_5O_{23}]^{6-}$ subunit is linked with adjacent four same subunits by four $[Cu(en)(enH)]^{3+}$ bridges	2-D	[44]
16	$(H_2en_6)\{[Zn(H_2O)_4] (P_2Mo_5O_{23})\}_3.10H_2O$ (*en* = ethanediamine)	$\{P_2Mo_5\}$	$[Zn(H_2O)_4]^{2+}$ connects adjacent $[P_2Mo_5O_{23}]^{6-}$ clusters to form 1-D chain	1-D	[45]
17	$(H_2en)[Cu(en)(H_2O)$	$\{P_2Mo_5\}$	Dinuclear Cu clusters	1-D	[46]

	Cu(*en*)(H$_2$O)$_3$][P$_2$Mo$_5$O$_{23}$].5.5H$_2$O (*en* = ethanediamine)		alternate with [P$_2$Mo$_5$O$_{23}$]$^{6-}$ clusters in 1-D chains		
18	(NH$_4$)$_{2n}${[Cu(*en*)$_2$][Cu(*en*)(H$_2$O)][P$_2$Mo$_5$O$_{23}$]}$_n$.3nH$_2$O (*en* = ethanediamine)	{P$_2$Mo$_5$}	The two different copper(II) fragments are connected to [P$_2$Mo$_5$O$_{23}$]$^{6-}$ clusters to form a 12-membered macrocycle. Cu(1) fragment is coordinated to the two phosphate oxygen atoms, and Cu(2) centre is bound to the 2 molybdenum oxygen atoms	1-D	[47]
19	(NH$_4$)$_{4n}${[Cu(*en*)(H$_2$O)][P$_2$Mo$_5$O$_{23}$]}$_n$.3.5nH$_2$O (*en* = ethylenediamine)	{P$_2$Mo$_5$}	1-D chains which is constructed from [P$_2$Mo$_5$O$_{23}$] clusters linked through [Cu(*en*)(H$_2$O)] subunits	1-D	[47]
20	[{Cu(H$_2$*biim*)(H$_2$O)}$_2${μ -Cu(H$_2$*biim*)(H$_2$O)}(P$_2$Mo$_5$O$_{23}$)].20H$_2$O (*biim* = 2,2' – biimidazole)	{P$_2$Mo$_5$}	Two tetra-supporting heteropolyoxoanions linked via two Cu(II) complex fragments	3-D	[48]
21	[Cu(H$_2$*biim*)$_2$(H$_2$O)][Cu(H$_2$*biim*)$_2$(HPO$_4$)$_2$(Mo$_5$O$_{15}$)].6H$_2$O	{P$_2$Mo$_5$}	Constructed from a [Cu(H$_2$*biim*)$_2$(H$_2$P$_2$Mo$_5$O$_{23}$)]$^{2-}$ polyoxoanion and a [Cu(H$_2$*biim*)$_2$(H$_2$O)]$^{2+}$ cation	3-D	[48]
22	[H$_2$*dahex*]$_4$[Zn(H$_2$O)]$_2${Zn[Mo$_6$O$_{12}$(OH)$_3$(HPO$_4$)$_2$(PO$_4$)$_2$]$_2$}.6H$_2$O (*dahex* = 1,6-diaminylhexane)	{P$_4$Mo$_6$}	Zn[P$_4$Mo$_6$]$_2$ clusters are linked by transition metal ions	3-D	[49]
23	(H$_2$*en*)$_3$(H$_2$*enme*)$_4$(H$_3$O){Cu[Mo$_6$O$_{12}$(OH)$_3$(HPO$_4$)(PO$_4$)$_3$]$_2$}.6H$_2$O (*en* = ethylene diamine *enme* = 1,2-diaminopropane)	{P$_4$Mo$_6$}	Cu bridges two [P$_4$Mo$_6$] clusters by six μ_3-O to form a sandwich-type anion. Clusters are bridged through N-H…O bonds from PO$_4$ tetrahedra and protonated organic amines	3-D	[50]
24	(H$_2$*enme*)$_4${Cu$_2$[Mo$_6$O$_{12}$(OH)$_3$(PO$_4$)(HPO$_4$)$_2$(H$_2$PO$_4$)]$_2$}.3H$_2$O (*enme* = 1,2-diaminopropane)	{P$_4$Mo$_6$}	Two Cu atoms are in two coordination environments. Cu(1) is four coordinate by 2 oxygen atoms from two adjacent anion. Cu(2) bridges two[P$_4$Mo$_6$] clusters via μ_3-O to form a	3-D	[50]

			sandwich-type anion		
25	(*L*)$_2$[Co(H$_2$O)$_4$ P$_2$Mo$_5$O$_{23}$].6H$_2$O *L*= 3-(ammoniomethyl) pyridine	{P$_2$Mo$_5$}	{P$_2$Mo$_5$} units linked by Co cations to form 1-D chain. The protonated ligands and the uncoordinated H$_2$O molecules connect adjacent chains into a 3-D supramolecular framework through hydrogen bonds	3-D	[51]
26	[Ag$_3$(*p*-H$_2$*pyttz*) (*p*-H*pyttz*)Cl] [H$_2$PMo$_{12}$O$_{40}$].6H$_2$O *p*-H$_2$pyttz = 3-(pyrid-4-yl)- 5(1H-1,2,4-triazol-3-yl)- 1,2,4-triazolyl)	{PMo$_{12}$}	PMo$_{12}$ anions are the building blocks facilitating the extension of the framework. Three Ag^I ions are independent with three kinds of distinct coordination	3-D	[69]

I.3.2. Class II

In this class of solids, PMO cluster exists as a discrete moiety and the negative charges of the anion is compensated by TMC cations. In some cases, along with TMC ions, protonated organic moieties also contribute towards charge compensation. {P$_2$Mo$_5$} and {P$_4$Mo$_6$} type anions mainly constitute Class II solids. For example, the structure of [Cu(*L*)$_2$ (H$_2$O)$_2$]$_2$H$_2$[P$_2$Mo$_5$O$_{23}$].2CH$_3$OH (*L* = pyridine-2-carboxamide) described by Ji *et. al.* [14] consists of one {P$_2$Mo$_5$O$_{23}$}$^{6-}$, two [Cu(*L*)$_2$(H$_2$O)$_2$]$^{2+}$ and two methanol molecules. Two Cu(II) ions are in similar coordination environment, with six coordinated distorted geometry. Each Cu(II) ion is coordinated by two N atoms and two oxygen atoms from two ligands and with two oxygen atoms of water molecules. Four negative charges on the doubly protonated cluster anion were compensated by two [Cu(*L*)$_2$(H$_2$O)$_2$]$^{2+}$ complexes (Figure I.6). The limited examples of Class II solids reported in literature have been summarized in Table I.2.
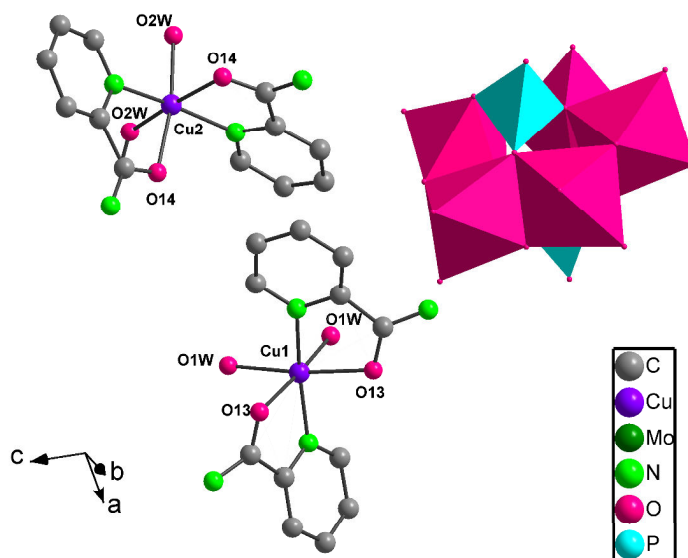
Figure I.6. Ball-and-stick and polyhedral representation of $[Cu(L)_2(H_2O)_2]_2H_2[P_2Mo_5O_{23}].2$ CH_3OH (L = pyridine-2-carboxamide). The hydrogen atoms and methanol molecules have been removed for clarity.

Table I.2. Class II solids having discrete PMO clusters with TMCs as counter cations

Sl No	Solid	Cluster	Structure description	Dimens-ionality	Ref.
1	$[Cu(L)_2(H_2O)_2]_2H_2$ $[P_2Mo_5O_{23}].2CH_3OH$ (L = pyridine-2-carboxamide)	{P_2Mo_5}	Doubly protonated $[P_2Mo_5O_{23}]^{6-}$ is surrounded by two $[Cu(L)_2(H_2O)_2]^{2+}$ complex ions	Discrete cluster	[14]
2	$(Himi)_6\{Cu(imi)_2\}_2$ $\{Cu(imi)_2(H_2O)\}_2$ $[Na\{(HPO_4)_4Mo_6(OH)_3O_{12}\}_2].$ $7H_2O$	{P_4Mo_6}	The crystal packing is mediated by Na $\{P_4Mo_6O_{31}\}_2$, Cu(I) complex, Himi^+ moieties and lattice water molecules	Discrete cluster	[40]
3	$[Ni(HL)_2]_2H_2[P_2Mo_5O_{23}].4H_2O$ (L = 2-acetylpyridine-thiosemicarbazone)	{P_2Mo_5}	It consists of $[P_2Mo_5O_{23}]^{6-}$ unit, two $[Ni(HL)_2]^{2+}$ cations, two protons and four lattice H_2O molecules	Discrete cluster	[52]
4	$[Co(L)_2(H_2O)_2]_2H_2[P_2Mo_5O_{23}].$	{P_2Mo_5}	Doubly protonated	Discrete	[53]

	2H$_2$O (*L* = pyridine-2-carboxamide)		[P$_2$Mo$_5$O$_{23}$]$^{6-}$ is surrounded by two [Co(*L*)$_2$(H$_2$O)$_2$]$^{2+}$ complex ions	cluster	
5	{(*Nhep*H$_2$)$_2$[Co(H$_2$O)$_6$]} [P$_2$Mo$_5$O$_{23}$].2H$_2$O *Nhep* = N-(2-hydroxyethyl)-piperazine	{P$_2$Mo$_5$}	[P$_2$Mo$_5$O$_{23}$]$^{6-}$ ion exists as a discrete moiety and the negative charges are compensated by both [Co(H$_2$O)$_6$]$^{2+}$ and *Nhep*H$_2$$^{2+}$	Discrete cluster	[54]

I.3.3. Class III

Class III consists of solids in which a metal ion may either substitute or cap the molybdenum centre. When one or more metal centers of classic PMO clusters are replaced by some transition metals (eg. Fe^{III}, Mn^{II}, Co^{II}, Ni^{II}, Zn^{II}) or any other element with similar properties (eg. W^{VI}, V^{V}), the resulting structure is known as 'lacunary' PMOs [55,56]. In this context, *Patel et. al*. have described the structure of Cs$_5$[PCo(H$_2$O)Mo$_{11}$O$_{39}$].6H$_2$O in which, Co was distributed over the 12 positions and Co could not be distinguished from the 11 Mo's distributed equally over the 12 addenda atoms in the Keggin structure [57]. Although this feature can be considered as a disorder; it releases possibilities for a new range of applications, particularly, in catalysis [58]. In some cases, the cluster anions are connected through a common oxygen atom to the metal centre [59]. Mainly keggin-type PMOs are included in this class. There are only limited examples of derivatized {P$_2$Mo$_5$} reported in the literature (refer Table I.3). In 2011, Jin *et. al*. have reported Mg[Cu(*bim*)(H$_2$O)]$_2$[P$_2$Mo$_5$O$_{23}$].4H$_2$O wherein each {P$_2$Mo$_5$} is decorated with [Cu(*bim*)(H$_2$O)]$^{2+}$ subunits (where *bim* = 2,2'-biimidazole) and the Mg atom which is positioned in between two {P$_2$Mo$_5$} clusters interacting with six oxygen atoms of the cluster anion and is extended to a 1-D chain as shown in Figure I.7 [59].
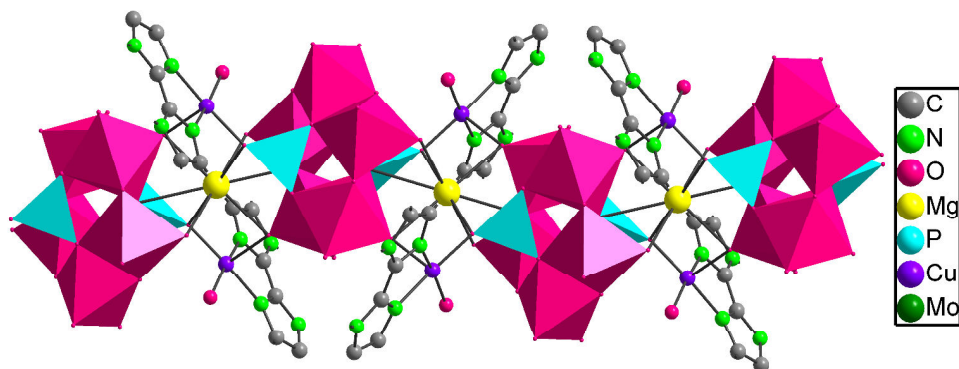
Figure I.7. 1-D chain of Mg[Cu(*bim*)(H$_2$O)]$_2$[P$_2$Mo$_5$O$_{23}$].4H$_2$O which depicts the linkage of Mg^{2+} ion through the oxygen atoms of the {P$_2$Mo$_5$}cluster anion.

Table I.3. Class III solids in which PMO clusters derivatized by TMCs.

Sl No	Solid	Cluster	Structure description	Dimens-ionality	Ref.
1	[Cu$_4$(*tea*)$_6$ (H$_4$PMo$_{11}$CuO$_{39}$) (PMo$_{12}$O$_{40}$)]$_2$.33H$_2$O (*tea* =2-[1,2,4]triazol-4-yl-ethylamine)	{PMo$_{11}$Cu}	Consists of tetra-nuclear clusters [Cu$_4$(tea)$_6$], linking a pair mono copper(II)-substituted and saturated Keggin anions	2-D	[13]
2	[Cu$_3$(*tea*)$_6$(H$_2$O)$_2$ (H$_2$PMo$_{11}$CuO$_{39}$)$_2$]$_2$. 30H$_2$O (*tea* =2-[1,2,4]triazol-4-yl-ethylamine)	{PMo$_{11}$Cu}	Contains tri-nuclear clusters [Cu$_3$(tea)$_6$], fusing four mono copper(II) substituted anions	Discrete cluster	[13]
3	(H*imi*)$_3$[{Cu (*imi*)$_3$(H$_2$O)$_2$ } {HP$_2$Mo$_5$O$_{23}$}].3H$_2$O	{P$_2$Mo$_5$}	The copper complex {Cu(*imi*)$_3$(H$_2$O)$_3$ derivatizes the {P$_2$Mo$_5$} cluster through Cu-O coordination to form {Cu(*imi*)$_3$(H$_2$O)$_2$} {HP$_2$Mo$_5$O$_{23}$}units	Discrete cluster	[40]
4	(*imi*)(H*imi*)$_2$[{Cu(*imi*)$_2$}$_2$ H$_2$P$_2$Mo$_5$O$_{23}$]	{P$_2$Mo$_5$}	Cu(I) complex derivatizes the {P$_2$Mo$_5$} cluster through Cu-O coordination. Oxygen atoms involved in derivatization belong to the same Mo centre	Discrete cluster	[40]

17

5	(*imi*)(H*imi*)$_2$[{Cu(*imi*)$_2$}$_2$ H$_2$P$_2$Mo$_5$O$_{23}$].H$_2$O	{P$_2$Mo$_5$}	Cu(I) complex derivatizes the {P$_2$Mo$_5$} cluster through Cu-O coordination. Oxygen atoms involved in derivatization belong to the neighboring Mo centre	Discrete cluster	[40]
6	(C$_5$H$_7$N$_2$)$_6$[Cu(H$_2$O)$_3$ HP$_2$Mo$_5$O$_{23}$]$_2$.4H$_2$O	{P$_2$Mo$_5$}	Two bridging Cu(II) atoms link two adjacent P$_2$Mo$_5$ polyanions to give a centrosymmetric dimer Cu$_2$(P$_2$Mo$_5$)$_2$	Discrete cluster	[42]
7	Cs$_5$[PCo(H$_2$O)Mo$_{11}$O$_{39}$]. 6H$_2$O	{PMo$_{11}$Co}	Transition metal Co and Mo atoms are distributed over 12 positions of Keggin cation	Discrete cluster	[57]
8	[Cu(H$_2$O)(*bim*)$_2$]{[Cu(H*bim*)$_2$][P$_2$Mo$_5$O$_{23}$]}.2H$_2$O *bim* = 2,2'-biimidazole	{P$_2$Mo$_5$}	Consists of one mono-supporting [Cu(H*bim*)$_2$] [P$_2$Mo$_5$O$_{23}$]}$^{2-}$ anion, one [Cu(H$_2$O)(*bim*)$_2$]$^{2+}$ counter ion and two lattice water molecules	Discrete cluster	[59]
9	[Cu(H*bim*)$_2$]{[Cu(*bim*) (H$_2$O)$_2$]$_2$[Cu(*bim*)$_2$]$_2$ [(P$_2$Mo$_5$O$_{23}$)$_2$]}.20H$_2$O *bim* = 2,2'-biimidazole	{P$_2$Mo$_5$}	Consists of one [Cu(H*bim*)$_2$] cation and an isolated bi-supporting {[Cu(*bim*)(H$_2$O)$_2$]$_2$[Cu (*bim*)$_2$]$_2$[(P$_2$Mo$_5$O$_{23}$)$_2$]}$^{4-}$ unit where the P$_2$Mo$_5$ cluster is supported by two distinct [Cu(*bim*)(H$_2$O)$_2$]$^{2+}$ and [Cu(*bim*)$_2$]$^{2+}$ fragments	Discrete cluster	[59]
10	[Cu(*phen*)(H$_2$O)][Cu (*bim*)$_2$]$_2$[P$_2$Mo$_5$O$_{23}$].H$_2$O *phen* =1,10-phenanthroline *bim* = 2,2'-biimidazole	{P$_2$Mo$_5$}	Consists of a tri-supporting [Cu(*phen*)(H$_2$O)] [Cu(*bim*)$_2$]$_2$[P$_2$Mo$_5$O$_{23}$] metal fragment and one lattice water molecule	Discrete cluster	[59]
11	Mg[Cu(*bim*)(H$_2$O)]$_2$ [P$_2$Mo$_5$O$_{23}$].4H$_2$O	{P$_2$Mo$_5$}	Consists of a Mg^{2+} cation, one {[Cu(*bim*) (H$_2$O)]$_2$[P$_2$Mo$_5$O$_{23}$]}$_2$ anion and four lattice water molecules. The neighboring {P$_2$Mo$_5$}	1-D	[59]

			clusters connect to each other via two [Cu(*bim*)(H$_2$O)]$^{2+}$ units and a Mg ion to form an unusual 1-D chain		
12	[Cu(*phen*)(*en*)] [Cu(*phen*)(*en*)(H$_2$O)]$_2$ [PMo$_8$Mo$_4$O$_{40}$ {Cu(*phen*)}$_2$]$_2$.6H$_2$O (*en* = ethylenediamine, *phen* = 1,10'-phenanthroline)	{PMo$_{12}$}	The reduced [PMo$_8$Mo$_4$O$_{40}$]$^{7-}$ is capped by two divalent Cu atoms through four bridging oxo groups on two opposite {Mo$_4$O$_4$} faces	3-D	[60]
13	[Cu(*L*)$_2$(H$_2$O)]H$_2$[Cu(*L*)$_2$ (P$_2$Mo$_5$O$_{23}$)].4H$_2$O (*L* = pyridine-2-carboxamide)	{P$_2$Mo$_5$}	(Cu*L*$_2$)(P$_2$Mo$_5$O$_{23}$)]$^{6-}$ polyanion, [Cu*L*$_2$]$^{2+}$ complex fragments and four water molecules	Discrete cluster	[61]
14	[Cu(*dmf*)$_6$][PMo$_{12}$O$_{40}$ Cu(*dmf*)$_4$]. *dmf* *dmf* = dimethyl formamide	{PMo$_{12}$}	Cu(1) interconnects two [PMo^{V}Mo$^{VI}_{11}$O$_{40}$]$^{4-}$ anion subunits and each [PMo^{V}Mo$^{VI}_{11}$O$_{40}$]$^{4-}$ polyoxoanion acts as a didentate ligand to link two Cu centers 1-D chain	1-D	[62]

I.3.4. Class IV

Class IV consists of solids in which organic ligands coordinated metal units are repeated and PMO clusters are incorporated within these metal-organic networks. Structure directing role of TMCs and multi-dentate ligands are equally important in the formation of coordination polymers [63-65]. Further, they can extend their dimensionality through H-bonding to form 2-D sheets and 3-D networks. For example, Hou *et. al.* have reported the formation 1-D chain in [Cu$_3$(4,4'-bis(pyrazol-1-ylmethyl)biphenyl)$_3$][PMo$_{12}$O$_{40}$] (refer Figure I.8). In this solid, the bidentate ligands bridges Cu(I) ions to form 1-D cationic chain. The {PMo$_{12}$} anion acts as a template, directing the {[Cu$_3$(*L*$_2$)$_3$]$^{3+}$} coordination chains. Solids belonging to this type have been summarized in Table I.4.

	C
	H
	Cu
	Mo
	N
	O
	P
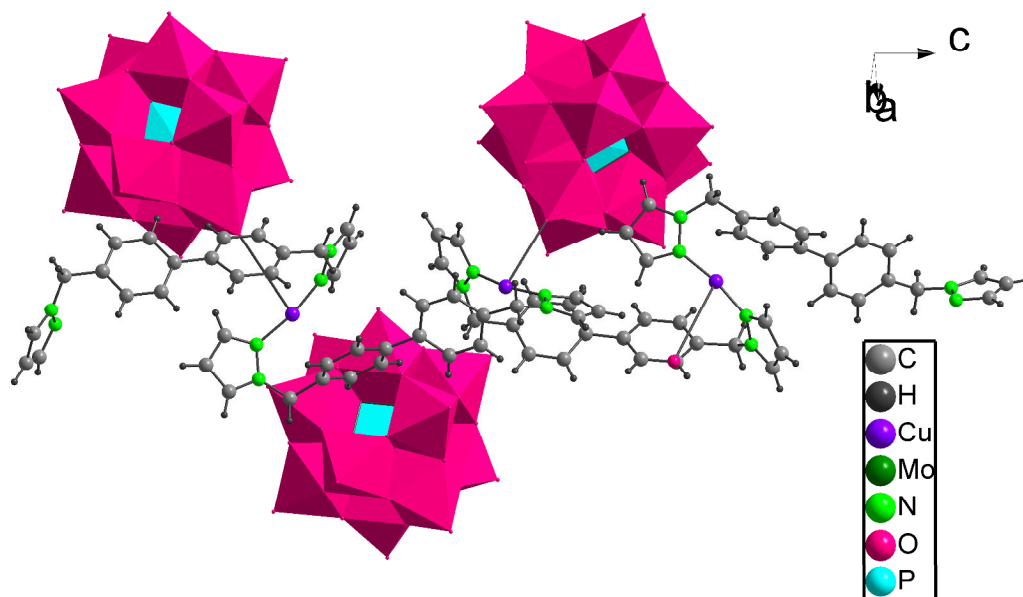
Figure I.8. 1-D chain formed in $[Cu_3(4,4'\text{-bis(pyrazol-1-ylmethyl)biphenyl})_3][PMo_{12}O_{40}]$

Table I.4. Class IV solids having coordination polymers incorporating PMOs.

Sl No	Solid	Cluster	Structure description	Dimens-ionality	Ref.
1	$(NH_4)_8[Co(bpy)_3]_2$ $\{[Ca(H_2O)_3]_2$ $[P_2Mo_5O_{23}]_3\}.21H_2O$ ($bpy = 2,2'$-bipyridine)	$\{P_2Mo_5\}$	Each Ca^{2+} cation is linked with three polyoxoanions, the formal $[Ca(P_2Mo_5O_{23})_{3/2}]$ subunits represent 3-connecting points forming a well-defined 3-D structure	3-D	[66]
2	$(NH_4)_5[Co(bpy)_3]$ $\{[Ca(H_2O)_4]_2[Ca(H_2O)]_6$ $[PMo_6O_{22}(PO_4)_3]_2\}.17H_2O$ ($bpy = 2,2'$-bipyridine)	$\{P_4Mo_6\}$	Ca^{2+} ions not only link polyoxoanions into the polymeric network but also connect phosphomolybdate clusters in dimers	3-D	[66]
3	$[Cu_3(L)_3][PMo_{12}O_{40}]$ $L = 4,4'$-bis(pyrazol-1-ylmethyl) biphenyl]	$\{PMo_{12}\}$	3-D supramolecular framework, which is formed by POM anions and $\{[Cu_3(L)_3]^{3+}\}_n$ cationic chains via hydrogen bonds	3-D	[67]
4	$[Cu_3(L)_4][PMo_{12}O_{40}]$	$\{PMo_{12}\}$	PMo_{12} cluster bridging	2-D	[67]

	[L = 1,4-bis (pyrazol-1-ylmethyl) benzene]		the Cu^I ions to form infinite straight POM anion based chains. These chains graft onto the cationic skeletons by sharing the Cu1 ions giving rise to a POM containing a 2-D form		
5	[$Cu_3(bmtr)_3(PMo_{12}O_{40})$] ($bmtr$ = 1,3-bis(1-methyl-5-mercapto-1,2,3,4-tetrazole)propane)	{PMo_{12}}	{$Cu_3(bmtr)_3$} forms a 1-D chain with [$PMo_{12}O_{40}$]$^{3-}$ polyanions and trinuclear clusters arranging alternately	1-D	[68]
6	[$Cu_6(m$-$pyttz)_2(H_2O)$] [$HPMo_{12}O_{40}$] (m-H_2pyttz = 3-(pyrid-3-yl)-5(1H-1,2,4-triazol-3-yl)-1,2,4-triazolyl)	{PMo_{12}}	m-$pyttz$ ligands link Cu^I ions to generate 2-D layers	2-D	[69]

I.4. Structural features in PMO cluster based solids

Supramolecular self-assembly of PMOs consists of a basic building block which is the cluster anion. The secondary building units such as metal ions / metal complex, organic moieties and solvent molecules play a vital role in the construction of desired structures. Besides, factors like temperature, pH, molar ratio of metal and organic part are also vital for the supramolecular self-assembly [70]. A careful examination of the reported PMO structures show unique structural features particularly supramolecular isomerism, association of water clusters and porosity.

I.4.1. Supramolecular isomerism

According to Moulton and Zaworotko, "Supramolecular isomerism in this context is the existence of more than one type of network superstructure for the same molecular building blocks and is therefore related to structural isomerism at the molecular level. In other words,

the relationship between supramolecular isomerism and molecules is similar to that between molecules and atoms. In some instances, supramolecular isomerism can be a consequence of the effect of the same molecular components generating different *supramolecular synthons* and could be synonymous with polymorphism" [71]. In context of PMO cluster based solids, it can be explained using the following example. Thomas *et. al*. have reported two supramolecular isomers (*imi*)(H*imi*)$_2$[{Cu(*imi*)$_2$}$_2$H$_2$P$_2$Mo$_5$O$_{23}$] and (*imi*)(H*imi)*$_2$[{Cu(*imi*)$_2$}$_2$H$_2$P$_2$Mo$_5$O$_{23}$].H$_2$O [40] (Figure I.9). In both the isomers, Cu(I) complex derivatizes the {P$_2$Mo$_5$} cluster anion; but the manner of derivatization is different. In the first solid Cu^I-*imi* complex derivatizes {P$_2$Mo$_5$} cluster through oxygen atoms belonging to same Mo atom whereas in the second solid the derivatization occurs through oxygen atoms bonded to neighboring Mo atoms.

I.4.2. Aggregation of water clusters

Presence of water molecules in crystal structure provides dynamism in dimensionality and properties. The possibility of H-bonding increases the stability of the crystal packing. Occurrence of water clusters such as tetramers, pentamers and hexamers in metal–organic frameworks and the role of these water clusters in the supramolecular interactions have been reported in literature [72]. Thomas *et. al.* explained the crystal structure of (H*imi*)$_3$[{Cu(*imi*)$_3$(H$_2$O)$_2$} {HP$_2$Mo$_5$O$_{23}$}].3H$_2$O in which the decameric water cluster played a vital role in crystal packing of the solid (refer Figure I.10) [40].
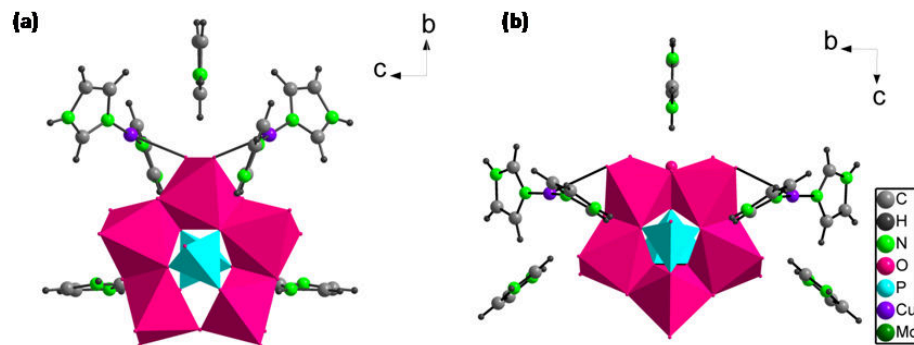
Figure I.9. Supramolecular isomerism exhibited by (a) (*imi*)(H*imi*)$_2$[{Cu(*imi*)$_2$}$_2$ H$_2$P$_2$Mo$_5$O$_{23}$].
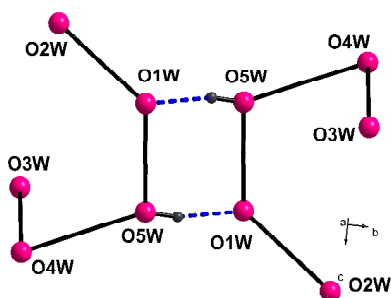
Figure I.10. Decameric water cluster in (H*imi*)$_3$[{Cu(*imi*)$_3$(H$_2$O)$_2$}{HP$_2$Mo$_5$O$_{23}$}].3H$_2$O.

1.4.3. Porosity

Usually POMs exhibit microporous or mesoporous behavior and extensive macroporosity has not been observed. Ammonium phosphomolybdate {NH$_4$}$_3$[PMo$_{12}$O$_{40}$].xH$_2$O, a Keggin-type PMO is a well studied example of porous PMOs [73-74]. The {PMo$_{12}$} cluster anions are linked by ammonium ions through H-bonding to form a 2-D sheet (refer Figure I.11). In 2011, Monge *et. al.* investigated the role of anions in ammonium salts used as precursor for the formation of ammonium phosphomolybdate. It was observed that the microporous / mesoporous pore size could be altered depending upon the anionic part in the ammonium salts. They tested the following salts: NH$_4$Cl, NH$_4$NO$_3$, (NH$_4$)$_2$SO$_4$, NH$_4$F, NH$_4$CH$_3$CO$_2$, (NH$_4$)$_2$C$_2$O$_4$, and (NH$_4$)$_2$CO$_3$ and found that nature of anion counter part of the ammonium

salt played a crucial role in the development of pore texture and pore size of microporous / mesoporous material [75]. On account of their porosity, PMOs are widely used as heterogeneous catalysts and adsorbents [76-78].
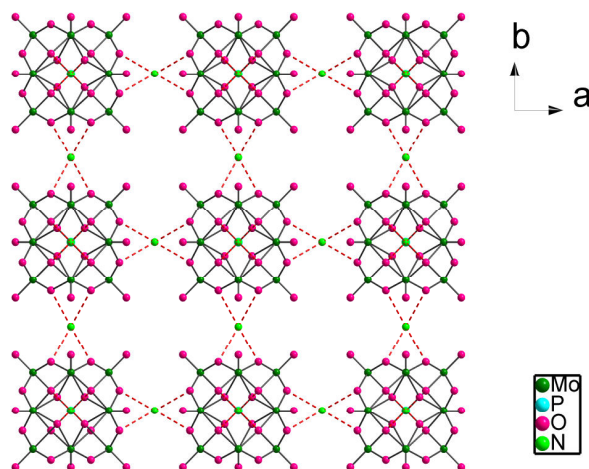
Figure I.11. $\{PMo_{12}\}$ clusters are linked by ammonium ions through H-bonding interaction (shown in dashed red lines) to form porous 2-D sheet in ammonium phosphomolybdate.

I.5. Synthetic strategies

In order to synthesize PMO cluster based solids mainly solvent evaporation technique and hydrothermal synthesis have been adopted in the present work. A brief explanation of each technique is given below.

I.5.1. Solvent evaporation technique

For the synthesis of $\{P_2Mo_5\}$ based solids, two different aqueous solutions with calculated molar ratio of $Na_2MoO_4.2H_2O$ (as the source of Mo) and metal chloride (to which organic ligand was added) were prepared. These two solutions are mixed while stirring and acidified with 1M H_3PO_4 (H_3PO_4 acts as the source of PO_4) and desired pH was adjusted with the same. The resultant solution was filtered in case of suspended particles and the clear solution

was kept undisturbed for crystallization in room temperature. The crystallized solids were filtered, washed with water and acetone and allowed to dry at room temperature.

I.5.2. Hydrothermal synthesis

One-pot hydrothermal synthesis is a commonly employed technique for the synthesis of PMOs. The reaction is carried out under autogenous pressure in a sealed Teflon container. All the precursors were added along with water. The reduced viscosity and iconicity of the solvent under high temperature and pressure conditions enhances the diffusion of the reactants and results in the self-assembly of the products. A temperature range from 100-$250^{o}C$ can be used in a time span of 3-5 days. The slow cooling of the apparatus is allowed and product obtained was washed with water and acetone. The problem of low solubility of organic ligands in water can be resolved using this technique. A number of PMO based solids have been synthesized by hydrothermal method.

I.6. Applications of PMOs

PMOs on account of their tunable topology structures and reversible redox characteristics have found potential applications in various areas. The combination of metal-organic coordination with classical PMOs lead to a fascinating world of hybrid solids with potential magnetic, electronic, catalytical, optical, electrochemical and biological properties. Some dominant fields in which PMOs found remarkable applications are explained below.

I.6.1. Biomedicinal applications

The anticancer activity of PMOs were first reported in 1965, as the *in vivo* application of a mixture of $H_3[PW_{12}O_{40}]$, $H_3[PMo_{12}O_{40}]$ and caffeine, on patients suffering from

gastrointestinal cancer [79] and it was not subjected to further clinical studies. But today promising biological activities of PMOs are well documented in the literature; although the mechanism of action is still veiled. PMOs were found as potential inorganic drugs as anti-bacterial, anti-viral, anti-Alzheimer and anti-cancer agents [41,45,80]. It has been proposed that the therapeutic effects of some PMOs on cancerous cells are better than those of commercially available cancer drugs [41]. However, the cytotoxicity of PMOs on normal cells is a challenge. The biological properties of Strandberg-type PMOs are well established as compared to other cluster anions. Ji *et. al.* reported the effective *in vitro* activity of three $\{P_2Mo_5\}$ based solids $[Cu(L)_2(H_2O)_2]_2$ $[H_2P_2Mo_5O_{23}].2CH_3OH$, $[Cu(L)_2(H_2O)][Cu(L)_2(H_2P_2Mo_5O_{23})].4H_2O$ and $[Cd(L)_2(H_2O)_2]_2$ $[H_2P_2Mo_5O_{23}].2CH_3OH$, (where L = pyridine-2-carboxamide) against HepG2 cells, HCT-116 cells and SMMC-7721 [81]. It is notable that both the coordination mode and the type of metal ion played important role in the cytotoxicity. $[Co(L)_2(H_2O)_2]_2[H_2P_2Mo_5O_{23}].2H_2O$ (where L = pyridine-2-carboxamide) disclosed potent activities against both HepG2 (human hepatocellular carcinoma) cells and HCT-116 (human colorectal cancer) cells and lower toxicity against normal HL-7702 (human normal hepatocyte) cells [53]. A nano-linear Zn-substituted $(H_2en)_6\{[Zn(H_2O)_4][P_2Mo_5O_{23}]\}_3.10H_2O$ (where en = ethanediamine) could inhibit the proliferation of *Escherichia coli (E. coli).* Zhao *et. al.* investigated the biological studies of $[\{Cu(HL)(H_2O)\}_2(H_2P_2Mo_5O_{23})].5H_2O$ (where L=2-acetylpyrazine thiosemicarbazone) and reported it's moderate antibacterial activity against *E. coli* and *Staphylococcus aureus (S. aureus)*, and a better cytotoxicity against human hepatic cancer line (SMMC-7721) than Mitoxantrone , the current clinical anti-cancer drug [41]. In all the cases, researchers

mentioned that the synergistic effect of metal ion, organic moiety and the cluster anion was responsible for the biological activity.

On the other hand, there are studies which show that even without the presence of metal ion, the combination of organic ligands and PMO cluster alone can produce desirable results. For example, the *in vitro* anti-tumoral activity of the solid [{4,4'-H$_2$*bpy*}{4,4'-H*bpy*}$_2${H$_2$P$_2$Mo$_5$O$_{23}$}].5H$_2$O (where 4,4'-*bpy* = 4,4'-bipyridine) was tested against human breast cancer (MCF-7), human lung cancer (A549) and human liver cancer (HepG2) cells by Joshi *et. al.* and it was found that the solid showed anti-tumoral activity comparable to that of the commonly used chemotherapeutic agent Methotrexate [27]. [H*biz*]$_5$[HMo$_5$P$_2$O$_{23}$].5H$_2$O (where *biz*=benzimidazole) also showed *in vitro* anti-tumor activities against human neuroblastoma SHY5Y cells [82]. Advanced research is going on to develop PMO based next generation anti-tumor drugs which can selectively inhibit the affected cells while protecting the normal ones.

I.6.2. Applications in catalysis

PMOs have good catalytic properties by virtue of its super acidity and structural stability by which it can undergo multi-electron redox cycles. The catalytic behavior is remarkable both in activity and reusability. On account of the steric effect of the cluster based solids, they show regioselectivity and even enantioselectivity [83]. POM solids can also be used as both photocatalyst and electrocatalyst [84-87]. For example, three efficient and reusable catalysts for the protection of carbonyl compounds with glycol were reported by Li *et. al.* namely {H$_4$(H$_2$*biim*)$_3$}[Zn(H$_2$*biim*)(H$_3$*biim*)(H$_2$O)(HP$_2$Mo$_5$O$_{23}$)]$_2$.3H$_2$O, {H$_9$(H$_2$*biim*)$_7$}[(μ-*biim*){(Zn(H$_2$O)$_2$)$_{0.5}$(HP$_2$Mo$_5$O$_{23}$)}$_2$].7H$_2$O and {H$_7$(H$_2$*biim*)$_7$}[Zn(H$_2$*biim*)(H$_2$O)$_2$(HP$_2$Mo$_5$O$_{23}$)][H$_2$P$_2$Mo$_5$O$_{23}$].8H$_2$O (where *biim* = 2,2'-biimidazole) [88]. These are considered as the first

example where Strandberg-type PMOs are used as acid catalysts in an organic reaction. Paul *et. al.* synthesized two hybrid solids based on PMOs, $(NHEPH_2)_5$ $[Ni(P_4Mo_6O_{31})_2].6H_2O$ and $\{(NHEPH_2)_2[Co(H_2O)_6]\}[P_2Mo_5O_{23}].2H_2O$ (where *NHEP* = N-(2-hydroxyethyl)-piperazine) under hydrothermal conditions [54]. Both these solids were reported as excellent heterogeneous catalysts for the oxidation of styrene in the presence of an environmentally benign oxidant H_2O_2 under mild conditions to obtain benzaldehyde with more than 80% selectivity.

Solvent free green selective oxidation of alcohols catalysed by mono transition metal substituted Keggin-type $PMo_{11}M$ (M = Co, Mn, Ni) using hydrogen peroxide was reported by Pathan and co-workers with higher selectivity for the desired product [58]. Zhang *et. al.* tested the catalytic activity of three Keggin-type PMOs namely $(2\text{-}C_5H_7N_2)_4(PMo_{12}O_{40})_2(2\text{-}C_5H_6N_2)_6(C_4H_8N_4).H_2O$, $(3\text{-}C_5H_7N_2)_6(PMo_{12}O_{40})_2(3\text{-}C_5H_6N_2)_4H_8O_4(H_2O)_8$ and $(4\text{-}C_5H_7N_2)_6(PMo_{12}O_{40})_2(4\text{-}C_5H_6N_2)_4(C_4H_6N_3)$ towards the oxidation of acetone [78]. The first and third solids were found to be more effective than the second one due to the different intensity and number of H-bonds which could be responsible for the adsorption ability of the reactants.

The most attractive group among PMOs in the area of catalysis are the fully reduced type $\{P_4Mo_6\}$, in which all the Mo atoms are in the reduced +5 valences. The reduced Mo^V centers of $\{P_4Mo_6\}$ exhibit d^1 electronic configuration, resulting a greater distribution of electronic density throughout the entire cluster. Moreover, they exist as hourglass-type structure where two half units of $[P_4Mo_6O_{31}]^{12-}$ are bridged in a centrally antisymmetric manner through a metal atom. A number of studies have been reported in literature on the effective reduction of hexavalent chromium, a highly toxic environmental pollutant [89-90].

Wang *et. al*. described the reduction of Cr^{VI} using three hybrid solids based upon hourglass-type $\{Mn[P_4Mo_6]_2\}$ units surrounded by protonated 1,3-bi(4-pyridyl)propane (abbreviated as *bpp*) ligands which are $(H_2bpp)_5[Na(Hbpp)]_6H_{10}\{Mn [Mo_6O_{12} (OH)_3(HPO_4)_4]_2\}_4.14H_2O$, $Na_4(H_2bpp)_2[Mn(H_2O)_7]\{Mn[Mo_6O_{12}(OH)_3(HPO_4)_3(PO_4)]_2\}.2H_2O$ and $Na(H_2O)_2(Hbpp)_3[Na_2(bpp)(H_2O)][Mn_2(H_2O)_5]\{Mn[Mo_{12}O_{24}(OH)_6(HPO_4)_6(H_2PO_4)(PO_4)]\}$ $(HPO_4).H_2O$. Formic acid is used as the reducing agent and no secondary pollutants are formed during the process [37]. Compared to the traditionally used Pt/Pd nanoparticle catalyst these are less expensive and easy to prepare. Gong *et. al*. reported the same set of three $\{P_4Mo_6\}$ based PMOs as effective molecular catalysts for performing inorganic electron transfer reaction of ferricyanide to ferrocyanide by thiosulphate with high rate constants under mild conditions [84]. A series of Zn based $\{P_4Mo_6\}$ solids were reported as good photocatalysts for Cr^{VI} reduction on account of their wide visible-light absorption, suitable energy band structures and specific spatial arrangements of polyanionic species [91]. Recently, a few groups are developing composite materials based on PMOs such as sodium carboxymethyl cellulose – ammonium phosphomolybdate composites and phosphomolybdic acid – polyaniline – graphene composites as efficient and cost-effective heterogeneous catalysts [92].

I.6.3. Applications in magnetism

PMOs with electronic configurations other than d^0 like d^1 exhibit magnetic properties. Designing PMOs and their derivatives with unpaired electron system or with encapsulated small clusters of magnetic metal ions like Co(II) and nickel (II) can result in interesting magnetic behavior. According to Clemente-Juan *et. al*. PMOs have some advantages when compared to other coordination compounds. The robust POM molecule can keep their

integrity in solid state and in solutions. They can accommodate magnetic ions at the specific sites of their rigid structure leading to magnetic molecules [93]. By maintaining their structure they can accept electrons leading to a mixed valence system in which the extra electrons are widely delocalized over the framework. For example, Hu *et. al.* have reported two Strandberg-type PMOs $[H_3O]_2[Cu_2(Pyim)_2(H_2O)_3][P_2Mo_5O_{23}].6H_2O$ and $[Cu_3(Pyim)_3(H_2O)_4][P_2Mo_5O_{23}].7H_2O$ (where *Pyim* = 2-(2′-pyridyl)-imidazole) which exhibit antiferromagnetic interactions between copper ions [39].

I.6.4. Electrochemical applications

One of the fascinating properties of PMOs is their reversible multivalent reduction capability. Most of them have the ability to accept and release specific number of electrons without any change in their structural arrangement. However, PMOs face some challenges while they are used in electrocatalysis and other electrochemical applications. The main drawbacks are,

  (i) low specific surface area

  (ii) high water solubility

  (iii) requirement of additional potential energy to increase the rate of electrochemical reactions

  (iv) lack of selectivity and

  (v) possible precipitation or adsorption of some PMO species on the substrate that may interfere with the measurements [94].

These problems can be solved by dispersing or immobilizing PMOs on various supports like polymers, nanoparticles, silica and carbon materials to enhance the number of active sites and to improve their electrochemical properties. In literature, a number of PMO based

composite materials based on Keggin-type PMO_{12} have been reported (discussed in Chapter VI). They can undergo multi-electron reversible redox processes. So, they have been exploited in a broad range of electrochemical applications such as electrocatalysts, energy storage systems and sensors. For example, Attapulgite/polyaniline/phosphomolybdic acid-based modified electrodes were used for the electrochemical determination of iodate [95]. The method showed advantages like good reproducibility, fast amperometric response and rapid preparation. Phosphomolybdic acid-polypyrrole/graphene composite modified glassy carbon electrode has been fabricated by Wang *et. al.* for the sensitive determination of folic acid based on the inhibitory activity of folic acid on account of the redox behavior of Keggin-type phosphomolybdic acid [96]. Papagianni *et. al*. introduced PMo_{12}-polyaniline composite as an electrochemical sensor for the determination of BrO_3^- ions [97]. On the contrary, the electrochemical properties of only few Strandberg-type PMOs have been investigated. For example, Wang *et. al.* reported three electrocatalysts $Na_{10}[Ag(P_2Mo_5O_{23})]_2.8H_2O$, $Na_8[\{Cu(H_2O)_4(HP_2Mo_5O_{23})_2\}].8H_2O$ and $Na_8[\{Co(H_2O)_4\}(HP_2Mo_5O_{23})_2].6H_2O$ for the reduction of hydrogen peroxide [29].

I.7. Motivation for the present study

PMOs are an important subclass of polyoxometalates with multi-faceted structures and distinctive properties. It is evident from literature that the area of PMOs is growing fast due to its promising applications. In this context, exploring the synthesis, characterization and investigation of properties of structurally diverse PMOs is an emergent area of interest. The self-assembly process of PMOs facilitates the incorporation of TMCs and organic cations during the aggregation of molecular precursors. Moreover, the properties of the solids can vary with the size and type of organic ligands; and the coordination complexes incorporated.

Transition metal containing molybdates are potential solids due to enhanced catalytic activity especially as oxidative catalysts. Incorporating TMCs can result in various solids ranging from discrete clusters to 3-D architectures. The ability to exhibit variable oxidation states enables the metal centers to exhibit different coordination preferences. In addition, TMCs are capable of exhibiting supramolecular interactions such as hydrogen bonding, CH…π and π…π stacking which influence the self-assembly of various architectures. Besides, TMCs based solids can also function as model systems to explore magnetic interactions such as localized spin interactions and can expand its application in the area of magnetism. Therefore based on the above observations, the major objectives of the thesis are,

(i) Systematically investigate the effect of metal ion/complex, organic moiety and reaction condition (ambient or hydrothermal) in the formation of PMO cluster based solids.

(ii) Explore the role of supramolecular interactions particularly hydrogen bonding, CH…π and π...π stacking in crystal packing of the synthesized solids.

(iii) Investigate electrochemical and magnetic properties of amine and TMC incorporated PMO solids respectively.

(iv) Evaluate the effectiveness of various PMO based solids in removing dye-stuffs from contaminated fresh water sources.

(v) Synthesize ammonium phosphomolybdate / polymer composites and investigate the properties along with the efficiency towards the removal of Cr(VI) from its aqueous solution.

References

1. Pope, M. T.; Muller, A. *Angew. Chem. Ind. Ed. Engl*. **1991**, 30, 34-48.

2. Zheng, S. T.; Yang, G. Y. *Chem. Soc. Rev*. **2012**, 41, 7623-7646.

3. Zong, L.; Wu, H.; Lin, H.; Chen, Y. *Nano Res*. **2018**, 11, 4149-4168.

4. Streb, C. *Dalton Trans*. **2012**, 41, 1651-1659.

5. Zhang, J.; Huang, Y.; Li. G.; Wei, Y. *Coord. Chem. Rev*. **2019**, 378, 395-414.

6. Ma, P.; Hu, F.; Wang, J.; Niu, J. *Coord. Chem. Rev*. **2019**, 378, 281-309.

7. Jiao, Y. Q.; Zang, H. Y.; Wang, X. L.; Zhou, E, L.; Song, B. Q.; Wang, C. G.; Shao, K. Z.; Su, Z. M. *Chem. Commun*. **2015**, 51, 11313-11316.

8. Berzelius, J. J. *Annalen der physic*. **1826**, 83, 261-288.

9. Keggin, J. F. *Nature* **1933**, 131, 908-909.

10. Niu, J.; Ma, J.; Zhao, J.; Ma, P.; Wang, J. *Inorg. Chem. Commun*. **2011**, 14, 474-477.

11. Zhang, L.; Li, X.; Zhou, Y.; Wang, X. J. *Mol. Struct*. **2009**, 928, 59-66.

12. Yan, D.; Fu, J.; Zheng, L.; Zhang, Z.; Xu, Y.; Zhu, X.; Zhu, D. *CrystEngComm*. **2011**, 13, 5133-5141

13. Tian, A.; Ni, H.; Tian, Y.; Ji, X.; Liu, G.; Ying, J. *Inorg. Chem. Commun*. **2016**, 68, 50-55.

14. Ji, Y. M.; Fang, Y.; Han, P. P.; Li, M. X.; Chen, Q. Q.; Han, Q. X. *Inorg. Chem. Commun.* **2017**, 86, 22-25.

15. Peng, Z. S.; Huang, Y. L.; Lu, S. Z.; Tang, J. T.; Cai, T. J.; Deng, Q. *Synth. React. Inorg. Met.-Org. Nano-Metal Chem.* **2014**, 44, 376-382.

16. Hu, G.; Dong, Y.; He, X.; Miao, H.; Zhou, S.; Xu, Y. *Inorg. Chem. Commun*. **2015**, 60, 33-36.

17. Qi, M.; Yu, K.; Su, Z.; Wang, C.; Wang, C.; Zhou, B.; Zhu, C. *Inorg. Chim. Acta* **2013**, 400, 59-66.

18. Qi, M. L.; Yu, K.; Su, Z. H.; Wang, C. X.; Wang, C. M.; Zhou, B. B.; Zhu, C. C. *Dalton Trans.* **2013**, 42, 7586-7594.

19. Meng, F. X.; Lv, J. H.; Yu, K.; Zhang, M. L.; Wang, K. P.; Zhou, B. B. *New. J. Chem.* **2018**, 42, 19528-19536.

20. Fu, Y. H.; Chen, X. Y.; Yang, W.; Bai, Y.; Dang, D. B. *Mater. Lett.* **2015**, 155, 48-50.

21. Wang, X.; Peng, J.; Alimaje, K.; Zhang, Z.; Shi, Z. *Inorg. Chem. Commun.* **2013**, 36, 141-145.

22. Yan, D.; Zheng, L.; Zhang, Z.; Wang, C.; Yuan, Y.; Zhu, D.; Xu, Y. *J. Coord. Chem.* **2010**, 63, 4215-4225.

23. Ren, Y.; Wang, M.; Chen, X.; Yue, B.; He, H. *Materials* **2015**, 8, 1545-1567.

24. Strandberg, R. *Acta Chem. Scand.* **1973**, 27, 1004-1018.

25. Gao, G.; Hong, H, G.; Mallouk, T. E. *Acc. Chem. Res.* **1992**, 25, 420.

26. Thomas, J.; Ramanan, A. *Inorg. Chim. Acta* **2011**, 372, 243-249.

27. Joshi, A.; Gupta, R.; Singh, B.; Sharma, D.; Singh, M. *Dalton Trans.* **2020**, 49, 7069-7077.

28. Asnani, M.; Kumar, D.; Duraisamy, T.; Ramanan, A. *J. Chem. Sci.* **2012**, 124, 1275-1286.

29. Wang, C.; Shi, J.; Yu, K.; Zhou, B. B. B. *J. Coord. Chem.* **2018**, 71, 3970-3979.

30. Lu, T.; Feng, S. L.; Zhu, Z. M.; Sang, X. J.; Su, F.; Zhang, L. C. *J. Solid State Chem.* **2017**, 253, 52-57.

31. Sun, S.; Liu, X.; Yang, L.; Tan, H.; Wang, E. *Eur. J. Inorg. Chem.* **2016**, 2016, 4179-4184.

32. Feng, S. L.; Lu, Y.; Zhang, Y. X.; Su, F.; Sang, X. J.; Zhang, L. C.; You, W. S.; Zhu, Z. M. *Dalton Trans.* **2018**, 47, 14060-14069.

33. Li, D.; Ma, P.; Niu, J.; Wang, *J. Coord. Chem. Rev.* **2019**, 392, 49-80.

34. Han, Z.; Gao, Y.; Zhai, X.; Peng, J.; Tian, A.; Zhao, Y.; Hu, C. *Cryst. Growth Des.* **2009**, 9, 1225-1234.

35. Li, L.; Ma, P.; Wang, J.; Niu, J. *Inorg. Chem. Commun.* **2013**, 34, 23-26.

36. Amman, M. *J. Mater. Chem. A* **2013**, 1, 6291-6312.

37. Wang, X.; Wang, J.; Geng, Z.; Qian, Z.; Han, Z. *Dalton Trans.* **2017**, 46, 7917-7925.

38. Dong, Y.; Dong, Z.; Zhang, Z.; Liu, Y.; Cheng, W.; Miao, H.; He, X.; Xu, Y. *ACS Appl. Mater. Interfaces* **2017**, 27, 22088-22092.

39. Hu, G.; Dong, Y.; He, X.; Miao, H.; Zhou, S.; Xu, Y. *Inorg. Chem. Commun.* **2015**, 60, 33-36.

40. Thomas, J. ; Kumar, D. ; Ramanan, A. *Inorg. Chim. Acta* **2013**, 396, 126–135.

41. Zhao, H.; Li, J.; Fang, Y.; Chang, B.; Meng, Q.; Li, M.; Wang, C.; Zhu, X. *Bioorg. Med. Chem. Lett.* **2020**, 30, 126781-126786.

42. Ammari, Y.; Dhahri, E.; Rzaigui, M.; Hlil, E. K.; Abid, S. *J. Clust. Sci.* **2016**, 27, 1213-1227.

43. Hu, J. K.; Yu, X. Y.; Luo, Y. H.; Wang, X. F.; Yue, F. X.; Zhang, H.; *Inorg. Chem. Commun.* **2013**, 32, 37-41.

44. Zhao, W. J.; Li, Y. Y.; Wang, Y. H.; Shi, D. Y.; Luo, J.; Chen, L. J. *Russ. J. Coord. Chem.* **2013**, 39, 519-523.

45. Ma, X.; Zhou, F.; Yue, H.; Hua, J.; Ma, P. *J. Mol. Struct*. **2019**, 1198, 126865-126872.

46. Ma, X.; Zhang, C.; Hua, J.; Ma, P.; Wang, J.; Niu, J. *CrystEngComm.* **2019**, 21, 394-398.

47. Buvailo, H. I.; Makhankova, V. G.; Kokozay, V. N.; Zatovsky, I. V.; Omelchenko, I. V.; Shishkina, S. V.; Zabierowski, P.; Matoga, D.; Jezierska, J. *Eur. J. Inorg. Chem.* **2016**, 2016, 5456-5466.

48. Wang, Y. ; Zhang, L. C. ; Zhu, Z. M. ; Li, N. ; Deng, A. F. ; Zheng, S. Y. *Transition Met. Chem*. **2011**, 36, 261-267.

49. Xu, X.; Ju, W.; Yan, D.; Jian, N.; Xu, Y. *J. Coord. Chem*. **2013**, 66, 2669-2678.

50. Xu, X.; Yan, D.; Fan, X.; Xu, Y. *J. Coord. Chem*. **2012**, 65, 3674-3683.

51. Ammari, Y.; Baaalla, N.; Hlil, E.K. *Sci. Rep.* **2020**, 10, 1316-1328.

52. Li, J.; Zhao, H.; Ma, C.; Han, Q.; Li, M.; Liu, H. *Nanomaterials* **2019**, 9, 649.

53. Ji, Y. M.; Zhao, M.; Han, P. P.; Fang, Y.; Han, Q. X.; Li, M. X. *J. Inorg. Nano-Met. Chem*. **2018**, 48, 421-425.

54. Paul, L.; Dolai, M.; Panja, A.; Ali, M. *New J. Chem.* **2016**, 40, 6931-6938.

55. Patel, A.; Narkhede, N.; Singh, S.; Pathan, S. *Cat. Rev. - Sci. Eng*. **2016**, 58, 337-370.

56. Gaunt, A. J.; May, L.; Sarsfield, M. J.; Collison, D.; Helliwell, M.; Denniss, L. S. *Dalton Trans.* **2003**, 13, 2767-2771.

57. Patel, A.; Pathan, S. *J. Coord. Chem*. **2012**, 65, 3122-3132.

58. Pathan, S.; Patel, A. *Appl. Catal. A* **2013**, 459, 59-64.

59. Jin, H. J.; Zhou, B. B.; Yu, Y.; Zhao, Z. F.; Su, Z. H. *CrystEngComm* **2011**, 13, 585-590.

60. Ma, F. X.; Chen, Y. G.; Yang, H. Y.; Dong, X. W.; Jiang, H.; Wang, F.; Li, J. H. *J. Clust. Sci.* **2018**, 30, 123-129.

61. Fang, N.; Ji, Y. M.; Li, C. Y.; Wu, Y. Y.; Ma, C. G.; Liu, H. L.; Li, M. X. *RSC Adv.* **2017**, 7, 25325-25333.

62. Bai, Y.; Zheng, G. S.; Dang, D. B.; Gao, H.; Qi, Z. Y.; Niu, J. Y. *Spectrochim. Acta Part A* **2010**, 77, 727-731.

63. Jiang, K.; Ma, L. F.; Sun, X. Y.'; Wang, L. Y. *CrystEngComm* **2011**, 13, 330-338.

64. Song, X.; Zhu, W.; Yan, Y.; Gao, H.; Gao, W.; Zhang, W.; Jia, M. *Microporous Mesoporous Mater.* **2017**, 242, 9-17.

65. Batten, S. R.; Champness, N. R.; Chen, X. M.; Martinez, J. G.; Kitagawa, S.; Ohrstrom, L.; O'Keeffe, M.; Suh, M. P.; Reedijk, J. *Pure Appl. Chem.* **2013**, 85, 1715-1724.

66. Buvailo, H. I.; Makhankova, V. G.; Kokozay, V. N.; Omelchenko, I. V.; Shishkina, S. V.; Zabierowski, P.; Matoga, D.; Jezierska, J. *Eur. J. Inorg. Chem.* **2017**, 2017, 3525-3532.

67. Hou, G.; Bi, L.; Li, B.; Wu, L. *Inorg. Chem.* **2010**, 49, 6474-6483.

68. Wang, X. L.; Gao, Q.; Tian, A. X.; Hu, H. L.; Liu, G. C. *J. Solid State Chem.* **2012**, 187, 219-224.

69. Li, X.; Wang, Y.; Zhou, K.; Wang, Y.; Han, T.; Sha, J. *J. Coord. Chem.* **2018**, 71, 468-482.

70. Meng, J, X.; Lu, Y.; Li, Y. G.; Fu, H.; Wang, E. B. *CrystEngComm* **2011**, 7, 2479-2486.

71. Moulton, B.; Zaworotko, M. J. *Chem. Rev.* **2001**, 101, 1629-1658.

72. Upreti, S.; Datta, A.; Ramanan, A. *Cryst. Growth Des.* **2007**, 7, 966-971.

73. Kendell, S. M.; Alston, A. S.; Ballam, N. J.; Brown, T. C.; Burns, R. C. *Catal. Lett.* **2011**, 141, 374-390.

74. Ghalebi, H. R.; Aber, S.; Karimi, A. *J. Mol. Catal. A: Chem.* **2016**, 415, 96-103.

75. Monge, J. L.; Trautwein, G.; Martinez, M. C. R. *Solid State Sci.* **2011**, 13, 30-37.

76. Chen, Q.; Shen, L. M.; Xia, J.; Chen, X. W.; Wang, J. H. *J. Sep. Sci.* **2014**, 37, 2716-2723.

77. Huynh, Q.; Schuurman, Y.; Delichere, P.; Loridant, S.; Millet, J. M. M. *J. Catal.* **2009**, 261, 166-176.

78. Zhang, C.; Shen, X.; Lu, S.; Peng, Z.; Zhu, W.; Cai, T. *J. Mol. Struct.* **2012**, 1016, 155-162.

79. Mukherjee, H. N. *J. Indian Med. Assoc.* **1965**, 44, 477-479.

80. Bijelic, A.; Aureliano, M.; Rompel, A. *Angew. Chem. Int. Ed.* **2019**, 58, 2980-2999.

81. Ji, Y. M.; Fang, Y.; Han, P. P.; Li, M. X.; Chen, Q. Q.; Han, Q. X. *Inorg. Chem. Commun.* **2017**, 86, 22-25.

82. Qu, X.; Feng, H.; Ma, C.; Yang, Y.; Yu, X. *Inorg. Chem. Commun.* **2017**, 81, 22-26.

83. Ren, Y.; Wang, M.; Chen, X.; Yue, B.; He, H. *Materials* **2015**, 8, 1545-1567.

84. Gong, K.; Liu, Y.; Han, Z. *RSC Adv.* **2015**, 5, 47004-47009.

85. Shi, S.; Chen, Y.; Zhao, X.; Ren, B.; Cui, X.; Zhang, J. *Inorg. Chim. Acta* **2018**, 482, 870-877.

86. Xu, M.; Li, F.; Wang, T.; Xu, L. *Inorg. Chem. Commun.* **2018**, 94, 123-126.

87. Wan, S.; Yu, K.; Wang, L.; Su, Z.; Zhou, B. *Inorg. Chem. Commun.* **2015**, 61, 113-117.

88. Li, Z. L.; Wang, Y.; Zhang, L. C.; Wang, J. P.; You, W. S.; Zhu, Z. M. *Dalton Trans*. **2014**, 43, 5840-5846.

89. Xin. X.; Tian, X.; Yu, H.; Han, Z. *Inorg. Chem.* **2018**, 57, 11474-11481.

90. Tian, X.; Hou, L.; Wang, J.; Xin, X.; Zhang, H.; Ma, Y.; Wang, Y.; Zhang, L.; Han, Z. *Dalton Trans*. **2018**, 47, 15121-15130.

91. Hou, L.; Zhang, Y.; Ma, Y.; wang, Y.; Hu, Z.; Gao, Y.; Han, Z. *Inorg. Chem.* **2019**, 58, 16667-16675.

92. Zhang, N.; Chen, S.; Hu, J.; Shi, J.; Guo, Y.; Deng, T. *RSC Adv*. **2020**, 10, 6139.

93. Juan, J. M. C.; Coronado, E.; Arino, A. G. *Chem. Soc. Rev*. **2012**, 41, 7464-7478.

94. Fernandes, D. M.; Freire, C. *ChemElectroChem* **2015**, 2, 269-279.

95. Zhang, S.; He, P.; Lei, W.; Zhang, G. *J. Electroanal. Chem.* **2014**, 724, 29-35.

96. Wang, Z.; Han, Q.; Xia, J.; Xia, L.; Bi, S.; Shi, G.; Zhang, F.; Xia, Y.; Li, Y.; Xia, L. *J. Electroanal. Chem.* **2014**, 726, 107-111.

97. Papagianni, G. G.; Stergiou, D. V.; Armatas, G. S.; Kanatzidis, M. G.; Prodromidis, M. I. *Sens. Actuators, B* **2012**, 173, 346-353.

CHAPTER II

Role of supramolecular interactions in crystal packing of Strandberg-type cluster based hybrid solids

Summary

Two new Strandberg-type cluster based phosphomolybdates $\{H\text{-}2a3mp\}_5$ $[\{PO_3(OH)\}\{PO_4\}Mo_5O_{15}]$, **1** and $\{H\text{-}2a4mp\}_5[\{PO_3(OH)\}\{PO_4\}Mo_5O_{15}].6H_2O$, **2** have been crystallized *via* solvent evaporation technique using 2-amino-3-methylpyridine (*2a3mp*) and 2-amino-4-methylpyridine (*2a4mp*) respectively. The solids were characterized using single crystal X-ray diffraction, powder X-ray diffraction, fourier transform infrared spectroscopy, thermogravimetric analysis, scanning electron microscopy and cyclic voltammetry. The solid **1** crystallized in monoclinic system with space group $P2_1/c$, $a = 8.394(1)$, $b = 27.398(6)$, $c = 21.521(4)$ Å, $\beta = 97.68(3)°$, Z = 4. The solid **2** crystallized in triclinic system with space group $P\text{-}1$, $a = 11.728(1)$, $b = 14.234(1)$, $c = 19.589(1)$ Å, $\alpha = 68.906(3)$, $\beta = 89.454(3)$, $\gamma = 66.559(3)°$, Z = 2. The solids **1** and **2** formed a supramolecular framework stabilized by hydrogen bonding interaction between cluster anions and organic moieties. CH…π interactions between the organic moieties reinforced the crystal packing in **1** and **2**. While crystal packing effects resulted in the formation of solvent accessible voids in **1**; aggregation of lattice water molecules in **2** facilitated the formation of pentameric water cluster. The electrochemical behavior of **1** and **2** has been investigated. In addition, the optical band gap energy of the solids have also been calculated using UV-DRS data.

II.1. Introduction

Supramolecular assemblies based on phosphomolybdate (PMO) cluster anions are captivating organic-inorganic hybrid solids on account of their diverse topologies, tuneable size and structural versatility [1,2]. Owing to their unique structural features, they exhibit a wide range of applications in multiple areas such as catalysis [3,4], magnetism [5], ion-exchange [6,7] and electrochemistry [8-10]. Among the PMO cluster anions, Strandberg-type $\{P_2Mo_5O_{23}\}^{6-}$ is the most stable cluster anion that can be crystallized under ambient conditions [11-13]. It was first reported by Strandberg in 1973 [14] and so far several hybrid solids have been reported based on $\{P_2Mo_5\}$ cluster anion with promising properties [15-18]. Majority of these solids have been crystallized along with protonated organic ligands having nitrogen donor atoms [19-21]. Since, $\{P_2Mo_5\}$ cluster anion is stable in the pH range 1-7, organic ligands tend to be protonated (at pH < pK_a) and electrostatic interaction between the organic cations and inorganic polyanions enables the crystallization of hybrid solids. The protonated ligands exhibit hydrogen bonding interactions along with CH…π and/or π…π interactions which leads to the stabilization of the supramolecular aggregates and result in fascinating 3-D networks [22-24].

For the past decade, a few groups have been investigating the role of supramolecular interactions in stabilizing the crystal packing in $\{P_2Mo_5\}$ cluster based solids [25-28]. It was observed that these solids demonstrate remarkable structural characteristics such as porosity, aggregation of water clusters and supramolecular isomerism [28,29]. However, the electrochemical behavior of Strandberg-type cluster based solids is proportionately less investigated. Therefore, in this chapter, an attempt has been made to crystallize hybrid solids based on Strandberg-type $\{P_2Mo_5\}$ cluster, examine the role of supramolecular interactions

in stabilizing the crystal packing in the solids and explore the electrochemical nature of the synthesized solids. Under ambient temperature, {H-2*a3mp*}$_5$[{PO$_3$(OH)}{PO$_4$}Mo$_5$O$_{15}$], **1** and {H-2*a4mp*}$_5$[{PO$_3$(OH)}{PO$_4$}Mo$_5$O$_{15}$].6H$_2$O, **2** were crystallized from an aqueous medium using isomeric ligands *viz.* 2-amino-3-methylpyridine (2*a3mp*) and 2-amino-4-methylpyridine (2*a4mp*) respectively by means of solvent evaporation technique. A detailed structural analysis of the solids revealed the role of H-bonding and CH…π interactions in the self-assembly of **1** and **2**. Moreover, the electrochemical nature of **1** and **2** was explored by means of three electrode system using 1 mM K$_4$[Fe(CN)$_6$] in 0.1 M KCl as supporting electrolyte. Previously, electrochemical behavior of {P$_2$Mo$_5$} cluster based solids has been investigated only in acidic medium [30,31]. This is the first attempt to examine the nature of {P$_2$Mo$_5$} cluster based solids when K$_4$[Fe(CN)$_6$] is used in KCl as supporting electrolyte. The band gap energies (E$_g$) of the as-synthesized solids were calculated to understand the changes in E$_g$ when monoprotonated cluster anion is surrounded by isomeric ligands.

II.2. Experimental Section

II.2.1. Synthesis

0.4 g of Na$_2$MoO$_4$.2H$_2$O (1.65 mmol, Merck) was dissolved in 20 ml of distilled water and labeled as Solution A. Solution B was prepared by dissolving 0.15 ml of 2-amino-3-methylpyridine (1.47 mmol, Aldrich) in 20 ml of distilled water. Subsequently, Solution B was slowing added to Solution A and kept under stirring for five minutes. Upon stirring a turbid solution was obtained. Thereafter, 1M orthophosphoric acid (H$_3$PO$_4$, Merck, 85%) was added drop wise to obtain a clear solution (pH ~ 1) and the resultant solution was left undisturbed for crystallization. After two weeks, needle shaped crystals of **1** were obtained

(Yield: 65-70% based on molybdenum). The crystals were washed with distilled water and acetone and allowed to dry at room temperature.

The same procedure was repeated using 2-amino-4-methylpyridine instead of 2-amino-3-methylpyridine and block shaped crystals of **2** were obtained (Yield: 65-70% based on molybdenum).

II.2.2. Characterization

II.2.2.1. X-ray crystallographic studies

X-ray diffraction studies of crystal mounted on a capillary were carried out on a BRUKER AXS SMART-APEX diffractometer with a CCD area detector (MoKα = 0.71073Å, monochromator: graphite) [32]. Frames were collected at T = 293K (for **1**) and 296K (for **2**) by ω, φ and 2θ-rotation at 10s per frame with SAINT [33]. The measured intensities were reduced to F^2 and corrected for absorption with SADABS [33]. Structure solution, refinement, and data output were carried out with the SHELXTL program [34]. Non-hydrogen atoms were refined anisotropically. C-H and N-H hydrogen atoms were placed in geometrically calculated positions by using a riding model. Images were created with the DIAMOND program [35]. Hydrogen bonding interactions in the crystal lattice were calculated with SHELXTL and DIAMOND [34,35]. Crystal and refinement data are summarized in Table II.1.

II.2.2.2. Powder X-ray diffraction (PXRD)

PXRD data was collected on a Malvern Panalytical Aeris diffractometer using Ni-filtered CuKα radiation. Data were collected with a step size of 0.02° and count time of 2s per step

over the range $5° < 2\theta < 60°$.

II.2.2.3. **Fourier transform infrared spectroscopy (FTIR)**

FTIR spectra were recorded on KBr pellets using Shimadzu FTIR spectrophotometer (model: IR Affinity).

Table II.1. Crystallographic details for **1** and **2**.

	1	2
Formula	$C_{30}H_{45}Mo_5N_{10}O_{23}P_2$	$C_{30}H_{45}Mo_5N_{10}O_{29}P_2$
Formula weight	1455.40	1551.4
T (K)	293(2)	296(2)
Space Group	$P2_1/c$	P -1
a, Å	8.394(1)	11.728(1)
b, Å	27.398(6)	14.234(1)
c, Å	21.521(4)	19.589(1)
α, °	90.00	68.906(3)
β, °	97.68(3)	89.454(3)
γ, °	90.00	66.559(3)
V, Å^3	4905.1(18)	2765.1(4)
Z	4	2
d_{calc}, g·cm^{-3}	1.971	1.863
$\mu_{MoK\alpha}$, cm^{-1}	1.397	1.254
λ (Å)	0.71073	0.71073
$R_1(I>2\sigma I)$, WR_2(all)	0.0408, 0.1114	0.0391, 0.1153
GOF	1.080	1.111
CCDC No.	1999772	1999773

II.2.2.4. Thermogravimetric analysis (TGA)

TGA was done on Perkin-Elmer TGA7 from room temperature to 900°C at a heating rate of 10°C/min. in nitrogen atmosphere to determine water and organic content as well as overall thermal stability of the product.

II.2.2.5. Scanning electron microscopy (SEM)

SEM studies were carried out on crystals mounted on carbon tape using FEI FESEM Quanta 200 at an accelerating voltage of 20 kV.

II.2.2.6. Cyclic voltammetric studies

The electrochemical measurements were carried out on CH1608 electrochemical work station using three-electrode system with saturated Ag/AgCl as the reference electrode and platinum wire as a counter electrode. The working electrode was fabricated by coating solids **1** and **2** separately on glassy carbon electrode (GCE) by simple drop casting method. 1 mM $K_4[Fe(CN)_6]$ in 0.1 M KCl was used as the supporting electrolyte to study the electrochemical properties.

II.2.2.7. Band gap energy calculations

Band gap energy calculations were done using data collected from UV-Vis spectrophotometer (UV-2600 spectrometer, Shimadzu, Japan).

II.3. Results and Discussion

II.3.1. Crystal structure of 1 and 2

The solids **1** and **2** are based on {P_2Mo_5} cluster anion which consists of edge and corner sharing MoO_6 octahedra forming a Mo_5O_{15} ring capped by two PO_4 tetrahedra; the anion is identical to the one found in many solids [28].

The crystal structure of {H-2*a*3*mp*}$_5$[{$PO_3(OH)$}{PO_4}Mo_5O_{15}], **1** and {H-2*a*4*mp*}$_5$[{$PO_3(OH)$}{PO_4}Mo_5O_{15}].$6H_2O$, **2** suggests the presence of one cluster anion and five monoprotonated ligand moieties per asymmetric unit (Figure II.1). In addition six lattice water molecules per asymmetric unit are present in **2**. Bond valence sum (BVS) calculations [36] indicate that in both **1** and **2**, one of the phosphate groups per cluster anion is protonated (henceforth referred to as {HP_2Mo_5}). Moreover in both **1** and **2**, {HP_2Mo_5} cluster anion exhibits extensive H-bonding interactions with ligand moieties; however, the nature of supramolecular interactions in **1** and **2** is quite different.

In **1**, protonation of terminal oxygen i.e. O22 on the phosphate group results in a strong H-bonding interaction (2.411(12) Å) between P=O and P-OH groups of neighboring clusters thereby dictating the formation of 1-D chains of {HP_2Mo_5} cluster anions as shown in Figure II.2a. While, four of the {H-2*a*3*mp*}$^+$ moieties *viz.* {N3N4}, {N5N6}, {N7N8} and {N9N10} are connected to {HP_2Mo_5} cluster anion through NH…O interactions; the fifth {H-2*a*3*mp*}$^+$ moiety i.e. {N1N2} also links the adjacent {HP_2Mo_5} cluster anions through CH…O interactions to form 1-D chains (Figure II.2b). H-bonding interactions in **1** have been summarized in Table II.2. The 1-D chains are further linked via {N9N10} moieties through H-bonding (N9H9C…O8: 2.324(24) Å) interaction to form 2-D zig-zag sheet. The

formation of 2-D sheets is also reinforced by $\pi\ldots\pi$ interactions (3.551(5) Å) mediated by {N7N8} and {N9N10} moieties of neighboring 1-D chains (refer Figure II.2c). The packing of 2-D sheets is facilitated by CH$\ldots\pi$ interactions as shown in Figure II.3. It is noteworthy that the structure showed solvent accessible voids of diameter 3.8 nm (refer Figure II.3c).
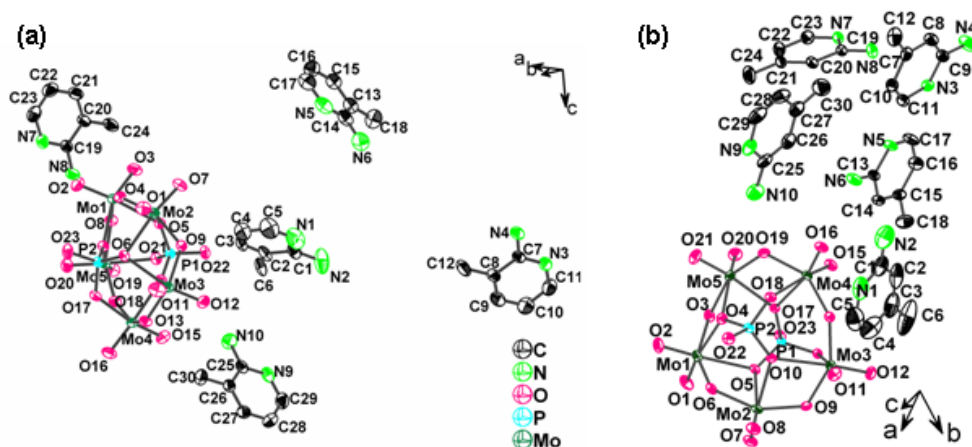
Figure II.1. An ORTEP view of (a) **1** and (b) **2**. The lattice water molecules in **2** have been removed for clarity.

Table II.2. Hydrogen bonding interactions in **1**.

D-H…A	D-H (Å)	H…A (Å)	D…A (Å)	∠ D-H…A (°)
N3-H3C…O17	0.861(8)	2.073(5)	2.874(11)	154.36(22)
N4-H4A…O23	0.860(9)	2.123(15)	2.969(23)	167.95(23)
N6-H6A…O21	0.859(10)	2.226(19)	3.076(29)	169.87(28)
N5-H5C…O1	0.86(1)	1.892(17)	2.691(28)	153.91(25)
N8-H8B…O4	0.860(4)	1.960(17)	2.798(20)	164.61(23)
N8-H8A…O22	0.860(14)	2.134(27)	2.956(42)	159.82(21)
N9-H9C…O13	0.860(14)	1.838(29)	2.680(44)	165.52(20)
N10-H10A…O17	0.860(14)	2.239(22)	3.050(37)	157.20(24)
N10-H10B…O15	0.859(6)	2.214(3)	2.956(5)	144.55(24)
C6-H6F…O22	0.961(4)	2.229(5)	3.094(10)	149.12(21)
C6-H6D…O8	0.960(15)	2.036(35)	2.978(50)	166.62(23)
C3-H4C…O9	0.931(3)	1.833(2)	2.713(4)	156.75(22)
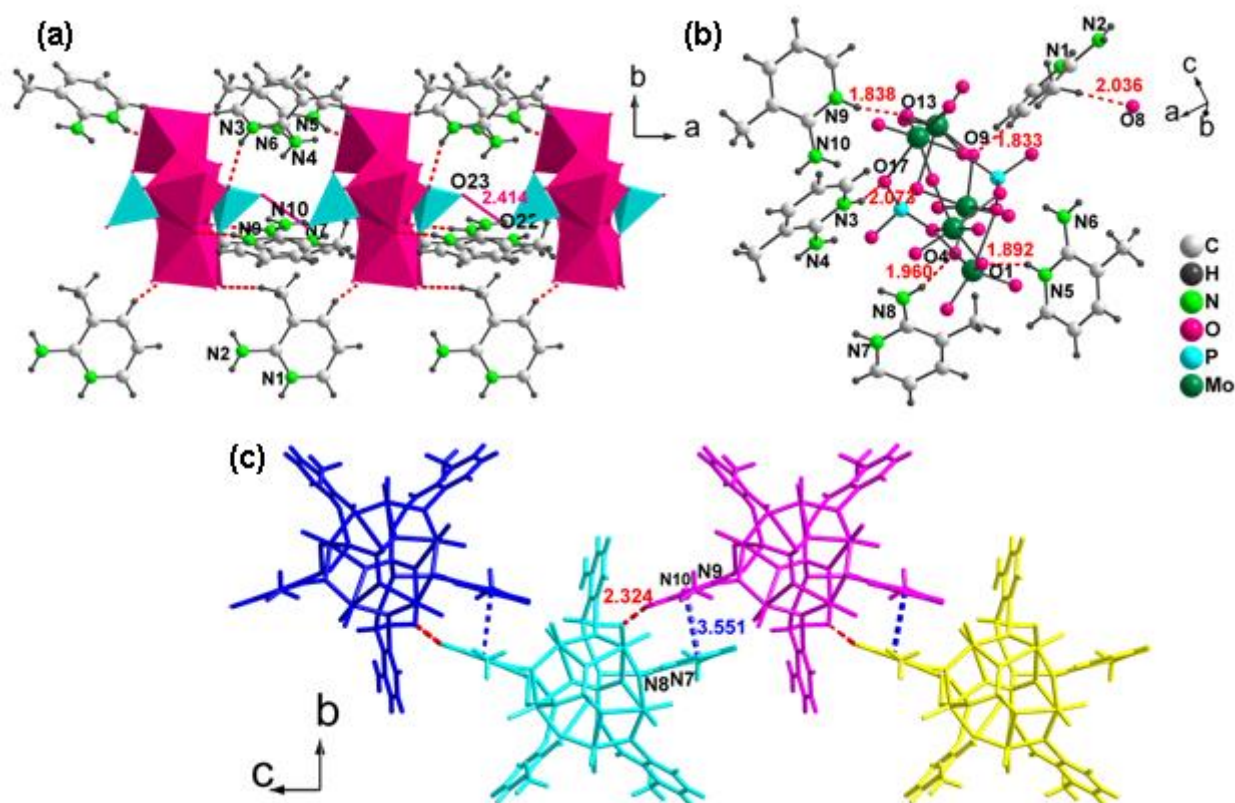
Figure II.2. (a) 1-D chains in **1** mediated by O…O interactions (shown in solid red lines) between terminal oxygen atoms O22 and O23 of phosphate groups of neighboring cluster anions. Formation of 1-D chains is also facilitated by CH...O interactions (shown in dashed red lines) mediated by {N1N2} moieties. (b) H-bonding interactions exhibited by {HP$_2$Mo$_5$} cluster anion in **1**. (c) Formation of zig-zag 2-D sheet through CH…O and π…π interactions (shown in dashed red and blue lines respectively) between neighboring 1-D chains. Four such chains are shown in blue, cyan, purple and yellow.
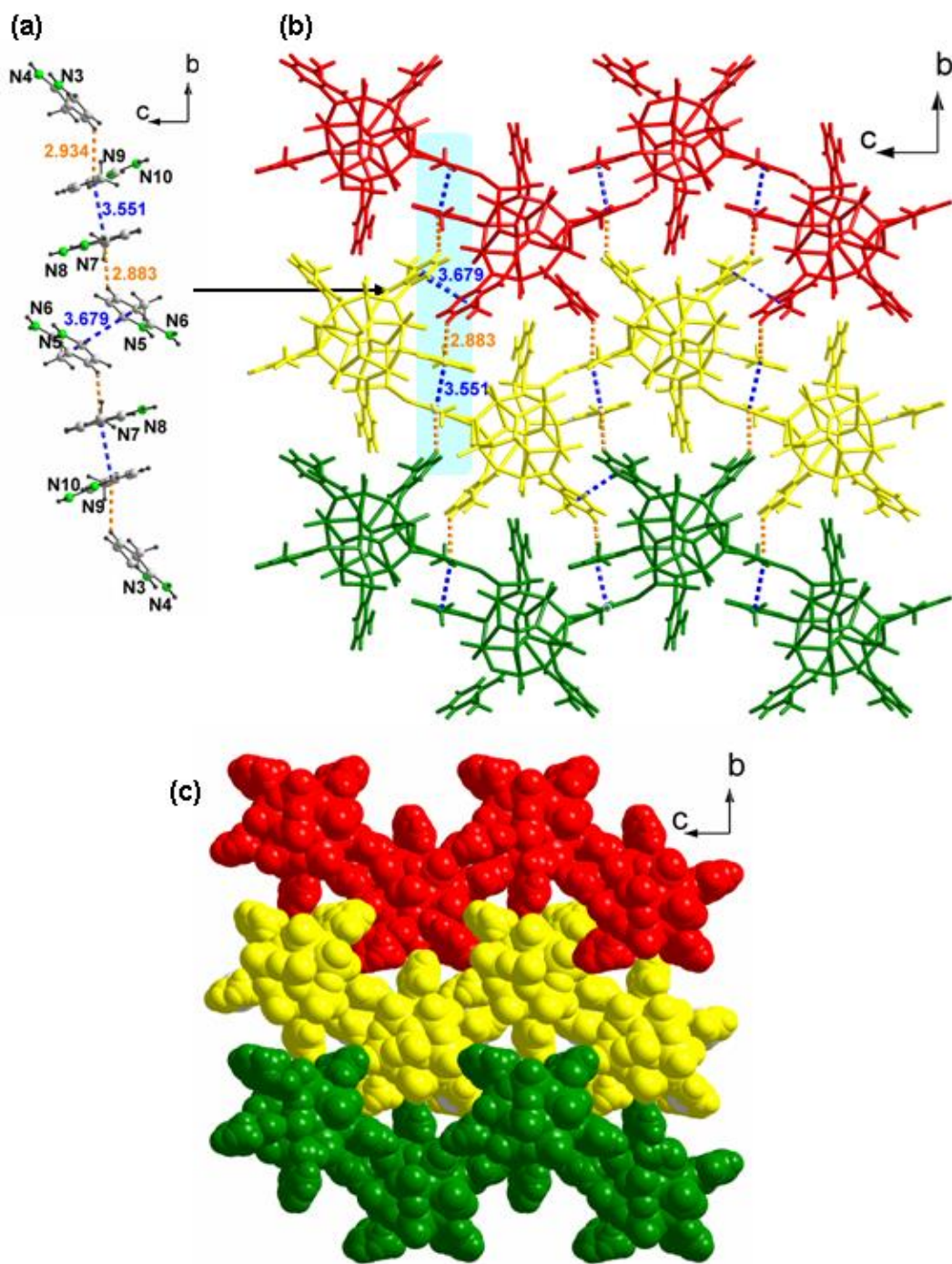
Figure II.3. (a) CH…π and π...π interactions (shown in dashed orange and blue lines) form a octameric unit. (b) Crystal packing in **1** is facilitated by CH…π interactions between neighboring sheets. Three such sheets are shown in red, yellow and green. (c) CPK representation of **1** showing solvent accessible voids.

The crystal structure analysis of **2** suggests the formation of a dimeric unit of $\{HP_2Mo_5\}$ cluster anions linked via H-bonding interaction mediated by {N7N8} moiety. {N1N2}, {N3N4} and {N5N6} moieties along with five lattice water molecules are attached to the dimeric unit through NH…O and O…O interactions respectively (refer Table II.3 and II.4 for H-bonding and O…O interactions respectively). Each of the dimers is further connected through pentameric water cluster to form 1-D chains which propagate along *b* axis as shown in Figure II.4c. The packing resulted in voids which are occupied by {N9N10} moieties. The occurrence of {N9N10} moieties in the voids is induced by the pentameric water cluster through O6W (N10H10A…O6W: 2.131(6) Å). Inter-chain H-bonding interaction mediated by {N5N6} moiety (N6H6B…O16: 2.127(5) Å) results in 2-D sheet in *ab* plane. Unlike in **1**, CH…π interactions between neighboring chains facilitated the packing of 1-D chains in **2**. The 2-D sheets are stacked parallel to each other along the *c* axis through lattice water molecule, O1W.

Table II.3. Hydrogen bonding interactions in **2**.

D-H…A	D-H (Å)	H…A (Å)	D…A (Å)	∠ D-H…A (°)
N1-H1…O21	0.859(8)	1.910(5)	2.742(9)	162.70(52)
N3-H3…O18	0.860(5)	1.960(5)	2.819(7)	175.31(29)
N4-H4A…O16	0.859(7)	2.061(5)	2.881(8)	159.45(40)
N5-H5…O23	0.861(5)	1.793(4)	2.647(7)	171.18(34)
N7-H7…O13	0.861(4)	2.010(6)	2.863(8)	171.06(26)
N8-H8A…O23	0.860(4)	2.014(6)	2.860(9)	167.62(27)
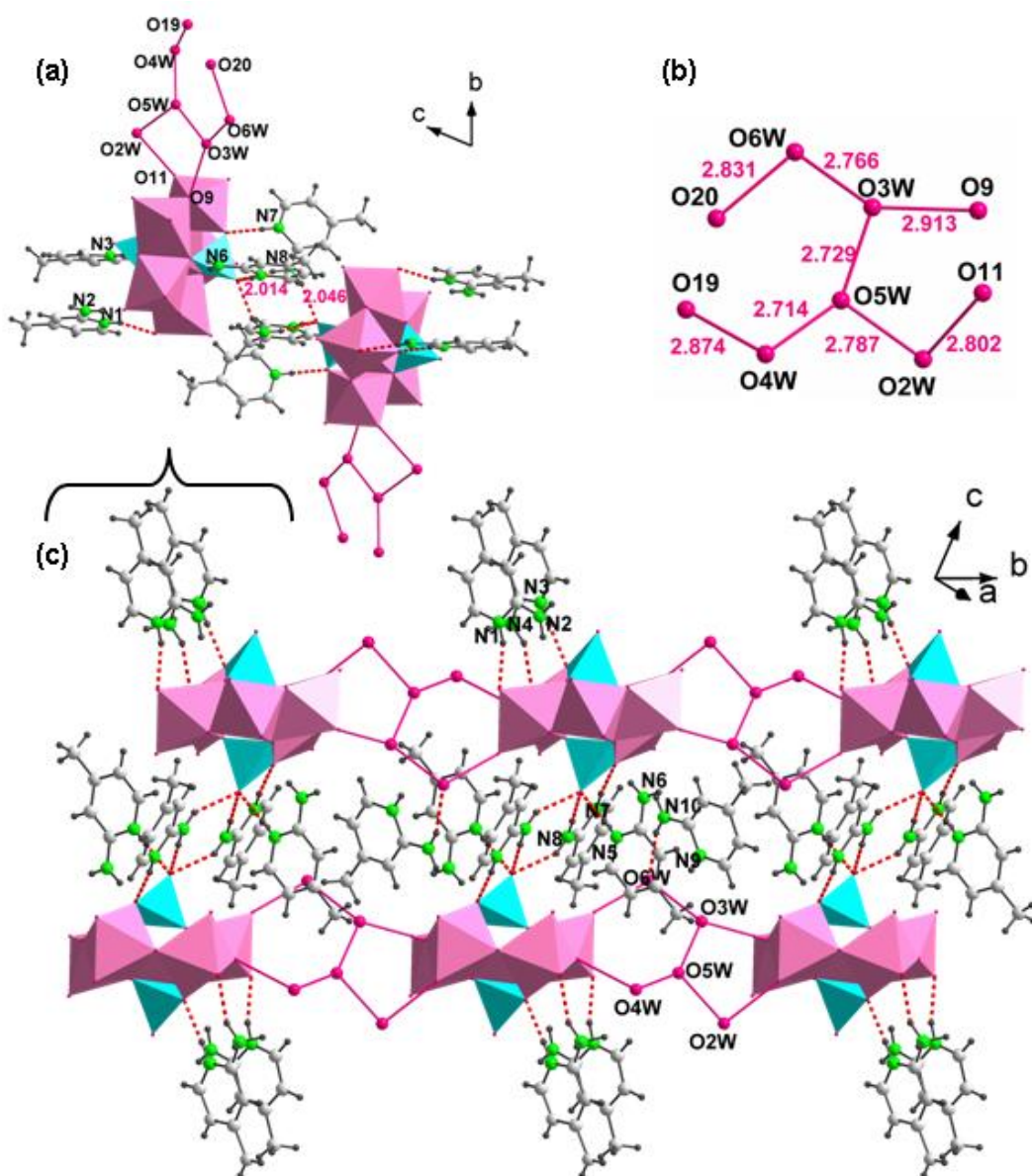
Figure II.4. (a) Dimeric unit in **2** wherein {HP$_2$Mo$_5$} cluster anions are linked through H-bonding (shown in dashed red lines) mediated by {N7N8} moiety. The pentameric water cluster is anchored to the dimer through O...O interactions shown in solid red lines. (b) The pentameric water cluster in **2**. (c) Dimer units linked through water clusters to form 1-D chain propagating along *b* axis. The 1-D chains result in voids which are occupied by {N9N10} moieties.
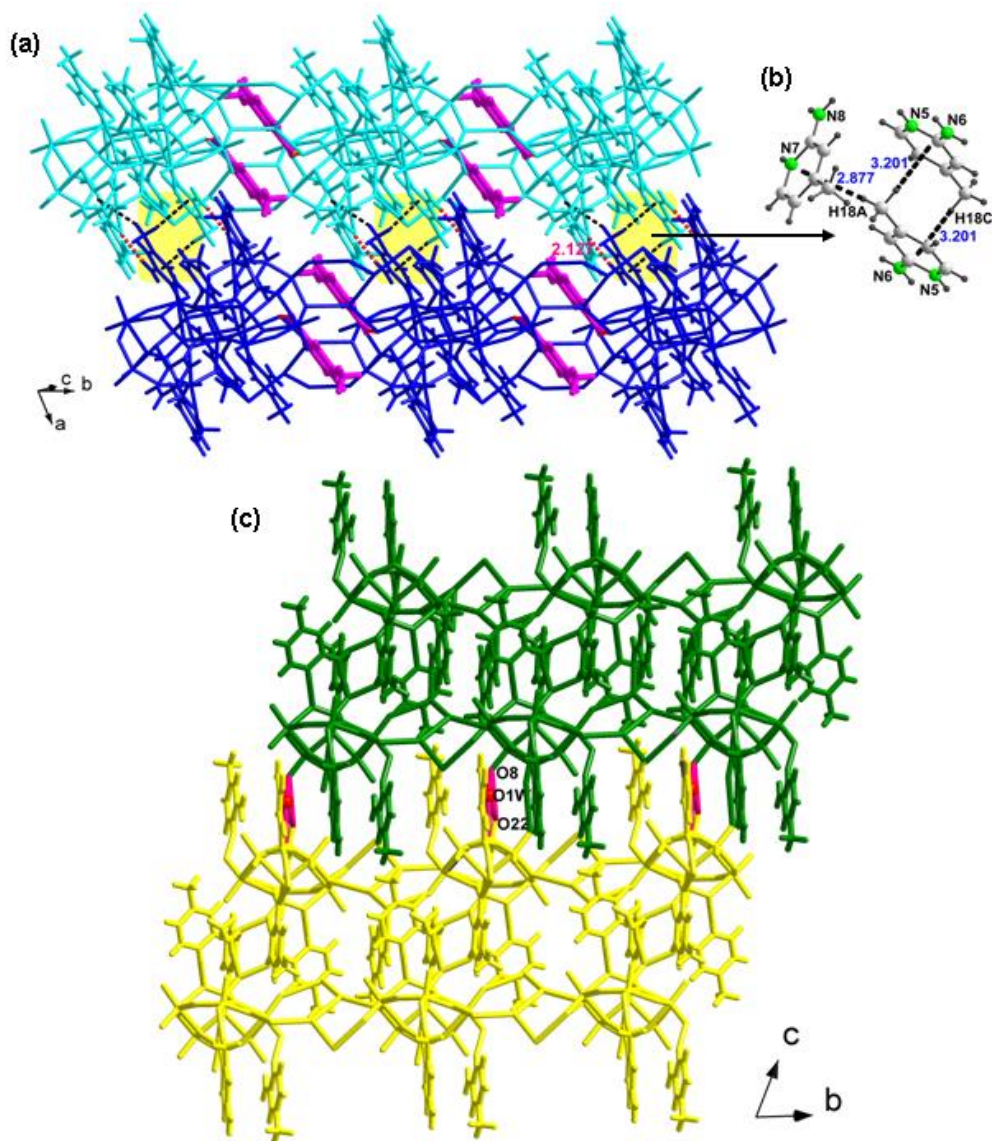
Figure II.5. (a) The connection between chains through H-bonding interaction (N6H6B…O16: 2.127(5) Å) and CH…π interactions to form a sheet. Two such chains are shown in cyan and blue. The voids in 1-D chains are occupied by {N9N10} moieties shown in purple color. (b) CH…π interactions in **2** are shown in dashed black lines. (c) Neighboring 2-D sheets (shown in green and yellow) are further linked by lattice water molecule, O1W to form a 3-D supramolecular network. O…O interactions are shown in solids red lines (refer Table II.3 for O…O interactions).

Table II.4. O…O interactions in **2**.

Sl. No.	O…O	Distance (Å)
1	O2W…O11	2.802(13)
2	O2W…O5W	2.787(16)
3	O3W…O9	2.913(9)
4	O3W…O5W	2.729(15)
5	O3W…O6W	2.766(12)
6	O4W…O5W	2.714(14)
7	O4W…O19	2.874(12)
8	O6W…O20	2.831(9)
9	O1W…O22	3.068(9)
10	O1W…O6	2.814(6)
11	O1W…O8	3.019(8)

II.3.2. Analysis of solids 1 and 2

FTIR spectra of **1** and **2** showed bands in the region 650-690, 750-830 and 900-930 cm^{-1} which are characteristic of molybdenum oxygen stretching. Bands at 1000-1100, 1400-1420 and 1620-1640 cm^{-1} were assigned to P-O stretching, N-H bending and C-H bending vibrations respectively [37]. In addition, FTIR spectrum of **2** showed bands at 3100-3400 cm^{-1} which could be attributed to O-H stretching (Figure II.6). SEM images of **1** and **2** showed the formation of well defined elongated needles and block-like morphology respectively (refer Figure II.7).
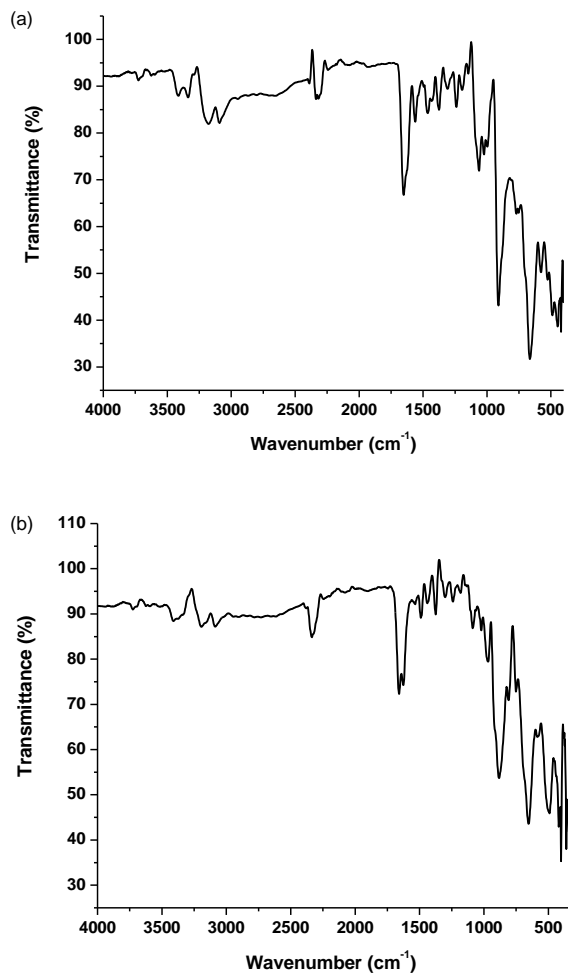
Figure II.6. FTIR Spectrum of (a) **1** and (b) **2**.
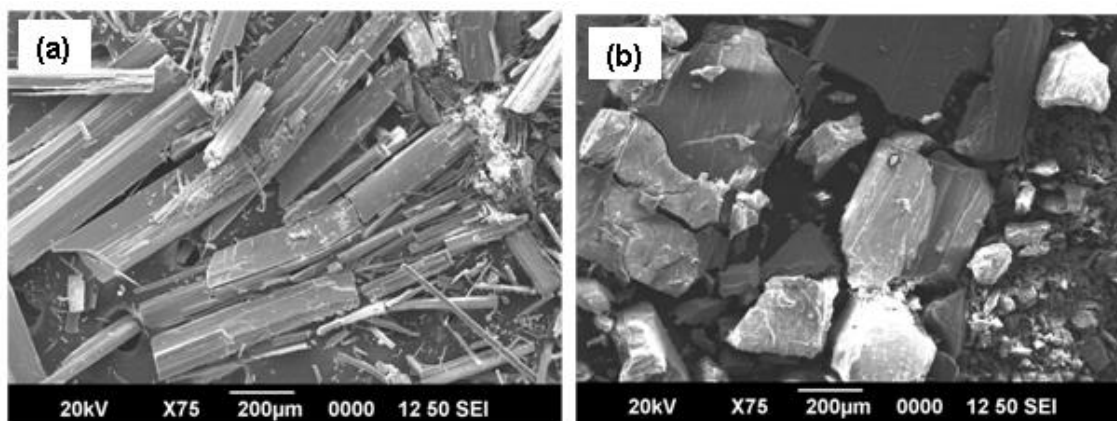
Figure II.7. SEM images of (a) **1** and (b) **2**.

TG analysis of **1** and **2** (Figure II.8) showed weight loss in two and three steps respectively. In **1**, the first weight loss upto 350ºC corresponding to 36.7% was due to the thermal degradation of five organic moieties. The second weight loss upto 800ºC could be assigned to the decomposition of {HP$_2$Mo$_5$} cluster anion. On the contrary, **2** showed an initial weight loss of 1.1 % at 100°C corresponding to loss of one water molecule. The loss of remaining water molecules along with protonated organic moieties was observed at slightly higher temperature (upto 350°C), as water molecules formed a pentameric water cluster in **2**. The third weight loss could be attributed to the decomposition of {HP$_2$Mo$_5$} cluster anion. In both **1** and **2**, the phase purity of the solids was established by comparing the experimental PXRD pattern with simulated powder pattern of the single crystal structure as shown in Figures II.9-II.10.
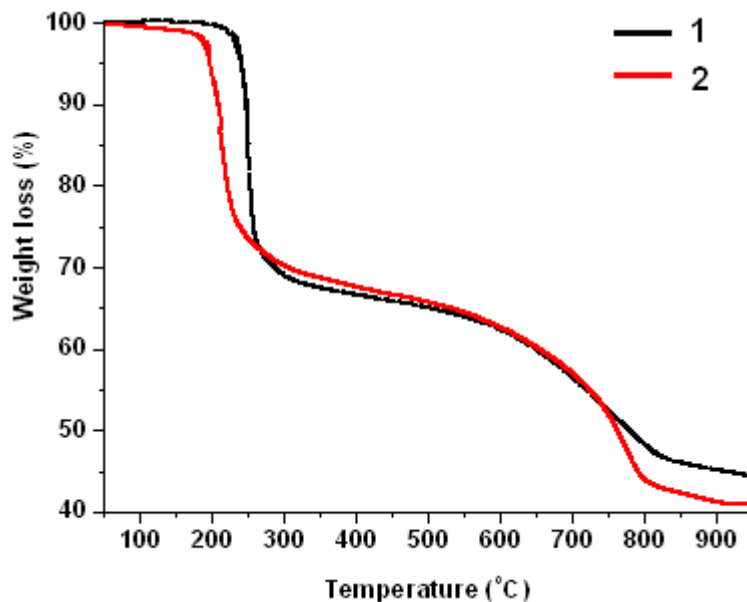
Figure II.8. TGA curve of **1** and **2**.
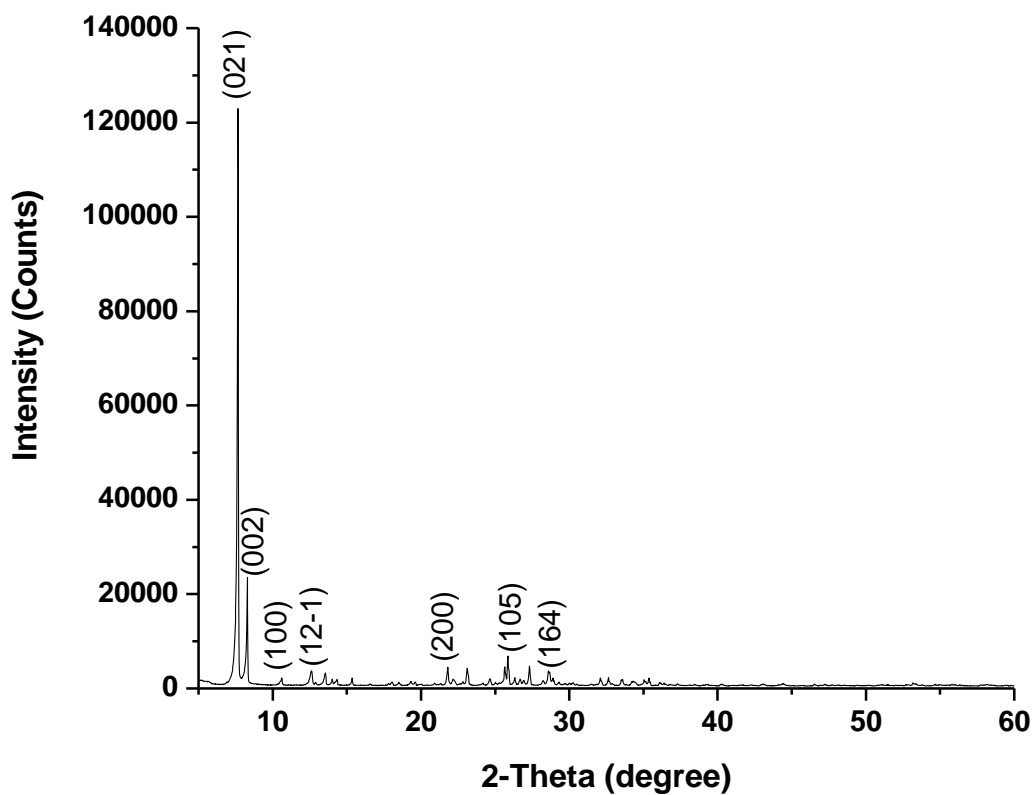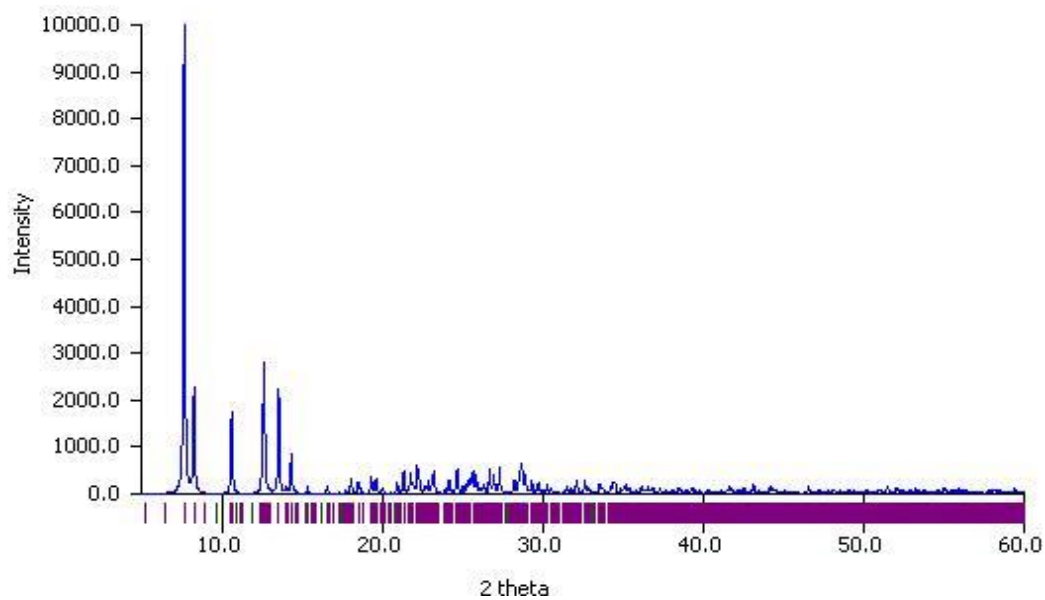
Figure II.9. Simulated (top) and Experimental (bottom) PXRD of **1**.
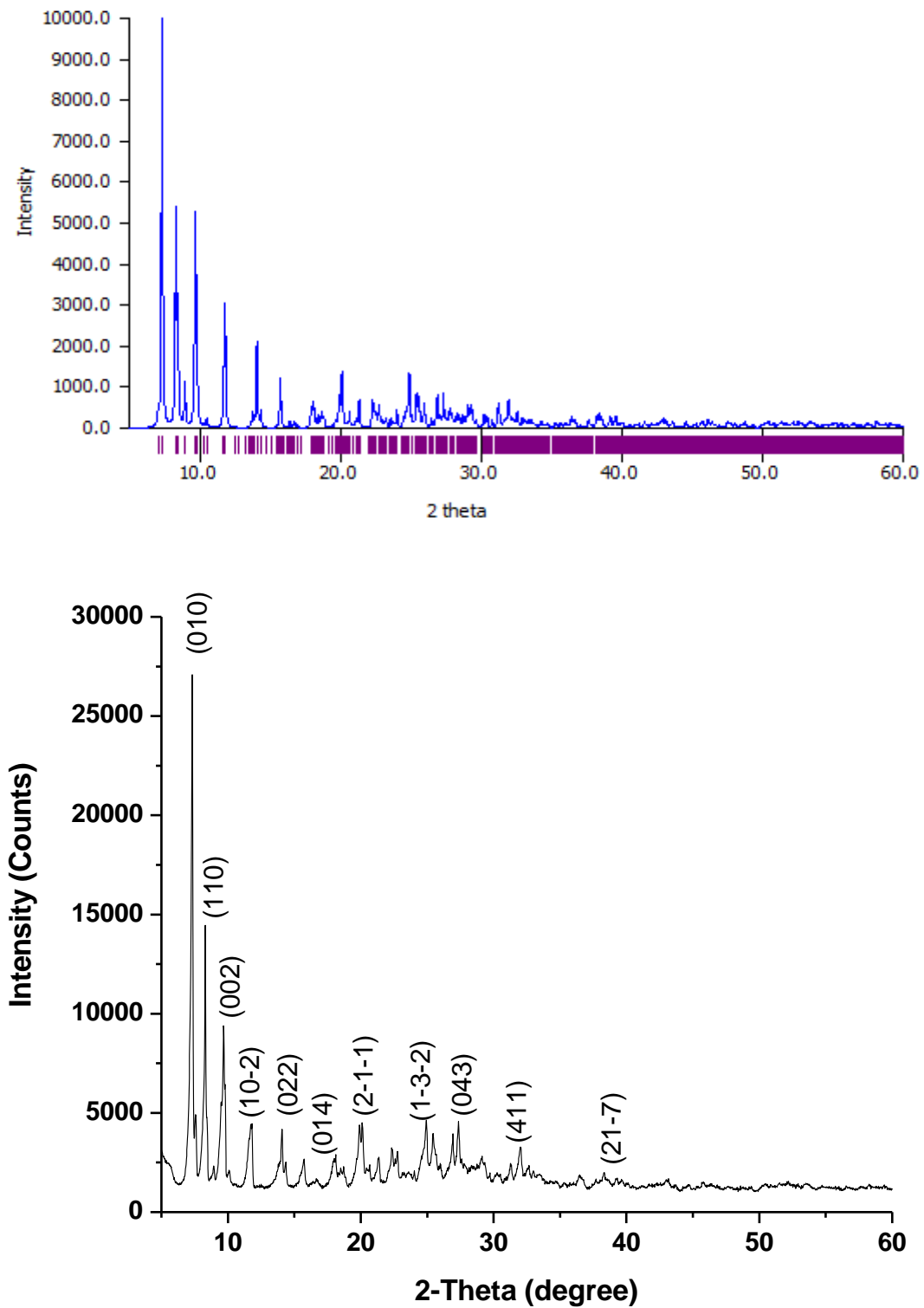
Figure II.10. Simulated (top) and Experimental (bottom) PXRD of **2**.

II.3.3. Electrochemical behavior

The redox behavior of the solids was investigated using cyclic voltammetry in 1 mM K$_4$[Fe(CN)$_6$] with a scan rate of 50 mVs^{-1}. In both **1** and **2**, two reversible waves (I-I' & II-II') were observed in the potential range between -0.2 and +0.8 V (Figure II.11a). The bare GCE gives a redox peak for K$_4$[Fe(CN)$_6$] with mean peak potential E*1/2* = (*Epa + Epc)/2* at 0.317 V which can be attributed to Fe^{II}/Fe^{III} [38]. The oxidation-reduction couple I-I' (+0.275 V and +0.279 V for **1** and **2** respectively) could be attributed to potassium ferrocyanide which shows a shift towards negative potential. The redox peak II-II' in **1** and **2** with half wave potentials +0.087 V and +0.072 V could be attributed to Mo^{VI}/Mo^{V} electron process. The slight deviations in the values can be ascribed to the different structural environment of {HP$_2$Mo$_5$} clusters. The responses at +0.087 V and +0.072 V for solids **1** and **2** corresponding to Mo^{VI}/Mo^{V} electron process of the Strandberg cluster was further confirmed by comparing the cyclic voltammogram of the solid with that of the organic ligand used in its synthesis. For example, 2-amino-4-methylpyridine (*2a4mp*) is the organic ligand used for the synthesis of **2**. The value of E*1/2* = +0.275 V was observed for *2a4mp* which is quite distinct from the redox peaks detected for solid **2** corresponding to Fe^{II}/Fe^{III} and Mo^{VI}/Mo^{V} processes (refer Figure II.11).
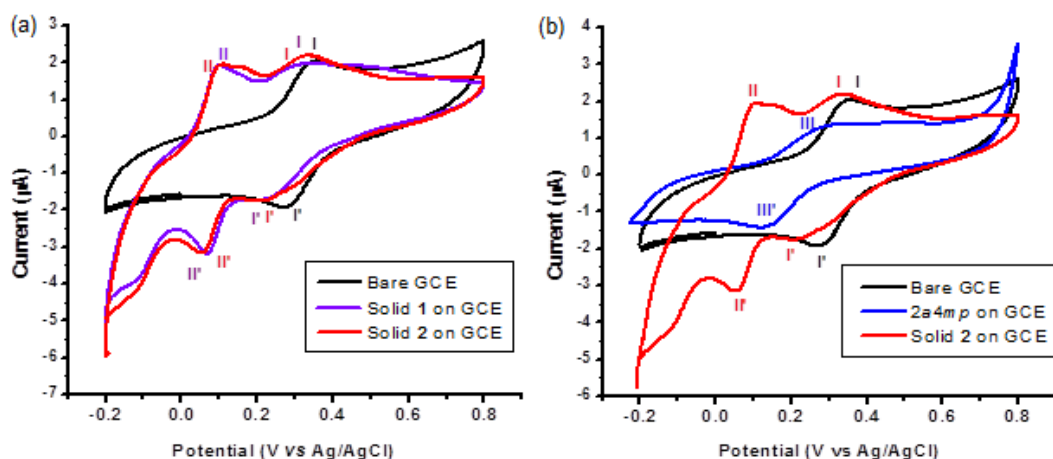
Figure II.11. (a) Cyclic voltammogram for **1** and **2** in the presence of 1 mM $K_4[Fe(CN)_6]$ in 0.1 M KCl with a scan rate of 50 mVs^{-1}. (b) Comparison of voltammogram of 2*a*4*mp* with bare GCE and Solid **2**.

II.3.4. Band gap energy calculations

Optical band gap energy (E_g) of **1** and **2** were detrmined applying Kubelk- a–Munk (KeM or F(R)) function in Tauc method [39,40]. E_g could be determined using Tauc method where ($\alpha h\upsilon)^n$ is ploted against energy (hυ) in eV; here α is molar extintion coefficient. For solid powdered samples, often Kubelk- a–Munk (KeM or F(R)) is applied in Tauc method where the α is replaced by a function F(R) as given by equation (1); where R is the reflectance obtained from UV-Vis spectra.

$$F(R)=(1-R)^2/2R \quad ……………….(1).$$

The plot F(R) v/s hυ(eV) when extrapolated on hυ axis gives the E_g of the sample. The E_g hence obtained is irrespective of transition (direct or indirect).

In order to obtain the E_g with respect to the type of transition , the function F(R) is multiplied with hυ and raised to the power *n* corresponding to the type of transitions ((F(R) h$\upsilon)^n$) which is then plotted against hυ(eV). For direct allowed transition, value of n=2 and

for indirect allowed transition, value of n=1/2. Figure below represents the plot of $F(R) \, h\upsilon)^2$ v/s $h\upsilon(eV)$ where direct allowed transition is determined.

Plots of $F(R)$ and $(F(R)h\upsilon)^n$ (where n = ½ and 2 for indirect allowed transition and direct allowed transition respectively) versus $h\upsilon(eV)$ for **1** and **2** are given in Figure II.12 and II.13 respectively. The optical band gap energies of solids **1** and **2** calculated from UV-DRS data has been tabulated in Table II.5. Although, the band gap energies are comparable in both the cases, a slight higher value is observed for solid **2.** The difference in band gap energy could be attributed to the difference in the nature of the isomeric ligands since the anion is monoprotonated in both cases.
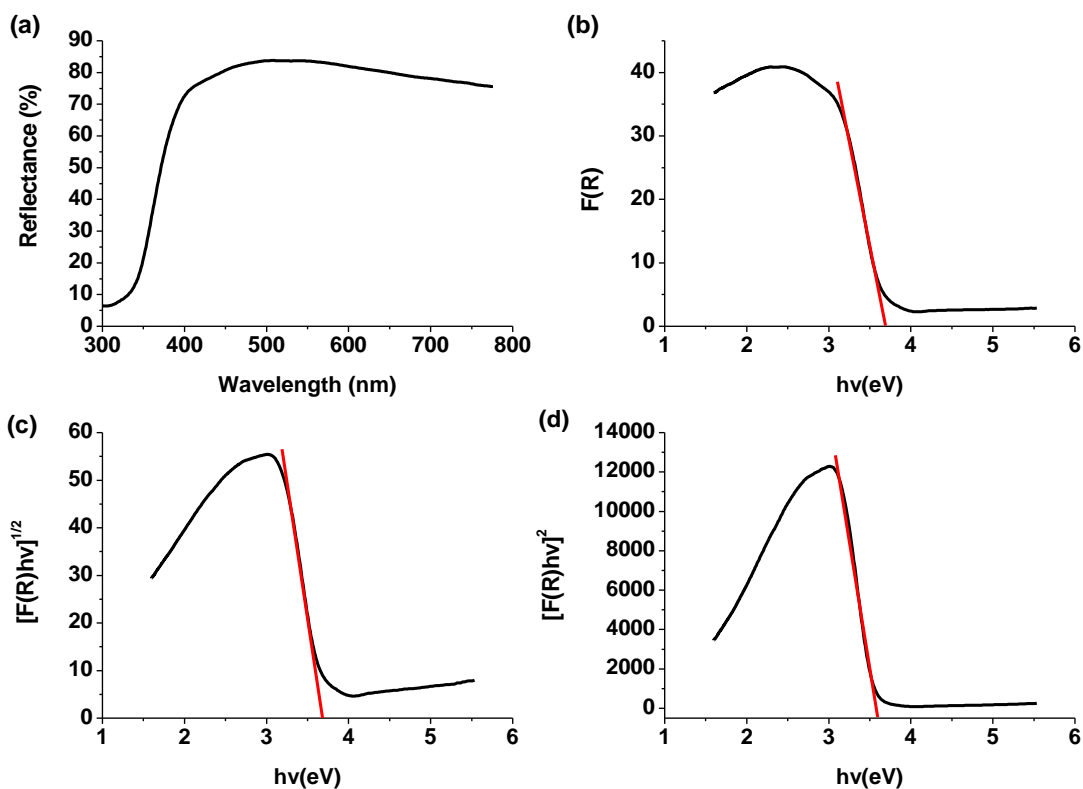
Figure II.12. Plots of (a) Reflectance versus wavelength (b) F(R) versus $h\upsilon(eV)$, (c) $(F(R)h\upsilon)^{1/2}$ versus $h\upsilon(eV)$ and (d) $(F(R)h\upsilon)^2$ versus $h\upsilon(eV)$ for **1.**
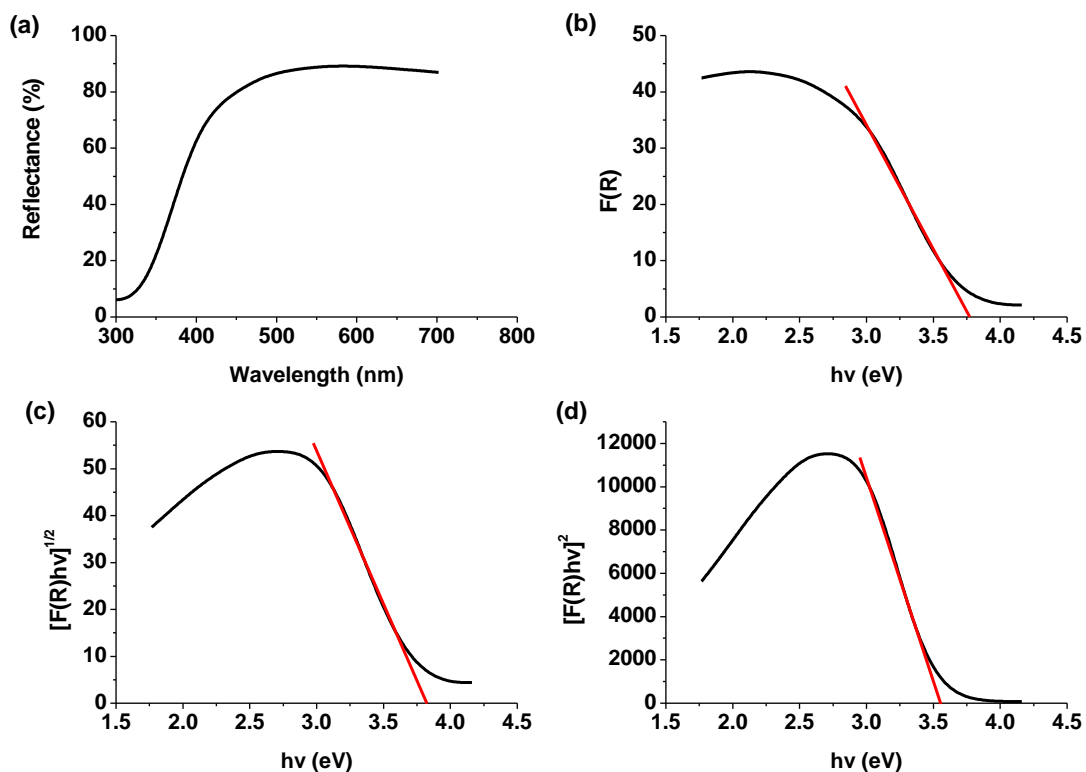
Figure II.13. Plots of (a) Reflectance versus wavelength (b) F(R) versus hυ(eV), (c) $(F(R)h\upsilon)^{1/2}$ versus hυ(eV) and (d) $(F(R)h\upsilon)^2$ versus hυ(eV) for **2.**

Table II.5. Table tabulates the irrespective, allowed indirect and allowed direct band gaps of **1** and **2**.

Solids	F(R) vs hυ (band gap energy irrespective of direct or indirect in eV)	$[F(R) h\upsilon]^{1/2}$ (allowed indirect band gap energy in eV)	$[F(R) h\upsilon]^2$ (allowed direct band gap energy in eV)
1	3.68	3.66	3.59
2	3.75	3.81	3.55

II.3.5. Chemistry of Formation

Solvent evaporation technique is one of the most facile methods employed for the crystallization of hybrid solids. The synthetic methodology used in the current study involves mixing of aqueous molybdate solution with organic ligand under constant stirring. However, mixing of the two solutions results in immediate precipitation of an amorphous solid. Therefore the solution is acidified using H_3PO_4 to obtain a clear solution. The latter when left undisturbed results in crystallization of solids **1** and **2**. The addition of H_3PO_4 has a two-fold effect. Firstly, it acts as a source of phosphate ions. Hence crystallization of PMO cluster based solids is facilitated. Secondly the pH of the reaction medium is adjusted to ~1. The highly acidic pH favors the formation of $\{HP_2Mo_5\}$ cluster anion [25] and results in protonation of the organic ligands (L). The formation of the solids can be visualized using the following equations wherein the Strandberg type polyoxometalate cluster is formed by protonation of tetrahedral molybdate; which under highly acidic conditions undergoes protonation:

$$5[MoO_4]^{2-} + 2\ PO_4^{3-} + 10H^+ \rightarrow [\{PO_4\}_2Mo_5O_{15}]^{6-} + 5H_2O$$

$$[\{PO_4\}_2Mo_5O_{15}]^{6-} + H^+ \rightarrow [\{PO_3(OH)\}\{PO_4\}Mo_5O_{15}]^{5-}$$
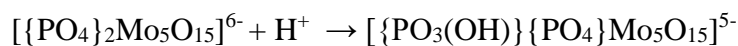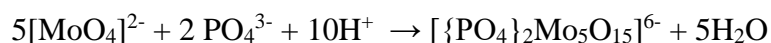
Initially, an electrostatic attraction between negativity charged $\{HP_2Mo_5\}$ cluster anion and positively charged organic moieties $(HL)^+$ initiates the self-assembly of solids **1** and **2**. The supramolecular assembly is further supported by secondary interactions which play a crucial role in crystal packing of these solids. Both the ligands have readily available $-NH_2$ and $-NH$ groups which induce H-bonding interactions between the cluster anions and $(HL)^+$ units. The presence of the aromatic ring in organic moieties ensures the possibility for $\pi\ldots\pi$ and

CH…π interactions between (HL)$^+$ counter ions [41,42]. Therefore, the role of H-bonding, π…π and CH…π interactions in crystal packing in **1** and **2** seems obvious. Additionally, the crystal structure of **2** also showed the presence of lattice water molecules. Earlier we have demonstrated in several examples that aggregation of water cluster is a secondary factor in the crystal packing of such complex structures [27]. Protonation of Strandberg-type cluster anion [1] and synthesis under ambient conditions [25] are the key factors responsible for the aggregation of water molecules in PMO cluster based solids. Strikingly, of the two solids, only **2** favored the formation of a pentameric water cluster. This could be attributed to directionality of substituents on the organic ligands. While, the hydrophobic methyl group is in close proximity to the amino group in 2*a3mp*, the comparatively distant position of methyl group in 2*a4mp* allows –NH$_2$ group to form H-bond with lattice water molecules in **2**. Therefore, aggregation of water cluster is induced in **2**.

II.4. Conclusions

Two new Strandberg-type cluster based solids *viz.* {H-2*a3mp*}$_5$[{PO$_3$(OH)}{PO$_4$}Mo$_5$O$_{15}$], **1** and {H-2*a4mp*}$_5$[{PO$_3$(OH)}{PO$_4$}Mo$_5$O$_{15}$].6H$_2$O, **2** were successfully synthesized and characterized. Detailed structural analysis revealed the role of supramolecular interactions in the crystal packing of these solids. In addition, the formation of pentameric water cluster in **2** was rationalized on the basis of supramolecular interactions and directionality of substituents on the organic ligands. Further, the electrochemical nature of **1** and **2** was explored by means of three electrode system using 1 mM K$_4$[Fe(CN)$_6$] in 0.1 M KCl as supporting electrolyte. To the best of our knowledge the redox behavior of {P$_2$Mo$_5$} cluster based solids in the presence of K$_4$[Fe(CN)$_6$] has not been examined so far. The facile synthetic methodology used for the preparation of solids **1** and **2** can be successfully applied

for the crystallization of new hybrid solids based on Strandberg-type cluster anion. Moreover, a careful selection of the organic counterpart can modify electrochemical behavior along with porosity in hybrid solids. The optical band gap energies of the solids showed slight difference on account of their difference in the nature of the ligands.

References

1. Upreti, S.; Ramanan, A. *Cryst. Growth Des.* **2006**, 6, 2066-2071.

2. Shi, S.; Chen, L.; Zhao, X.; Ren, B.; Cui, X.; Zhang, J. *Inorg. Chim. Acta* **2018**, 482, 870-877.

3. Pathan, S.; Patel, A. *Catal. Sci. Technol.* **2014**, 4, 648-656.

4. Li, C.; Mizuno, N.; Yamaguchi, K.; Suzuki, K. *J. Am. Chem. Soc.* **2019**, 141, 7687-7692.

5. Xun, S.; Guo, T.; He, M.; Ma, R.; Zhang, M.; Zhu, W.; Li, H. *J. Colloid Interface Sci.* **2019**, 534, 239.

6. Joseph, J.; Radhakrishnan, R. C.; Johnson, J. K.; Joy, S. P.; Thomas, J. *Mater. Chem. Phys.* **2020**, 242, 122488-122496.

7. Abu, Z. B. M.; Farrag, A. A. A.; Asiri, A. M. *Powder Technol*. **2013**, 246, 643-649.

8. Lu, L.; Xie, Y. *J. Mater. Sci*. **2018**, 54, 4842-4858.

9. Manivel, A.; Anandan, S. *J. Solid State Electrochem.* **2011**, 15**,** 153-160.

10. Liu, J.; Wang, J.; Chen, M.; Qian, D. *J. Nanopart. Res.* **2017**, 19**,** 264-275.

11. Niu, J.; Ma, J.; Zhao, J.; Ma, P.; Wang, J. *Inorg. Chem. Commun*. **2011**, 14, 474-477.

12. Ma, X.; Zhou, F.; Yue, H.; Hua, J.; Ma, P. *J. Mol.Struct*. **2019**, 1198, 126865-126872.

13. Li, Z. L.; Wang, L. C.; Wang, J. P.; You, W. S.; Zhu, Z. M. *Dalton Trans*. **2014**, 43, 5840-5846.

14. Strandberg, R. *Acta. Chem. Scand*. **1973**, 27, 1004-1018.

15. Shi, Z.; Li, F.; Zhao, J.; Yu, Z. Y.; Zheng, Y.; Chen, Z.; Guo, Q.; Zhang, G.; Luo, Y. *Inorg. Chem. Commun.* **2019**, 102, 104-107.

16. Ji, Y. M.; Zhao, M.; Han, P. P.; Fang, Y.; Han, Q. X.; Li, M. X. *Inorg. Nano-Met. Chem*. **2018**, 48, 421-425.

17. Xu, M.; Li, F.; Wang, T.; Xu, L. *Inorg. Chem. Commun*. **2018**, 94, 123-126.

18. Zhao, H.; Li, J.; Fang, Y.; Chang, B.; Meng, Q.; Li, M.; Wang, C.; Zhu, X. *Bioorg. Med. Chem. Lett*. **2020**, 30, 126781-126786.

19. Ganesan, S. V.; Natarajan, S. *J. Chem. Sci*. **2005**, 117, 219-226.

20. Upreti, S.; Ramanan, A. *Synth. React. Inorg. Metal-org. Nano-Metal Chem.* **2008**, 38, 69-75.

21. Yan, D.; Zheng, L.; Zhang, Z.; Wang, C.; Yuan, Y.; Zhu, D.; Xu, Y. *J. Coord. Chem.* **2010**, 63, 4215-4225.

22. Ma, F. X.; Chen, Y. G.; Yang, H. Y.; Dong, X. W.; Jiang, H.; Wang, F.; Li, J. H. *J. Cluster. Sci*. **2019**, 30, 123-129.

23. Paul, L.; Dolai, M.; Panja, A.; Ali, M. *New J. Chem.* **2016**, 40, 6931-6938.

24. Qu, M.; Feng, H.; Ma, C.; Yang, Y.; Yu, X. *Inorg. Chem. Commun*. **2017**, 81, 22-26.

25. Joshi, A.; Gupta, R.; Singh, B.; Sharma, D.; Singh, M. *Dalton Trans*. **2020**, 49, 7069-7077.

26. Asnani, M.; Kumar, D.; Duraisamy, T.; Ramanan, A. *J. Chem. Sci*. **2012**, 124, 1275-1286.

27. Wang, Y.; Zhang, L. C.; Zhu, Z. M.; Li, N.; Deng, A. F.; Zheng, S. Y.; *Transition Met. Chem*. **2011**, 36, 261-267.

28. Thomas, J. Ph.D. Thesis, Indian Institute of Technology, Delhi, India, **2010**.

29. Zhai, Q.; Wu, X.; Chen, S.; Chen, L.; Lu, C. *Inorg. Chim. Acta* **2007**, 360, 3484-3492.

30. Harchani, A.; Haddad, A. *J. Clust. Sci*. **2015**, 26, 1645-1653.

31. Song, L.; Yu, K.; Su, Z.; Wang, C.; Wang, C.; Zhou, B. *J. Coord. Chem.* **2014**, 67, 522-532.

32. Bruker Analytical X-ray Systems, SMART: Bruker Molecular Analysis Research Tool, Version 5.618, **2000**.

33. Bruker Analytical X-ray Systems, SAINT-NT, Version 6.04, **2001**.

34. Bruker Analytical X-ray Systems, SHELXTL-NT, Version 6.10, **2000**.

35. Klaus B., University of Bonn, Germany DIAMOND, Version 4.1

36. Brown I D and Altermatt D **1985** Bond-valence parameters obtained from a systematic analysis of the Inorganic Crystal Structure Database *Acta Crystallogr*. **B41** 244.

37. Nakamoto K **1978** Infrared and Raman spectra of inorganic and coordination compounds (New York: John Wiley & Sons).

38. Jose, J.; Rajamani, A. R.; Anandaram, S.; Jose, S. P.; Peter, S. C.; Sreeja, P. B. *Appl. Organometal. Chem*. **2019**, e5063.

39. Lopez, R.; Gomez, R. *J. Sol-Gel Sci.Technol*. **2012**, 61, 1-7.

40. Reddy, K. M.; Manorama, S. V.; Reddy, A. R. *Mater. Chem. Phys*. **2003**, 78, 239-245.

41. Desiraju, G. R.; Vittal, J. J.; Ramanan, A. **2011**, Crystal Engineering - A Textbook (Singapore: World Scientific Publishing)

42. Das, D.; Biradha, K. *Austr. J. Chem.* **2019**, 72, 742-750.

CHAPTER III

Supramolecular isomerism in {P₂Mo₅} cluster based solids

Summary

Self-assembly of molybdate and phosphate precursors in the presence of zinc ions and organic ligands *viz.* benzimidazole (*bimi*), 4-aminopyridine (*4-ap*) and pyrazole (*pz*) resulted in the crystallization of Strandberg cluster based solids {H*bimi*}$_5$[HP$_2$Mo$_5$O$_{23}$].5H$_2$O (**3**), {H*bimi*}$_6$[P$_2$Mo$_5$O$_{23}$].H$_2$O (**4**), {4-H*ap*}$_4$[H$_2$P$_2$Mo$_5$O$_{23}$].2H$_2$O (**5**), {4-H*ap*}$_5$[HP$_2$Mo$_5$O$_{23}$] (**6a**) and {H*pz*}$_6${Zn(*pz*)$_4$(H$_2$O)$_2$}[{Zn(*pz*)$_2$P$_2$Mo$_5$O$_{23}$}$_2$].8H$_2$O (**7**) under hydrothermal condition. While, Solid **4** is the new supramolecular isomer of {H*bimi*}$_5$[HP$_2$Mo$_5$O$_{23}$].5H$_2$O (**3**); Solids **5** and **6a** are new supramolecular isomers of {4-H*ap*}$_6$[P$_2$Mo$_5$O$_{23}$].5H$_2$O (**6b**) which was reported earlier in literature. Under our reaction conditions, while pyrazole readily formed complex with zinc centers to form a derivatized Strandberg-type cluster; benzimidazole and 4-aminopyridine formed only organic-inorganic hybrid solids **3-6a**. The chapter, therefore, provides a rationale for the formation of Solids **3-6a** in terms of the reaction conditions. In addition, supramolecular isomerism in 4-aminopyridine based {P$_2$Mo$_5$} cluster anions varies due to the extent of protonation on the cluster anion. Therefore, the extent of protonation on cluster anion and the nature of the organic ligands on the optical band gap energies (E_g) of the synthesized solids were investigated.

III.1. Introduction

Designing polyoxometalates (POMs) through the self-assembly of entirely different counterparts is of great interest on account of their structural versatility and emerging applications. Strandberg-type phosphomolybdates (PMOs) are an important sub-family of POMs which plays a vital role in this area of research. A number of $\{P_2Mo_5\}$ cluster based PMO solids with or without the incorporation of metal ions have been reported in literature [1-4]. The main synthetic methodologies adopted for crystallization of $\{P_2Mo_5\}$ cluster based solids are solvent evaporation and hydrothermal synthesis [5,6]. While synthetic parameters such as temperature and pH of the reaction medium dictate the formation on PMO cluster anion [7-9]; selection of metal centers (for example, transition or rare earth metal ions) and organic ligands can induce structural features such as aggregation of water clusters, interpenetration and supramolecular isomerism [10-12].

As discussed in Chapter I, according to Moulton and Zaworotko, "Supramolecular isomerism in this context is the existence of more than one type of network superstructure for the same molecular building blocks and is therefore related to structural isomerism at the molecular level. In other words, the relationship between supramolecular isomerism and molecules is similar to that between molecules and atoms." [13]. With respect to PMO cluster based solids, there are only limited examples of supramolecular isomers based on $\{P_2Mo_5\}$ cluster anion. Therefore, in the present chapter, an attempt has been made to crystallize supramolecular isomers based on $\{P_2Mo_5\}$ cluster in the presence of zinc chloride and ligands *viz.* benzimidazole (*bimi*), 4-aminopyridine (*4-ap*) and pyrazole (*pz*). The synthesis under hydrothermal condition resulted in four new $\{P_2Mo_5\}$ cluster based solids. While, the solids **4** and **5** & **6a** are new supramolecular isomers of previously reported

hybrid solids {H*bimi*}$_5$[HP$_2$Mo$_5$O$_{23}$].5H$_2$O [14] and {4-H*ap*}$_6$[P$_2$Mo$_5$O$_{23}$].5H$_2$O [15] respectively; {H*pz*}$_6${Zn(*pz*)$_4$(H$_2$O)$_2$}[{Zn(*pz*)$_2$P$_2$Mo$_5$O$_{23}$}$_2$].8H$_2$O, **7** can be considered as a pseudopolymorph of previously reported solid (*pz*)[{Zn(*pz*)$_3$}$_3${P$_2$Mo$_5$O$_{23}$}].2H$_2$O [16]. The chapter highlights the structural differences in the supramolecular isomers; and the effect of supramolecular isomerism in {P$_2$Mo$_5$} cluster based solids and nature of ligands on the optical band gap energy (E$_g$) of the synthesized solids. A comparative study has been done on the effect of protonation of the cluster anion with same organic ligands on the band gap energy.

III.2. Experimental Section

III.2.1. Synthesis

A mixture of zinc chloride (ZnCl$_2$, 0.075 g, 0.55 mmol, Aldrich, 98%), benzimidazole (3.3 mmol, Aldrich, 98%) and sodium molybdate (Na$_2$MoO$_4$.2H$_2$O, 0.40 g, 1.65 mmol, Merck, 99%) was taken in 6 ml of distilled water, sealed in a 10 ml Teflon lined stainless steel container and heated at 150°C for three days. The initial pH was adjusted using 1 M orthophosphoric acid. After slow cooling to room temperature, the white crystals of **3** (refer Scheme III.1) were washed with water and acetone and allowed to dry in air. The same procedure was repeated for the synthesis of solids **4**-**7** using benzimidazole, 4-aminopyridine and pyrazole. The same molar ratio was used for the synthesis **4**, however the molar ratio of Mo:Zn:ligand was adjusted to 1:1:6 for **5** and **6a** and 3:1:6 for **7**. The Solid **6b** was reproduced as reported in literature [15]. The yield of solids was found to be 70-75% based on Mo.

Interestingly, Solid **3** was synthesized by Z. Que *et. al.* via solvent evaporation technique using water-alcohol solution of Na$_2$MoO$_4$.2H$_2$O and *bimi* in the molar ratio 1:0.73 [14]. However, synthesis of **3** under hydrothermal conditions has not been reported so far.
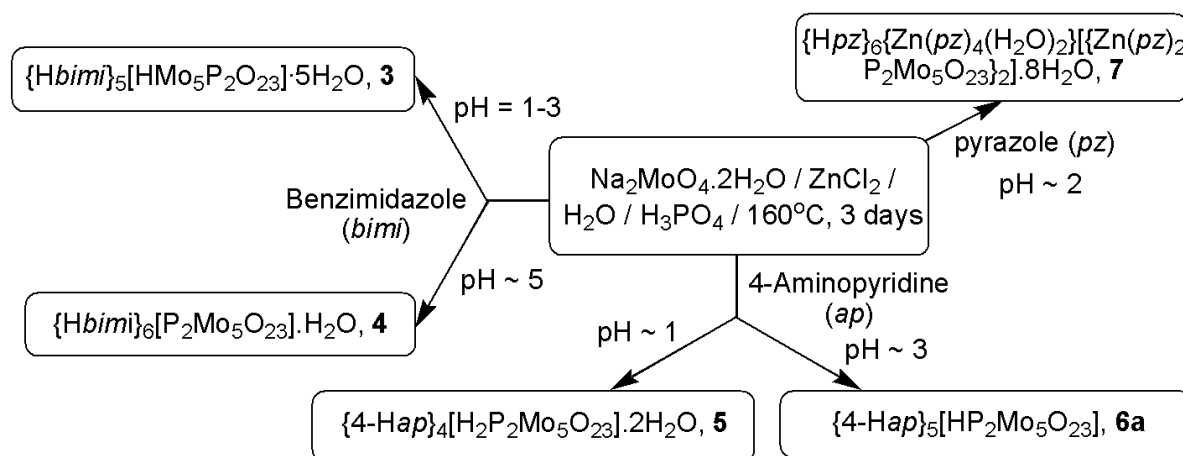
Scheme III.1. Scheme showing the experimental procedure to crystallize solids **3**-**7**.

III.2.2. Characterization

The solids were characterized using single crystal X-ray diffraction, powder X-ray diffraction, fourier transform infrared spectroscopy and thermogravimetric analysis. Band gap energy calculations were done using data collected from UV-Vis spectrophotometer as discussed under Section II.2.2 in Chapter II. The crystal and refinement data for solids **4**-**6** have summarized in Table III.1. The data for solid **7** will be discussed in Chapter IV along with other metal pyrazole complex incorporated {P$_2$Mo$_5$} cluster based solids.

III.3. Results and Discussion

The solids **3-6** are based on {P$_2$Mo$_5$} cluster anion and its structure has been discussed under Section II.3 in Chapter II.

Table III.1. Crystal and Refinement Data for Solids **4**-**6a**.

	4	**5**	**6a**
Formula	C$_{42}$H$_{42}$Mo$_5$N$_{12}$O$_{24}$P$_2$	C$_{20}$H$_{28}$Mo$_5$N$_8$O$_{25}$P$_2$	C$_{25}$H$_{35}$Mo$_5$N$_{10}$O$_{23}$P$_2$
Formula weight, g	1640.52	1322.14	1385.27
T (K)	298	298	296
Space Group	$P\,2_12_12_1$	P2$_1$/c	$P\,2_1$/m
a, Å	10.7210(12)	19.858(5)	8.7972(18)
b, Å	14.7139(17)	11.326(3)	19.266(4)
c, Å	35.271(4)	17.957(4)	13.190(3)
α, °	90	90	90
β, °	90	105.289(4)	91.58(3)
γ, °	90	90	90
V, Å^3	5563.8(11)	3895.7(17)	2234.7(8)
Z	4	4	2
d$_{calc}$, g·cm^{-3}	1.959	2.254	2.059
$\mu_{MoK\alpha}$, cm^{-1}	1.247	1.749	1.528
λ (Å)	0.71073	0.71073	0.71073
R$_1$(I>2σI), WR$_2$(all)	0.0856, 0.1718	0.0662, 0.1172	0.0568, 0.1471
GOF	1.364	1.323	1.114

III.3.1. Crystal structure of 3

The crystal structure of **3** consists of monoprotonated cluster {HP$_2$Mo$_5$}, {H*bimi*}$^+$ cations and lattice water molecules. The protonation of only one of the phosphate groups was confirmed using Bond Valence Sum (BVS) calculations [17]. Crystal structural analysis revealed that N–H...O interactions aggregate {HP$_2$Mo$_5$} cluster anions and {H*bimi*}$^+$ cations to form a dimeric unit as shown in Figure III.1 (also refer Table III.2). These dimeric units are connected by {N1N3} moiety to form ladder-like 1-D chains which propagate along *a* axis. The lattice water molecules *viz.* O2W, O3W, O4W and O5W form a terameric unit which links the 1-D chains to form a 3-D supramolecular assembly (Figure III.1c, Table III.3). The packing of {H*bimi*}$^+$ moieties in **3** is reinforced by CH…π and π…π interactions as shown in Figure III.2. The crystal structure of **3** was earlier reported by Qu *et*. *al*. [14] as a 3-D supramolecular structure stabilized through electrostatic attraction, H-bonding and π...π interactions between {HP$_2$Mo$_5$} polyanion, {H*bimi*}$^+$ moieties and lattice water molecules.

Table III.2. H-bonding interactions in **3**.

D–H…A	D–H (Å)	H…A (Å)	D…A (Å)	∠ D–H…A (°)
N1-H1C…O3	0.775(47)	1.86(5)	2.617(5)	165.35(489)
N3-H3C…O13	0.753(61)	2.023(59)	2.760(5)	166.03(610)
N4-H4C…O2W	0.928(51)	1.795(52)	2.704(7)	165.84(465)
N6-H6C…O9	0.796(57)	2.023(56)	2.799(5)	164.53(567)
N7-H7C…O3	0.904(55)	1.979(54)	2.704(5)	136.18(477)
N9-H9D…O7	0.895(41)	1.837(44)	2.685(5)	157.30(342)
N12-H12C…O1W	0.804(54)	1.950(54)	2.734(6)	164.64(538)
N13-H13C…O22	0.821(58)	2.129(57)	2.864(5)	149.08(537)
N15-H15C…O10	0.780(47)	1.942(48)	2.718(5)	172.92(489)
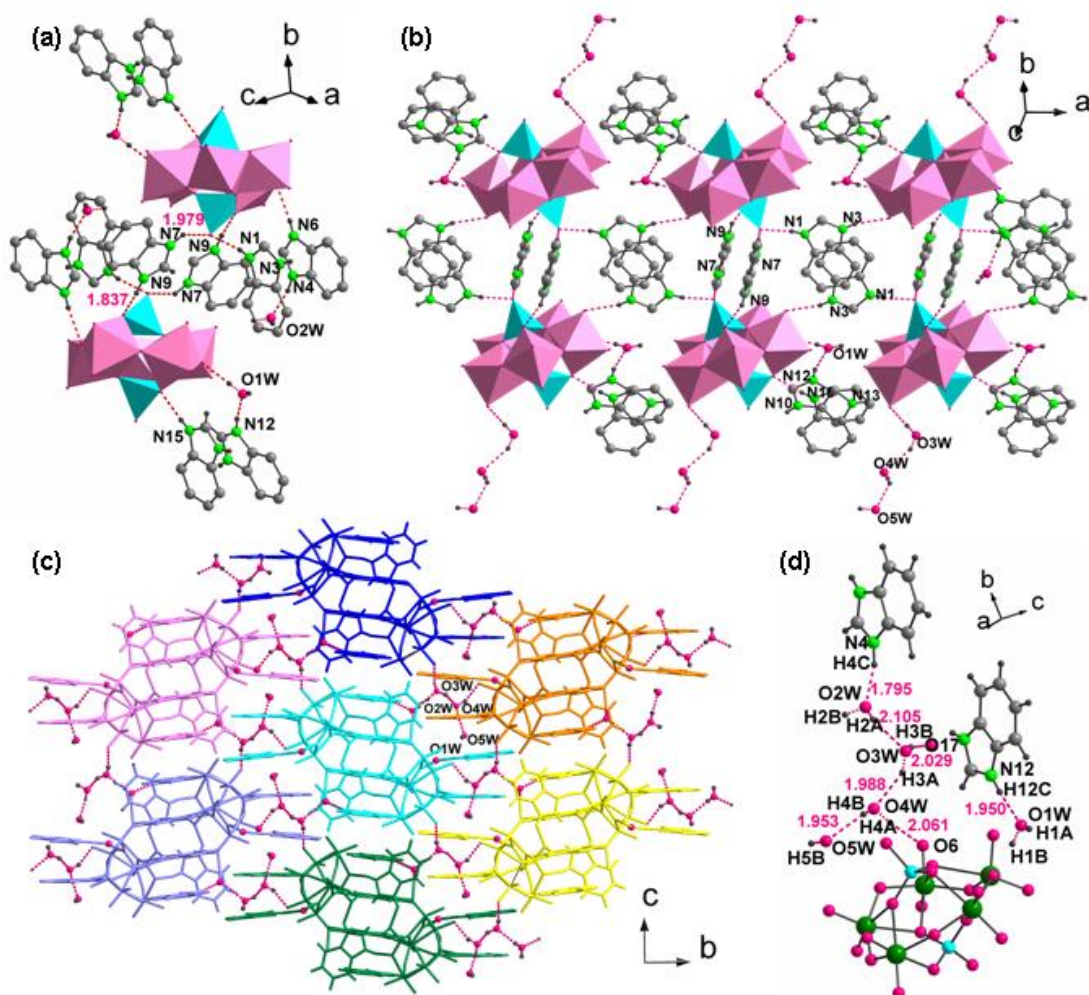
Figure III.1. (a) {HP₂Mo₅} anion shows extensive H-bonding interaction with the five {H*bimi*}⁺ moieties, of which {N7N9} unit connects two {HP₂Mo₅} units to form a dimeric unit. For clarity only hydrogen atoms involved in N-H…O interactions (dashed red lines) have been shown in the figure. (b) The dimeric units are connected by {N1N3} moiety to form ladder-like 1-D chains propagating along *a* axis ({N4N6} moiety and lattice water molecule, O2W have been omitted). (c) View along *a* axis showing the connection between one 1-D chain (depicted in cyan color) with six others. The packing of chains is facilitated by water tetramer consisting of O2W, O3W, O4W and O5W. (d) H-bonding interactions exhibited by lattice water molecules.

Table III.3. H-bonding interactions in water tetrameric unit of **3**.

D–H…A	D–H (Å)	H…A (Å)	D…A (Å)	∠ D–H…A (°)
O2W-H2A…O3W	0.740(65)	2.105(66)	2.827(6)	165.13(705)
O3W-H3A…O4W	0.898(44)	1.988(57)	2.786(9)	147.30(398)
O4W-H4B…O5W	0.908(68)	1.953(72)	2.666(10)	134.19(486)
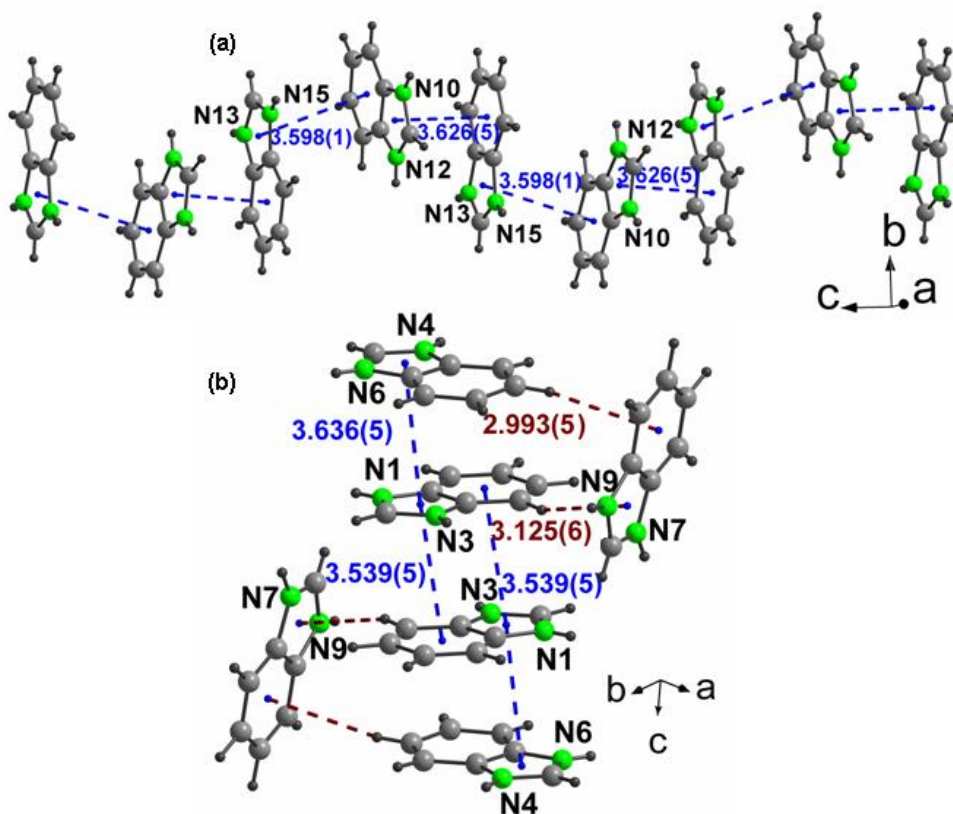
Figure III.2. (a) π…π interactions between {N10N12} and {N13N15} moieties. (b) CH…π and π…π interactions between {N1N3}, {N4N6} and {N7N9} moieties forming a hexameric unit. CH…π and π…π interactions have been shown in dashed brown and blue lines respectively.

III.3.2. Crystal structure of 4

Unlike **3**, the crystal structure analysis of **4** suggested the presence of one $\{P_2Mo_5\}$ cluster anion, six $\{Hbimi\}^+$ cations and one lattice molecule per asymmetric unit (refer Figure III.3). Of the six $\{Hbimi\}^+$ moieties, H-bonding interactions mediated by $\{N5N6\}$ link neighboring $\{P_2Mo_5\}$ cluster anions to form 1-D chains which propagate along *a*-axis. The other four $\{Hbimi\}^+$ moieties $\{N3N4\}$, $\{N7N8\}$, $\{N9N10\}$ and $\{N11N12\}$ exhibit extensively H-bonding interactions with the $\{P_2Mo_5\}$ cluster anion. The 1-D chains are further connected through H-bonding interactions mediated by $\{N7N8\}$ moieties to form 2-D corrugated sheet. N11-H11…O3 (2.019(10) Å) interactions between neighboring 2-D corrugated sheets facilitates the crystal packing in **4**. The packing of 2-D sheets results in the formation of voids which are occupied by the sixth benzimidazole moiety *viz.* $\{N1N2\}$ along with the lattice water molecule, O1W (refer Figure III.3d). CH…π interactions also play a crucial role in crystal packing of **4**. While, three of the $\{Hbimi\}^+$ moieties *viz.* $\{N5N6\}$, $\{N7N8\}$ and $\{N9N10\}$ are linked to each other though CH…π interactions; $\{N3N4\}$ and $\{N11N12\}$ form a dimer which further reinforce the H-bonding in 1-D chains of **4** (Figure III.4). In addition, the packing of 1-D chains to form 2-D corrugated sheets is favored by CH…π interactions exhibited by $\{N7N8\}$ moieties (Figure III.5, also refer Table III.4 and III.5). It is noteworthy that **4** is the first supramolecular isomer of $\{Hbimi\}_5[HP_2Mo_5O_{23}].5H_2O$ reported by Qu *et*. *al*. [14].
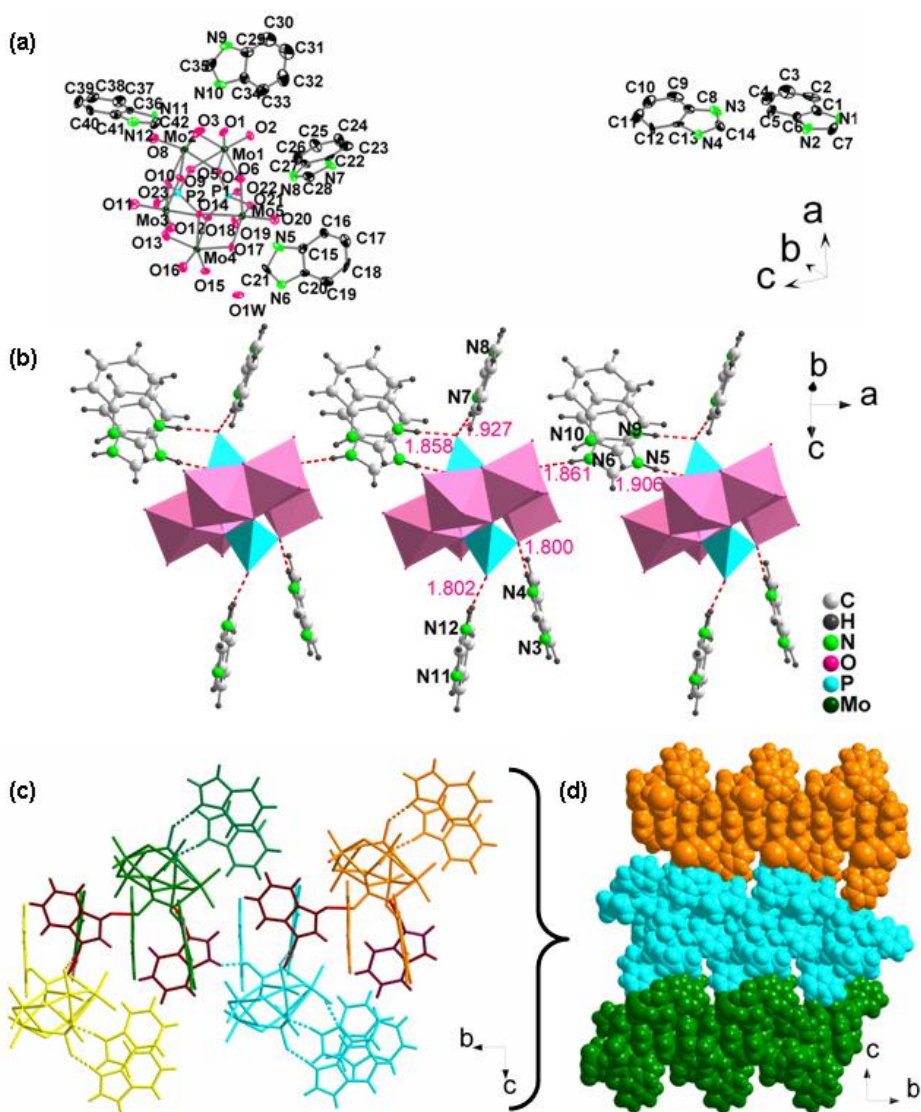
Figure III.3. (a) ORTEP view of **4**. The hydrogen atoms have been omitted for clarity. (b) 1-D chains formed via H-bonding interactions (shown in dashed red lines) mediated by protonated {N5N6} moieties. (c) NH…O interactions mediated by {N7N8} moiety (shown in brown color) link neighboring 1-D chains to form a 2-D corrugated sheet. The connection between four of these 1-D chains depicted in yellow, cyan, green and orange is shown herein. (d) View along *a* axis showing the crystal packing of 2-D corrugated sheets. The voids seen in figure are occupied by the sixth protonated benzimidazole moiety {N1N2} along with lattice water molecule, O1W.
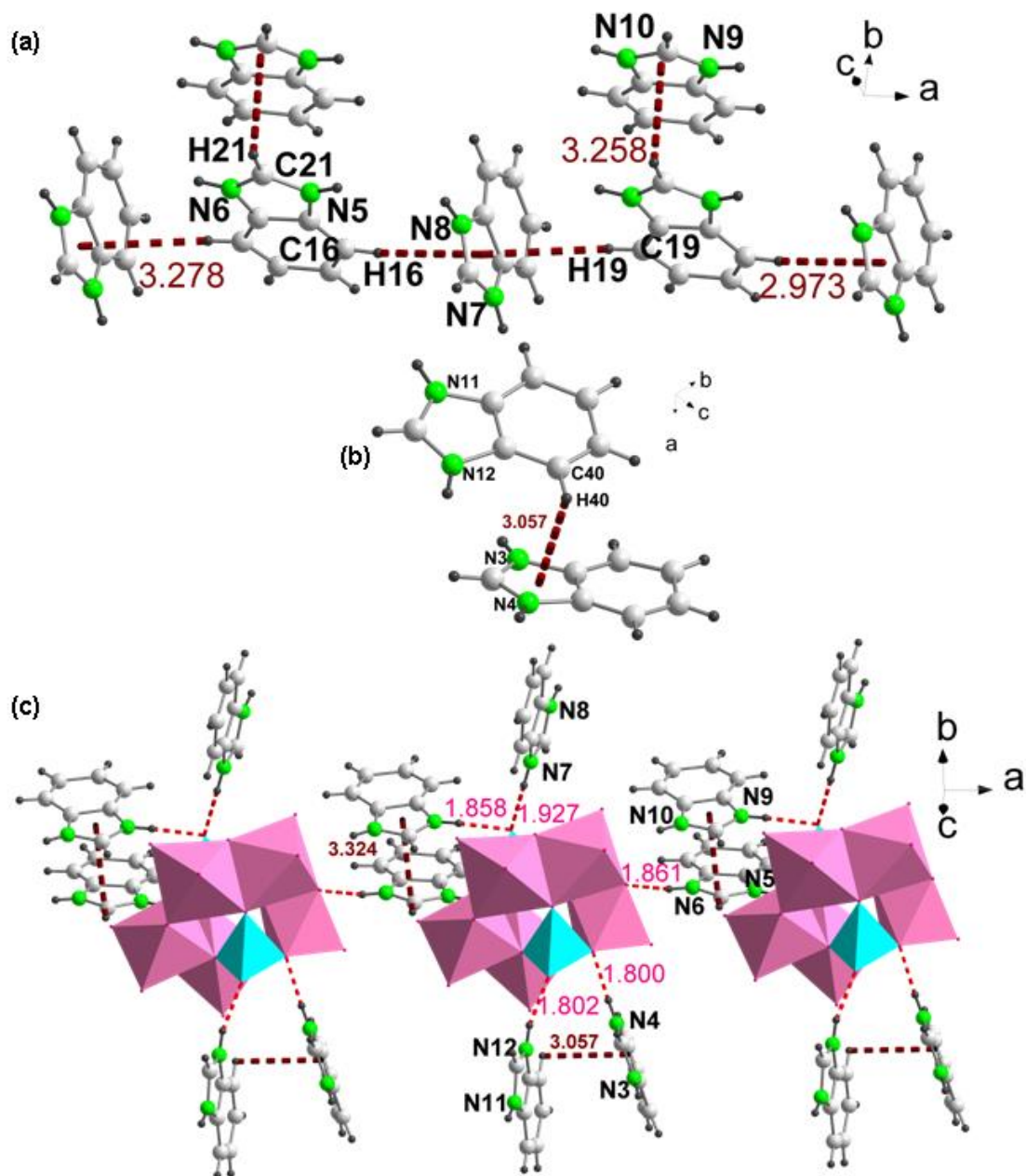
Figure III.4. (a) While three of the {H*bimi*}$^+$ moieties *viz.* {N5N6}, {N7N8} and {N9N10} are linked to each other though CH…π interactions (shown in dashed brown color); {N3N4} and {N11N12} merely form a dimer as seen in (b). (c) The H-bonding in 1-D chains of **4** is reinforced through CH…π interactions.
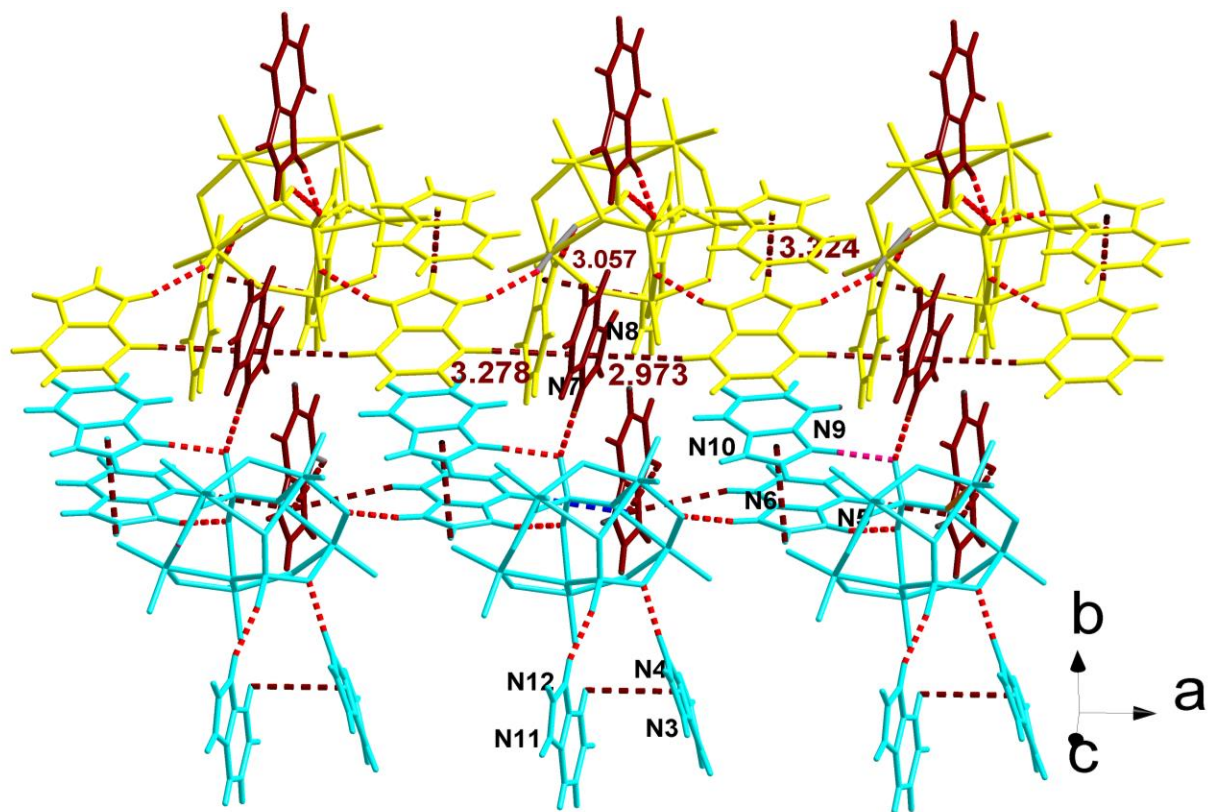
Figure III.5. The packing of 1-D chains is also facilitated through CH…π interactions. CH…π interactions mediated by {N7N8} moieties (shown in brown color) favors the crystal packing in **4**. Two neighboring 1-D chains are shown here in blue and yellow color. The dashed red lines represent H-bonding interactions.

Table III.4. H-bonding interactions in **4**.

D–H…A	D–H (Å)	H…A (Å)	D…A (Å)	∠ D–H…A (°)
N1-H1…O10	0.858(14)	2.255(8)	3.010(16)	146.86(96)
N2-H2…O1W	0.860(14)	1.903(11)	2.734(18)	162.12(98)
C7-H7A…O23	0.929(18)	2.163(10)	2.955(20)	142.66(11)
N3-H3…O11	0.861(14)	2.259(10)	3.012(18)	146.02(10)
N3-H3…O13	0.861(14)	2.084(11)	2.773(18)	136.58(98)
N4-H4…O5	0.860(11)	1.800(9)	2.653(14)	171.06(75)
N5-H5…O21	0.859(11)	1.906(8)	2.732(14)	160.57(79)
N6-H6…O2	0.860(13)	1.861(10)	2.695(16)	162.99(92)
C21-H21…O15	0.932(14)	2.332(11)	3.234(18)	162.89(91)
N7-H7…O22	0.860(12)	1.927(7)	2.700(14)	148.91(81)
N8-H8…O21	0.860(14)	1.952(8)	2.780(16)	161.08(94)
N9-H9…O22	0.859(13)	1.858(9)	2.697(15)	164.91(90)
N10-H10…O3	0.859(15)	2.353(10)	3.075(19)	141.98(10)
N10-H10…O7	0.859(15)	2.305(10)	3.052(18)	145.59(10)
N11-H11…O3	0.861(11)	2.019(10)	2.815(16)	153.22(79)
N12-H12…O23	0.861(14)	1.802(9)	2.644(17)	165.55(10)
C40-H40…O19	0.927(20)	2.328(7)	3.19(2)	154.55(11)

Table III.5. CH...π interactions in **4**.

CH...π	H...π (Å)
C40-H40...π {N3N4}	3.057(1)
C21-H21...π {N9N10}	3.258(1)
C16-H16...π {N7N8}	2.973(1)
C19-H19...π {N7N8}	3.278(1)

III.3.3. Crystal structure of 5 and 6

5 and **6a** are new supramolecular isomers of previously reported hybrid solid {4-H*ap*}$_6$[P$_2$Mo$_5$O$_{23}$].5H$_2$O, **6b** [15]. BVS calculations indicated that both the phosphate groups per cluster anion of **5** were protonated. On the other hand in **6a**, only one of the phosphate groups of cluster anion was protonated and in **6b**, the phosphate groups are not protonated. Interestingly, the topology of {4-H*ap*}$^+$ moieties, the cluster anion and lattice water molecules varies significantly in the three supramolecular isomers. While asymmetric unit of **5** consists of one {H$_2$P$_2$Mo$_5$} cluster anion, four monoprotonated {4-H*ap*}$^+$ moieties and two lattice water molecules; **6a** showed the presence of one {HP$_2$Mo$_5$} cluster anion and five {4-H*ap*}$^+$ moieties per asymmetric unit (refer Figure III.6).

The crystal structure analysis of **5** suggested that of the four {4-H*ap*}$^+$ moieties, {N1N2} and {N5N6} moieties linked {H$_2$P$_2$Mo$_5$} cluster anions to form 2-D sheet through N-H…O interactions (2.069(3)-2.208(3) Å) as shown in Figure III.7 (also refer Table III.6). The 2-D sheet showed the presence of voids which were occupied by the third {4-H*ap*}$^+$ moieties *viz.* {N7N8}. Each 2-D sheet was connected to two other sheets to form a 3-D supramolecular assembly (refer Figure III.8a) through {N1N2} and lattice water molecule, O1W via C-H…O (2.287(4) Å) and O…O interactions (refer Table III.7) respectively. The crystal packing of 2-D sheets further resulted in voids which were occupied by the fourth {4-H*ap*}$^+$ moiety *viz.* {N3N4} along with lattice water molecule, O2W. The occurrence {N3N4} moiety in the voids between 2-D sheets is also assisted by CH…π interactions between {N5N6}, {N3N4} and {N1N2} moieties as shown in Figure III.8b.
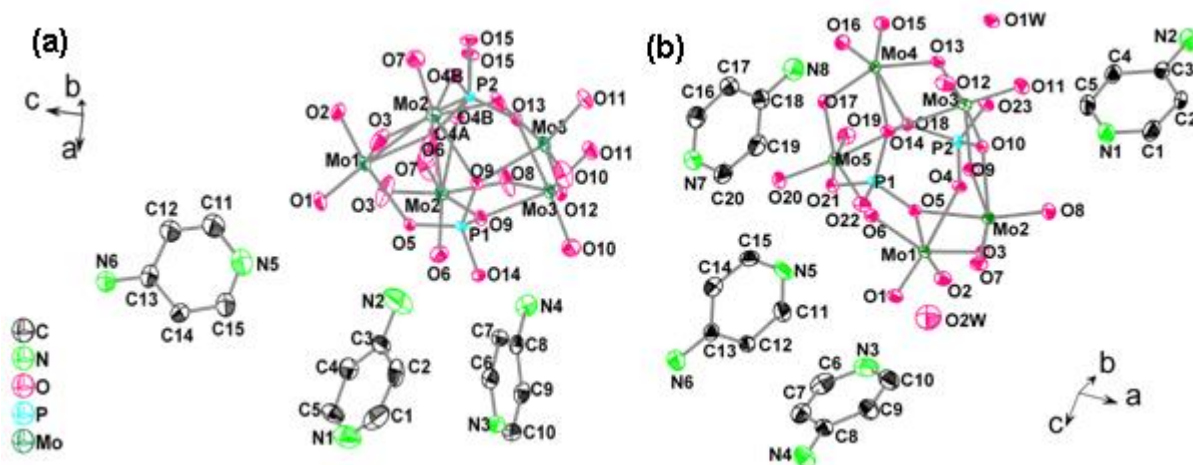
Figure III.6. ORTEP view of (a) **5** and (b) **6a**. The hydrogen atoms have been omitted for clarity.

Table III.6. H-bonding interactions in **5**.

D–H…A	D–H (Å)	H…A (Å)	D…A (Å)	∠ D–H…A (°)
N1-H1...O8	0.859(6)	2.087(4)	2.917(7)	162.32(34)
C1-H1A…O7	0.930(5)	2.287(4)	3.055(8)	139.57(35)
N2-H2A…O4	0.859(6)	2.208(3)	3.014(7)	156.03(41)
N3-H3…O2W	0.860(6)	2.045(7)	2.877(10)	162.46(39)
N4-H4A…O11	0.860(5)	2.377(2)	3.003(5)	130.07(31)
N5-H5…O21	0.860(5)	2.069(3)	2.812(5)	144.24(27)
N6-H6B…O17	0.860(4)	2.208(3)	3.047(5)	165.30(29)
N7-H7…O12	0.860(6)	2.346(5)	2.973(8)	130.03(32)
N8-H8Y2…O16	0.859(6)	2.286(4)	2.955(8)	134.88(39)
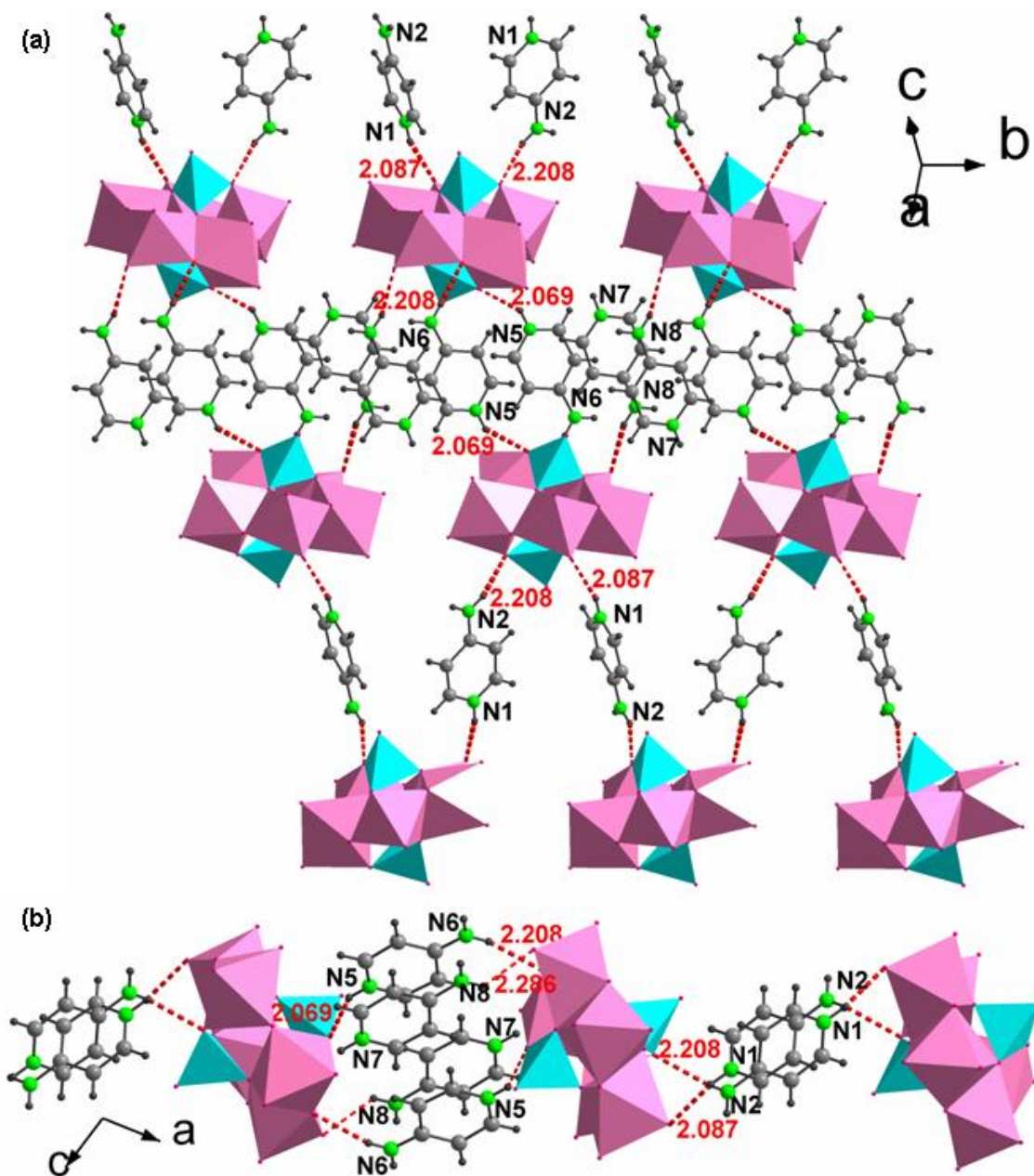
Figure III.7. (a) NH…O interactions mediated by {N1N2} and {N5N6} moiety link {H$_2$P$_2$Mo$_5$} cluster anions to form 2-D sheet through N-H…O interactions (2.069(3)-2.208(3) Å). The third (H*ampy*)$^+$ moiety *viz.* {N7N8} is encapsulated in the voids of 2-D sheet through N-H…O interaction (2.286(4) Å). (b) View along *b* axis.
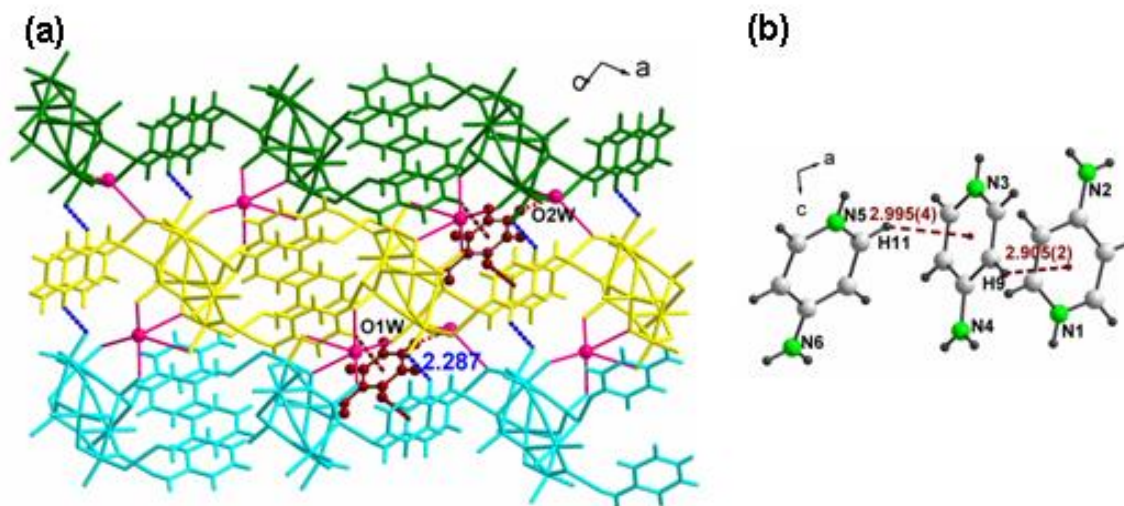
Figure III.8. (a) Figure showing packing of sheets. Three such sheets are shown in green, yellow and cyan. Two of the sheets are connected via H-bonding interactions mediated by {N1N2} and lattice water molecule, O1W. The inter-sheet H-bonding and O…O interactions are depicted in dashed blue and solid red color respectively. The voids formed as a result of crystal packing of 2-D sheets are occupied by {N3N4} moieties and lattice water molecule, O2W shown in brown and pink color respectively. (b) CH…π interactions between {N5N6}, {N3N4} and {N1N2} are shown in dashed brown lines.

Table III.7. O...O interactions in **5**.

Sl. No.	O…O	Distance (Å)
1	O1W…O1	2.767(5)
2	O1W…O13	2.655(6)
3	O1W…O22	2.719(7)
4	O1W…O23	2.622(5)
5	O2W…O8	2.933(7)
6	O2W…O2	2.902(5)

On the other hand, in **6a**, through H-bonding interactions mediated by {N3N4}, {4-H*ap*}⁺ moieties and {P₂Mo₅} cluster anions form 1-D zig-zag chains. The 1-D chains propagate

85

along *b*-axis. The 1-D chains are connected through H-bonding interactions mediated by {N5N6} moieties to form 2-D corrugated sheet having voids which are occupied by {N1N2} moieties. CH…π and π…π interactions between {N1N2}…{N3N4} and {N3N4}…{N3N4} moieties respectively favor the incorporation of {N1N2} units in the voids of the 2-D corrugated sheets. CH…π and π…π interactions between {N1N2} and {N3N4} moieties form a tetrameric unit which is incorporated within the 2-D corrugated sheet (refer Figure III.9, III.10 and III.11). Further {N1N2} moieties link neighboring 2-D corrugated sheets via H-bonding interactions (shown in dashed red lines) to form a supramolecular 3-D framework. CH…π interactions between the tetrameric units and {N5N6} moieties of neighboring 2-D corrugated sheets form 1-D zig-zag chains which further reinforces the supramolecular crystal packing in **6a**.
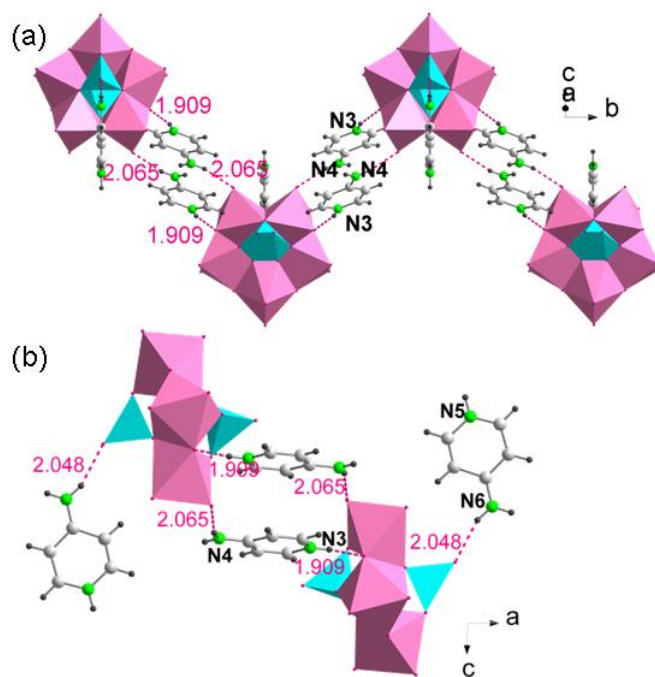
Figure III.9. (a) H-bonding interactions (shown in dashed red lines) between {4-H*ap*}⁺ moieties and {P₂Mo₅} cluster anions forming 1-D zig-zag chains in **6a**. (b) View along *b*-axis.
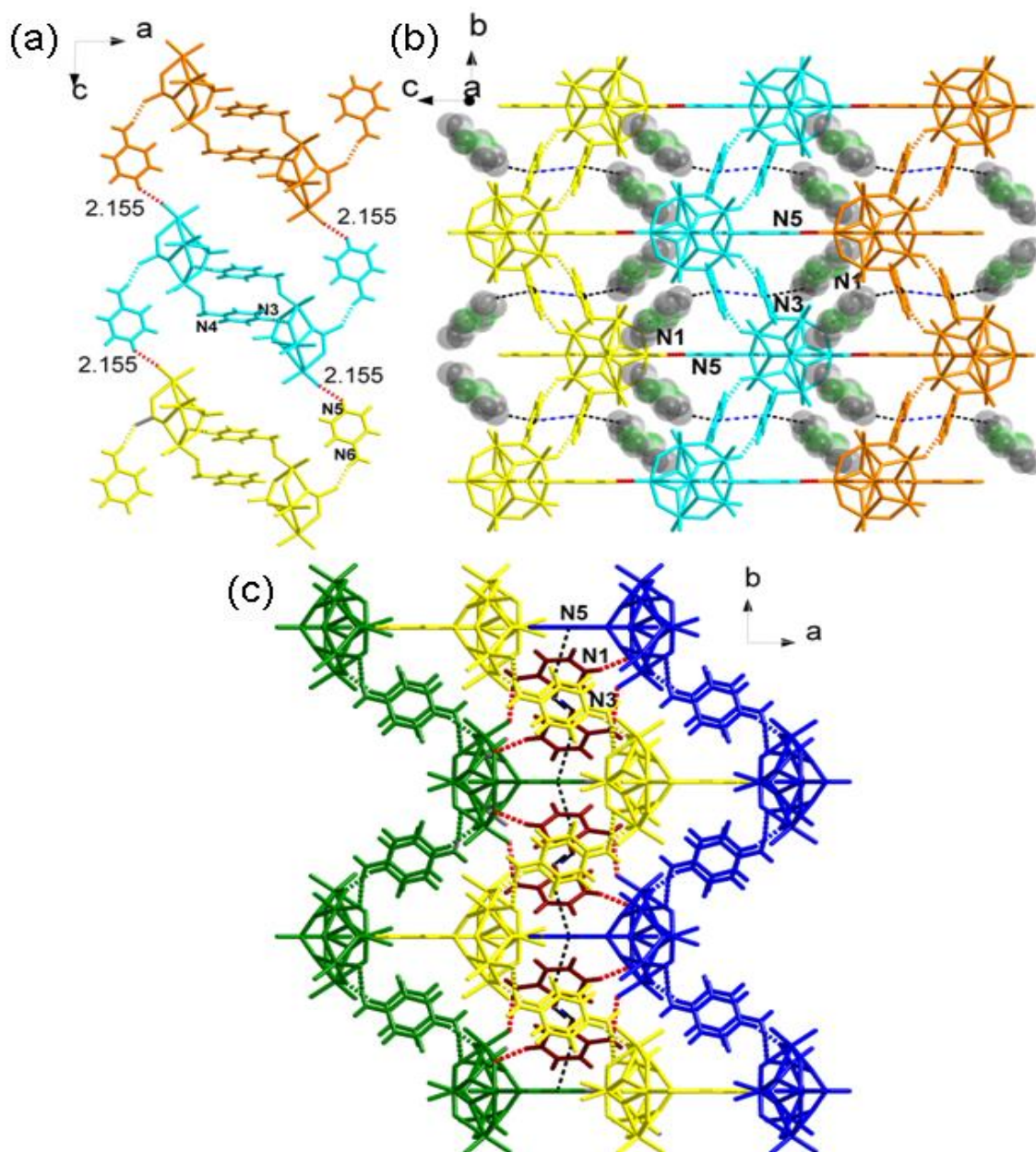
Figure III.10. (a) The 1-D chains are connected through H-bonding interactions mediated by {N5N6} moieties to form 2-D corrugated sheet having voids. Three such chains are shown in orange, cyan and yellow color. (b) Figure showing 2-D corrugated sheet having voids are occupied by {N1N2} moieties CH…π and π…π interactions between {N1N2} and {N3N4} moieties form a tetrameric unit. The interactions are shown in dashed black and blue color respectively. (c) Three of the 2-D corrugated sheets are shown in green, yellow

and blue. Each sheet exhibits H-bonding interactions with neighboring sheets through {N1N2} moieties (shown in brown color) accommodated in its voids. The tetramers are connected through CH…π interactions mediated by {N5N6} moieties belonging to neighboring 2-D corrugated sheets.

Table III.8. H-bonding interactions in **6a**.

D–H…A	D–H (Å)	H…A (Å)	D…A (Å)	∠ D–H…A (°)
N1-H1...O3	0.860(13)	2.201(22)	3.032(31)	162.50(75)
N2-H2B…O6	0.859(12)	2.194(6)	2.984(14)	152.94(79)
N3-H3…O8	0.860(7)	1.909(9)	2.722(13)	157.11(46)
N4-H4A…O11	0.861(8)	2.065(5)	2.886(10)	159.26(53)
N5-H5…O1	0.860(16)	2.155(32)	2.867(47)	139.84(97)
N6-H6B…O14	0.860(16)	2.048(25)	2.874(40)	160.47(72)
C1-H1A…O7	0.930(16)	2.381(12)	3.283(23)	163.45(85)
C5-H5A…O5	0.930(12)	2.385(19)	3.204(30)	146.69(61)
C6-H6…O15	0.929(8)	2.331(10)	3.243(14)	166.95(52)
C10-H10…O10	0.929(10)	2.426(31)	3.254(38)	148.46(53)
C12-H12…O12	0.931(20)	2.263(32)	3.190(48)	173.83(89)

Table III.9. CH…π and π…π interactions in **6a**.

CH…π	CH…π (Å)	π…π	π…π (Å)
C2-H2...π{N3N4}	2.837(18)	π{N3N4}… π{N3N4}	3.610(5)
C9-H9...π{N5N6}	3.244(9)		
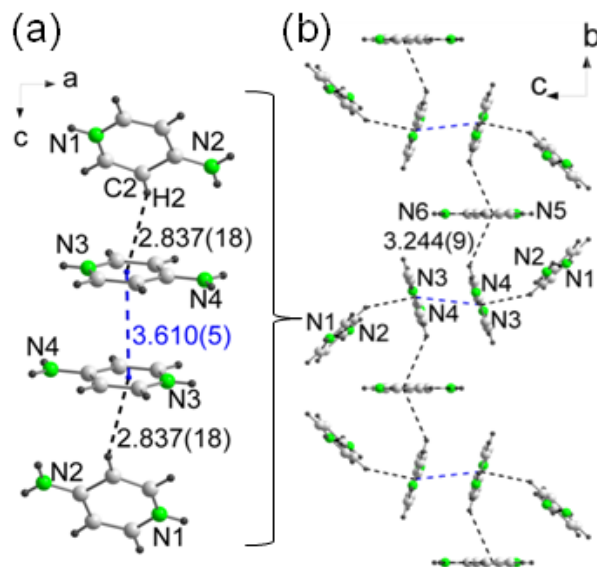
Figure III.11. (a) CH…π and π…π interactions between {N1N2} and {N3N4} moieties form a tetrameric unit. The interactions are shown in dashed black and blue color respectively. (b) The tetramers are connected through CH…π interactions mediated by {N5N6} moieties.

In {4-H*ap*}$_6$[P$_2$Mo$_5$O$_{23}$].5H$_2$O, **6b** {P$_2$Mo$_5$} cluster anions are linked by {N3N4} moieties to form a dimeric unit, which are further connected via {N11N12} moieties (N12H12B…O11: 2.018(8) Å) to form 1-D chains. {N1N2}, {N7N8} and {N9N10} units remain anchored to the dimeric units through NH…O interactions as shown in Figure III.12 (also refer Table III.10 for H-bonding interactions in **6b**). The 1-D chains are connected through H-bonding interactions mediated by {N9N10} moiety to form 2-D sheet. The formation of sheet resulted in inter-chain voids which are occupied by {N3N4} moieties (refer Figure III.13). These moieties act as templates through which 2-D sheets are formed along with lattice water molecules. It is interesting to note the interpenetrating nature of 2-D sheets in **6b** (Figure III.14).
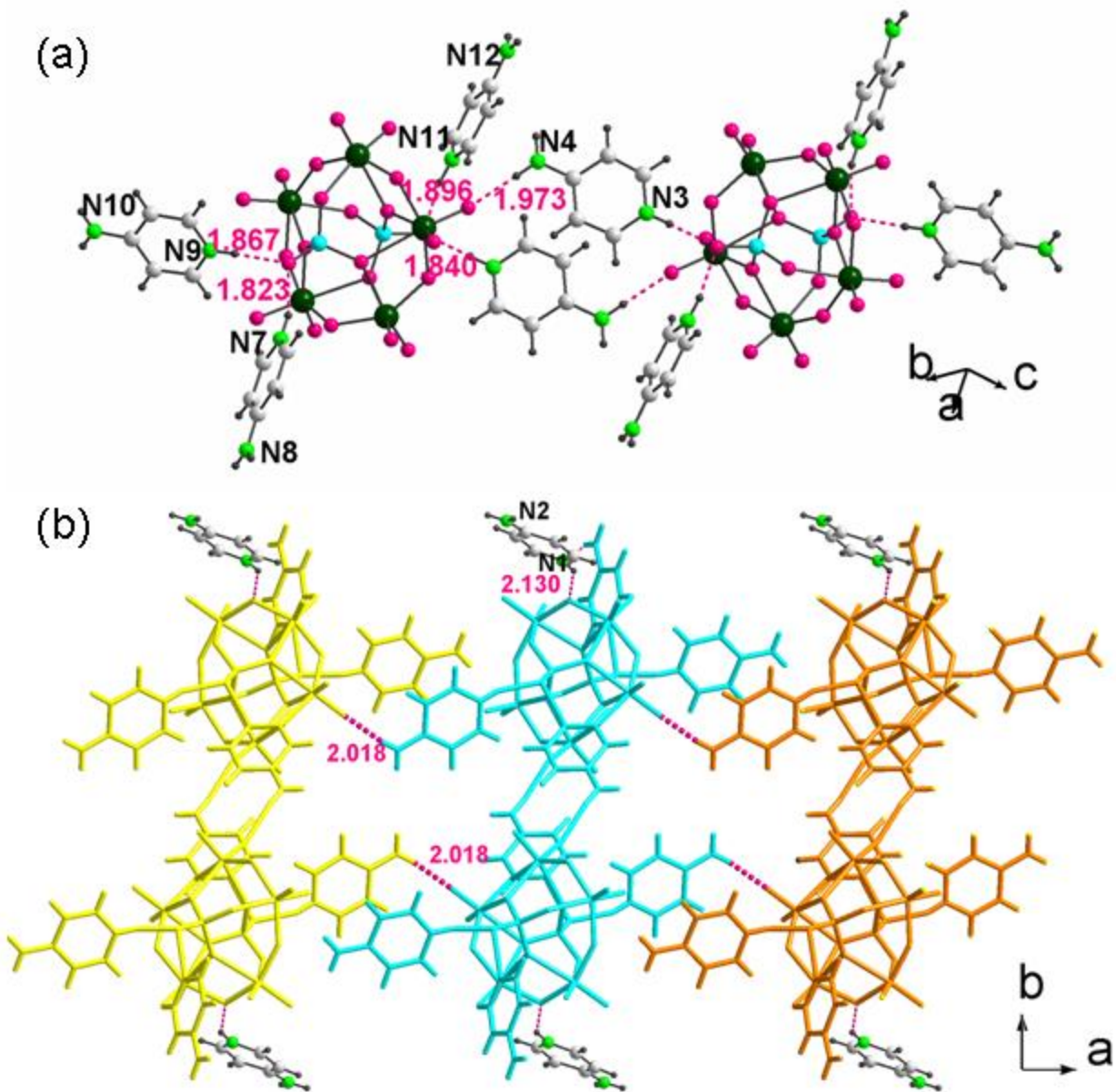
Figure III.12. (a) Figure showing the formation of dimeric unit in **6b**. (b) Each of the dimeric units (three such dimeric units are shown in yellow, cyan and orange) is connected via H-bonding interactions to form 1-D chains.
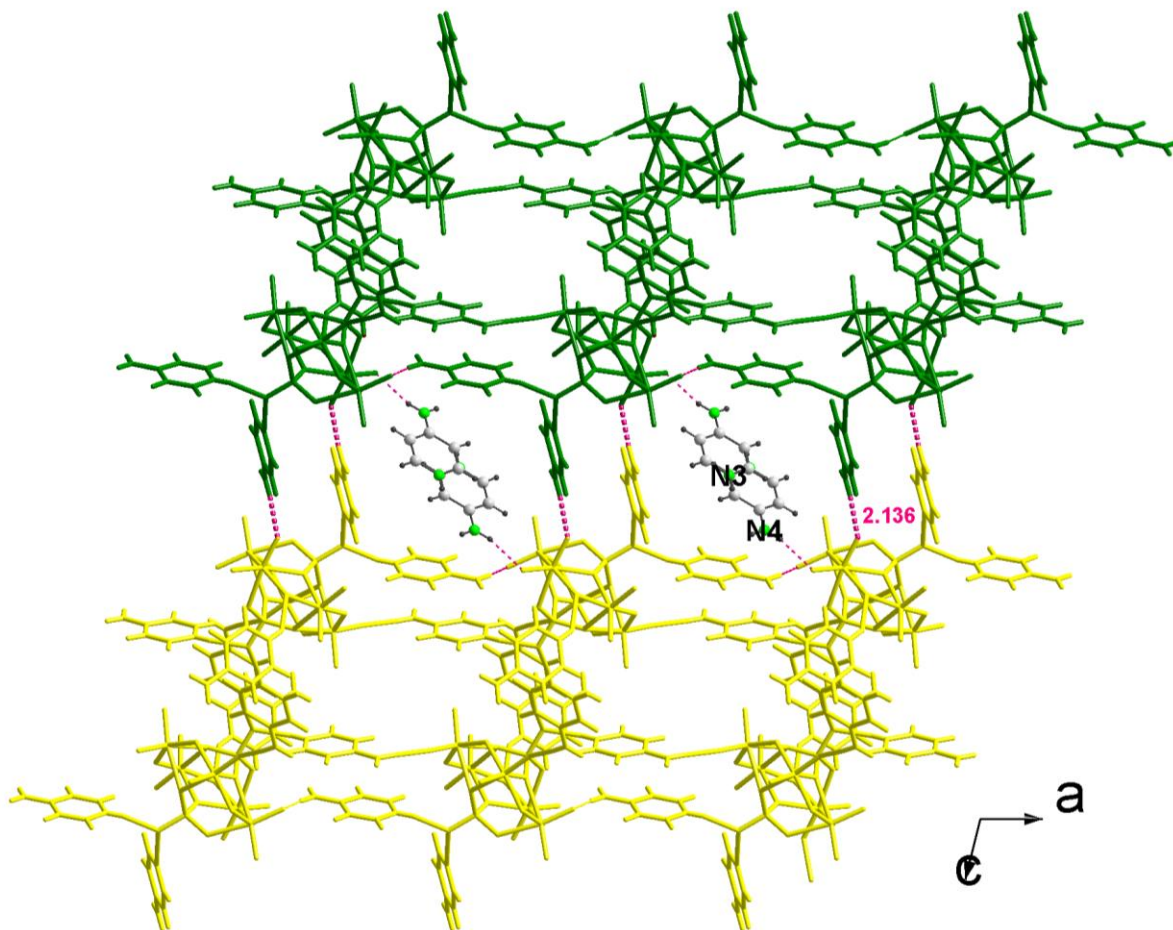
Figure III.13. Figure showing two 1-D chains (depicted in yellow and green color) connected via H-bonding mediated by {N9N10} moieties (2.136 (25) Å). The inter-chain voids are occupied by {N3N4} units.

Table III.10. H-bonding interactions in **6b**.

D–H…A	D–H (Å)	H…A (Å)	D…A (Å)	∠ D–H…A (°)
N1-H1...O15	0.859(18)	2.316(12)	3.010(16)	138.12(99)
N1-H1…O17	0.859(18)	2.130(7)	2.847(17)	140.84(95)
N2-H2A…O2	0.861(14)	2.248(38)	3.054(51)	155.95(63)
N2-H2B…O14	0.862(12)	2.210(14)	3.060(24)	169.09(56)
N3-H3…O23	0.861(11)	1.840(15)	2.692(23)	170.11(60)

N4-H4A…O7	0.86(1)	1.973(7)	2.822(13)	168.69(62)
N4-H4B…O19	0.860(15)	2.159(40)	3.003(54)	166.78(59)
N5-H5A…O5W	0.859(15)	2.006(22)	2.851(35)	167.88(63)
N6-H6A…O3	0.861(15)	2.305(19)	3.073(25)	148.55(93)
N6-H6B…O16	0.859(16)	2.312(36)	3.159(48)	168.69(88)
C15-H15…O3W	0.93(1)	2.365(11)	3.288(15)	171.38(59)
N7-H7…O22	0.86(1)	1.823(22)	2.660(28)	163.86(60)
N8-H8B…O1	0.859(9)	2.180(7)	2.996(13)	158.50(58)
N9-H9…O22	0.860(8)	1.867(7)	2.724(11)	174.93(54)
N10-H10B…O20	0.861(16)	2.136(25)	2.971(39)	163.26(71)
C25-H25…O16	0.929(17)	2.312(7)	3.150(18)	149.88(66)
N11-H11…O23	0.859(9)	1.896(10)	2.720(17)	160.14(58)
N12-H12B…O11	0.86(1)	2.018(8)	2.871(14)	171.37(61)
C26-H26…O7	0.930(11)	2.459(7)	3.386(14)	174.54(64)
C27-H27…O19	0.930(11)	2.369(6)	3.294(13)	172.61(69)

(a)
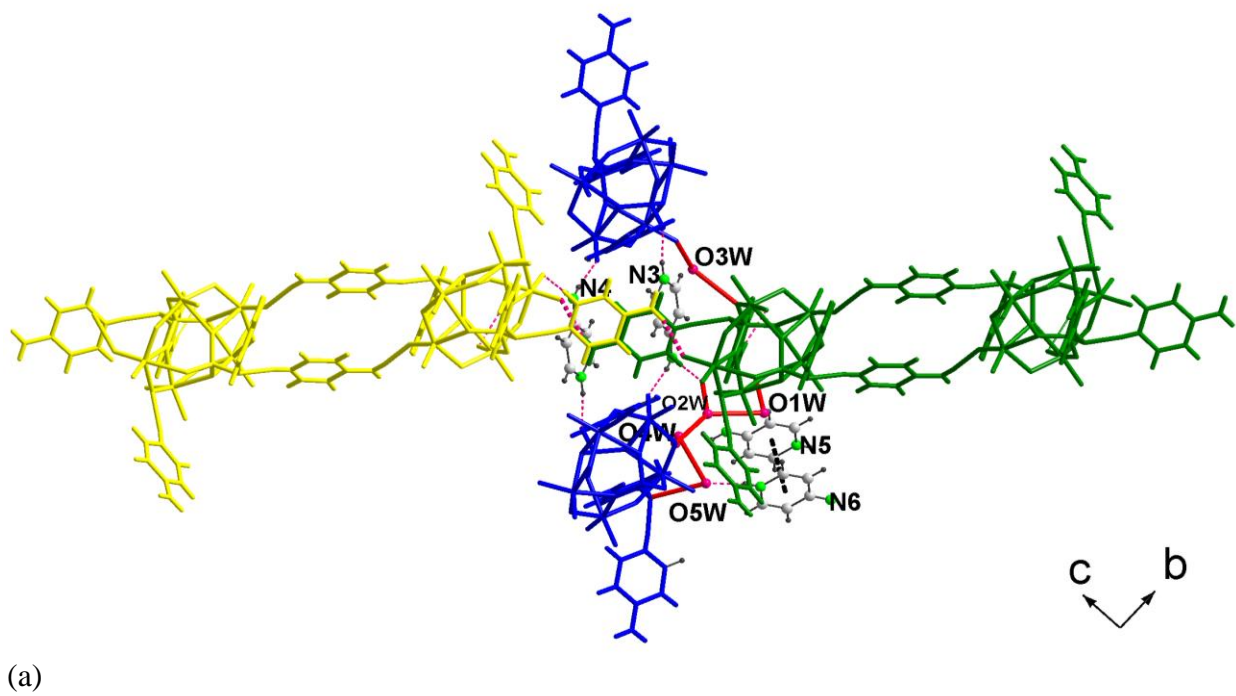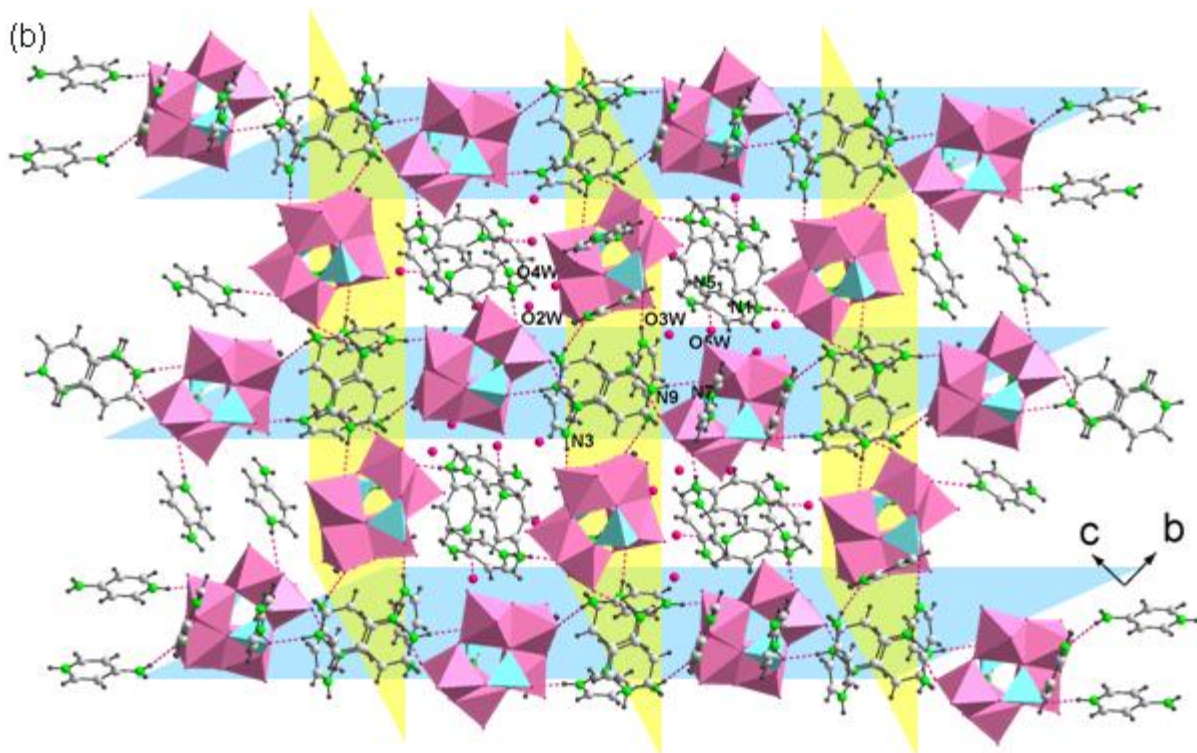
Figure III.14. (a) The {N3N4} units in inter-chain voids are part of interpenetrating 2-D sheets perpendicular to sheet shown in Figure III.13. The lattice water molecules along with {N3N4} units act as nodes connecting the interpenetrating sheets. Inter-sheet spaces are occupied by {N1N2} and {N5N6} moieties (π...π: 3.550 Å) which are anchored to lattice water molecule O5W. (b) Figure showing the two sets of interpenetrating sheets.

III.3.4. Analysis of solids 3-6

FTIR spectra (Figure III.15 and 16) exhibited bands characteristic of P–O and Mo–O stretching which indicated the presence of PMO cluster anion in Solids **3**-**6a**. The bands corresponding to organic moieties in **3**-**6a** were also found to be in good agreement with C-H, N-H, C-N and O-H stretching frequency with those reported in literature [18].
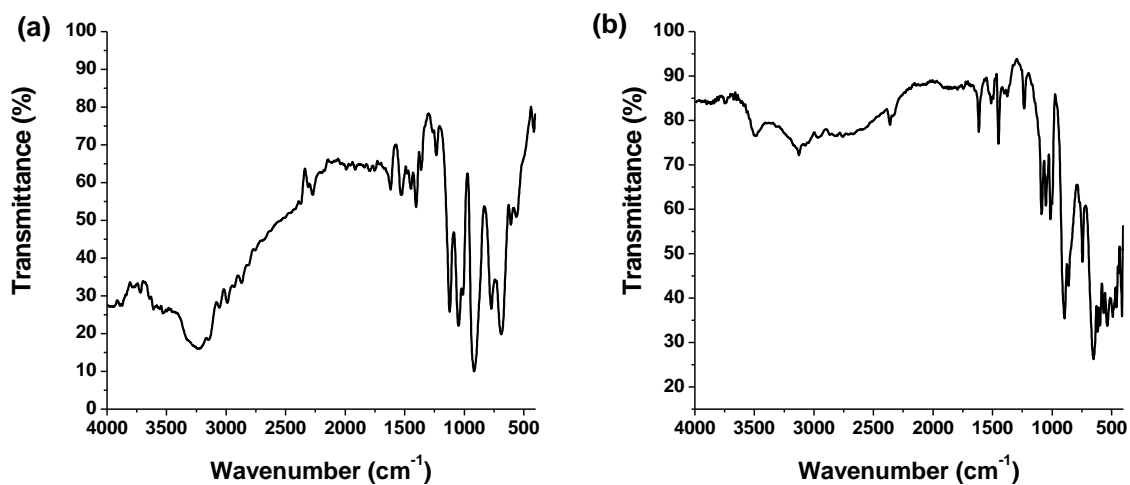
Figure III.15. FTIR spectrum of (a) **3** and (b) **4**.
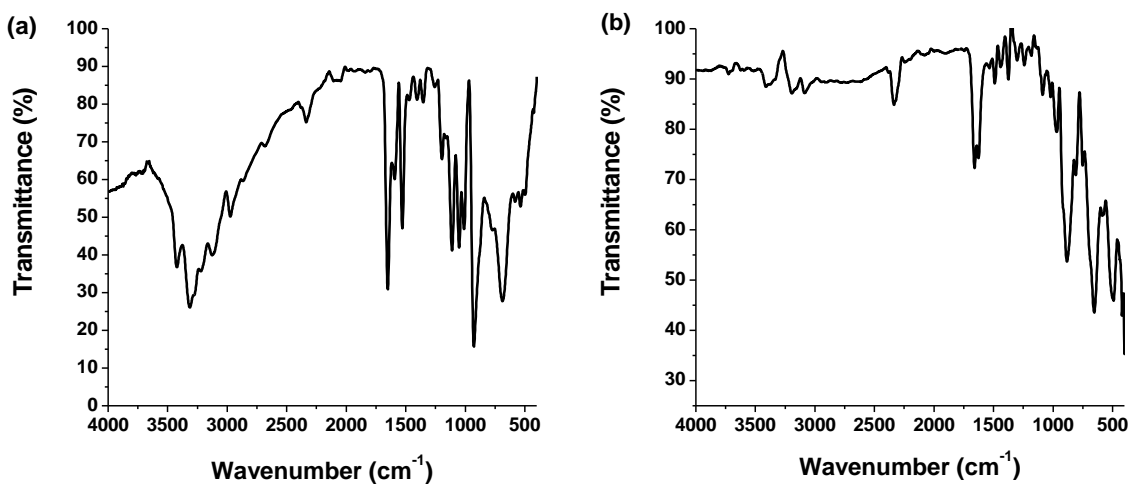
Figure III.16. FTIR spectrum of (a) **5** and (b) **6a**.

In solids **3**-**6**, the phase purity of the solids was established by comparing the experimental PXRD pattern with simulated powder pattern of the single crystal structure as shown in Figures III.17-21.
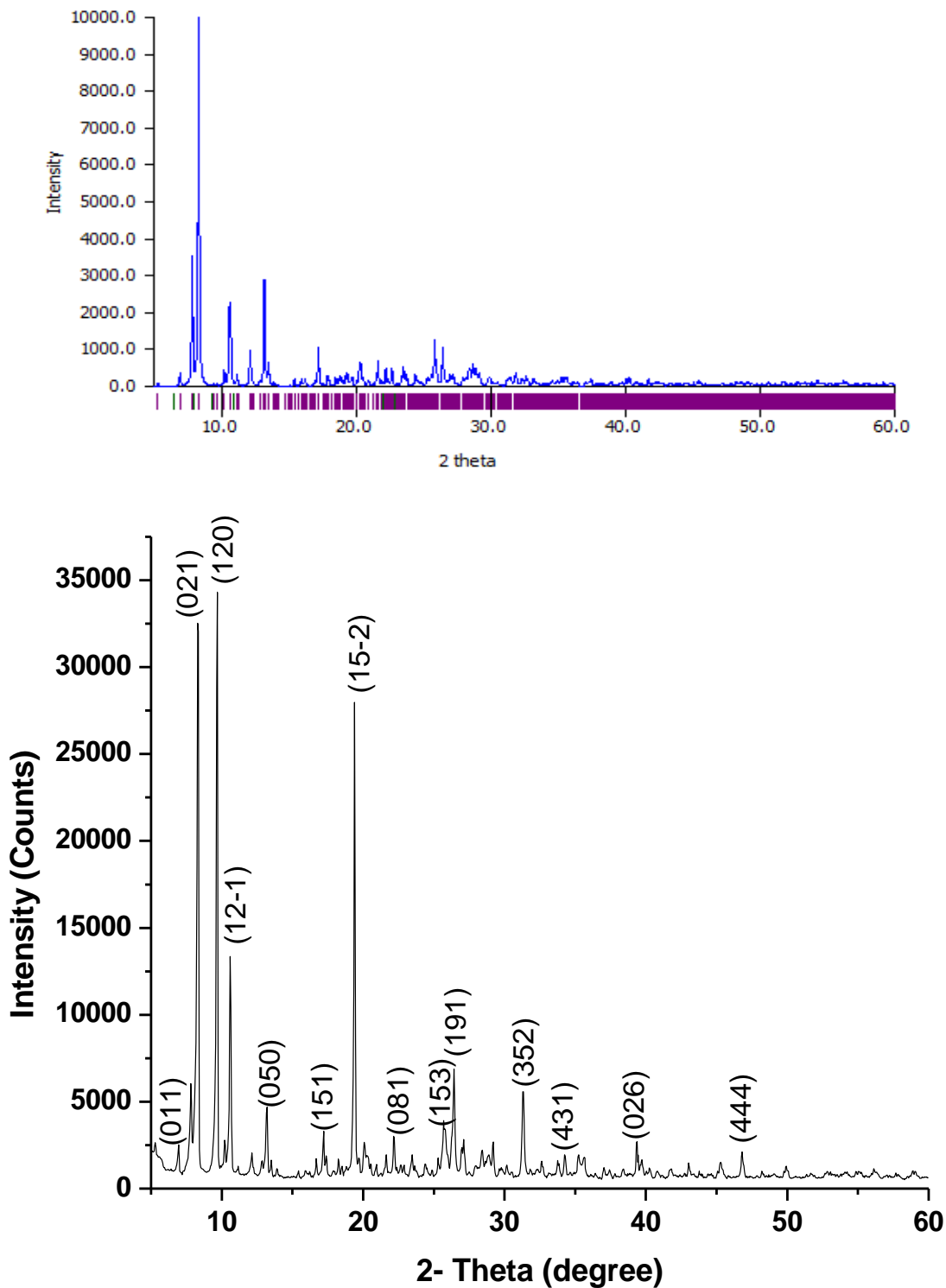
Figure III.17. Simulated (top) and Experimental (bottom) PXRD of **3**.
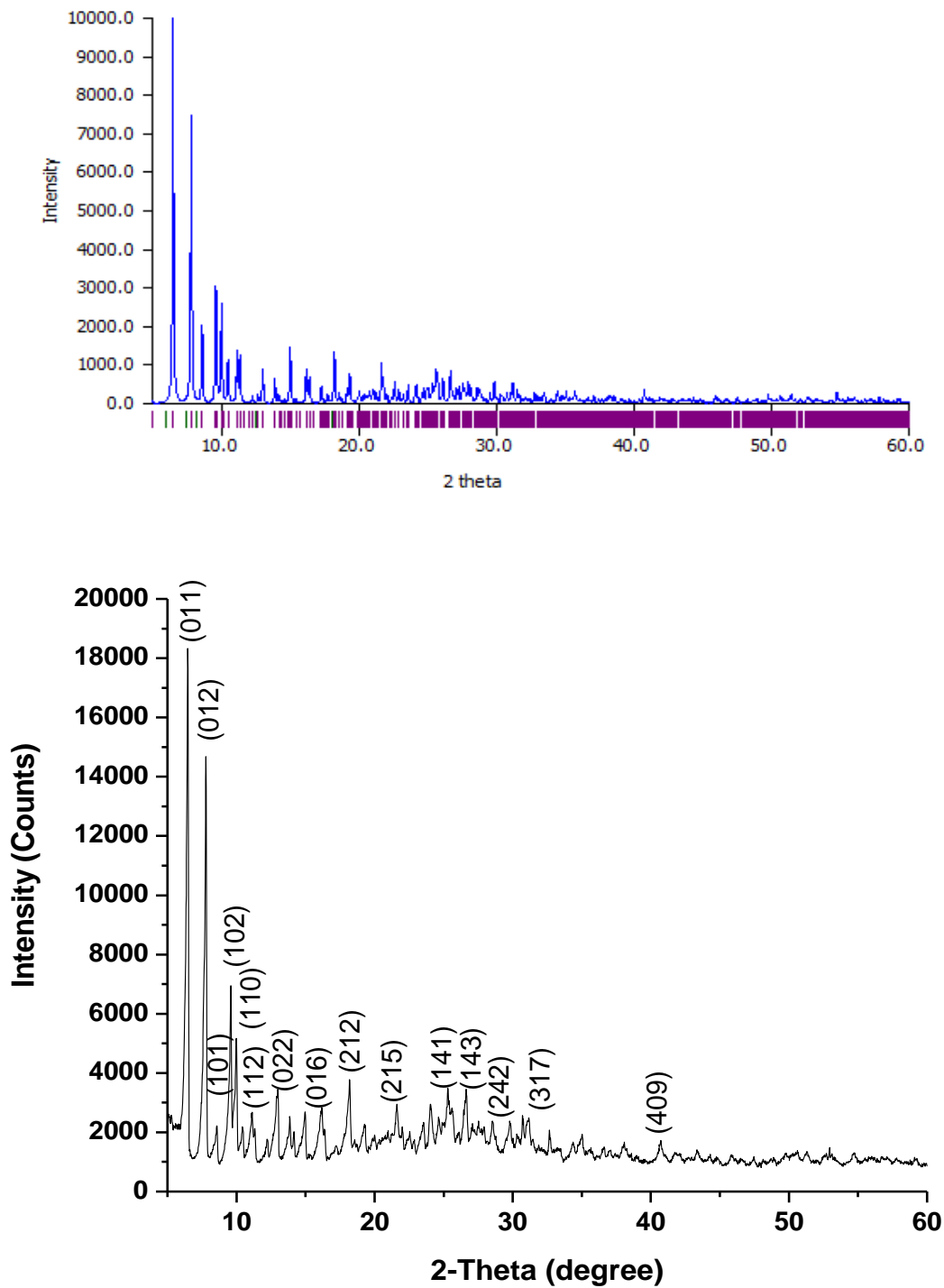
Figure III.18. Simulated (top) and Experimental (bottom) PXRD of **4**.
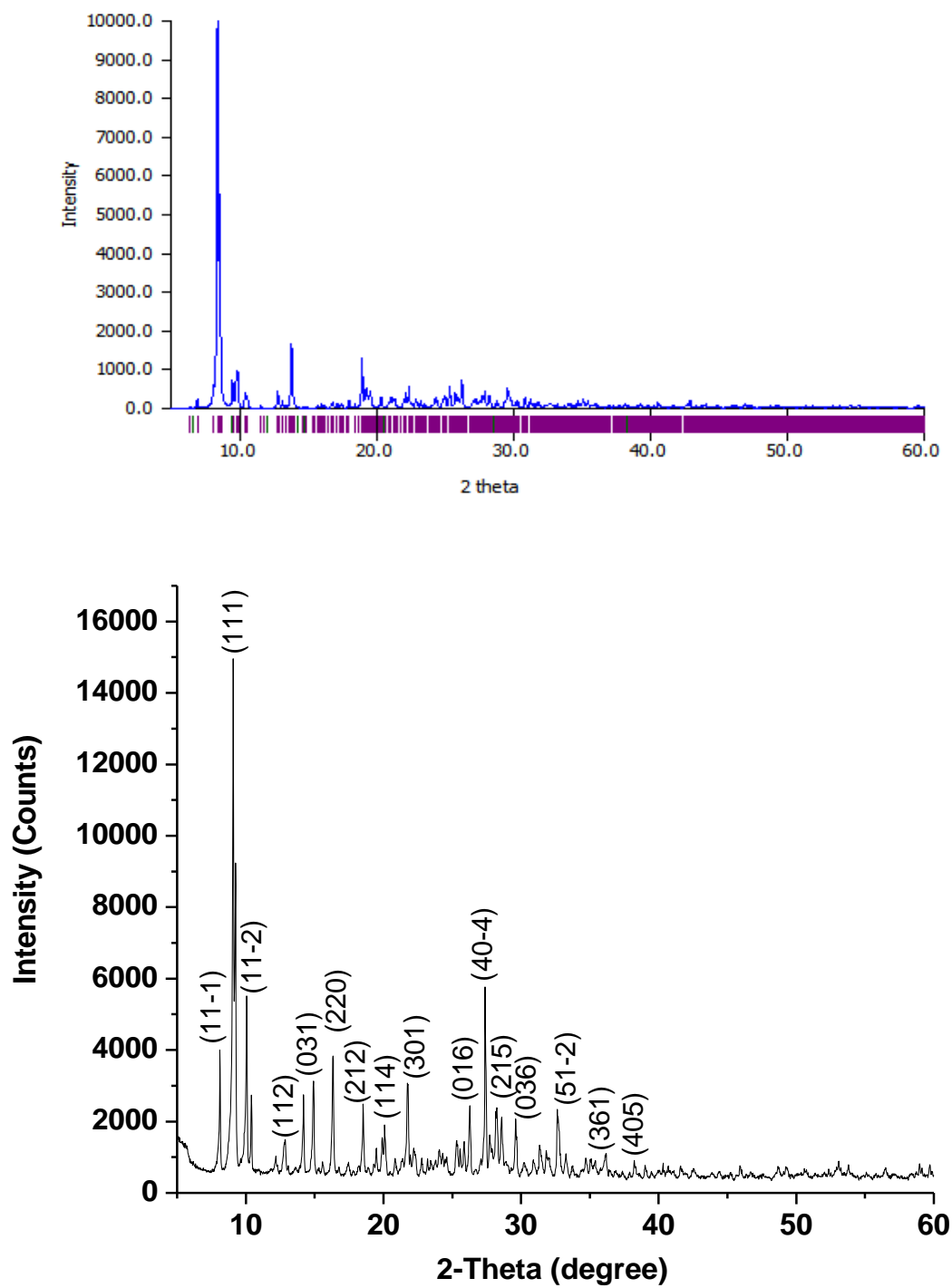
Figure III.19. Simulated (top) and Experimental (bottom) PXRD of **5**.
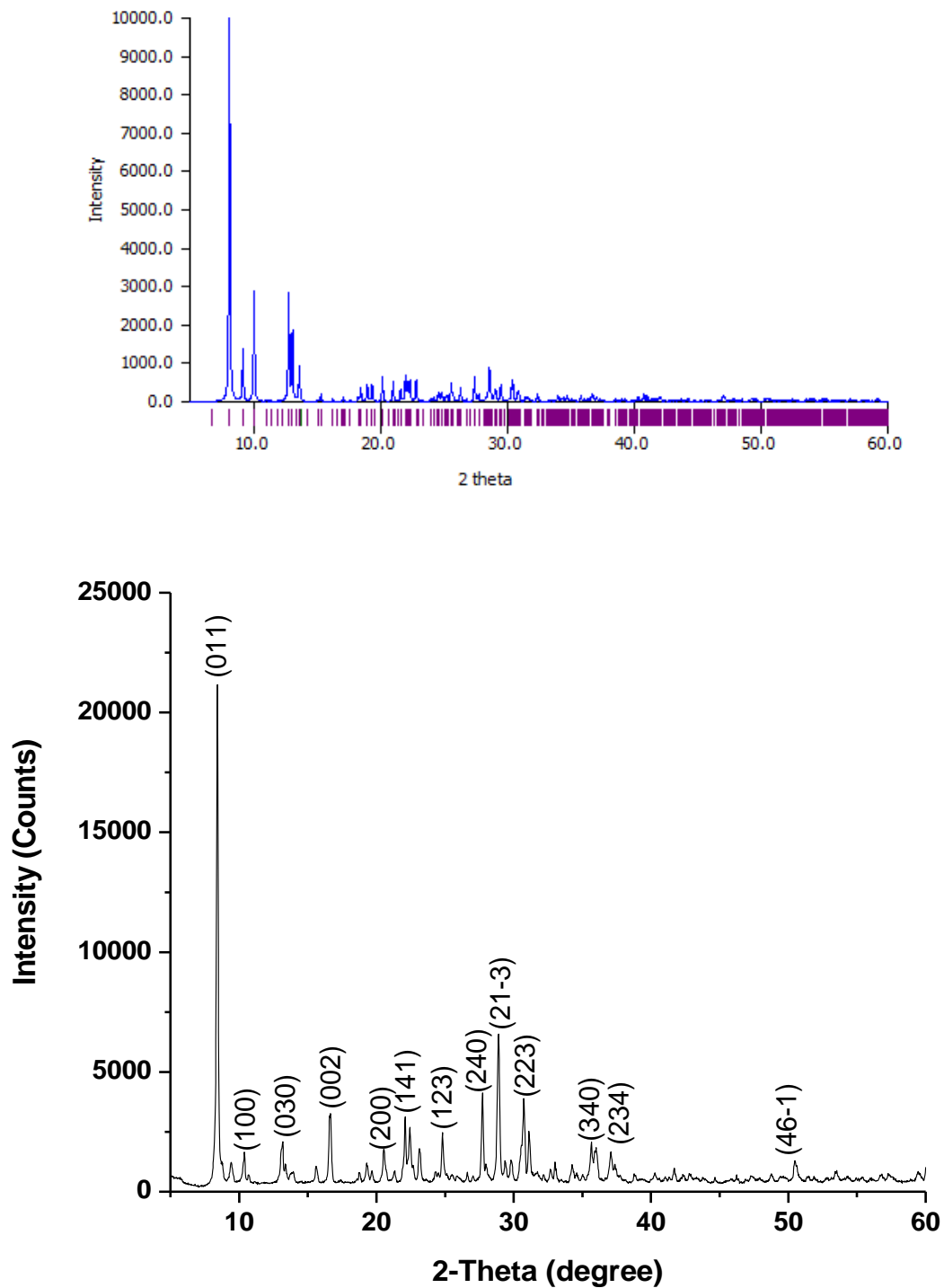
Figure III.20. Simulated (top) and Experimental (bottom) PXRD of **6a**.
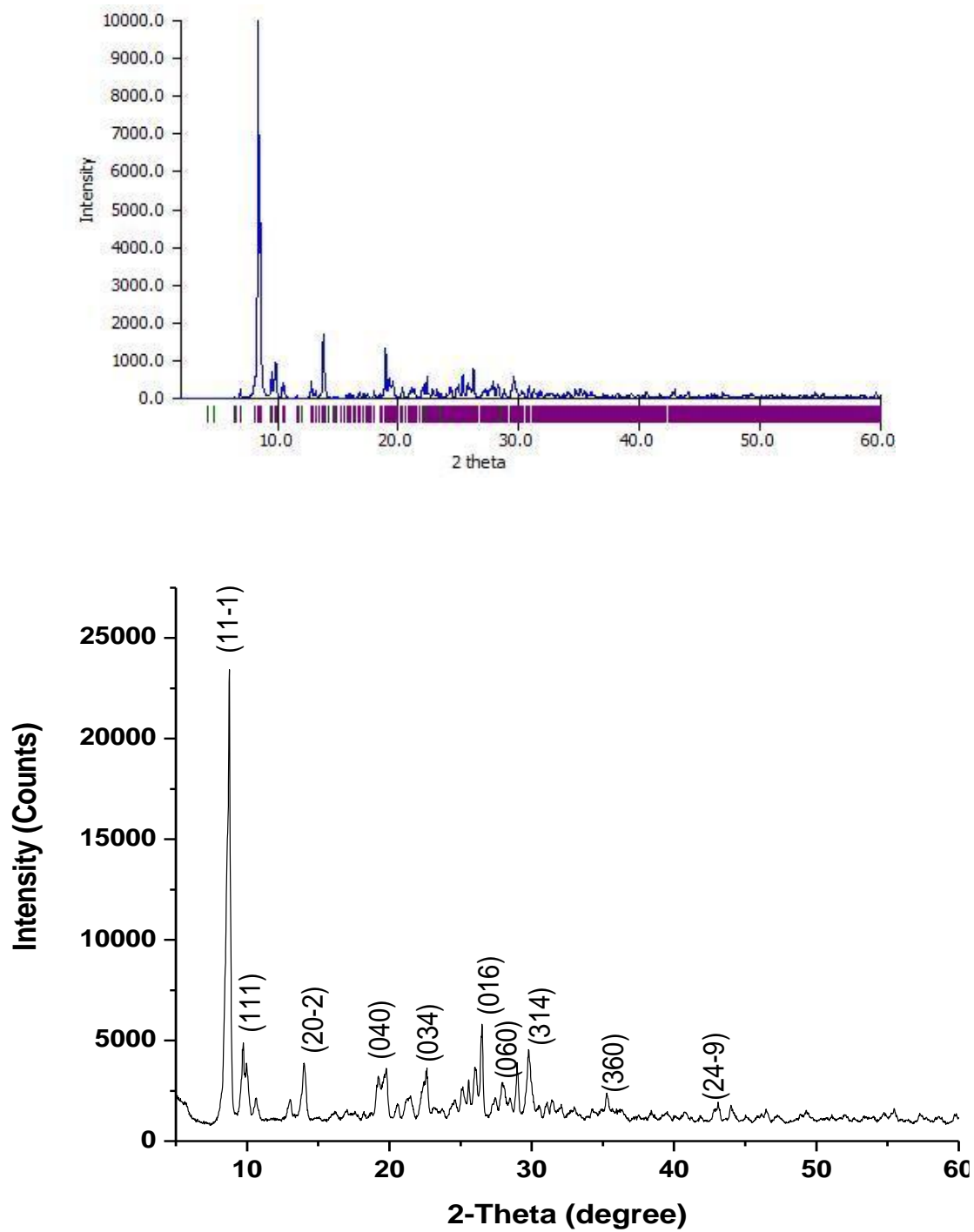
Figure III.21. Simulated (top) and Experimental (bottom) PXRD of **6b**.

Thermo gravimetric analysis (TGA) of only solids **4**, **5** and **6a** was carried out (refer Figure III.22) as TGA of **3** and **6b** has already been reported in literature. The TGA of **4** showed weight loss in two steps. The first weight loss corresponding to ~35% could be attributed to the thermal degradation of water molecule and five protonated benzimidazole moieties (theoretical value: 37.19%). The second step was attributed to the decomposition of {P₂Mo₅} cluster anion. In **5**, the first weight loss (~ 2%) at 120°C was attributed to the loss of two water molecules (theoretical value: 2.71%). The weight loss of ~19% (theoretical value: 21.4%) in the second step was attributed to the degradation of three protonated 4-*ap* moieties, followed by decomposition of {P₂Mo₅} cluster anion. The ~20% weight loss observed in **6a** below 400°C was assigned to the degradation of three protonated 4-*ap* moieties (theoretical value: 20.5%). The second weight loss upto 800°C attributed to the loss of the remaining two organic ligands and decomposition of {P₂Mo₅} cluster anion.
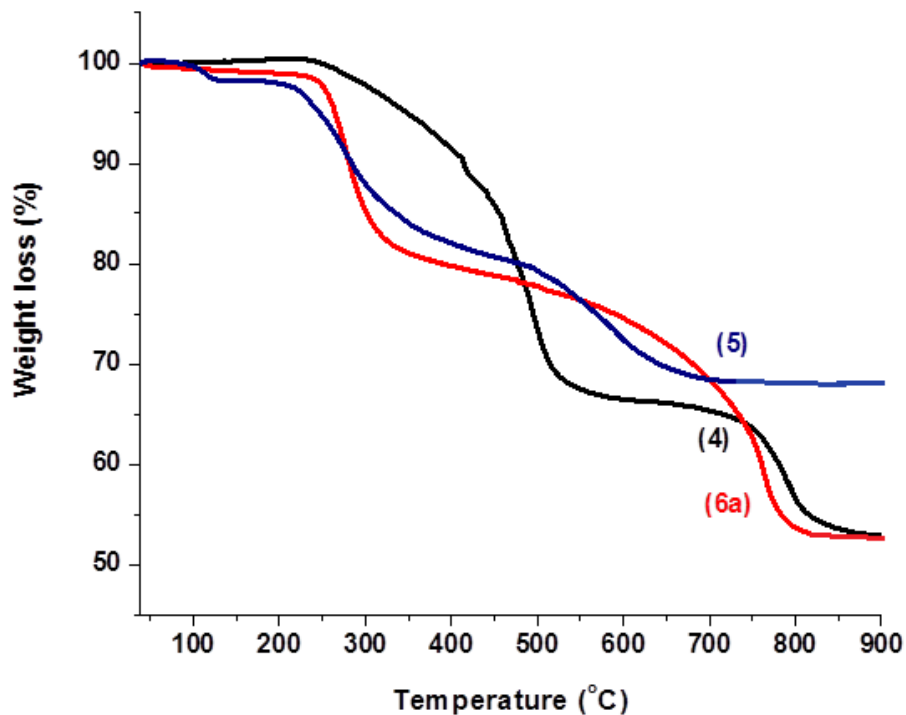
Figure III.22. TGA of **4**, **5** and **6a**.

III.3.5. Band gap energy calculations

The band gap enrgy was determined using Kubelk- a–Munk (KeM or F(R)) function in Tauc method. The method was discussed in Chapter II, section II.3.4.

III.3.5.1. Effect of ligands on band gap energy

In order to study the effect of ligands, the optical band gap energy was calculated from the DRS data for solids **3** and **6a** which are based on $\{HP_2Mo_5\}$ clusters (refer Figure III.23 and III.24) were also compared with the E_g of monoprotonated solids **1** and **2** discussed in Chapter II (refer Table III.11). The E_g values showed slight variations on account of different ligands present in the solids and difference in the coordination atmosphere of the monoprotonated cluster anion. While, in all the four cases, allowed direct band gap energy showed low value; $\{H\text{-}2a4mp\}_5[\{PO_3(OH)\}\{PO_4\}Mo_5O_{15}].6H_2O$ (**2**) and $\{Hbimi\}_5[HP_2Mo_5O_{23}].5H_2O$ (**3**) displayed the highest values for the irrespective, allowed indirect and allowed direct band gap energy which indicates that perphaps water of crystallization also plays some role in optical band gap energy. As discussed earlier, **2** and **3** have six and five molecules of water of crystallization associated with them respectively; however, **1** and **6a** are devoid of water of crystallization.
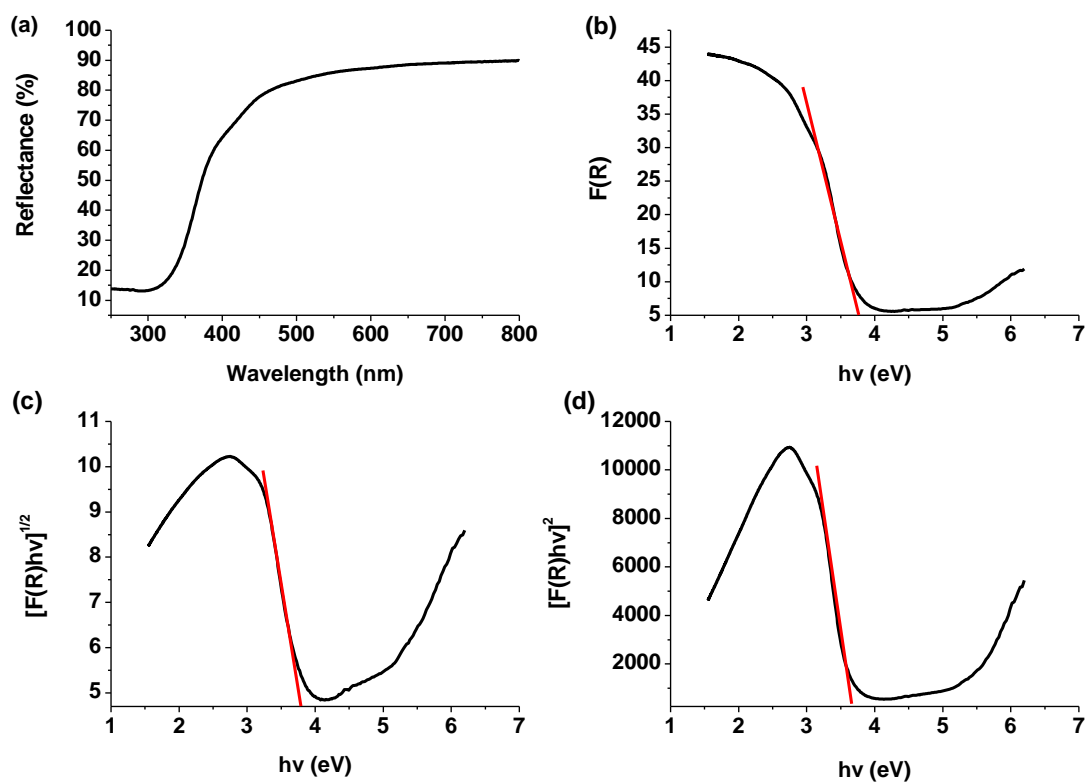
Figure III.23. Plots of (a) Reflectance versus wavelength (b) F(R) versus hυ(eV), (c) (F(R)hυ)$^{1/2}$ versus hυ(eV) and (d) (F(R)hυ)^2 versus hυ(eV) for **3**.
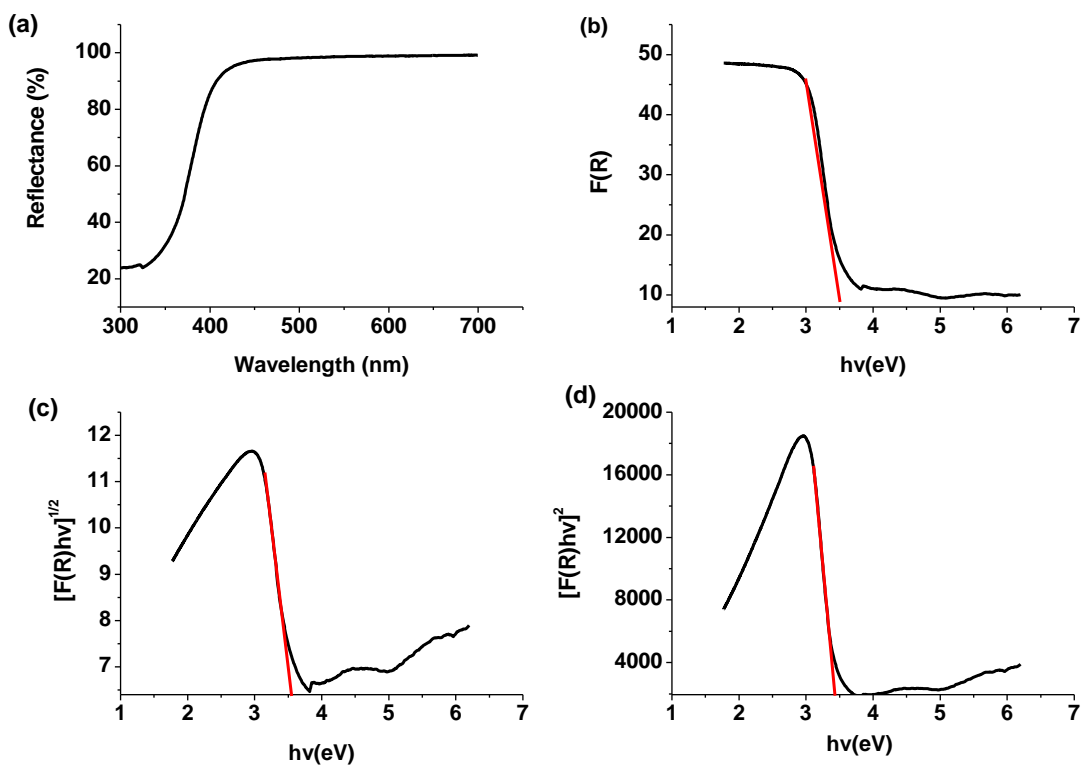
Figure III.24. Plots of (a) Reflectance versus wavelength (b) F(R) versus hυ(eV), (c) $(F(R)hυ)^{1/2}$ versus hυ(eV) and (d) $(F(R)hυ)^2$ versus hυ(eV) for **6a**.

Table III.11 Table tabulates the irrespective, allowed indirect and allowed direct band gaps of **1**, **2**, **3** and **6a**

Solids	F(R) vs hυ (band gap energy irrespective of direct or indirect in eV)	$[F(R) hυ]^{1/2}$ (allowed indirect band gap energy in eV)	$[F(R) hυ]^2$ (allowed direct band gap energy in eV)
1	3.67	3.66	3.53
2	3.75	3.81	3.55
3	3.75	3.78	3.63
6a	3.53	3.55	3.42

III.3.5.2. Effect of protonation on band gap energy

The optical band gap energy of **5**, **6a** and **6b** was calculated using DRS data to study the effect of protonation on E$_g$, since they are di-protonated, mono-protonated and unprotonated respectively (refer Figure III.24, 25, 26 and Table III.12). It is observed that the band gap energy decreased as the protonation increased. So, solid **6b** which has a non-protonated cluster centre showed highest band gap energy values.

Table III.12. Table tabulates the irrespective, allowed indirect and allowed direct band gaps of 5, **6a** and **6b**.

Solids	F(R) vs hυ (band gap energy irrespective of direct or indirect in eV)	$[F(R) hυ]^{1/2}$ (allowed indirect band gap energy in eV)	$[F(R) hυ]^2$ (allowed direct band gap energy in eV)
5	3.38	3.54	3.32
6a	3.53	3.55	3.42
6b	3.63	3.60	3.50
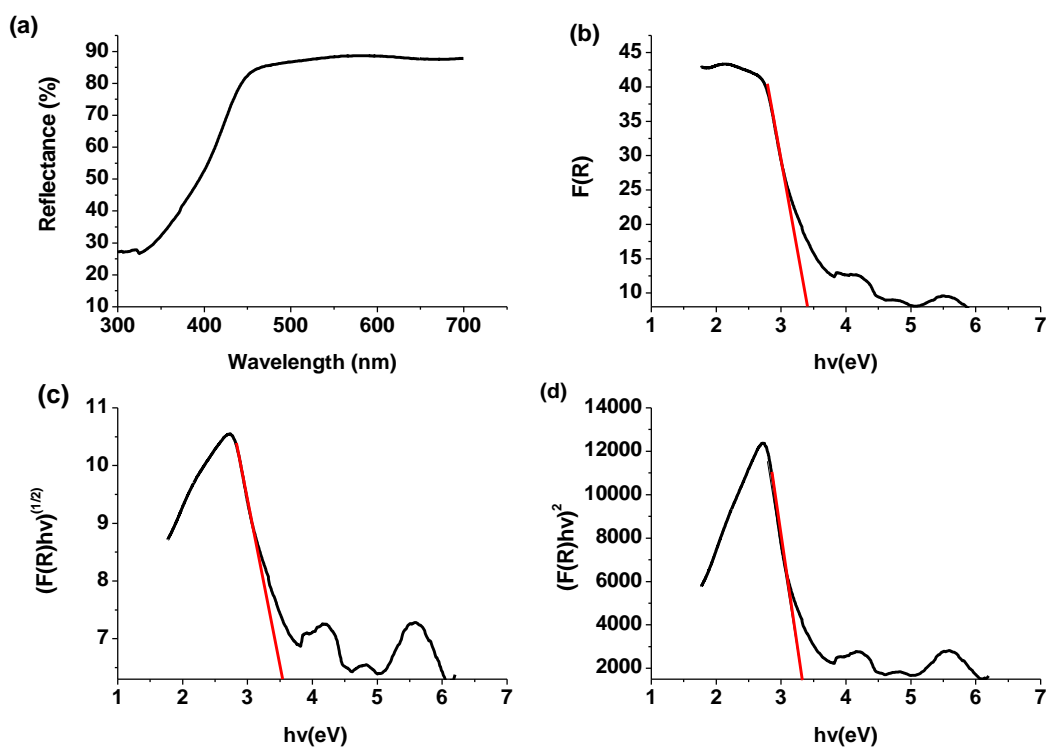
Figure III.25. Plots of (a) Reflectance versus wavelength (b) F(R) versus hυ(eV), (c) $(F(R)hυ)^{1/2}$ versus hυ(eV) and (d) $(F(R)hυ)^2$ versus hυ(eV) for **5**.

Figure III.26. Plots of (a) Reflectance versus wavelength (b) F(R) versus hυ(eV), (c) $(F(R)h\upsilon)^{1/2}$ versus hυ(eV) and (d) $(F(R)h\upsilon)^2$ versus hυ(eV) for **6b**.

III.3.6. Chemistry of Formation

Self-assembly of solids **3-7** can be visualized in terms of the *supramolecular synthons*: Strandberg cluster, zinc complex, protonated organic moieties and water molecules. pH plays a crucial role in the formation of these synthons. Our previous results have suggested that {P₂Mo₅} cluster is the most stable cluster anion upto pH = 7. Therefore, the formation of Standberg cluster based solids **3-6a** in the present study seems obvious. Since solids **3-6** were synthesized in the pH range 1-5, the ligands exist in their protonated form, which

inhibits their complexation with Zn^{2+} ions in solution (refer Table III.13) and aggregation of supramolecular synthons $(HL)^+$ and $\{H_2P_2Mo_5O_{23}\}^{4-}$ or $\{HP_2Mo_5O_{23}\}^{5-}$ or $\{P_2Mo_5O_{23}\}^{6-}$ is favored.

Table III.13. Ligands and their pK_a values [19].

Sl. No.	Ligand	pK_a
1	benzimidazole	5.4
2	4-aminopyridine	9.17
3	pyrazole	2.5

At pH ~ 2, pyrazole ($pK_a = 2.5$) can exist in two in ionic forms i.e. $\{pz\} \leftrightarrow \{Hpz\}^+$. This facilitates the formation of solid **7** as (pz) can readily complex with Zn^{2+} centers and $(Hpz)^+$ can exist as counter cations. On the other hand, 4-*ap* ($pK_a = 9.1$) is unable to complex with Zn^{2+} ions in solution as it exists in its protonated form in the pH range 1-9. Therefore, **5** and **6a** are formed via aggregation of supramolecular synthons $\{4\text{-H}ap\}^+$ and $\{H_2P_2Mo_5O_{23}\}^{4-}$ or $\{HP_2Mo_5O_{23}\}^{5-}$. Interestingly, among the two supramolecular isomers **5** and **6a**, water molecules get incorporated in **5** during aggregation of supramolecular synthons. **5** is crystallized from a more acidic medium as compared to **6a**. Therefore, $\{P_2Mo_5\}$ cluster anions predominantly exists as $\{H_2P_2Mo_5O_{23}\}^{4-}$. This in turn favors the aggregation of only four $\{4\text{-H}ap\}^+$ synthons per $\{H_2P_2Mo_5O_{23}\}^{4-}$ cluster anion. On the contrary, **6a** involves aggregation of five $\{4\text{-H}ap\}^+$ synthons per $\{HP_2Mo_5O_{23}\}^{5-}$ cluster anion. Thus, aggregation in the presence of an additional hydrophobic $\{4\text{-H}ap\}^+$ synthon perhaps prevents the incorporation of lattice water molecules in **5**. On the basis of above arguments, the self-assembly of $\{Hbimi\}_6[P_2Mo_5O_{23}].H_2O$ (**4**) seems quite reasonable. **4** is crystallized at pH ~ 5

wherein benzimidazole exist as {H*bimi*}$^+$ (pK$_a$ = 5.3). Consequently, it is unable to form complex with Zn^{2+} ions in solution and aggregates with {P$_2$Mo$_5$O$_{23}$}$^{6-}$ cluster anions. The high negative charge on {P$_2$Mo$_5$} cluster anions favors the aggregation of six {H*bimi*}$^+$ synthons per {P$_2$Mo$_5$O$_{23}$}$^{6-}$ cluster anion which in turn restricts the incorporation of large number of lattice water molecules in **4** as compared to **3** due to the high hydrophobicity induced by bulky organic moieties. Therefore, pH dictates the protonation of {P$_2$Mo$_5$} cluster anions which in turn influence the aggregation of supramolecular synthons {H*ligand*}$^+$, leading to supramolecular isomers.

III.4. Conclusions

Four new Strandberg cluster based solids were crystallized under hydrothermal condition. Under our reaction conditions, while pyrazole readily formed complex with zinc centers to form a derivatized Strandberg-type cluster *viz.* {H*pz*}$_6${Zn(*pz*)$_4$(H$_2$O)$_2$} [{Zn(*pz*)$_2$P$_2$Mo$_5$O$_{23}$}$_2$].8H$_2$O (**7**); benzimidazole and 4-aminopyridine formed organic-inorganic hybrid solids {H*bimi*}$_6$[P$_2$Mo$_5$O$_{23}$].H$_2$O (**4**), {4-H*ap*}$_4$[H$_2$P$_2$Mo$_5$O$_{23}$].2H$_2$O (**5**) and {4-H*ap*}$_5$[HP$_2$Mo$_5$O$_{23}$] (**6a**). The occurrence of supramolecular isomerism in the solids **3-6** is driven by pH of the reaction medium. pH directly affects the protonation of the ligands as well as {P$_2$Mo$_5$} cluster anion. A careful control of the pH of the reaction medium, inhibits the protonation of {P$_2$Mo$_5$} cluster anion which directly affects the {H*ligand*}$^+$:{P$_2$Mo$_5$} ratio resulting in supramolecular isomerism. Secondly, formation of water clusters in PMO cluster based solids seems to be dependent on {H*ligand*}$^+$:{P$_2$Mo$_5$} ratio. Higher the {H*ligand*}$^+$:{P$_2$Mo$_5$} ratio lower is the tendency to form water clusters. The results also suggest that subtle changes in reaction conditions can enable crystallization of new crystalline phases.

From band gap energy calculations two important observations were obtained: (i) the optical band gap energy showed variations when the monoprotonated cluster anion was surrounded by different type of organic ligands and number of water molecules. (ii) band gap energy decreased as the protonation $\{P_2Mo_5\}$ cluster anion increased, provided the associated organic ligand remained the same.

References

1. Ji, Y. M.; Fang, Y.; Han, P. P.; Li, M. X.; Chen, Q. Q.; Han, Q. X. *Inorg. Chem. Commun.* **2017**, 86, 22-25.

2. Hua, J.; Tian, Y.; Bian, Y.; Zhao, Q.; Zhou, Y.' Ma, X. *SN Appl. Sci.* **2020**, 2, 308-317.

3. Song, L.; Yu, K.; Su, Z.; Wang, C.; Wang, C.; Zhou, B. *J. Coord. Chem.* **2014**, 67, 522-532.

4. Yan, D.; Zheng, L.; Zhang, Z.; Wang, C.; Yuan, Y.; Zhu, D.; Xu, Y. *J. Coord. Chem.* **2010**, 63, 4215-4225.

5. Hu, G.; Dong, Y.; He, X.; Miao, H.; Zhou, S.; Xu, Y. *Inorg. Chem. Commun.* **2015**, 60, 33-36.

6. Asnani, M.; Kumar, D.; Duraisamy, T.; Ramanan, A. *J. Chem. Sci.* **2012**, 124, 1275-1286.

7. Lu, B.; Li, S.; Pan, J.; Zhang, L.; Xin, J.; Chen, Y.; Tan, X. *Inorg. Chem.* **2020**, 59, 1702-1714.

8. Ma, F. X.; Chen, Y. G.; Yang, H. Y.; Dong, X. W.; Jiang, H.; Wang, F.; Li, J. H. *J. Clust. Sci.* **2019**, 30, 123-129.

9. Shi, Z.; Li, F.; Zhao, J.; Yu, X. Y.; Zheng, Y.; Chen, Z.; Guo, Q.; Zhang, G.; Luo, Y. *Inorg. Chem. Commun.* **2019**, 102, 104-107.

10. Wang, Y.; Zhang, L. C.; Zhu, Z. M.; Li, N.; Deng, A. F.; Zheng, S. Y. *Transition Met. Chem.* **2011**, 36, 261-267.

11. Thomas, J. ; Kumar, D. ; Ramanan, A. *Inorg. Chim. Acta* **2013**, 396, 126-135.

12. Zhang, C. X.; Chen, Y. G.; Tang, Q.; Zhang, Z. C.; Liu, D. D.; Meng, H. X. *Inorg. Chem. Commun*. **2012**, 17, 155-158.

13. Moulton, B.; Zaworotko, M. J. *Chem. Rev.* **2001**, 101, 1629-1658.

14. Qu, X.; Feng, H.; Ma, C.; Yang, Y.; Yu, X. *Inorg. Chem. Commun*. **2017**, 81, 22-26.

15. Aranzabe, A.; Wery, A. S. J.; Martin, S.;   Gutiérrez-Zorrilla, J, M.; Luque, A.; Martinez-Ripoll, M.; Roman, P. *Inorg. Chim. Acta* **1997**, 225, 35-45.

16. Thomas, J.; Ramanan, A. *Inorg. Chim. Acta* **2011**, 372, 243-249.

17. Brown I D and Altermatt D **1985** Bond-valence parameters obtained from a systematic analysis of the Inorganic Crystal Structure Database *Acta Crystallogr*. **B41** 244.

18. Nakamoto K **1978** Infrared and Raman spectra of inorganic and coordination compounds (New York: John Wiley & Sons).

19. Finar I L **1962** Organic Chemistry, Volume 1 & 2 (London: Longman).

CHAPTER IV

Metal pyrazole complex incorporated PMO cluster based solids

Summary

The aggregation of phosphorous and molybdenum precursors in the presence of $MCl_2.xH_2O$ (M = Co, Ni, Cu and Zn) with pyrazole to form PMO cluster based solids of varying dimensionality is discussed in this chapter. The following solids were obtained under ambient conditions *viz.* $\{Hpz\}_6\{Zn(pz)_4(H_2O)_2\}[\{Zn(pz)_2P_2Mo_5O_{23}\}_2].8H_2O$ **(7),** $[\{Cu(pz)_4\}_2$ $\{H_2P_2Mo_5O_{23}\}].H_2O$ **(8),** $\{Ni(pz)_4\}[\{Ni(pz)_4\}_2\{H_2P_2Mo_5O_{23}\}]_2$ $[\{Ni(pz)_4\}\{Ni(pz)_4$ $(H_2O)\}$ $\{HP_2Mo_5O_{23}\}]_2.14H_2O$ **(9),** $[Ni(pz)_4Cl_2]$ **(10)** and $\{pz\}_2[\{Co(pz)_4\}_5$ $\{P_2Mo_5O_{23}\}_2].6H_2O$ **(11).** Under hydrothermal conditions, $[\{Cu(pz)_2\}_4\{CuMo_{12}O_{38}(OH)_2\}].8H_2O$ **(12)** was obtained. While, Solids **7-9** and **11** are Strandberg-type PMOs, **12** is a rare example of copper based Keggin cluster and **10** is merely a metal complex. The synthesized solids were characterized and their magnetic properties were investigated using Guoy Balance.

IV.1. Introduction

The role of organic ligands in the crystallization of PMO cluster based solids was explored in Chapters II and III. The ligands used were 2-amino-3-methyl pyridine (*2a3mp)*, 2-amino-4-methyl pyridine (*2a4mp*), benzimidazole (*bimi*), 4-aminopyridine (*4-ap)* and pyrazole (*pz*). It was observed that except *pz*, all other ligands exhibited poor complexation ability with zinc. Therefore, in this chapter an attempt has been made to synthesize PMO cluster based solids in the presence of metal chlorides and pyrazole. Pyrazole is well known in literature to form strong complexes with transition metals centers [1]. The previously reported pyrazole incorporated transition metal complexes (TMCs) with PMO cluster based solids have been summarized in Table IV.1.

In the present work, the synthesis was carried out at room temperature using solvent evaporation method and the following solids were obtained *viz.* $\{Hpz\}_6\{Zn(pz)_4(H_2O)_2\}[\{Zn(pz)_2P_2Mo_5O_{23}\}_2].8H_2O$ **(7)**, $[\{Cu(pz)_4\}_2 \{H_2P_2Mo_5O_{23}\}].H_2O$ **(8)**, $\{Ni(pz)_4\}[\{Ni(pz)_4\}_2\{H_2P_2Mo_5O_{23}\}]_2$ $[\{Ni(pz)_4\}\{Ni(pz)_4 (H_2O)\}$ $\{HP_2Mo_5O_{23}\}]_2.14H_2O$ **(9)**, $[Ni(pz)_4Cl_2]$ **(10)** and $\{pz\}_2[\{Co(pz)_4\}_5 \{P_2Mo_5O_{23}\}_2].6H_2O$ **(11)**. A slight variation in the reaction parameters resulted in the formation of $[\{Cu(pz)_2\}_4\{CuMo_{12}O_{38}(OH)_2\}].8H_2O$ **(12)** under hydrothermal conditions. The incorporation of metal centers in PMO cluster based solids has a two-fold effect: (i) Firstly, it enables PMO clusters to form multi-dimensional solids (refer Table IV.2 for the classification) which as comparatively difficult to crystallize as compared to organically templated solids. Figure IV.1 provides a statistical analysis of TMC incorporated PMO cluster based solids reported in literature during the last two decades [2]. (ii) Secondly, presence of transition metal centers having unpaired electrons opens the possibility to

Table IV.1. Table summarizing pyrazole incorporated TMC in PMO cluster based solids reported in literature during the past decade.

Sl No.	Formula	Cell parameters	Synthesis	Class	Crystal structure description	Dimensi-onality	Ref.
1	[{Cu(*pz*)(H$_2$O)} {Cu(*pz*)$_3$(H$_2$O)} {Cu(*pz*)$_4$} {P$_2$Mo$_5$O$_{23}$}]	*P*2$_1$/n *a*, Å =14.751(2) *b*, Å =21.635(3) *c*, Å =16.489(2) *β*, ° =110.343	Solvent evaporation technique Metal:Mo: ligand ratio is 1:3:1	I	{Cu^{II}(*pz*)$_3$(H$_2$O)O$_2$} and {Cu^{II}(*pz*)(H$_2$O)O$_3$} complex units covalently link adjacent {P$_2$Mo$_5$} clusters into linear chains ; each cluster is also capped by {Cu^{II}(*pz*)$_4$O} square pyramids	1-D	[3]
2	{Cu(*pz*)$_2$(H$_2$O)$_4$} [{Cu(*pz*)$_2$(H$_2$O)}$_2$ {Cu(*pz*)$_4$}$_2$ {HP$_2$Mo$_5$O$_{23}$}$_2$].6H$_2$O	*P*$\overline{1}$ *a*, Å =9.187(5) *b*, Å =12.409(7) *c*, Å =22.099(12) *α*, ° =90.640(10) *β*, ° =94.513(10) *γ*, ° =95.490(10)	Solvent evaporation technique Metal:Mo: ligand ratio is 1:3:2	I	The octahedral {Cu(*pz*)$_4$O$_2$} and the trigonal bipyramidal {Cu(*pz*)$_2$(H$_2$O)O$_2$} link the {P$_2$Mo$_5$} clusters into a 2-D sheet. A third complex unit, {Cu^{II}(*pz*)$_2$(H$_2$O)$_4$} occurs in between the sheets as counter cation	2-D	[3]
3	[{Cu(*pz*)$_4$}$_3${Cu(*pz*)$_3$ (H$_2$O)}$_2$ {HP$_2$Mo$_5$O$_{23}$}$_2$].9H$_2$O	*P*$\overline{1}$ *a*, Å =12.5446(9) *b*, Å =15.4392(12) *c*, Å =15.9536(12) *α*° =94.7020(10) *β*° =95.5840(10) *γ*° =100.2570(20)	Solvent evaporation technique Metal:Mo: ligand ratio is 1:3:3	I	The octahedral units {Cu^{II}(*pz*)$_4$O$_2$} covalently link neighboring {P$_2$Mo$_5$} clusters to form 1-D chain; two such chains are brought together by a second octahedral {Cu^{II}(*pz*)$_4$O$_2$} unit to form a double chain. Square pyramidal {Cu(*pz*)$_3$(H$_2$O)O} caps the double chains through oxygen of the phosphate group	1-D	[3]

4	[{Cu(*pz*)$_4$}$_2$ {H$_2$P$_2$Mo$_5$O$_{23}$}].H$_2$O	*Pcca* a, Å =16.1420(10) b, Å =13.9222(8) c, Å =23.3927(14)	Solvent evaporation technique Metal:Mo: ligand ratio is 1:3:4	I	{P$_2$Mo$_5$} cluster is linked to four octahedral copper units {Cu^{II}(*pz*)$_4$O$_2$}	3-D	[3]
5	(*pz*)$_2$[{Co(*pz*)$_4$}$_5$ {P$_2$Mo$_5$O$_{23}$}$_2$].6H$_2$O	*P2$_1$/c* a, Å =22.081(3) b, Å =18.644(2) c, Å =16.078(2) β, ° =109.137(2)	Hydrothermal synthesis Metal:Mo: ligand ratio is 1:3:6	I	Out of three cobalt octahedral {Co^{II}(*pz*)$_4$O$_2$} complexes, two covalently link {P$_2$Mo$_5$} clusters into 2-D sheets and the third one connect the sheets to form a double sheet	2-D	[4]
6	(*pz*){Ni(*pz*)$_4$(H$_2$O)$_2$} [{Ni(*pz*)$_4$}$_5$ {P$_2$Mo$_5$O$_{23}$}$_2$].2H$_2$O	*P2$_1$/c* a, Å =24.674(3) b, Å =18.137(2) c, Å =16.223(2) β, ° =95.495(2)	Hydrothermal synthesis Metal:Mo: ligand ratio is 1:3:6	I	Two octahedral Ni-*pz* complexes covalently link {P$_2$Mo$_5$} clusters into 2-D sheets and the third one connects the sheets to form a double sheet. {Ni(*pz*)$_4$(H$_2$O)$_2$} units occur in between the double sheets as counter cations	2D	[4]
7	{Cu(*pz*)$_4$(H$_2$O)$_2$} [{Cu(*pz*)$_4$} {Cu(*pz*)$_4$(H$_2$O)} {P$_2$Mo$_5$O$_{23}$}].2H$_2$O	*P$\overline{1}$* a, Å =12.302(3) b, Å =14.192(4) c, Å =19.351(5) α, ° =97.761(5) β, ° =97.555(4) γ, ° =98.569(5)	Hydrothermal synthesis Metal:Mo: ligand ratio is 1:3:6	I	Two asymmetric octahedral {Cu(*pz*)$_4$O$_2$}complexes link {P$_2$Mo$_5$} clusters into double chain which is capped by a third octahedral {Cu(*pz*)$_4$(H$_2$O)O} unit	2-D	[4]
8	(*pz*)[{Zn(*pz*)$_3$}$_3$ {P$_2$Mo$_5$O$_{23}$}].2H$_2$O	*P2$_1$2$_1$2$_1$* a, Å =15.516(3) b, Å =17.373(3) c, Å =21.437(4)	Hydrothermal synthesis Metal:Mo: ligand ratio is	I	{P$_2$Mo$_5$} cluster is linked to four trigonal pyramidal zinc units {Zn(*pz*)$_3$O$_2$}and one tetrahedral {Zn(*pz*)$_3$O}unit to	3-D	[4]

			1:3:6		form a 3-D framework		
9	$[Ag(pz)_2]_6[PMo_{12}O_{40}]_2 \cdot 3H_2O$	R-3 a, Å =20.437(2) c, Å =48.003(1)	Hydrothermal synthesis Metal:Mo: ligand ratio is 2:1:2	II	Two crystallographically independent $[PMo_{12}O_{40}]^{3-}$ clusters are arranged in an AB-AB mode to give two kinds of supramolecular layers. The layers are further connected by $[Ag(pz)_2]^+$ linkers to form complex 3-D supramolecular network	3-D	[5]
10	$[Ag(pz)_2]_3[PMo_{12}O_{40}]$	$P\bar{1}$ a, Å = 11.3185(17) b, Å = 11.3221(18) c, Å = 12.9277(19) α, ° = 113.086(2) β, ° = 113.086(2) γ, ° = 103.579(2)	Hydrothermal synthesis Metal:Mo: ligand ratio is 8:1:12	I	Four-supporting $[PMo_{12}O_{40}]^{3-}$ anions are fused by $[Ag(pz)_2]^+$ subunits to form a 1-D chain. Through weak interactions of Ag···O (3.091 Å) a 2-D supramolecular layer is constructed	2-D	[6]

Table IV.2. Classification of Solids **7,9** and **11**.

Sl. No.	Solid	Class	Dimensionality
1	$\{Hpz\}_6\{Zn(pz)_4(H_2O)_2\}[\{Zn(pz)_2 P_2Mo_5O_{23}\}_2] \cdot 8H_2O$, **7**	**Class I:** PMO clusters covalently linked by TMCs extending into multi-dimensions	1-D
2	$[\{Cu(pz)_4\}_2 \{H_2P_2Mo_5O_{23}\}] \cdot H_2O$, **8**	**Class I:** PMO clusters covalently linked by TMCs extending into multi-dimensions	2-D
3	$\{Ni(pz)_4\}[\{Ni(pz)_4\}_2\{H_2P_2Mo_5O_{23}\}]_2 [\{Ni(pz)_4\}\{Ni(pz)_4(H_2O)\}\{HP_2Mo_5O_{23}\}]_2 \cdot 14H_2O$, **9**	**Class I:** PMO clusters covalently linked by TMCs extending into multi-dimensions	2-D
4	$\{pz\}_2[\{Co(pz)_4\}_5\{P_2Mo_5O_{23}\}_2] \cdot 6H_2O$, **11**	**Class I:** PMO clusters covalently linked by TMCs extending into multi-dimensions	2-D

explore their magnetic properties as spin-spin interactions between metal centers can result in interesting magnetic behavior. Therefore, the magnetic behavior of Solids **8-11**, was investigated using Guoy Balance.
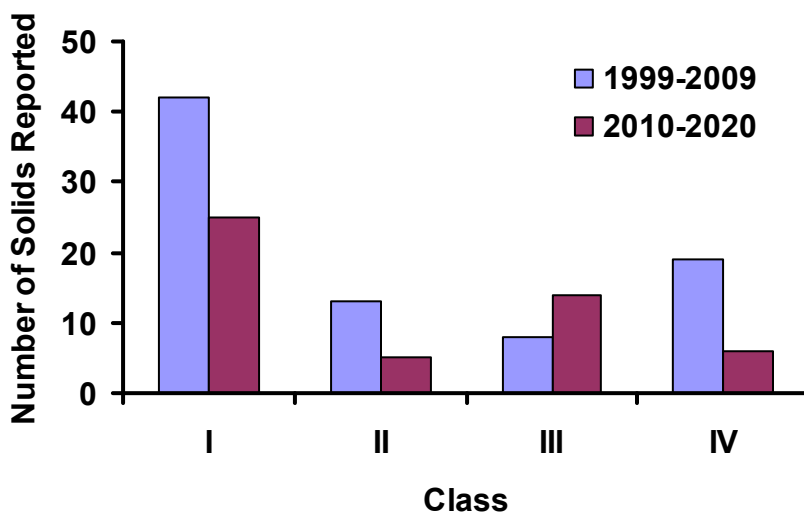
Figure IV.1. Statistical analysis of TMC incorporated PMO cluster based solids reported in literature during the last two decades.

$[\{Cu(pz)_2\}_4\{CuMo_{12}O_{38}(OH)_2\}].8H_2O$ (**12**) belongs to a unique class of polyoxometalates (POMs) called transition metal substituted POMs. This substitution can be of two types in Keggin polyanion, either by replacing the centre atom or one of the addenda atoms (refer Figure IV.2). Generally, the latter type of substitution is considered as a defect and the resultant product formed is named as lacunary POM. Only limited examples are reported in literature for copper substituted solids. The solid **12** draws special attention because only one solid is previously reported with copper as the centre of the Mo-O framework of Keggin type heteropolyanion. Zhang *et. al* synthesized $[CuMo_{12}O_{40}]^{6-}$ POM based MOF composite and studied its enhanced catalytic activities [7]. Two mono Cu(II) substituted phosphomolybdates $[Cu_4(tea)_6(H_4PMo_{11}CuO_{39})(PMo_{12}O_{40})]_2.33H_2O$ and $[Cu_3(tea)_6(H_2O)_2(H_2PMo_{11}CuO_{39})_2]_2.30H_2O$ (tea =2-[1,2,4]triazol-4-yl-ethylamine) have

been reported by Tian *et. al.* in 2016 [8]. Properties of sodium and potassium salts of copper substituted Keggin type phosphomolybdates $Na_7PMo_{11}CuO_{40}$ and $K_5PMo_{11}CuO_{39}$ have also been investigated [9,10].
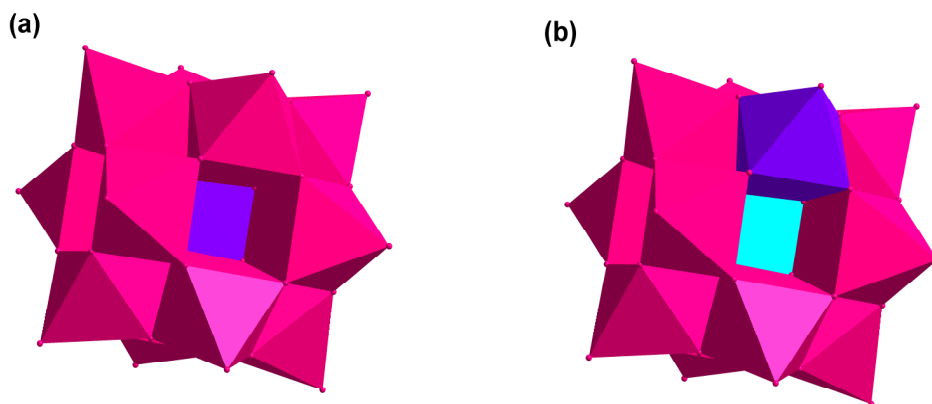
Figure IV.2. (a) Transition metal substituted Keggin type polyanion by replacing the central atom and (b) transition metal substituted Keggin type phosphomolybdate by replacing one of the addenda atoms.

IV.2. Experimental Section

IV.2.1. Synthesis

IV.2.1.1. Solvent evaporation method

Initially two different aqueous solutions were prepared. Solution A was prepared from metal chloride ($MCl_2.xH_2O$) and pyrazole (0.337 g, 4.95 mmol, Aldrich, 98%) in 20 ml of distilled water, while solution B was 20 ml of sodium molybdate solution ($Na_2MoO_4.2H_2O$, 0.2 g, 0.826 mmol, Merck, 99%). Solution B was added drop wise to solution A with constant stirring for 5-10 minutes. A precipitate was obtained upon stirring which was dissolved using 1M orthophosphoric acid (H_3PO_4, Merck, 85%). The resulting clear solutions were left

undisturbed for crystallization at room temperature. The resultant products were washed with water and acetone and allowed to dry in air. The experimental conditions have been summarized in Scheme IV.1.

IV.2.1.2. Hydrothermal synthesis

A mixture of metal chloride (MCl_2, 0.826 mmol, Aldrich, 98%), pyrazole (9.912 mmol, Aldrich, 98%) and sodium molybdate (0.826 mmol, Merck, 99%) was taken in 6 ml of distilled water, sealed in a 10 ml Teflon lined stainless steel container and heated at 180°C for 3 days. The initial pH was adjusted using 1 M orthophosphoric acid. After slow cooling to room temperature, the blue-black crystals were formed in the case of copper. The crystals were washed with water and acetone and allowed to dry in air. It is observed that except for $CuCl_2.2H_2O$, amorphous powder was obtained with other metal chlorides. The yield of **12** was found to be 70-75% based on Mo.
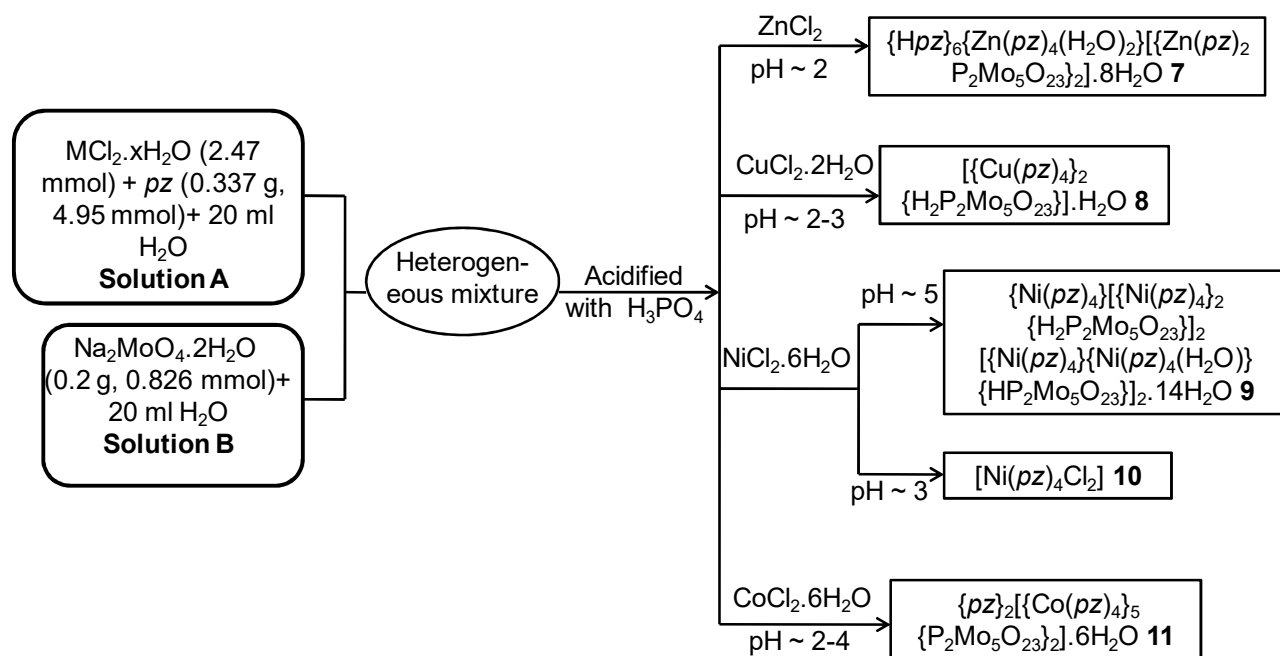
Scheme IV.1. Scheme showing the experimental procedure to crystallize solids **7-11**.

IV.2.2. Characterization

The solids were characterized using techniques discussed under Section II.2.2 in Chapter II. The crystal and refinement data for only solids **7, 9** and **12** have been summarized in Table IV.3 as details of solids **8**, **10** and **11** have already been reported in literature.

Table IV.3. Crystal and Refinement Data for Solids **7**, **9** and **12**.

	7	**9**	**12**
Formula	$C_{42}H_{64}Mo_{10}N_{28}$ $O_{56}P_4Zn_3$	$C_{108}H_{146}Mo_{20}$ $N_{72}Ni_9O_{108}P_8$	$C_{24}H_{32}Cu_5Mo_{12}$ $N_{16}O_{48}P$
Formula weight, g	3136.66	6875.75	2845.69
T (K)	293(2)	293(2)	293(2)
Space Group	P -1	C2/c	P-1
a, Å	9.5647(15)	41.244(8)	12.727(2)
b, Å	12.558(2)	12.328(3)	13.165(2)
c, Å	20.340(3)	44.169(9)	13.882(2)
α, °	75.907(7)	90	66.680(3)
β, °	84.727(6)	91.62(3)	83.383(3)
γ, °	87.525(7)	90	65.274(3)
V, Å^3	2359.0(6)	22449(8)	1936.6(5)
Z	1	4	1
d_{calc}, g·cm^{-3}	2.208	2.034	2.44
$\mu_{MoK\alpha}$, cm^{-1}	2.209	1.972	3.315
λ (Å)	0.71073	0.71073	0.71073
R_1(I>2σI), WR$_2$(all)	0.0590, 0.1491	0.0387, 0.0999	0.0782, 0.2165
GOF	1.063	1.116	1.107

IV.2.3. Magnetic susceptibility measurements

The magnetic moment and molar susceptibility are given by the following equations:

$$\text{Magnetic moment } (\mu) = 2.828 \ \sqrt{\chi_m} \text{ x T}$$

$$\chi_m = \chi_g \text{ x molecular weight}$$

$$\chi_g = \frac{C \text{ x } L \text{ x } (R-R_o)}{w \text{ x} 10^9}$$

where,   C   =   Calibration constant
          L   =   length of sample
          W   =   weight of sample
          R   =   sample reading
          R_o =   Empty tube reading

IV.3. Results and discussion

The solids **7-9** and **11** are based on $\{P_2Mo_5\}$ cluster anion and its structure has been discussed under Section II.3 in Chapter II. Solid **12** is based on Keggin type polyanion [11, 12], in which copper atom is located at the inversion center. The CuO_4 tetrahedron is surrounded by four Mo_3O_{13} units formed by edge-sharing octahedral which are connected to each other by corner sharing oxygen atoms.

IV.3.1. Crystal structure of 7

In $\{Hpz\}_6\{Zn(pz)_4(H_2O)_2\}[\{Zn(pz)_2P_2Mo_5O_{23}\}_2].8H_2O$ (**7**) **,** the zinc complex, $\{Zn(pz)_2O_3\}$ derivatizes the $\{P_2Mo_5\}$ cluster through Zn–O coordination to form 1-D chains (refer Figure IV.3) which further aggregates through non-bonding interactions with octahedral $\{Zn(pz)_4(H_2O)_2\}^{2+}$ complex and six $(Hpz)^+$ cations to form 2-D sheets (Figure IV.4). The 3-D crystal packing is facilitated by CH…π interaction between neighboring sheets (Figure

IV.5). **7** is a new pseudopolymorph of $(pz)[\{Zn(pz)_3\}_3\{P_2Mo_5O_{23}\}].2H_2O$ reported by Thomas *et. al.* [4].
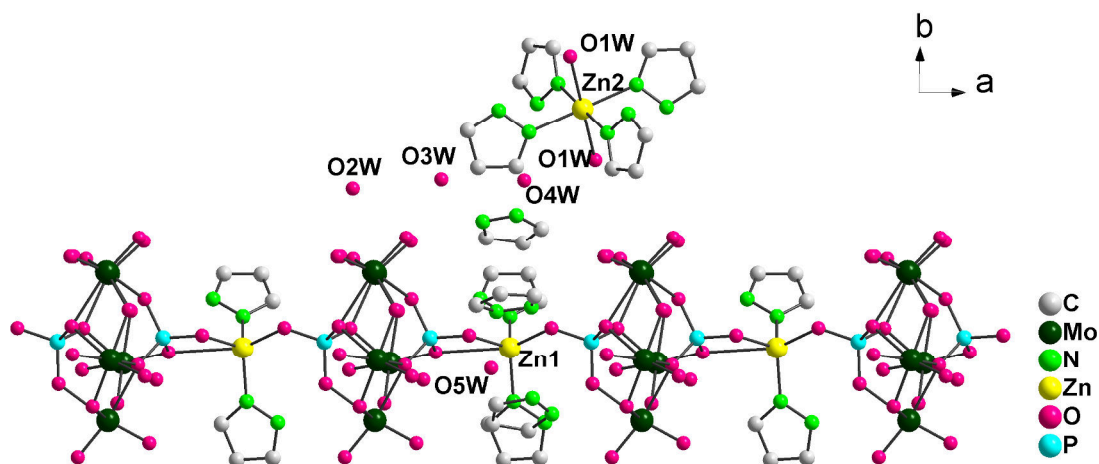
Figure IV.3. 1-D chains in **7**. H-atoms have been removed for clarity.
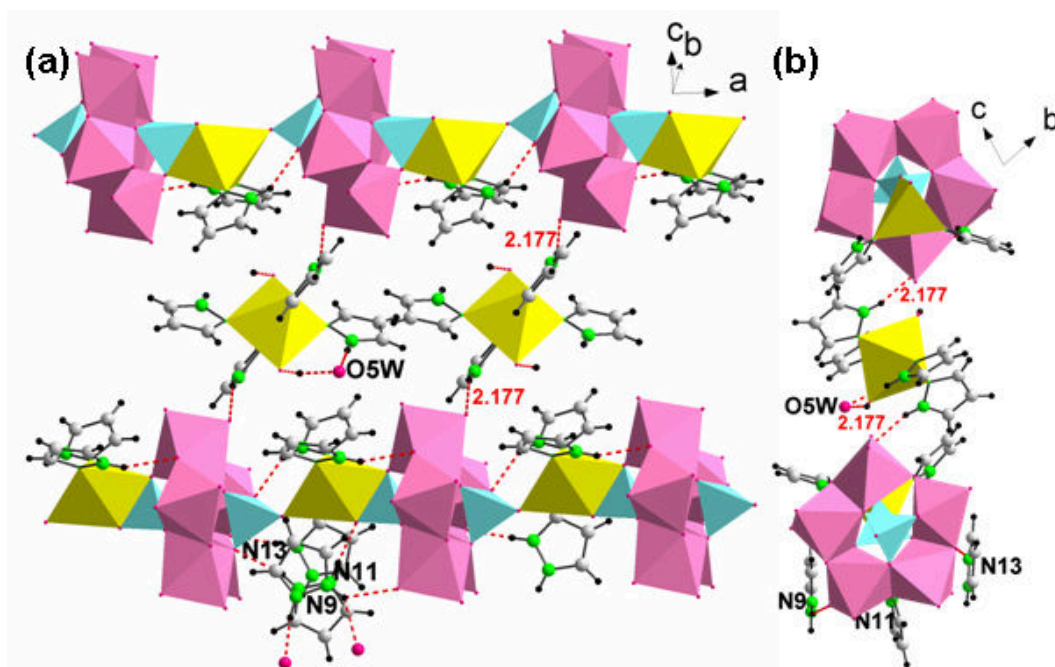
Figure IV.4. (a) Octahedral $\{Zn(pz)_4(H_2O)_2\}^{2+}$ complex links 1-D chains along with six $(Hpz)^+$ cations to form 2-D sheets (H-bonding interactions are shown in dashed red lines). (b) View along *a* axis.
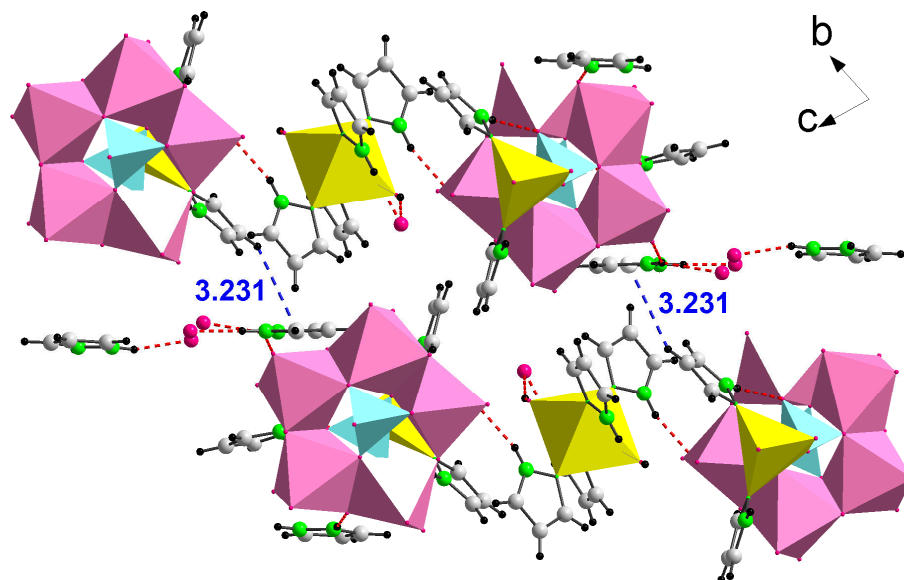
Figure IV.5. 3-D crystal packing is facilitated by CH…π interaction (shown in dashed blue lines) between neighboring sheets.

IV.3.2. Crystal structure of 8

The detailed crystal structure of $[\{Cu(pz)_4\}_2\{H_2P_2Mo_5O_{23}\}].H_2O$ (**8**) has already been reported by Thomas *et. al.* in 2008 [3]. The authors have reported that $\{P_2Mo_5\}$ cluster is linked to four octahedral copper units, $\{Cu^{II}(pz)_4O_2\}$ of which Cu2 covalently connects $\{P_2Mo_5\}$ clusters to form zig-zag chains which are further covalently linked by Cu1 complex to form a 3-D network (Figure IV.6).

IV.3.3. Crystal structure of 9

$\{Ni(pz)_4\}[\{Ni(pz)_4\}_2\{H_2P_2Mo_5O_{23}\}]_2$ $[\{Ni(pz)_4\}\{Ni(pz)_4(H_2O)\}\{HP_2Mo_5O_{23}\}]_2.14H_2O$ (**9**), is a novel polymeric solids in which the asymmetric unit consists of five nickel complexes and two $\{P_2Mo_5\}$ cluster anions as shown in Figure IV.7. Ni1 lies on inversion center which results in a tetrameric cluster unit as shown in Figure IV.7b. These units are connected Ni2

and Ni4 complexes to form a 2-D sheet. Of the lattice water molecules, only O2W is connected to Ni5 complex; remaining lattice water molecules occupy the voids in 2-D sheet. **9** is a new pseudopolymorph of $(pz)\{Ni(pz)_4(H_2O)_2\}[\{Ni(pz)_4\}_5\{P_2Mo_5O_{23}\}_2]\cdot 2H_2O$ reported by Thomas *et. al.* [4].
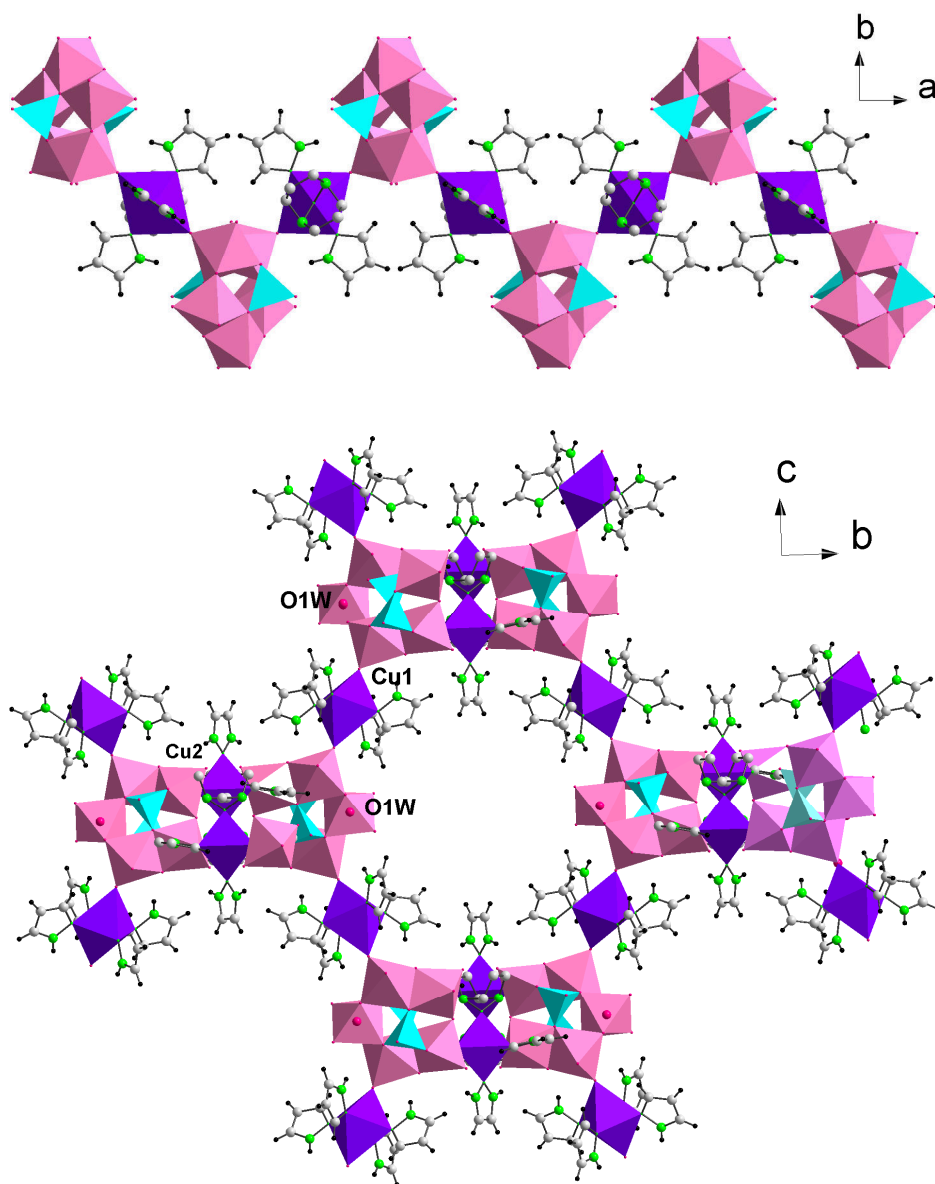
Figure IV.6. Zig-zag chains in **8** (top) connected by Cu1 to form 3-D structure of **8** (bottom).

IV.3.4. Crystal structure of 10

Crystal structure analysis of **10** showed that it is analogous to its cobalt and copper counterparts, reported in literature [13, 14]. In **10**, Ni center was coordinated to four *pz* units and two chlorine atoms to form an octahedral structure (refer Figure IV.8). The structure of [Ni(*pz*)$_4$Cl$_2$] has been reported earlier by Reimann *et. al.* in 1967 [15].
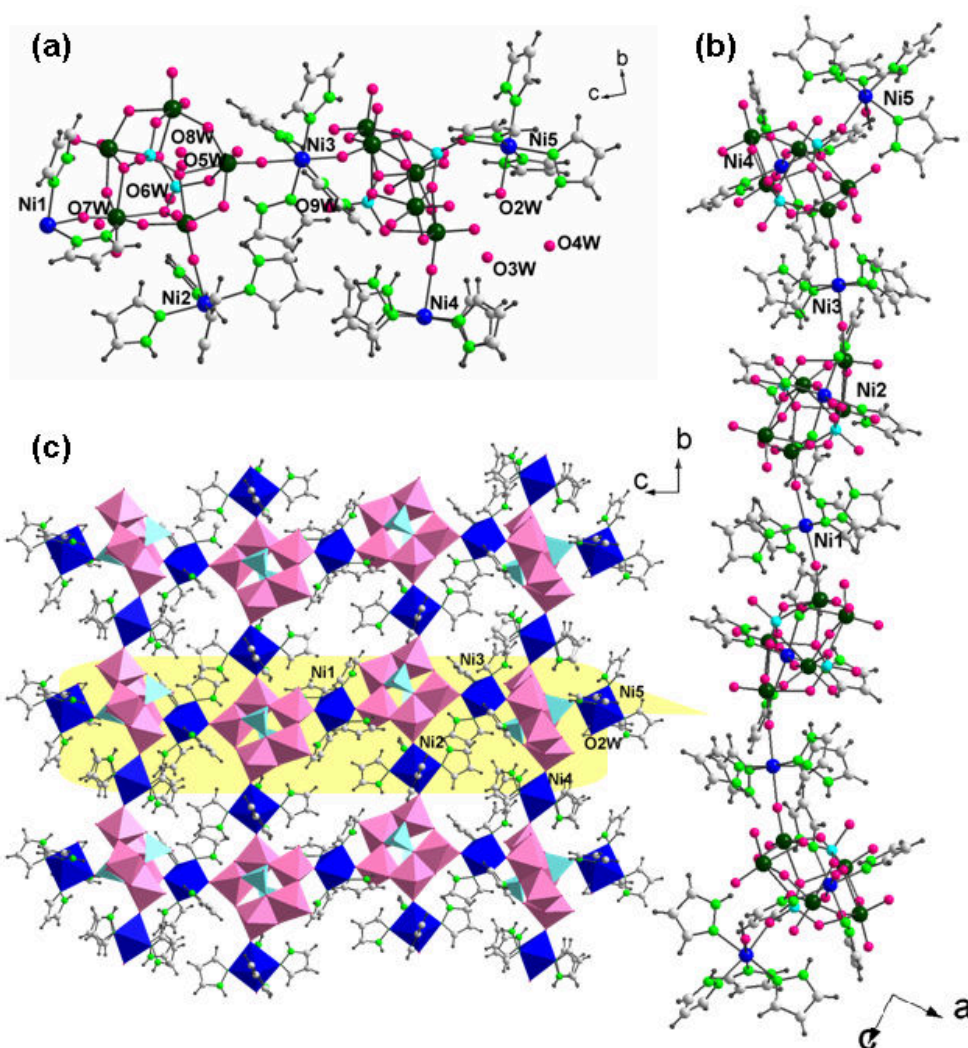
Figure IV.7. (a) Asymmetric unit in **9**. (b) Tetrameric cluster unit forming 2-D sheet as shown in (c). The lattice water molecules have been omitted for clarity.
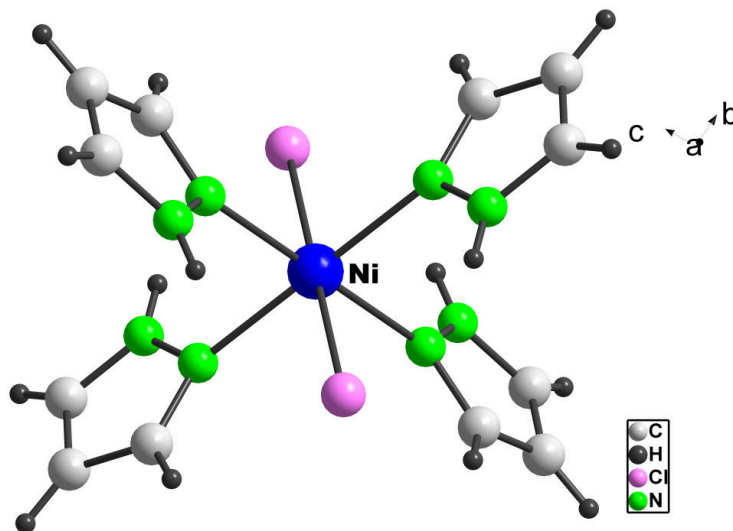
Figure IV.8. Six coordinated nickel complex of [Ni(*pz*)$_4$Cl$_2$], **10**.

IV.3.5. Crystal structure of 11

The crystal structure of {*pz*}$_2$[{Co(*pz*)$_4$}$_5$ {P$_2$Mo$_5$O$_{23}$}$_2$].6H$_2$O (**11**) has been described earlier by Thomas *et. al.* in 2011 [4]. It was reported that "three sets of octahedral {Co^{II}(*pz*)$_4$O$_2$} complexes (represented by three asymmetric cobalt, Co1, Co2 and Co3) are involved in the structure building. The Co1 and Co2 complex units covalently link {P$_2$Mo$_5$} clusters into 2-D sheets and Co3 complex units connect the sheets to form a double sheet. The voids in the double sheets are occupied by free *pz* groups and the stacking of the double sheets along the *ab* plane is mediated by lattice water molecules present in the inter-lamellar region." (refer Figure IV.9).
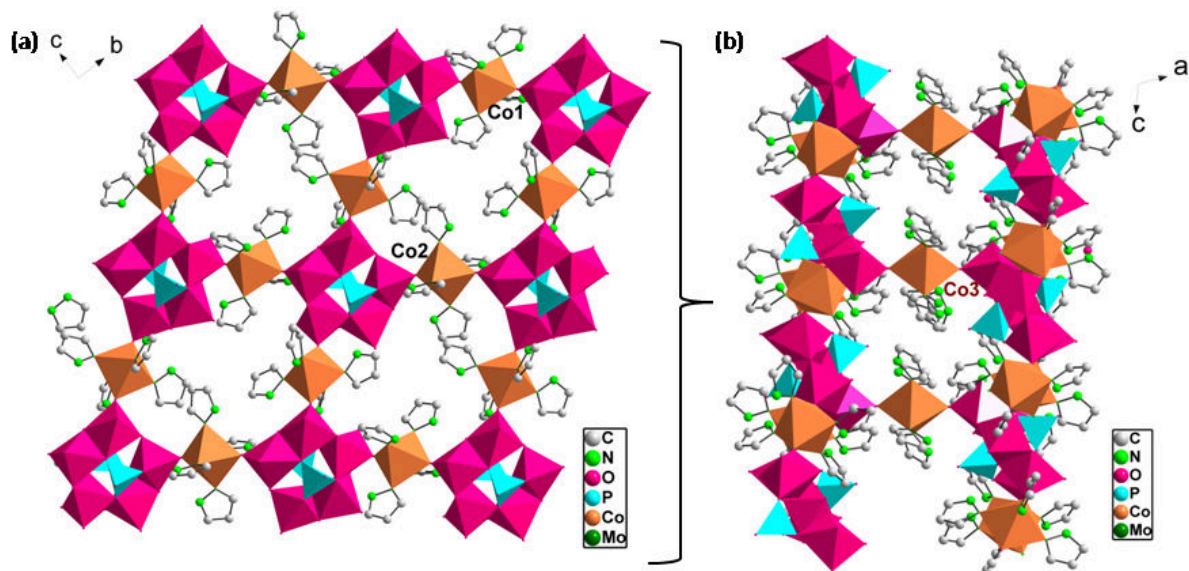
Figure IV.9. (a) Co1 and Co2 complex units covalently link {P_2Mo_5} clusters into 2-D sheets. (b) Co3 complex units connect the sheets to form a double sheet. H atoms, free *pz* moieties and lattice water molecules have been omitted for clarity.

IV.3.6. Crystal structure of 12

The solid **12** is isostructural to {$PMo_{12}O_{40}$}$^{3-}$ Keggin type phosphomolybdate. However, instead of phosphorous, Copper is present at the inversion centre of the cluster framework of **12** (refer Figure IV.10). The BVS calculations [16] reveal that two terminal O6 atoms are protonated (refer Table IV.4). The cluster anions are covalently linked through Cu2 and Cu3 to form a 2-D sheet as shown in Figure IV.11. Among the eight lattice water molecules present, while O2W lies within the voids of the 2-D sheet; O1W, O3W and O4W formed a hexameric cluster which connects the two neighboring 2-D sheets (Figure IV.12).

Table IV.4. BVS calculations of **12**.

O—Mo	Bond Length (Å)		BVS	O—Mo	Bond Length (Å)		BVS
O1—Mo1	1.671(13)	1.892	1.892	O12—Cu1	1.502(18)	1.613	2.225
				O12—Mo1i	2.499(16)	0.202	
O2—Mo1	1.884(10)	1.064	2.059	O12—Mo3	2.475(16)	0.215	
O2—Mo4i	1.909(10)	0.995		O12—Mo4	2.511(14)	0.195	
O3—Mo1	1.918(12)	0.974	1.999	O14—Mo4	1.918(11)	0.971	2.055
O3—Mo2	1.898(15)	1.025		O14—Mo5	1.877(14)	1.084	
O4—Mo1	1.926(12)	0.95	1.955	O15—Mo4	1.912(13)	0.987	2.054
O4—Mo6	1.905(13)	1.005		O15—Mo6	1.883(15)	1.067	
O5—Mo1	1.891(9)	1.044	2.066	O16—Mo5	1.917(11)	0.973	1.904
O5—Mo3i	1.899(10)	1.022		O16—Mo2i	1.919(11)	0.931	
O6—Mo2	1.675(9)	1.872	1.872	O17—Mo5	1.663(10)	1.934	1.934
O7—Mo3	1.891(11)	1.044	2.083	O18—Mo5	1.870(14)	1.105	2.017
O7—Mo2	1.893(15)	1.039		O18—Mo3i	1.941(10)	0.912	
O8—Mo2	2.491(13)	0.206	2.164	O19—Mo5	1.894(11)	1.036	2.047
O8—Mo3	2.440(18)	0.237		O19—Mo6	1.903(10)	1.011	
O8—Cu1	1.524(14)	1.52					
O8—Mo5i	2.500(14)	0.201	O20—Mo6	1.665(9)	1.923	1.923
O9—Mo2	1.878(13)	1.082	2.085	O21—Cu1	1.554(15)	1.402	2.068
O9—Mo6	1.906(11)	1.003		O21—Mo2i	2.451(14)	0.23	
				O21—Mo6i	2.466(15)	0.221	
O10—Mo3	1.657(12)	1.965	1.965	O21—Mo1i	2.476(18)	0.215	
O11—Mo3	1.891(10)	1.044	2.052	O22—Cu1	1.550(14)	1.417	2.086
O11—Mo4	1.904(10)	1.008		O22—Mo4i	2.453(17)	0.229	
				O22—Mo5i	2.457(14)	0.226	
				O22—Mo6i	2.478(14)	0.214	
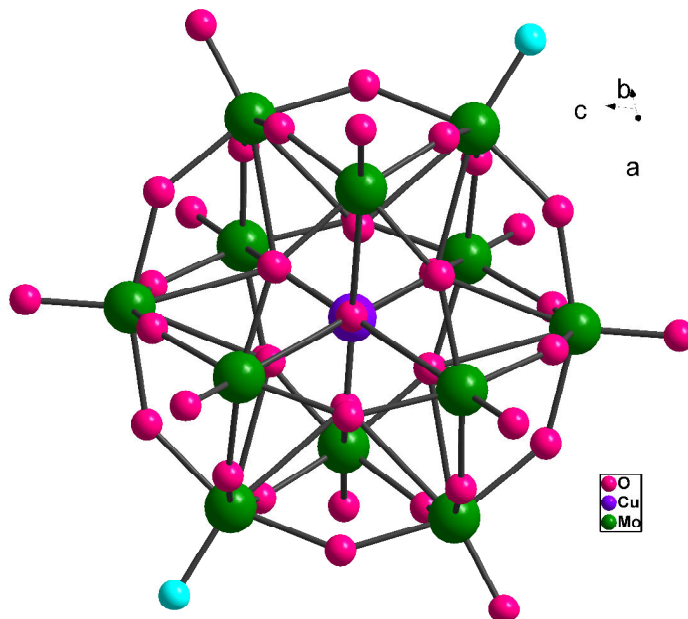
Figure IV.10. Keggin type polyanion which contains copper as the central atom. Two protonated terminal oxygen atoms (O6) are shown in cyan.
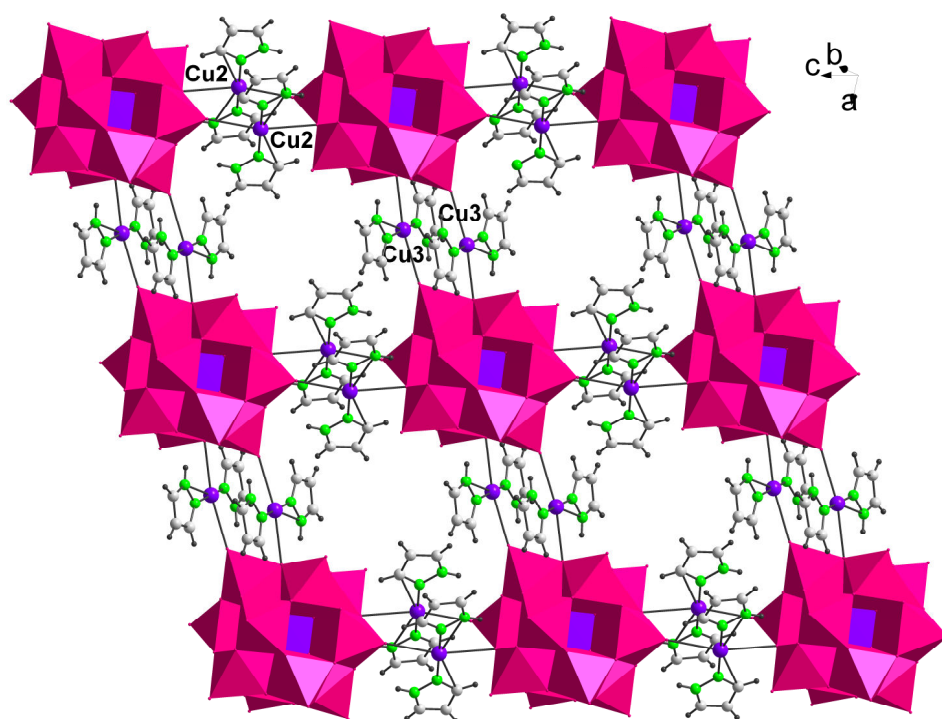
Figure IV.11. 2-D sheet formed connecting polyanions via copper- pyrazole complexes.
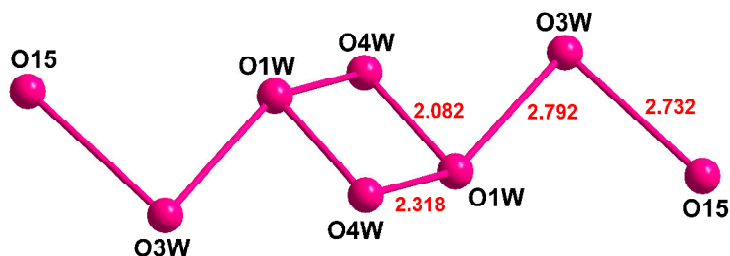
Figure IV.12. The hexameric water cluster in which the O…O interactions shown in solid lines.

IV.3.7. Analysis of solids 7 and 12

FTIR spectra of **7-11** shows the presence of characteristic P–O stretching and Mo–O stretching bands in the region 1000-1100 cm^{-1} and 640-930 cm^{-1} respectively. The finger print bands of Keggin type anions were observed in the region 700-1200 cm^{-1} for **12** [17-19]. The bands in the region 750-960 cm^{-1} could be attributed to Mo–O stretching vibrations. Broad band observed in solids **7-12**, in the region of ~ 3000-3500 cm^{-1} could be assigned to the stretching vibrations of O–H of water and N–H groups. (Figures IV.13-15).

The experimental and simulated powder X-ray pattern of solids **7-12** are given in Figures IV.16- IV.21. The comparison indicated that in all the cases, single phasic solids were obtained. The thermal degradation steps of TGA have been tabulated in Table IV.5 (also refer Figure IV. 22).

(a)

(b)
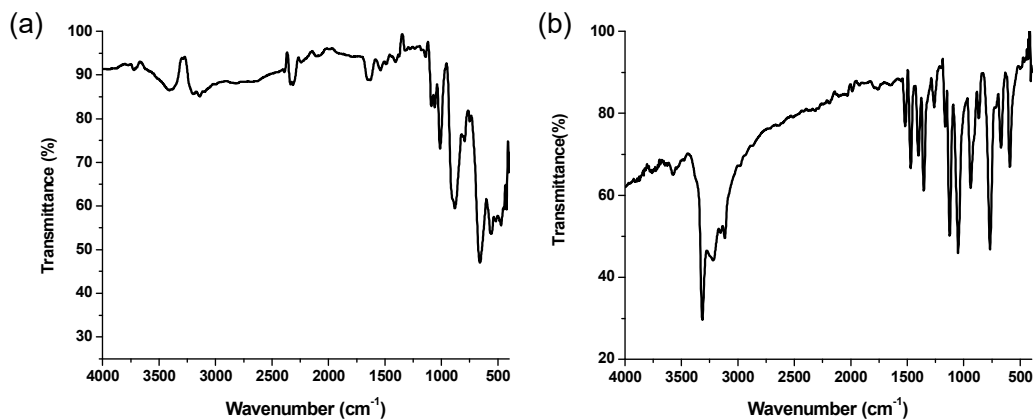
Figure IV.13. FTIR spectrum of (a) **7** and (b) **8**.

(a)

(b)
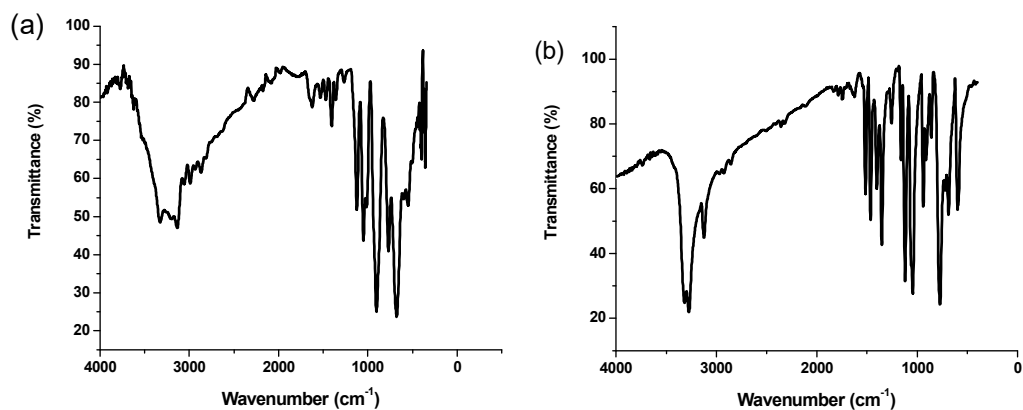
Figure IV.14. FTIR spectrum of (a) **9** and (b) **10**.

(a)

(b)
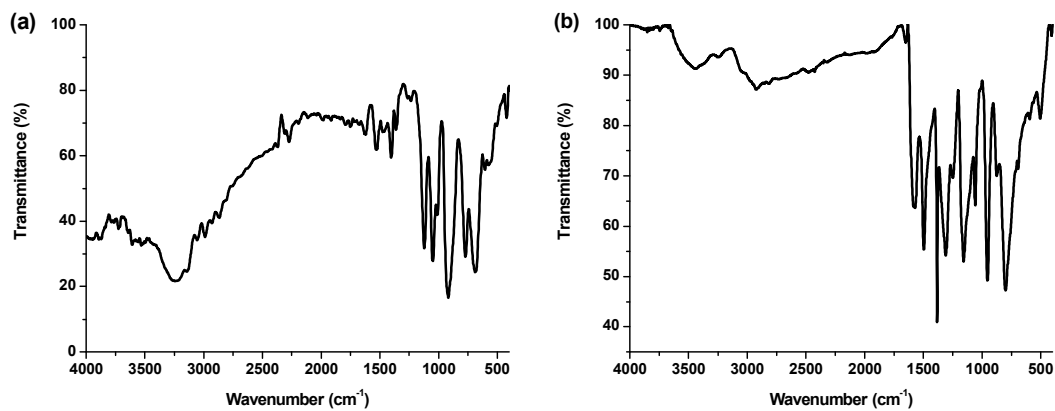
Figure IV.15. FTIR spectrum of (a) **11** and (b) **12**.
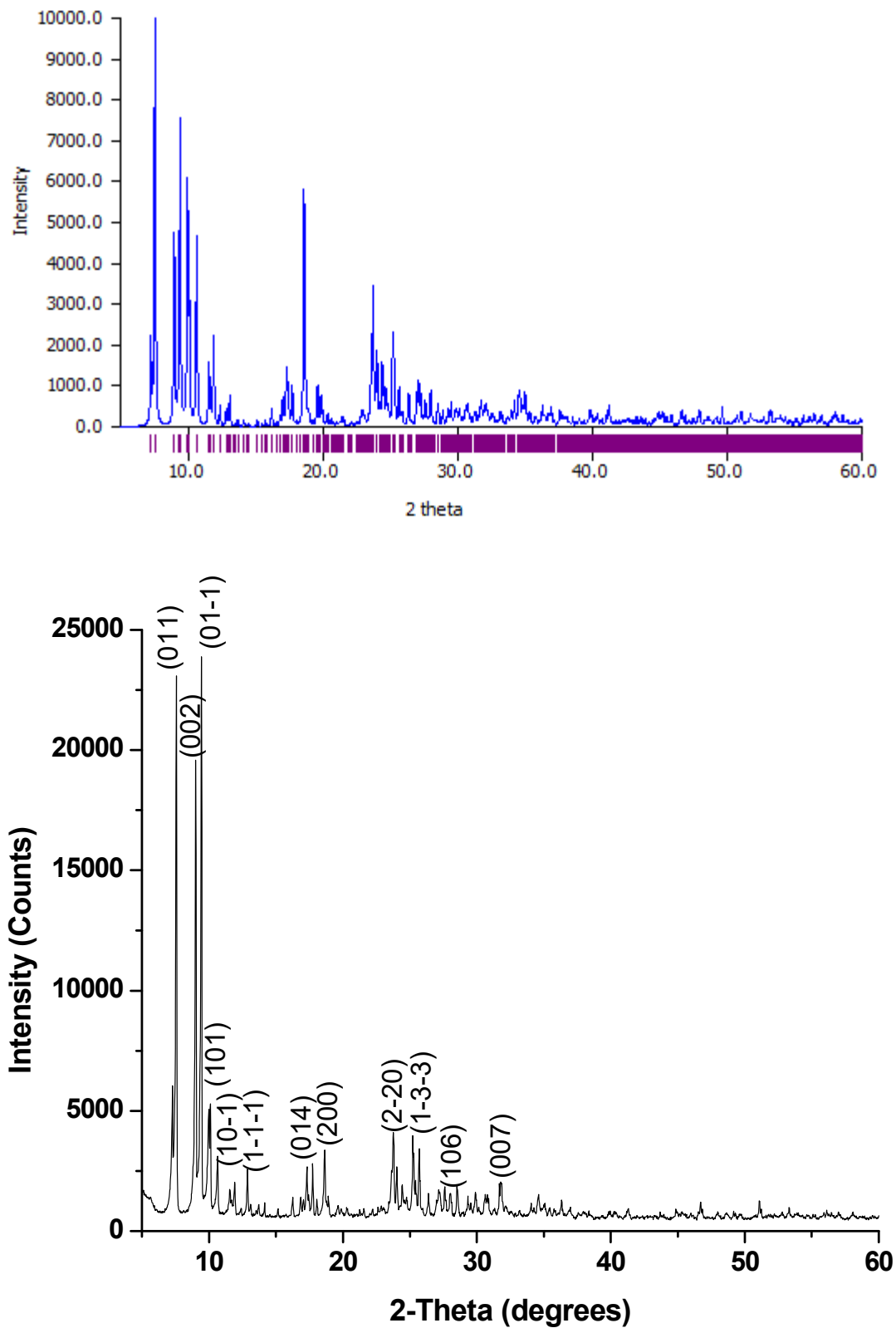
Figure IV.16. Simulated (top) and Experimental (bottom) PXRD of **7**.
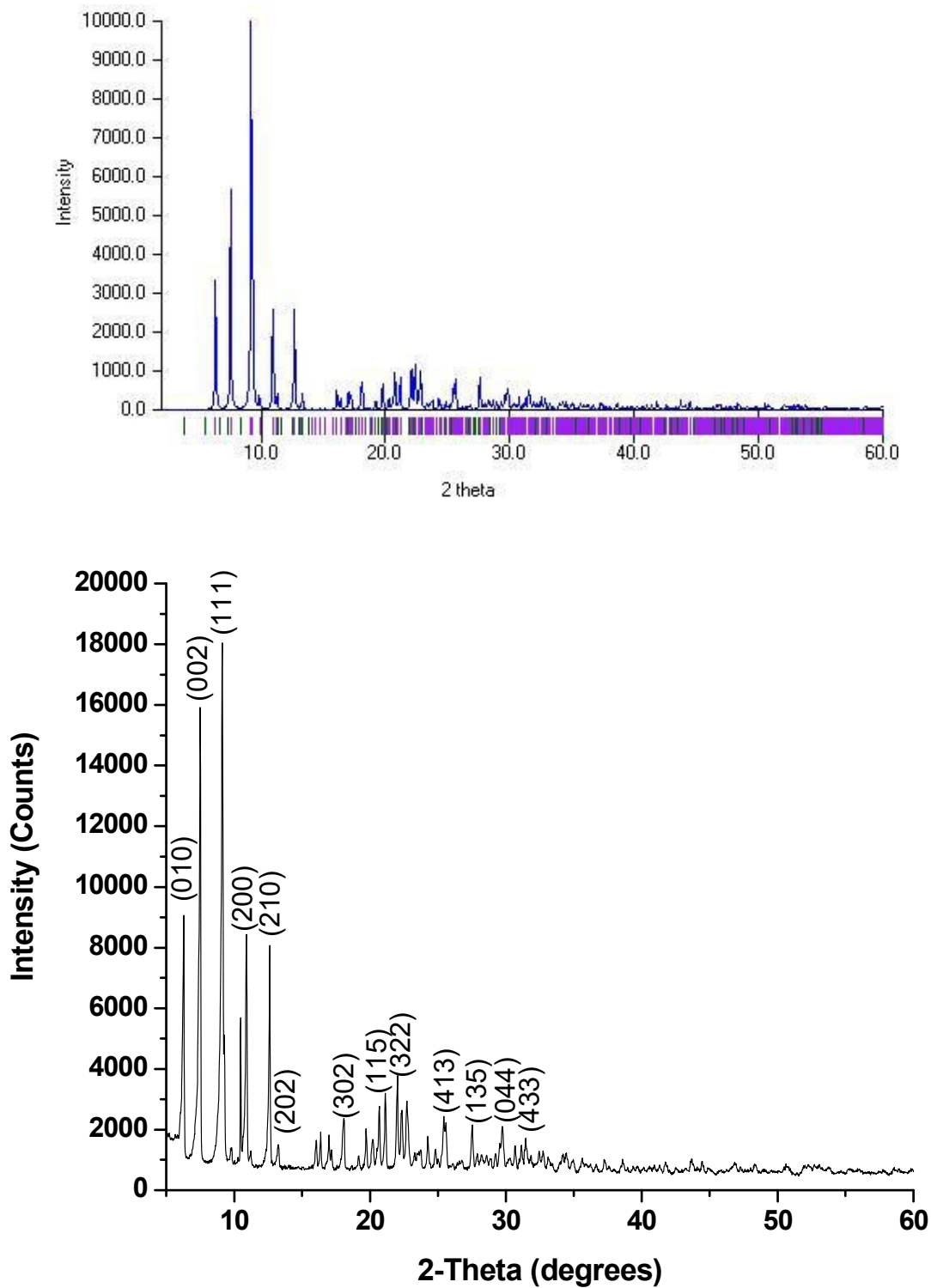
Figure IV.17. Simulated (top) and Experimental (bottom) PXRD of **8**.
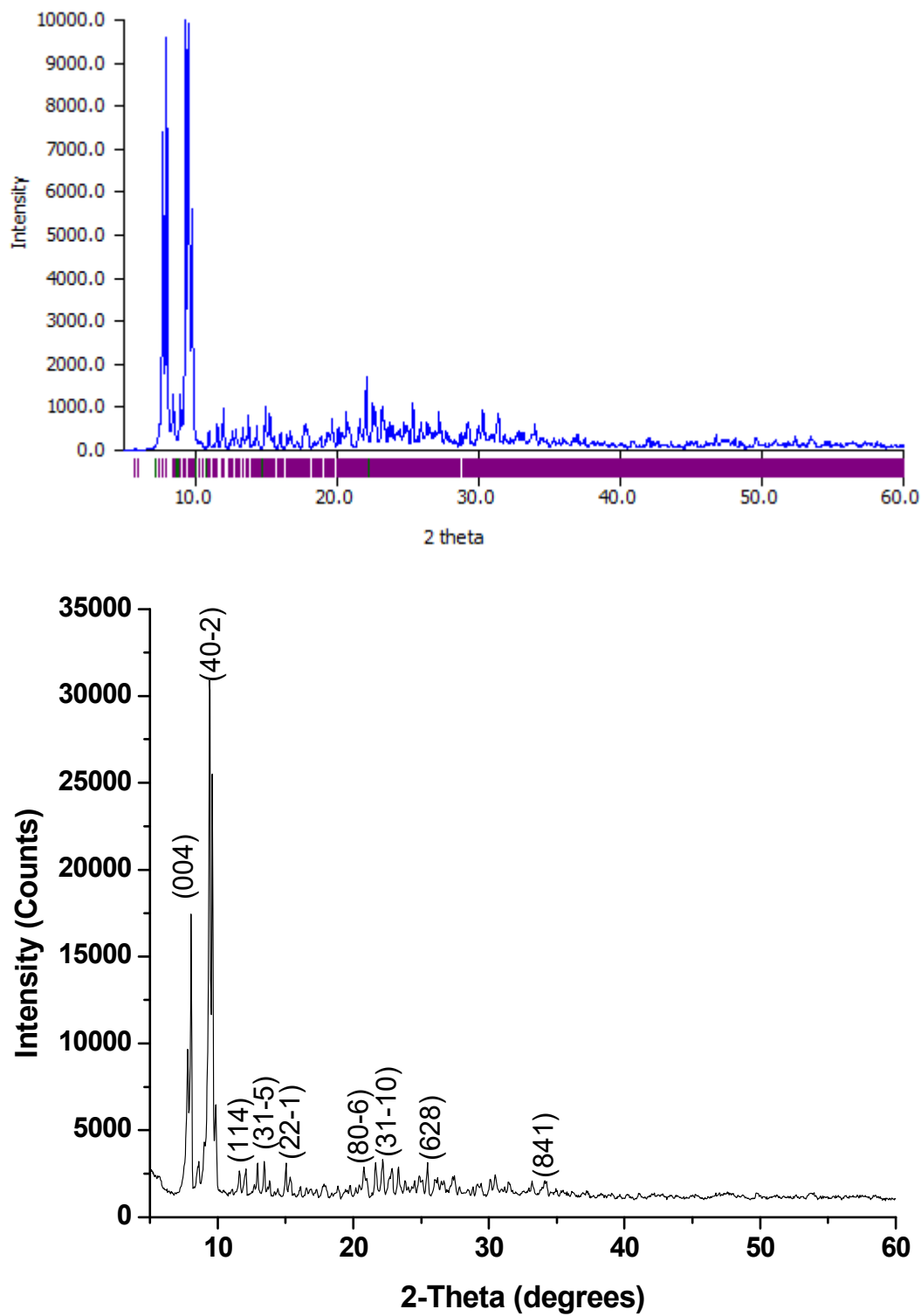
Figure IV.18. Simulated (top) and Experimental (bottom) PXRD of **9**.
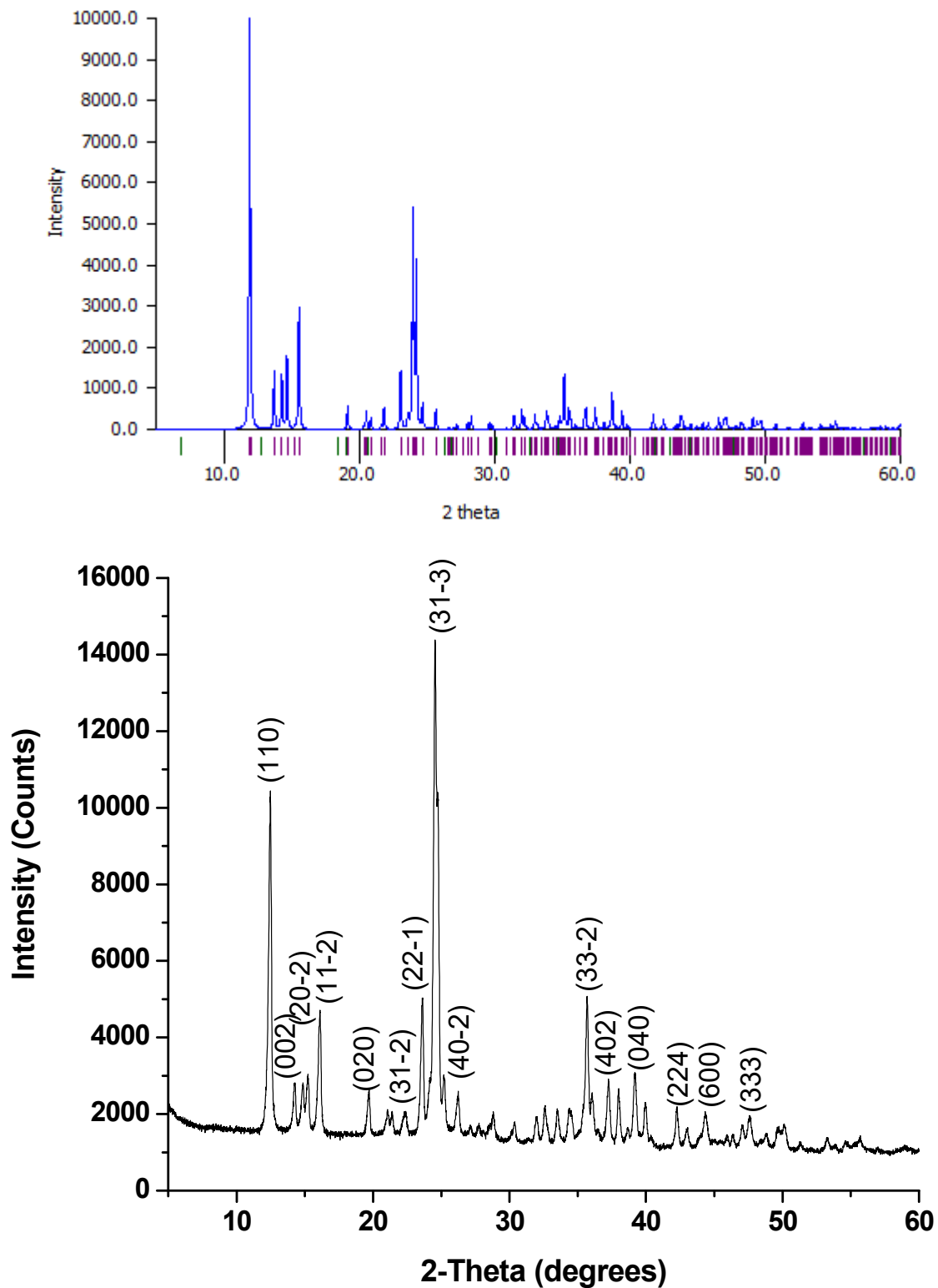
Figure IV.19. Simulated (top) and Experimental (bottom) PXRD of **10**.
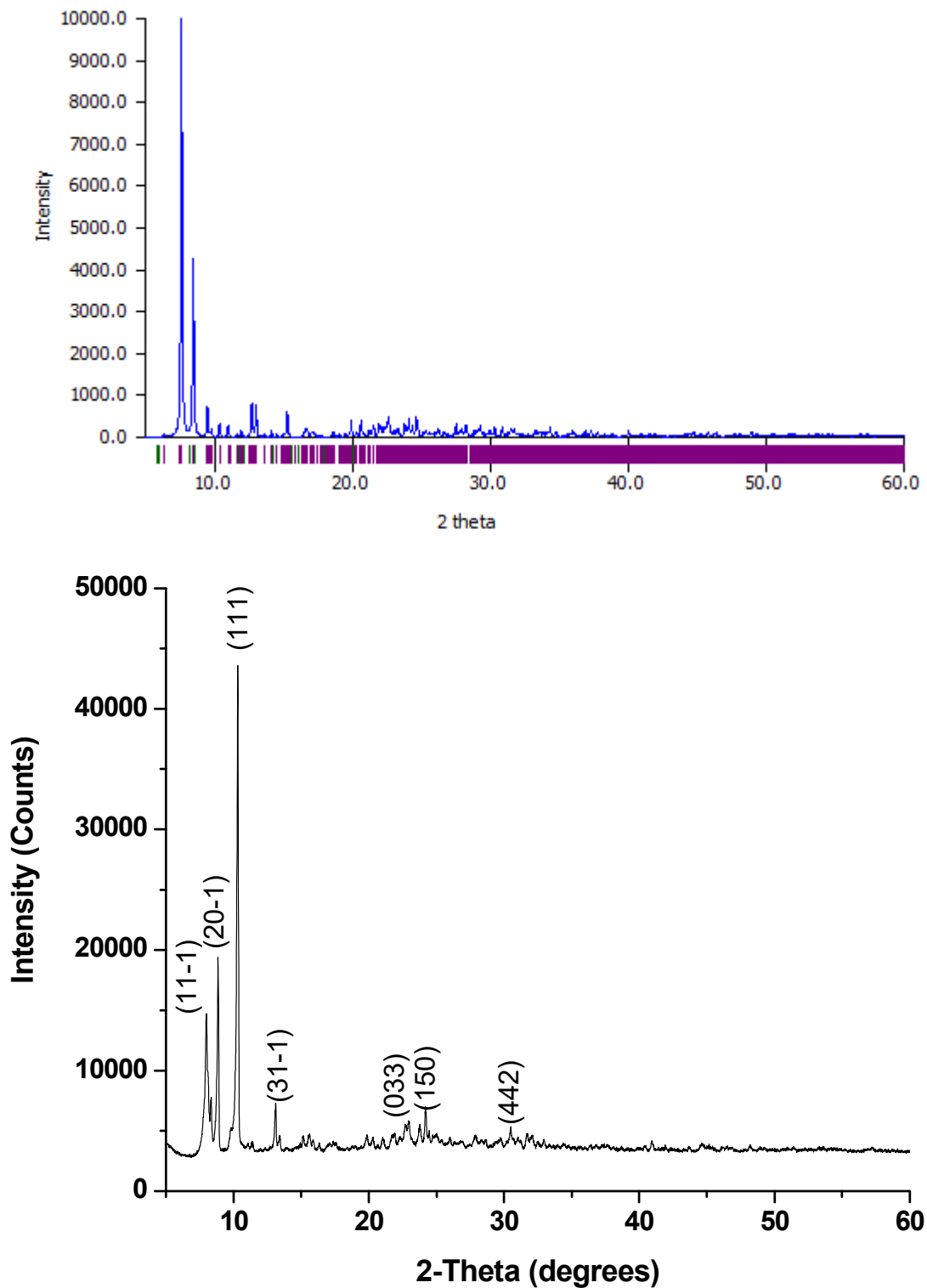
Figure IV.20. Simulated (top) and Experimental (bottom) PXRD of **11**.
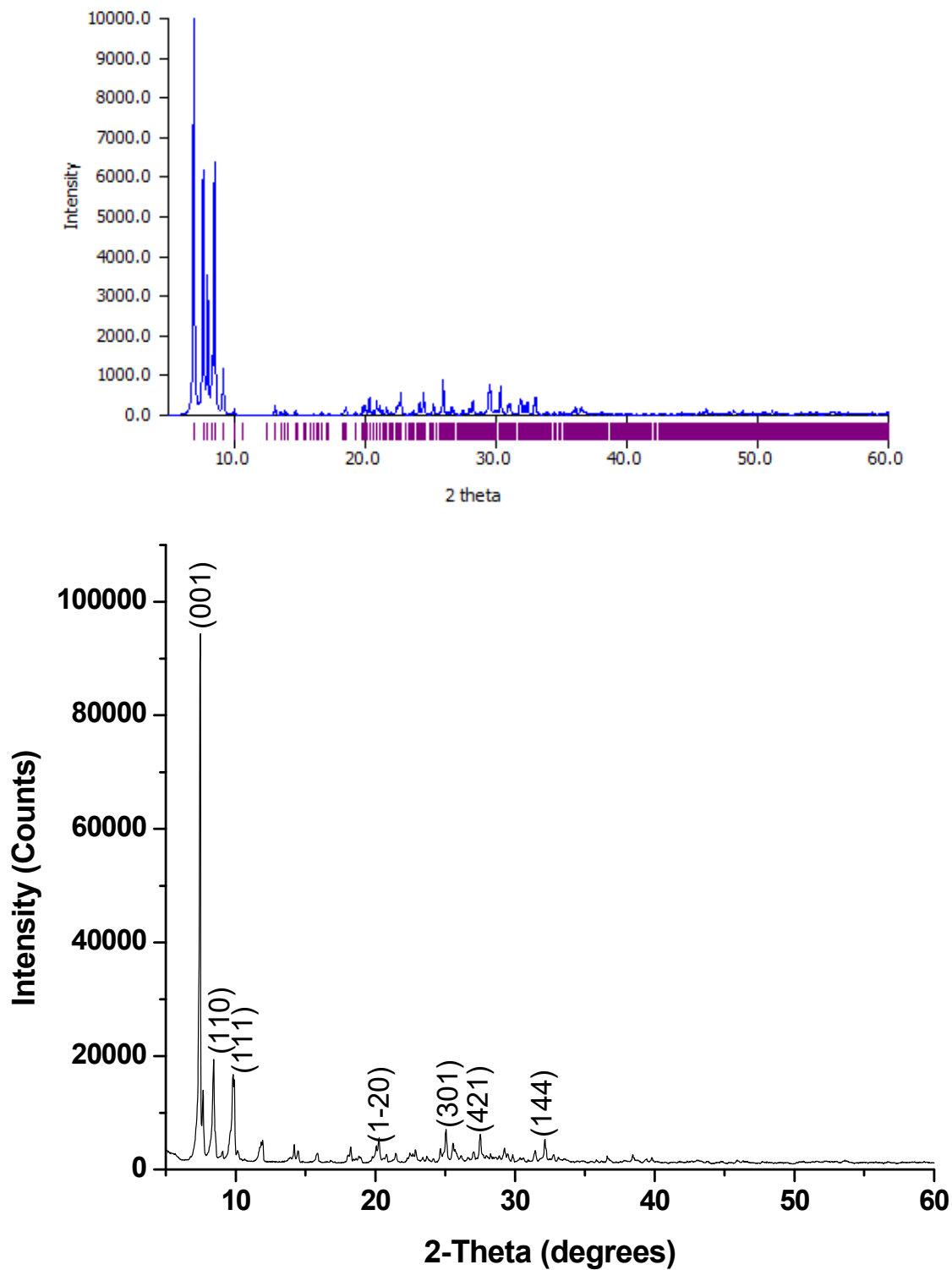
Figure IV.21. Simulated (top) and Experimental (bottom) PXRD of **12**.
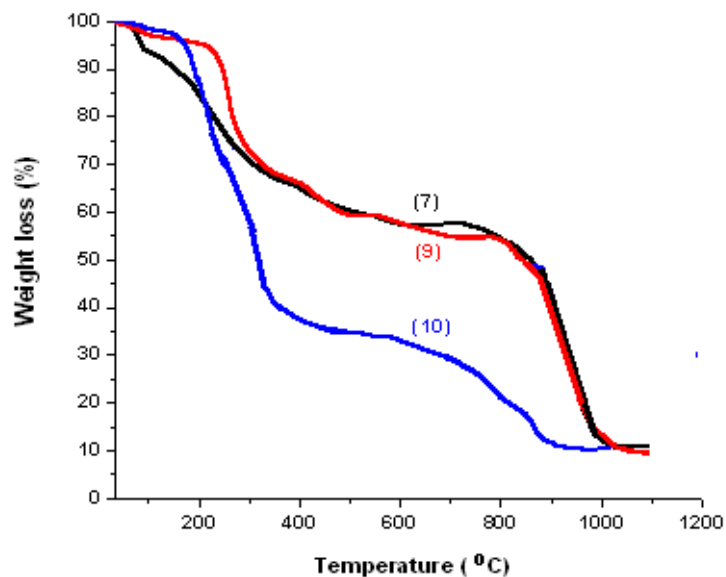
Figure IV.22. TGA of **7**, **9** and **10**.

Table IV.5. The summary of thermal degradation analysis of **7**, **9** and **10**.

Solid	Weight loss (%) TV= theoretical value	Temperature (°C)	Inference
7	~ 6 (TV = 4.5) ~37 (TV = 39.5)	Upto 100 Upto 625	Loss of 8 H_2O molecules Decomposition of six H*pz* moieties + *pz* ligands coordinated to Zn ions
		Above 780	Degradation of cluster anions
9	~ 3.5 (TV= 3.12) ~ 31.5 (TV = 30.3)	Upto 120 Upto 708	Loss of 14 H_2O molecules Decomposition of *pz* ligands coordinated to Ni ions
		Above 850	Degradation of remaining cluster unit
10	~ 1.5 ~ 84.6 (TV = 85.2)	100 Upto 853	Due to the moisture content of the solid surface Decomposition of two Cl and four *pz* ligands

IV.4. Magnetic properties

For solids **8-11**, the magnetic moment was calculated using spin only formula, $\mu = [n(n+2)]^{1/2}$ BM (where n is number of unpaired electrons).

In solid **8**, two copper centers are present and the observed magnetic moment obtained was 3.588. The calculated magnetic moment using spin only formula is 1.73. Therefore, the value obtained could be attributed to the contribution of two copper centers. In **10** which is a mere nickel complex, the calculated (2.82) and observed (2.84) values are in good agreement, confirming the presence of two unpaired electrons in the Ni center. However, in the case of **9** and **11**, the observed value showed a deviation from the calculated values. For **9**, the calculated and observed values are 2.82 and 10.799 respectively and for **11**, 3.87 and 11.738 respectively. Compared to the other solids, these solids have polymeric structures having more number of metal centers (9 Ni centers for **9** and 5 Co centers for **11**). Therefore, other parameters seem to be affecting the magnetic behavior of these two solids.

IV.5. Conclusions

The properties and dynamics of phosphomolybdates could be enhanced significantly by the incorporation of transition metal complexes. The association of ligands to the metal centers largely depends on the nature and pK_a value of the ligands used. In this chapter, *pz* has been selected on account of its coordination ability above pH 2.5. The pK_a value of pyrazole is 2.5 [4]. It can either be protonated or coordinated to a metal centre at acidic pH. So at pH ~2, *pz* existed in both forms: (*pz*) and (H*pz*)$^+$ such as in{H*pz*}$_6${Zn(*pz*)$_4$(H$_2$O)$_2$} [{Zn(*pz*)$_2$P$_2$Mo$_5$O$_{23}$}$_2$].8H$_2$O (**7**).

The ligand *pz* coordinated with Cu, Ni and Co in solids **8-12**, when the pH used was above 2.5. **7** and **9** are new pseudopolymorphs of solids (*pz*)[{Zn(*pz*)$_3$}$_3${P$_2$Mo$_5$O$_{23}$}]·2H$_2$O and (*pz*){Ni(*pz*)$_4$(H$_2$O)$_2$}[{Ni(*pz*)$_4$}$_5${P$_2$Mo$_5$O$_{23}$}$_2$]·2H$_2$O respectively reported by Thomas *et. al.* [4] prepared under hydrothermal conditions. The results thus suggest that subtle changes in

reaction conditions can result in formation of new solids. On the other hand, crystallization of **8** and **11** using solvent evaporation method suggests that these solids have stable phases as they were also obtained earlier by Thomas *et. al.* under hydrothermal conditions [4]. Solid **12** is a peculiar one which has Keggin type polyanion, with copper at its centre in the place of phosphorous. It has also *pz* coordinated copper centers in its structure.

References

1. Crow, D. R.; Westwood, J. V. *J. Inorg. Nucl. Chem*. **1968**, 30, 179-187.

2. Thomas, J. Ph.D. Thesis, Indian Institute of Technology, Delhi, India, **2010**.

3. Thomas, J.; Ramanan, A. *Cryst. Growth Des*. **2008**, 8, 3390-3400.

4. Thomas, J.; Ramanan, A. *Inorg. Chim. Acta* **2011**, 372, 243-249.

5. Yu, K.; Zhou, B. *Z. Naturforsch., B: Chem. Sci*. **2015**, 70, 311-316.

6. Tian, A, X.; Tian, Y.; Ni, H. P.; Ji, X. B.; Ning, Y. L.; Hou, X. *J. Coord. Chem*. **2016**, 69, 2855-2863.

7. Zhang, J.; Zhang, J. *J. Clust. Sci*. **2020**, 31, 1051-1059.

8. Tian, A.; Ni, H.; Tian, Y.; Ji, X.; Liu, G.; Ying, J. *Inorg. Chem. Commun*. **2016**, 68, 50-55.

9. Xing, R.; Wang, F.; Dong, L.; Zheng, A. P.; Wang, L.; Su, W. J.; Lin, T.; *Food Chem*. **2016**, 197, 205-211.

10. Rezvani, M. A.; Shaterian, M.; Akbarzadeh, F.; Khandan, S. *Chem. Eng. J*. **2018**, 333, 537-544.

11. Liu, S.; Chen, L.; Wang, G.; Liu, J.; Gao, Y.; Li, C.; Shan, H. *J. Energy Chem*. **2016**, 25, 85-92.

12. Pathan, S.; Patel, A. *Catal. Sci. Technol*. **2014**, 4, 648-656.

13. Bagley, M. J.; Nicholls, D.; Warburton, B. A. *J. Chem. Soc. A*, **1970**, 2694-2697.

14. Xing, Y. H.; Han, J.; Zhang, B, L.; Zhang, X, J.; Zhang, Y. H.; Zhou, G. H. *Acta Crystallogr. Sect. E Struct. Rep. Online* **2006**, 62, m3354-m3356.

15. Reimann, C. W.; Mighell, A. D.; Mauer, F. A. Acta Cryst. **1967**, 23, 135-140.

16. Brown, I. D.; Altermatt, D. *Acta Crystallogr*. **1985**, B41, 244-247.

17. Ghalebi, H. R.; Aber, S.; Karimi, A. *J. Mol. Catal. A: Chem*. **2016**, 415, 96-103.

18. Tahar, A.; Benadji, S.; Mazari, T.; Dermeche, L.; Roch, C. M.; Rabia, C. *Catal. Lett*. **2015**, 145, 569-575.

19. Qi, M.; Yu, K.; Su, Z.; Wang, C.; Wang, C.; Zhou, B.; Zhu, C. *Inorg. Chim. Acta* **2013**, 400, 59-66.

CHAPTER V

Removal of cationic dyes from water using APM

Summary

Micro-sized spherical ammonium phosphomolybdate (APM) particles were synthesized under ambient conditions. The composition and morphology of APM was established by powder X-ray diffraction, energy dispersive X-ray analysis, fourier transform infrared spectroscopy, thermogravimetric analysis and scanning electron microscopy. Further, the ability of APM particles to remove dye from dye-contaminated water was monitored with respect to nature of incident radiation, concentration, pH and nature of dye. APM could effectively remove cationic dyes from water as long as the pH range permitted the dye to retain its cationic behavior. The results suggested that the removal of dye-stuffs could be attributed to ion-exchange between ammonium ions in APM with cationic dye moieties. APM could be reused several times without affecting its efficiency. Removal efficiency of 94.6% could be retained upto 16th cycle and sensitivity to pH enabled APM to reverse the cation exchange process. The ion-exchange process was not dependent on exposure of APM particles to irradiation which confirmed that the mode of action of APM was not photocatalytic in nature.

V.1. Introduction

Rapid industrialization and increase in population density has resulted in severe contamination of water resources [1]. In particular, water pollution caused by dyes has become a serious threat due to its high toxicity and stability to resist degradation even under extreme conditions [2,3]. Extensive research over the past decades has resulted in various dye removal techniques that depend on physical, chemical and biological processes [4-8]. Among these, the techniques that rely on adsorption of dyes have a major advantage over other techniques that rely on degradation of dyes because potentially hazardous secondary metabolites can also be generated during degradation of dyes [9]. Conventionally adsorbents such as activated carbon [10], bio-waste [11], zeolites [12] and clay materials [13] have been used to treat dye-contaminated water but they suffer from low adsorption capacity and poor selectivity. Therefore, there has been a constant effort in developing new materials that can effectively remove dye moieties from water.

For the past few years, researchers have been involved in the synthesis of porous and functionalized phosphomolybdate (PMO) cluster based solids [14-17]. Owing to structural features such large surface area, porosity, tuneable shape and size; these solids have been explored for potential applications in areas of catalysis [18-20], electrical conductivity [21], luminescence [22-25], magnetism [26-27], non-linear optics [28] and as anti-tumour agents [29,30]. Among these, ammonium phosphomolybdate (APM), $\{NH_4\}_3[PMo_{12}O_{40}].xH_2O$ is a versatile PMO cluster based solid which was first synthesized by Berzelius in 1826 [31]. Although it has been used as electrode material, catalyst and adsorbent [32-34]; the ion-exchange behavior of APM for the removal of dye-stuffs from water has not been reported so far. However, in literature there are few
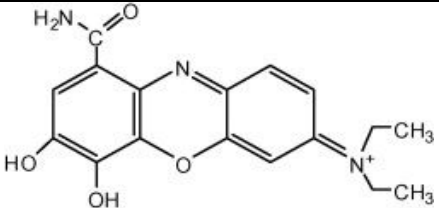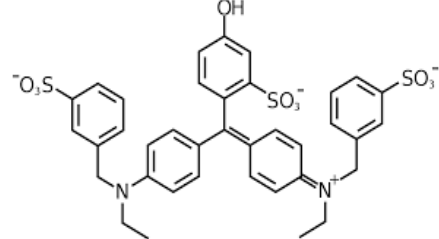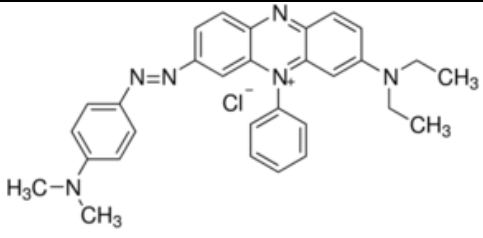
examples wherein it has been reported as a photocatalyst for the degradation of selected dye stuffs (Table V.1). It was reported that degradation was brought about by the photo excitation of the metal oxides, followed by the formation of electron–hole pair on its surface. The reactive intermediate which was responsible for the degradation of dye was hydroxyl radical (OH$^{\bullet}$). It was either formed by the decomposition of water or by the reaction of hole with OH$^-$ (available in form of base that is added to the reaction medium). Subsequently, the hydroxyl radical resulted in partial or complete degradation of dyes.

$$APM + hv \rightarrow APM\ (e^-_{cb} + h^+_{vb}) \ldots 1$$

$$h^+_{vb} + H_2O \rightarrow H^+ + OH^{\bullet} \ldots 2$$

$$h^+_{vb} + OH^- \rightarrow OH^{\bullet} \ldots 3$$

$$OH^{\bullet} + Dye \rightarrow Degradation\ of\ the\ dye \ldots 4$$
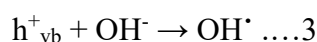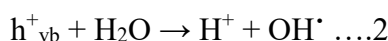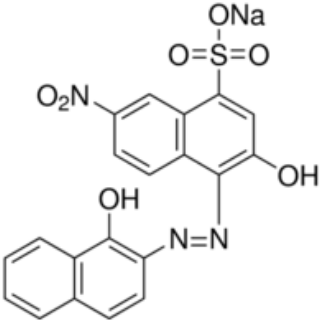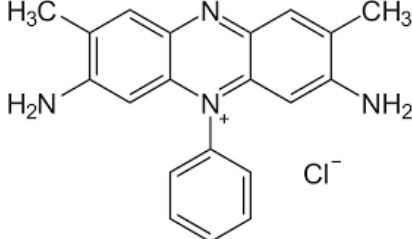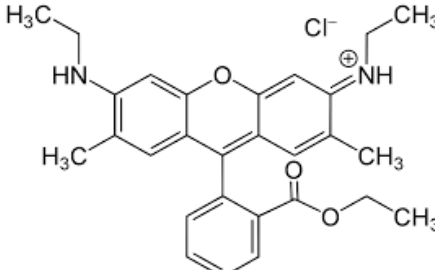
The mechanism for degradation of dyes and the results obtained have been summarized in Table V.1. Most of the results reported in literature with APM suggested that photo excitation of APM followed by absorption of OH$^{\bullet}$ radical in holes was responsible for the degradation of dyes (referred to as Mechanism **V.1** in Table V.1).

Based on the above considerations, in this chapter four dyes *viz.* Methylene Blue, Eosin Y, Malachite Green and Methyl Red were selected and their solution was treated with APM. The decolorization of dye-stuffs was recorded with respect to the change in intensity of absorption peaks using UV-Visible spectroscopy. Effect of variables such as nature, concentration and pH of dye-stuffs was further investigated and a plausible mechanism for the action of APM on dye-stuffs has been proposed.

Table V.1. Table summarizing the results obtained using APM for degradation of dye-stuffs.

Sl. No.	Dye	Structure	Nature of dye	Mechanism for degradation	Time taken for complete degradation	Reference
1.	Celestine blue B		Cationic dye	Photo excitation of the APM followed by absorption of OH radical in holes. Maximum degradation was observed in basic medium	97.7 % degradation in 4 hours	35
2.	Fast Green		Behaves as anionic dye above pH-6	The rate of photocatalytic bleaching of dye increases with increases in pH till 6.0 according to Mechanism **V.1**. Above pH 6 the anionic dye will face a force of repulsion from negatively charged surface of the dye which prevents the degradation	Not reported	36
3.	Janus Green B		Basic azo and cationic dye	The rate of photocatalytic degradation of Janus Green B increases with increase in pH (upto pH = 11) according to Mechanism **V.1**. Above pH 11, the approach of electron rich dye to the semiconductor surface is retarded which resulted in a decrease in the rate of photocatalytic degradation of dye	Color removal of 97.9% was achieved in 4 hours	37

4.	Eriochrome Black-T		Azodye	Under acidic conditions, dye was not degraded but in the basic range, the dye solution was degraded according to Mechanism **V.1**. The rate of photocatalytic degradation increases with increase in pH (upto pH = 11) Above pH 11, a decrease in the rate of photocatalytic degradation of dye was observed	Maximum degradation of 93.9 % was achieved after irradiation time of 5 hours	38
5	Safranin O dye		Heterocyclic azine dye	The degredation of safranin O on irradiation with visible light follow pseudo first order kinetics	96.8% of safranine O dye was degraded with the addition of 4g/L of APM	39
6	Rhodamine-6G		Cationic dye	Upto pH 9.0, the rate of photodegradation of dye increases with increase in pH (Mechanism **V.1**). However, above pH 9.0, decrease in the rate of photodegradation was observed	Not reported	40

V.2. Experimental Section

V.2.1. Synthesis of APM

All reagents were of reagent grade and were used as received from commercial sources without further purification. Initially, two solutions were prepared. Solution A was prepared by mixing 11.05 g of ammonium heptamolybdate, $(NH_4)_6Mo_7O_{24}.4H_2O$ with 15 ml of ammonia solution and 10 ml of distilled water. The solution was boiled and made upto 250 ml. Secondly, 40 ml of 0.067 M solution of $Na_2HPO_4 \cdot 12H_2O$ (disodium hydrogen phosphate dodecahydrate) was mixed with 20 ml of conc. HNO_3 and was labelled as solution B. Subsequently 100 ml of Solution A was added to Solution B and stirred for 10 minutes. The resultant solution was kept undisturbed for 18 hours and the precipitate formed was allowed to settle down. Finally, it was filtered and the canary yellow precipitate of APM thus obtained was washed with water and air-dried.

V.2.2. Synthesis of dye solutions

10^{-4} M stock solutions of Methylene Blue (MB), Eosin Y (EY), Malachite Green (MG) and Methyl Red (MR) were prepared by dissolving definite amount of dye in distilled water. The stock solutions were further diluted to 10^{-5} M for the present study.

V.2.3. Treatment of dye-contaminated water

MB, EY, MG and MR show absorbance peak between 650-700 nm, 500-550 nm, 600-650 nm and 500-550 nm respectively [41-44]. Initially, 25 ml of 10^{-5} M MB solution was taken and its pH was adjusted to 5.0±0.1 using 1M HCl. Subsequently, 0.125 g of APM was added

to it and the mixture was kept under stirring for 5 minutes. Thereafter, it was left undisturbed for 1 hour. Finally, the MB solution was centrifuged and the filtrate was analyzed using UV-Visible spectroscopy. The absence of absorbance peak at $\lambda_{max} = 660$ nm indicated that MB had been removed from the solution. Based on the result obtained (discussed later), the effect of various factors such as contact time, pH, nature of dye and amount of APM was further investigated.

The removal of dye-stuffs was monitored with respect to change in the intensity of the absorbance peaks using UV-Visible spectroscopy (Shimadzu UV-Visible 1800 double beam spectrophotometer).

The dye removal efficiency of APM was calculated by

Removal efficiency (%) = $\dfrac{(C_i - C_f)}{C_i} \times 100$

where, C_i and C_f concentration of dye before and after the treatment with APM [45].

V.3. Characterization

Fourier transform infrared (FTIR) spectrum was recorded on KBr pellets using Shimadzu FTIR spectrophotometer (model: IR Affinity). Before recording the FTIR spectrum, the sample was heated at 120°C for 1 hour. Thermogravimetric analysis (TGA) was done on Perkin-Elmer TGA7 from room temperature to 700ºC at a heating rate of 10ºC/min in nitrogen atmosphere to determine water content and overall thermal stability of the product. Scanning electron microscopic studies (SEM) were carried out on as-synthesized APM powder mounted on carbon tape using FEI FESEM Quanta 200 at an accelerating voltage of 10 kV. Powder X-ray diffraction (PXRD) data was collected on a Malvern Panalytical Aeris

diffractometer using Ni-filtered Cu Kα radiation. Data was collected with a step size of 0.02° and count time of 2 s per step over the range $5° < 2\theta < 60°$. Nitrogen adsorption and desorption (BELSORP-mini II machine, BEL Japan Inc., Japan) was employed to characterize and measure the pore volume. Before the nitrogen adsorption-desorption measurement, the sample was thoroughly dried at 150°C under vacuum for two hours.

V.4. Results and discussion

V.4.1. Characterization of APM particles

The PXRD pattern of APM particles was found to match well with JCPDS file no. 43-0315 indicating the formation of single-phasic cubic $\{NH_4\}_3[PMo_{12}O_{40}].xH_2O$ having lattice constant $a = 11.67$ Å (Figure V.1a). FTIR spectrum showed the presence of bands in the region 1100-700 cm^{-1} which are characteristic of Keggin type heteropoly anions [46]. The spectrum also showed four FTIR bands at 1067, 964, 869 and 788 cm^{-1} that could be attributed to P-O and Mo-O stretching respectively. Bands at 3212 and 1606 cm^{-1} were assigned as N-H stretching and N-H bending respectively due to the absorption of NH_4^+ ions [47].

The morphology and dimension of APM particles was characterized by SEM. SEM image of APM showed the formation of agglomerated particles having plane faces with diameter 4.5-9 μm (Figure V.1b). Figure V.1c shows the TGA thermogram obtained by heating as-synthesized APM, $\{NH_4\}_3[PMo_{12}O_{40}].xH_2O$ at 10°C/min from room temperature to 700°C. Two weight loss steps were observed. The initial weight loss of ~5.4% upto 120°C could be attributed to the dehydration of the as-synthesized APM, $\{NH_4\}_3[PMo_{12}O_{40}].xH_2O$ wherein

x was found to be 6. The value was in good agreement with theoretical value (5.44%) for weight loss corresponding to six molecules of water of crystallization.

$$\{NH_4\}_3[PMo_{12}O_{40}].6H_2O \rightarrow \{NH_4\}_3[PMo_{12}O_{40}] + 6H_2O ... (5)$$

The second weight loss of ~4.1% between 120-500°C indicated the decomposition of the Keggin anion and the evolution of constitutional water together with ammonia gas according to

$$\{NH_4\}_3[PMo_{12}O_{40}] \rightarrow 3NH_3 + 3/2\ H_2O + \frac{1}{2}\ P_2O_5 + 12\ MoO_3 ... (6)$$
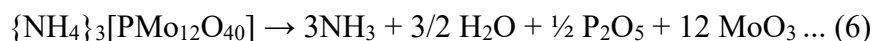
The second weight loss (4.1%) was also found to be in good agreement with the theoretical value (4.15%) and the values reported earlier in literature [48-49].
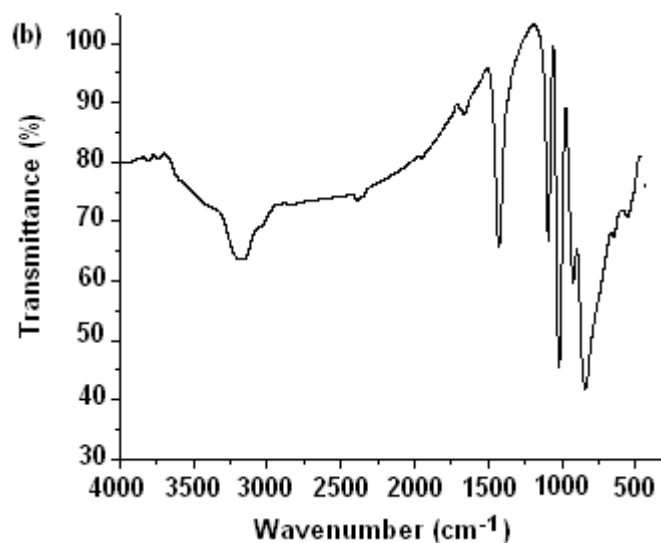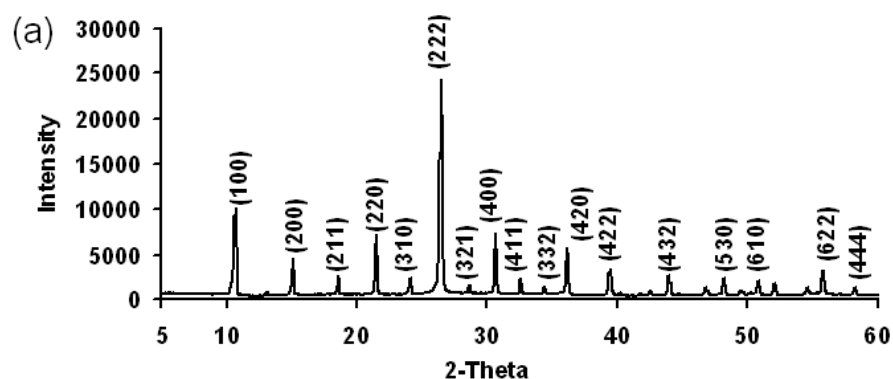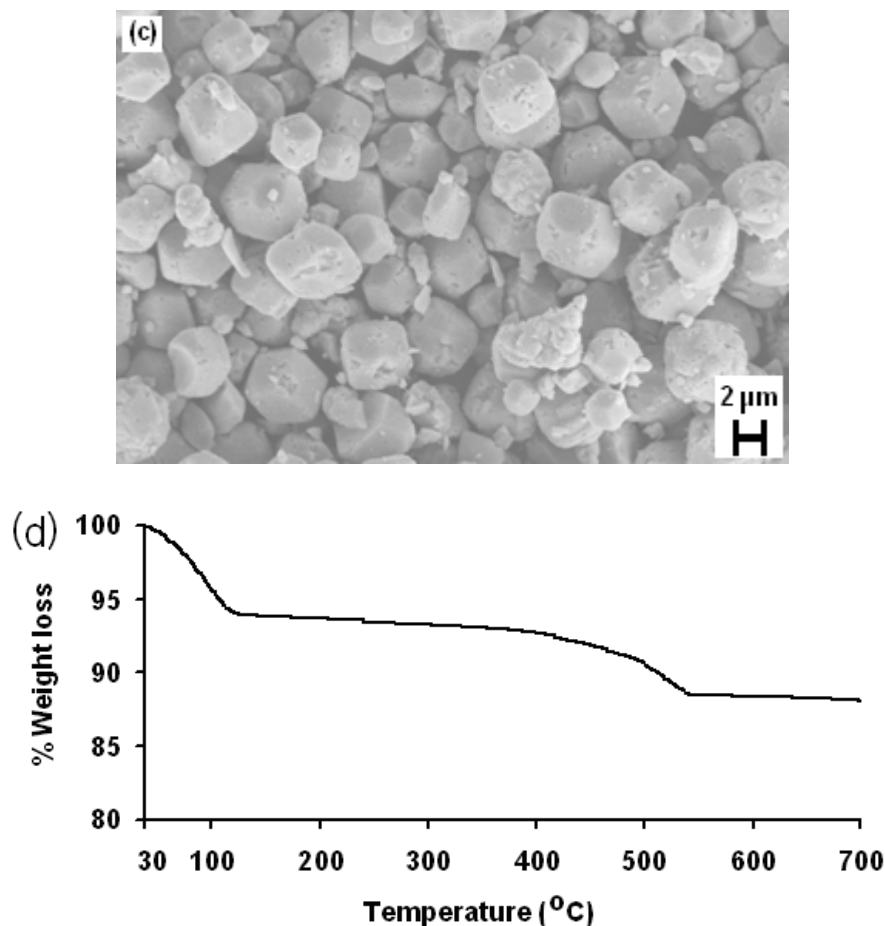
Figure V.1. (a) Indexed PXRD pattern (b) FTIR spectrum (c) SEM image and (d) TGA curve of as-synthesized APM particles.

V.4.2. Treatment of dye contaminated water

V.4.2.1. Effect of nature of light

Initially, 25 ml of 10^{-5} M Methylene Blue (MB) dye solution having pH = 5.0±0.1 was taken in three beakers. 0.125 g of APM was added to each of the beakers; the solutions were stirred for 5 minutes and kept undisturbed for 1 hour under the following conditions:

I) The first beaker was kept in dark.

II) The second beaker was kept in sunlight.

III) The third beaker was kept under UV light.

The above solutions were centrifuged after 1 hour and filtered. The filtrate was analyzed using UV-Visible spectroscopy. The absence of absorbance peak at λ_{max} = 660 nm indicated that MB had been removed from each of the beakers (Figure V.2, also refer Table V.2). The maximum dye removal efficiency of APM was found to be 94.6%. It was also observed that the colour of APM collected from beakers kept in dark, sunlight and UV light had changed from yellow to green after treatment with MB solution. A comparison of PXRD pattern of APM before and after treatment with MB solution confirmed that there were no structural changes in APM upon treatment with MB (Figure V.3). The above experiment also indicated that the mode of action of APM was not photocatalytic in nature.

Table V.2. Absorbance of MB solution upon treatment with APM at 660 nm after 1 hour of irradiation under different conditions.

Bottle	Type of irradiation	Absorbance
A	Initial MB solution	0.65
B	Dark	0.042
C	Sunlight	0.041
D	UV light	0.041
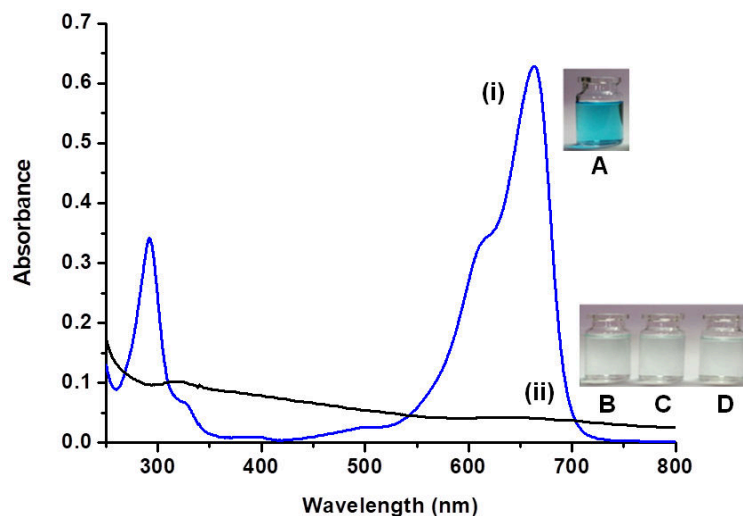
Figure V.2. Figure showing UV-Vis spectra of (i) original solution of Methylene Blue (MB) having pH = 5.0±0.1 and (ii) MB solution obtained after treatment with APM followed by exposure to dark, sun light and UV for 1 hour. Figures in the inset represent the original solution of MB (Bottle A) and filtrate of Bottle A obtained after treatment with APM followed by exposure to dark, sun light or UV for 1 hour (Bottle B-D) respectively.
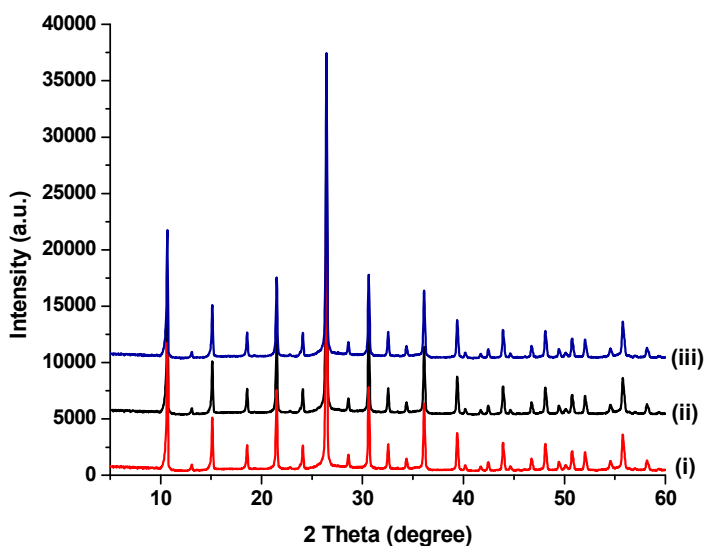
Figure V.3. Figure showing PXRD of APM collected from (i) Bottle B (ii) Bottle C and (iii) Bottle D.

V.4.2.2. Effect of contact time

25 ml of 10^{-5} M MB dye solution having pH = 5.0±0.1 was taken in five beakers. 0.125 g of APM was added to each of the beakers and the solutions were stirred for 5 minutes. The solutions were left undisturbed and centrifuged after different time intervals (0, 15, 30, 45 and 60 minutes). Subsequently, the filtrate from each beaker was monitored using UV-Visible spectroscopy Figure V.4. From Figure V.4 it is evident that the removal of MB (removal efficiency = 94.6%) takes place instantaneously i.e. as soon as the dye comes in contact with APM (also refer Table V.3).
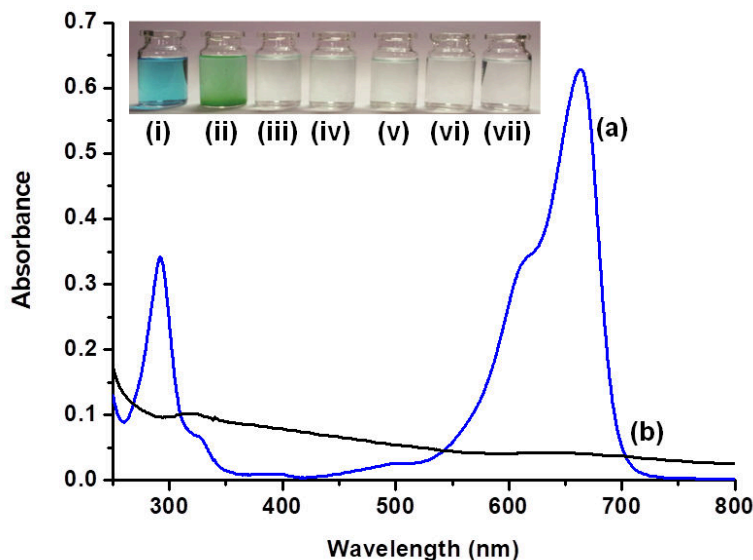
Figure V.4. Figure in the inset shows the results obtained for time bound decolourization of MB (pH = 5.0±0.1).

(i) Original dye solution

(ii) Dye solution immediately after adding APM.

(iii) - (vii) Filtrate collected after 0, 15, 30, 45 and 60 minutes respectively.

(a) and (b) Represent the corresponding UV-Visible spectra of original MB solution i.e. Bottle (i) and filtrate of Bottles (iii-vii) respectively.

Table V.3. Absorbance of MB solution upon treatment with APM at 660 nm upon varying time of contact.

Bottle	Time of contact (minutes)	Absorbance
(i)	Not applicable	0.650
(iii)	0	0.041
(iv)	15	0.040
(v)	30	0.042
(vi)	45	0.041
(vii)	60	0.040

V.4.2.3. Effect of amount of APM

25 ml of 10^{-5} M MB dye solution having pH = 5.0±0.1 was taken in five beakers and a definite amount of APM was added to each of the beakers. The solutions were stirred for 5 minutes and centrifuged. From UV- Visible spectroscopy (Figure V.5) it was evident that the maximum removal efficiency (i.e. 94.6%) was obtained within 5 minutes of stirring when 25 ml of 10^{-5} M MB dye solution was treated with 0.125 g of APM.
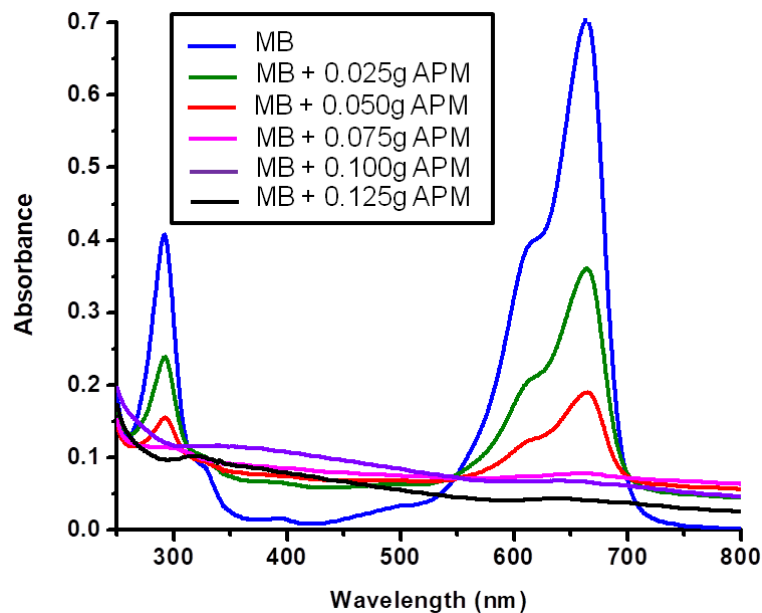
Figure V.5. Figure showing the decrease in intensity of absorbance peak of MB solution (λ_{max} = 660 nm) upon increasing the amount of APM.

V.4.2.4. Effect of nature of dye

In order to investigate the nature of dye, four different dyes *viz*. MB, EY, MG and MR were selected. 25 ml of 10^{-5} M solution of each dye (having pH = 5.0±0.1) was treated with 0.125 g of APM. The solutions were stirred for 5 minutes and centrifuged. In all the cases, the filtrate was analyzed using UV-Visible spectroscopy. The spectra indicated that MB, MR and MG had been removed from dye-contaminated water upon treatment with APM. The absence of absorbance peak between 650-700 nm, 500-550 nm and 600-650 nm respectively confirmed the removal of dye-stuffs from water (Figure V.6). However, in the case of EY there was no significant change in the absorbance peak before and after treatment with APM. The result suggested that APM was effective only for the removal of cationic dyes from water.
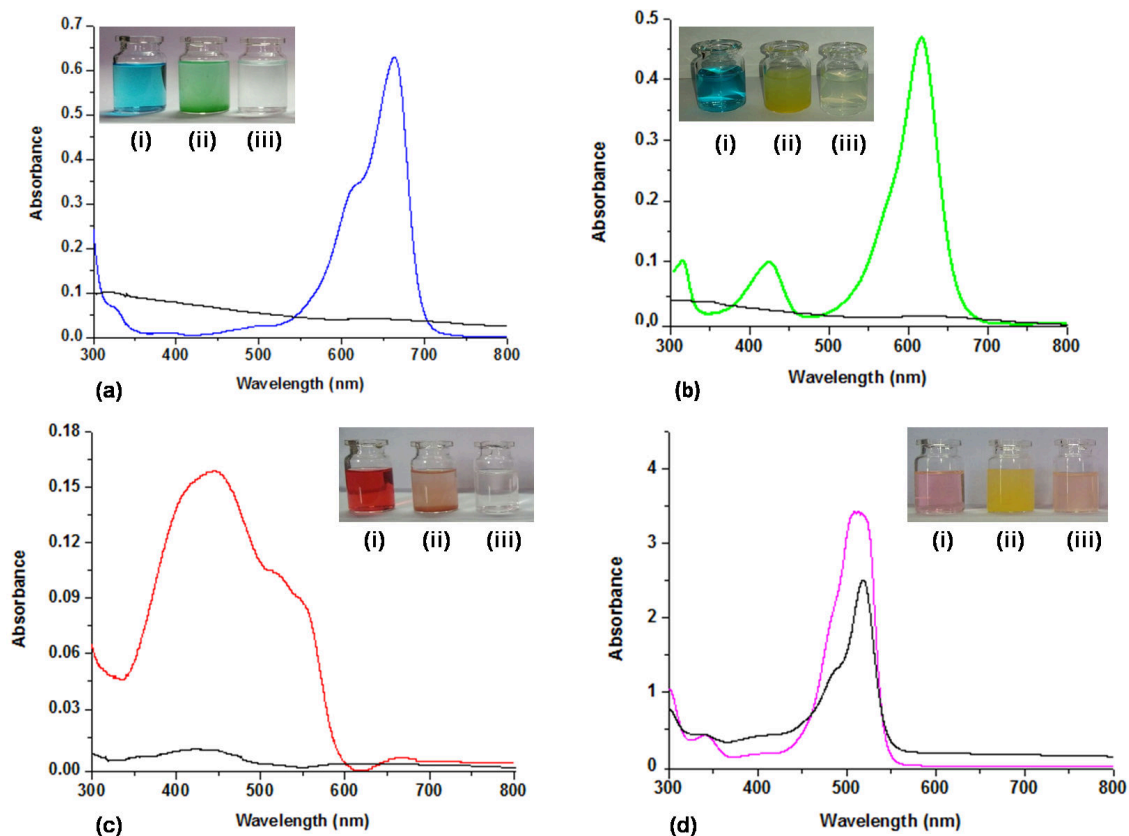
Figure V.6. UV-Visible spectra of 25 ml of 10^{-5} M dye solution having pH = 5.0±0.1 of (a) MB (b) MG (c) MR and (d) EY before (coloured curve) and after (black curve) treatment with 0.125 g of APM. Figure in the inset shows (i) original dye solution (ii) dye solution immediately after adding 0.125 g of APM (iii) filtrate of Bottle ii immediately after 5 minutes of stirring.

V.4.2.5. Influence of pH

25 ml each of 10^{-5} M MR, MG and MB solution was taken and its pH was adjusted between 1.0±0.1 to 6±0.1 using 1M HCl. The resultant dye solutions were treated with 0.125 g of APM. The investigations revealed that APM could effectively remove MB and MG from dye-contaminated water in the pH range 1-6. This could be attributed to the catioinic nature of MB and MG in the pH rage 1-6 (refer Figure V.7a and 7b). However, APM could not remove MR from solution at pH above 5 (refer Figure V.7c). A preview of literature suggested that MR exists as anionic dye at pH above 5 [42]. A similar result was obtained in the case of EY. EY exists either as a neutral or an anionic dye in the pH range 1-6 [43]. Therefore, there was no significant change in its absorbance peak before and after treatment with APM. The results suggested that perhaps ion-exchange of ammonium ions in APM with cationic dye moieties is responsible for the removal of dye-stuffs.

V.4.2.6. Reusability of APM

The reusability of APM for the removal of MB was analyzed for 20 cycles using 25 ml of 10^{-5} M dye solution having pH = 5.0±0.1. In the first cycle, 0.125 g of APM was added to MB solution, stirred for 5 minutes and centrifuged. APM thus obtained was air-dried and subsequently treated with 25 ml of 10^{-5} M dye solution having pH = 5.0±0.1 and this process was repeated for 20 cycles. The removal of MB was observed upto 16th cycles (Table V.4) wherein 94.6% removal efficiency was achieved. However, the contact time required to remove MB from dye-contaminated water increased with subsequent number of cycles. While only 5 minutes of stirring was required upto 4th cycle, 10 minutes of stirring was

required upto 8ᵗʰ cycle to achieve the removal efficiency of 94.6%. Therefore, the time of stirring was gradually increased 5 minutes per four cycles.
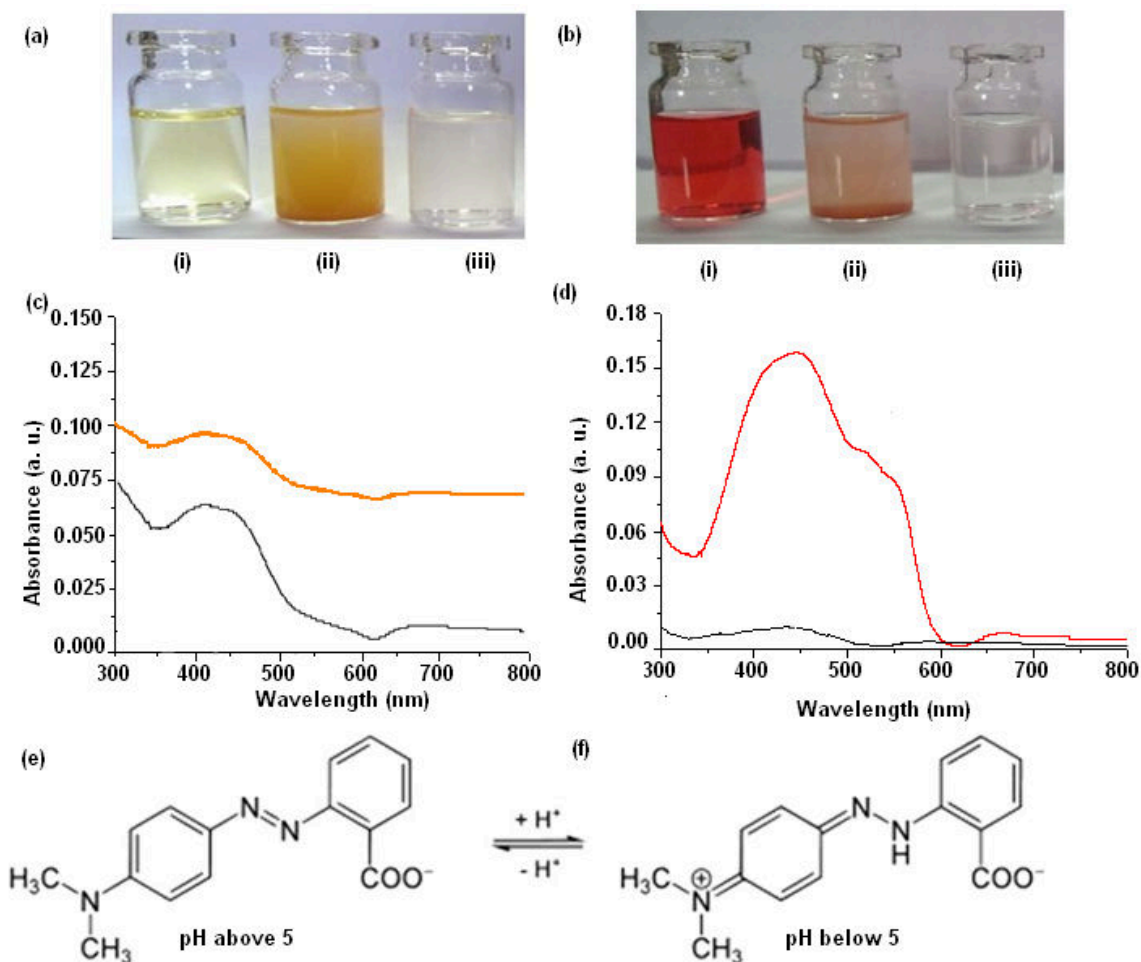
Figure V.7. (a) and (b) Dye solutions of MR at pH above and below 5 respectively with (i) original dye solution (ii) dye solution immediately after adding 0.125 g of APM (iii) filtrate of bottle (ii) immediately after 5 minutes of stirring. (c) and (d) UV-Visible spectra of dye solutions (i) and (iii) of MR shown in Figure 7a and 7b respectively. (e) and (f) Structure of MR at pH above and below 5 respectively.

Table V.4. Absorbance of MB solution upon treatment with APM at 660 nm after each cycle.

Number of cycles	Absorbance
Upto 16	0.041
17th	0.152
18th	0.343
19th	0.480
20th	0.650

V.4.2.7. Adsorption capacity of APM

The adsorption/desorption isotherm of APM, resembles that of Brunauer's Type I isotherm, that is the characteristic for microporous adsorbents (Figure V.8) [50]. The microporosity was confirmed from the mean pore diameter of 1.8158 nm obtained from Brunauer–Emmett-Teller (BET) plot. Further, the total pore volume of APM was estimated to confirm whether dye moieties could be adsorbed in the micro pores of APM. It was observed that pore volume had reduced from 8.013×10^{-2} to 3.0306×10^{-2} cm^3/g after APM had been treated with MB solutions for 16 cycles. The decrease in total pore volume confirmed the presence of MB moieties in the micropores of APM (refer Table V.5 for textural parameters of APM before and after the treatment of dye-stuffs).

Table V.5. Textural parameters of APM before (I) and after (II) the treatment of dye-stuffs.

Sl. No.	Textural parameter	I	II
1	Total pore volume (p/p^o=0.990) [cm^3/g]	8.0131 x 10^{-2}	3.0306 x 10^{-2}
2	Surface area (BET) [m^2/g]	1.7652 x 10^2	44.512
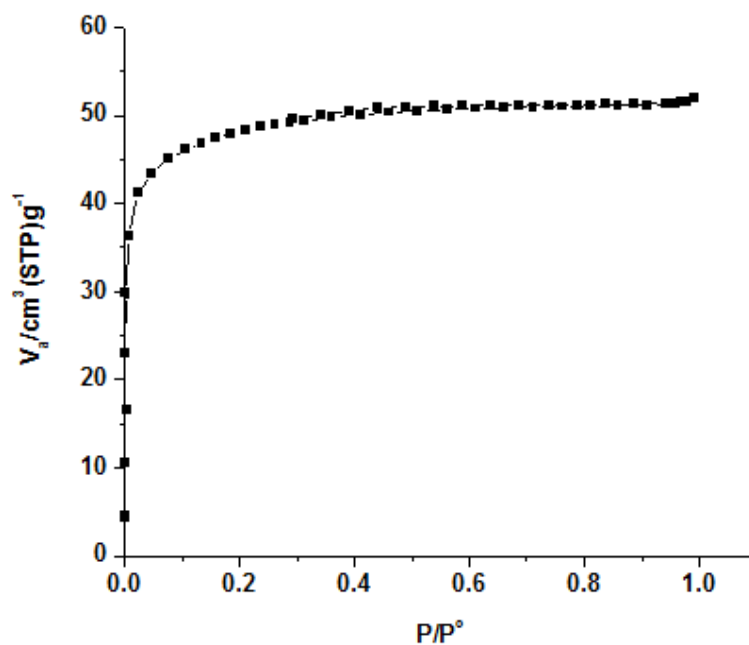
Figure V.8. The adsorption/desorption isotherm of APM which resembles that of Brunauer's Type I isotherm.

V.4.2.8. Mechanism

Based on the above observations it was evident that the presence of NH_4^+ ions in APM facilitates ion-exchange between NH_4^+ ions and cationic dye moieties. A preview of literature suggests that APM is an excellent adsorbent and it can adsorb metal ions such as Cs^+, K^+, Na^+, Sn^{2+}, Bi^{3+} etc. via ion-exchange between NH_4^+ ions and metal ions [51-53].

Therefore, a similar mechanism has been proposed herein. The removal of cationic dye-stuffs may be visualized as an ion-exchange process between NH_4^+ ions and cationic dye moieties (Figure V.9). It was confirmed by comparing the PXRD pattern of APM obtained after 16 cycles of treatment with MB with as-synthesized APM. A comparison of PXRD pattern indicated that APM maintains the cubic phase during the ion-exchange process between NH_4^+ ions and cationic dye moieties (Figure V.10). Further, sensitivity to pH enabled APM to reverse the cation exchange process.
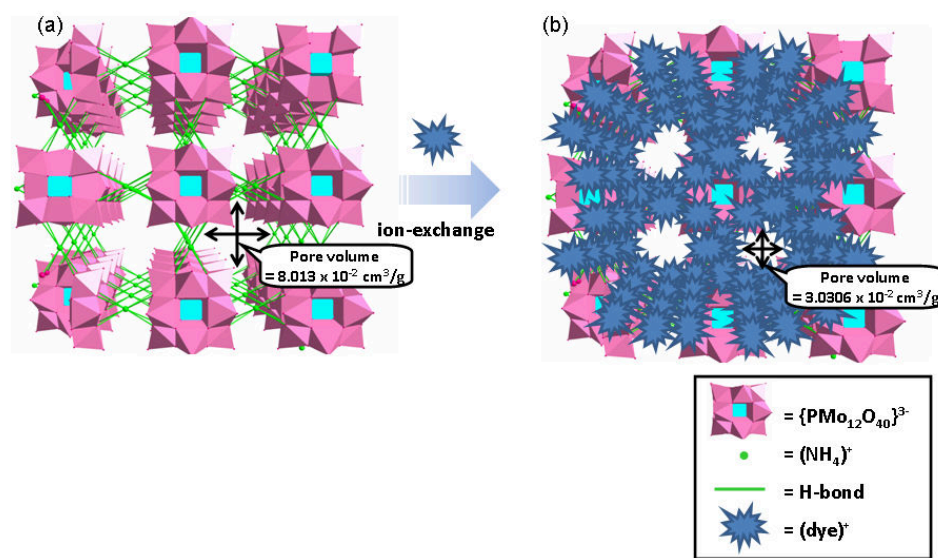
Figure V.9. (a) Crystal structure of APM. The lattice water molecules have been omitted for clarity. (b) Ion-exchange between NH_4^+ ions and cationic dye moieties.
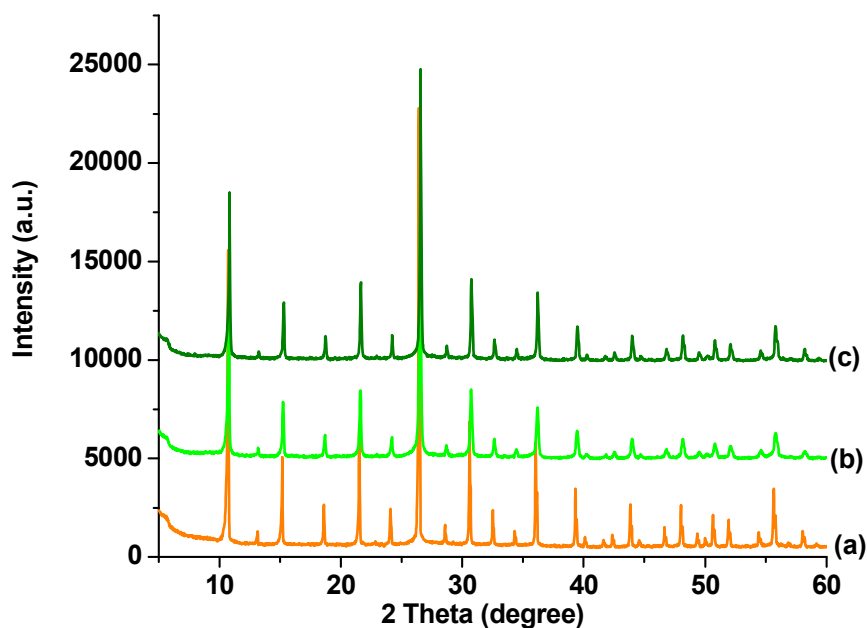
Figure V.10. Figure showing the PXRD pattern of (a) as-synthesized APM (b) APM obtained after 1st cycle of treatment with MB solution (c) APM obtained after 16th cycle of treatment with MB solution.

APM is stable only in acidic medium (pH ≤ 6) [14]. At pH > 6, it disintegrates into its soluble molecular precursors i.e. NH_4^+, $\{PO_4\}^{3-}$ and $\{Mo_xO_y\}^{z-}$ ions [54]. Therefore, the present investigation was carried out at pH ≤ 6. At pH = 1–6, cationic dyes readily replace NH_4^+ ions in APM to form $\{Dye\}_3[PMo_{12}O_{40}]$. Interestingly, the ion-exchanged dye moieties could be regenerated in solution when APM was treated with 10 ml of 1 M NH_4Cl and 0.5 ml of NH_3 (Figure V. 10). However, the addition of NH_4Cl/NH_3 solution increased the pH of the medium (pH > 7) and two outcomes are observed.

(a) In the case of MR, at pH > 7 a clear yellow solution (**V**, refer Figure V.11a) was observed due to disintegration of APM and change in color of MR into yellow. Upon adjusting the pH of the solution **V** using 1 M HCl i.e. at pH = 5–6, APM and MR could be regenerated and separated by centrifugation and filtration.

166

(b) In the case of MB and MG, at pH > 7 {Dye}$_3$[PMo$_{12}$O$_{40}$] disintegrates into its soluble molecular precursors i.e. Dye, {PO$_4$}$^{3-}$ and {Mo$_x$O$_y$}$^{z-}$ moieties resulting in a clear blue solution **V** (refer Figure V.11b). However, upon addition of 1 M HCl, pH of the solution was adjusted between 1 and 6 wherein APM and dye could be regenerated as {Dye}$_3$[PMo$_{12}$O$_{40}$] i.e. residue **IV**.
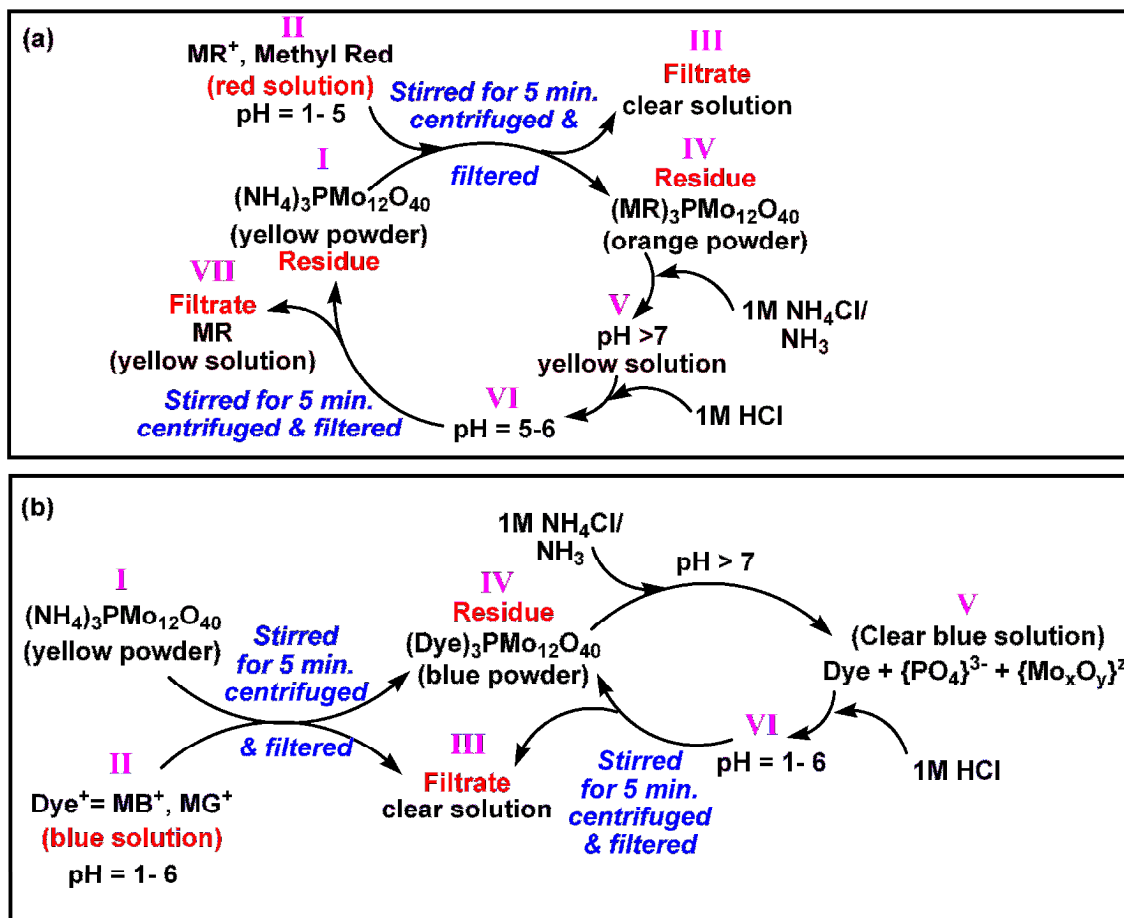
Figure V.11. Release of ion-exchanged dye moieties in solution upon treatment with 1M NH$_4$Cl and NH$_3$ solution. (a) Ion-exchange mechanism for MR. (b) Ion-exchange mechanism for MB and MG.

V.5. Conclusions

Micro-sized ammonium phosphomolybdate, $\{NH_4\}_3[PMo_{12}O_{40}].6H_2O$ particles were synthesized under ambient conditions and characterized. APM was found to be an effective medium for the removal of cationic dyes in acidic medium. While Methylene Blue and Malachite Green could be eliminated from dye-contaminated water in the pH range 1-6; Methyl Red could be removed only in the pH range 1-5. Dye removal efficiency as high as 94.6% was achieved upon treating 10^{-5} M MB solution (pH = 5.0±0.1) with APM. APM could be successfully re-used upto 16 cycles. The removal of dye-stuffs from contaminated water could be attributed to ion-exchange between ammonium ions in APM with cationic dye moieties. The ion-exchange process was found to be reversible which enabled APM and dye moieties to be regenerated in solution.

References

1. Parker, A. *Nature* **1932**, 130, 761-763.

2. Huang, Z.; Li, Y.; Chen, W.; Shi, J.; Zhang, N.; Wang, X.; Li, Z.; Gao, L.; Zhang, Y. *Mater. Chem. Phys.* **2017**, 202, 266-276.

3. Malarvizhi, R.; Ho, Y. S. *Desalination* **2010**, 264, 97-101.

4. Katheresan, V.; Kansedo, J.; Lau, S. Y. *J. Environ. Chem. Eng*. **2016**, 6, 4676-4697.

5. Tian, X.; Hou, L.; Wang, J.; Xin, X.; Zhang, H.; Ma, Y.; Wang, Y.; Zhang, Li.; Han, Z. *Dalton Trans*. **2018**, 47, 15121-15130.

6. Ali, I.; Peng, C.; Naz, I.; Lin, D.; Saroj, D. P.; Ali, M. *RSC Adv*. **2019**, 9, 3625-3646.

7. Khan, M. I.; Akhtar, S.; Zafar, S.; Shaheen, A.; Khan, M. A.; Luque, R.; Rehman, A. *Materials* **2015**, 8, 4147-4161.

8. Ahmad, A.; Setaper, S. H. M.; Chuo, S. C.; Khatoon, A.; Wani, W. A.; Kumar, R.; Rafatullah, M. *RSC Adv*. **2015**, 5, 30801-30818.

9. Erdemoglu, S.; Aksu, S. K.; Sayilkan, F.; Izgi, B.; Asilturk, M.; Sayilkan, H.; Frimmel, F.; Gucer, S. *J. Hazard. Mater*. **2008**, 155, 469-476.

10. Liu, L.; Lin, Y.; Liu, Y.; Zhu, H.; He, Q. *J. Chem. Eng. Data* **2013**, 58, 2248-2253.

11. Gupta, V. K.; Mittal, A.; Gajbe, V.; Mittal, J. *Ind. Eng. Chem. Res*. **2006**, 45, 1446-1453.

12. Wang, S.; Li, H.; Xu, L. *J. Colloid Interface Sci.* **2006**, 295, 71-78.

13. Kausar, A.; Iqbal, M.; Javed, A.; Aftab, K.; Nazli, Z.; Bhatti, H. N.; Noureen, S. *J. Mol. Liq*. **2018**, 256, 395-407.

14. Thomas, J.; Ramanan, *A. Cryst. Growth Des*. **2008**, 8, 3390-3400.

15. Thomas, J.; Ramanan, A. *Inorg. Chim. Acta* **2011**, 372, 243-249.

16. Thomas, J.; Kumar, D.; Ramanan, A. *Inorg. Chim. Acta* **2013**, 396, 126-135.

17. J. Thomas, Ph.D. Thesis, Indian Institute of Technology Delhi, India, **2010**.

18. Pathan, S.; Patel, A. *Catal. Sci. Technol*. **2014**, 4 648-656.

19. Wang, X.; Wang, J.; Geng, Z.; Qian, Z.; Han, Z. *Dalton Trans*. **2017**, 46, 7917-7925.

20. Gong, K.; Liu, Y.; Han, Z. *RSC Adv*. **2015**, 5, 47004-47009.

21. Ai, L.; Wang, Z.; He, F.; Wu, Q. *RSC Adv*. **2018**, 8, 34116-34120.

22. Pinto, T. V.; Fernandes, D. M.; Pereira, C.; Guedes, A.; Blanco, G.; Pintado, J. M.; Pereira, M. F. R.; Freire, C. *Dalton Trans*. **2015**, 44, 4582-4593.

23. Wang, J.; Shi, W.; Li, S.; Mao, Q.; Ma, P.; Niu, J. *Dalton Trans*. **2018**, 47, 7949-7955.

24. Sun, P.; Zhang, S.; Xiang, Z.; Zhao, T.; Sun, D.; Zhang, G.; Chen, M.; Guo, K.; Xin, X, *J. Coll. Inter. Sci*. **2019**, 547, 60-68.

25. Gong, Y.; Bai, F.; Yu, Z.; Bi, Y.; Xu, W.; Yu, L. *RSC Adv*. **2016**, 6, 8601-8604.

26. Clemente-Juan, J. M.; Coronado, E.; Gaita-Arino, A. *Chem. Soc. Rev*. **2012**, 41, 7464-7478.

27. Hu, G.; Dong, Y.; He, X.; Miao, H.; Zhou, S.; Xu, Y. *Inog. Chem. Commun*. **2015**, 60, 33-36.

28. Liu, C. G.; Guan, W.; Song, P.; Su, Z. M.; Yao, C.; Wang, E. B. *Inorg. Chem* **2009**, 48, 8115-8119.

29. Moll, H. E.; Zhu, W.; Oldfield, E.; Rodriguez-Albelo, L. M.; Mialane, P.; Marrot, J.; Vila, N.; Mbomekalle, I. M.; Riviere, E.; Duboc, C.; Dolbecq, A. *Inorg. Chem*. **2012**, 51, 7921-7931.

30. Qu, X.; Feng, H.; Ma, C.; Yang, Y.; Yu, X. *Inorg. Chem. Commun*. **2017**, 81, 22-26.

31. Berzelius, J. J. *Annalen der physic* **1826**, 83, 261-288.

32. Pandey, S. D.; Tripathi, P. *Electrochim. Acta* **1982**, 27, 1715-1721.

33. Basu, M.; Sarkar, S.; Pande, S.; Jana, S.; Sinha, A. K.; Sarkar, S.; Pradhan, M.; Pal, A.; Pal, T. *Chem. Commun*. **2009**, 7191-7193.

34. Gregg, S. J.; Stock, R. *Trans. Faraday Soc*. **1957**, 53, 1355-1362.

35. Sharma, S.; Sharma, M. K.; Chaturvedi, N. *Int. J. Chem. Res*. **2011**, 2, 20-22.

36. Sachdeva, D.; Parashar, B.; Bharadwaj, S.; Panjabi, P. B.; Sharma, V. K. *Int. J. Chem. Sci*. **2010**, 8, 1321-1328.

37. (a) Sharma, S.; Chaturvedi, N.; Chaturvedi, R. K.; Sharma, M. K. *J. Ind. Pollut. Control* **2010**, 26, 165-169.

    (b) Jakar, S.; Chaturvedi, R.; Sharma, M. K. *Int. J. Chem. Sci.* **2014**,12, 573-582.

38. Sharma, S.; Chaturvedi, N.; Chaturvedi, R. K.; Sharma, M. K. *Int. J. Chem. Sci*. **2010**, 8, 1580-1590.

39. Sharma, S.; Chaturvedi, N.; Chaturvedi, R. K.; Sharma, M. K. *Pollut. Res*. **2011**, 30, 165-168.

40. Bansal, A.; Sharma, D.; Ameta, R.; Sharma, H. S. *Int. J. Chem. Sci*. **2010**, 8, 2747-2755.

41. Joshi, A.; Vaidhya, S.; Singh, M. *J. Chem. Sci*. **2019**, 131, 1-7.

42. Ayed, L.; Mahdhi, A.; Cheref, A.; Bakhrouf, A. *Desalination* **2011**, 274, 272-277.

43. Sharma, N.; Jha, R.; Baghel, S.; Sharma, D. *J. Alloy. Comp*. **2017**, 695, 270-279.

44. Chauhan, N.; Singh, V.; Kumar, S.; Kumari, M.; Sirohi, K. *J. Mol. Struct*. **2019**, 1185, 219-228.

45. Abbassi, R.; Yadava, A. K.; Kumar, N.; Huanga, S.; Jaffea, P. R. *Ecol. Eng.* **2013**, 61, 366-370.

46. Qi, M.; Yu, K.; Su, Z.; Wang, C.; Wang, C.; Zhou, B.; Zhu, C. *Inorg. Chim. Acta* **2013**, 400, 59-66.

47. Tadjarodi, A.; Zad, A. I.; Imani, M. *Mater. Lett*. **2015**, 161, 464-467.

48. Ilhan, S.; Kahruman, C.; Yusufoglu, I. *J. Anal. Appl. Pyrolysis* **2007**, 78, 363-370.

49. Dermeche, L.; Thouvenot, R.; Hocine, S.; Rabia, C. *Inorg. Chim. Acta* **2009**, 362, 3896-3900.

50. Lowell S.; Shields J. E. *Adsorption isotherms. In: Powder Surface Area and Porosity*; Springer, Dordrecht **1984**, 11-13.

51. Abu-Zied, B. M.; Farrang, A. A.; Asiri, A. M. *Powder Tech*. **2013**, 246, 643-649.

52. Smit, J. V. R. *Nature* **1958**, 181, 1530-1531.

53. Park, Y.; Shin, W. S.; Choi, S. J. *Chem. Eng. J.* **2013**, 220, 204-213.

54. Alcaniz-Monge, J.; Trautwein, G.; Roman-Martinez, M. C. *Solid State Sci*. **2011**, 13, 30-37.

CHAPTER VI

Investigations using composites based on APM

Summary

In this chapter, two binary composites of ammonium phosphomolybdate (APM) with polyaniline (PAni) and poly (N-methylaniline) (PNMAni) have been synthesized and characterized. The composite of APM with poly (N-methylaniline), APM/PNMAni has not been reported in literature so far. The electrochemical behavior of APM/PAni and APM/PNMAni were investigated using cyclic voltammetry and the band gap energy was calculated using DRS data. Further, the role of these composites in the removal of hexavalent chromium from aqueous solution was explored. The removal of Cr(VI) from aqueous solution was monitored using UV-Vis spectroscopy. It was observed that APM/PNMAni exhibited enhanced ability to remove Cr(VI) as compared to APM and APM/PAni.

VI.1. Introduction

Composite materials have drawn the attention of researchers consistently, on account of their enhanced properties in comparison to its components. Keggin-type phosphomolybdates (PMOs) are a well defined sub-class of heteropolyanions with multifaceted peculiarities [1-2]. A number of polynary composites of Keggin-type PMOs have been developed recently with attractive applications as high performance sensors, supercapacitors, catalysts and electrodes [3-6]. A review of such binary composites reported in the past decade has been summarized in Table VI.1. From the table it is evident that PMo_{12} is an active composite component with polymers, reduced graphene oxide, and Bi_2O_3, exhibiting excellent properties [7-10]. It is also notable that, these composites have not been used to remove carcinogenic environmental pollutant inorganic hexavalent Cr(VI) from aqueous solutions. Only a few groups have reported the catalytic property of reduced phosphomolybdates *viz.* $\{P_4Mo_6\}$ cluster based solids in the reduction of Cr(VI) [11-13].

Ammonium phosphomolybdates (APM), $\{NH_4\}_3[PMo_{12}O_{40}].xH_2O$ is an established yellow colored cluster based solid, which is well known as a cesium ion absorber [14-15]. The synthesis, characterization and application of APM in removal of dye moieties have been described in Chapter V. In order to improve the properties of APM, it is convenient to convert it into a composite form with suitable materials. However, the binary composites containing PMOs are comparatively less studied (refer Table VI.1). Therefore, in this chapter, an attempt has been made to synthesize and characterize APM composites with two polymers *viz.* polyaniline and poly (N-methylaniline) namely, APM/PAni and APM/PNMAni respectively. The electrochemical behavior of the synthesized composites

was explored by means of three electrode system using 1 mM $K_4[Fe(CN)_6]$ in 0.1 M KCl as supporting electrolyte. Band gap energy of APM as well as the synthesized composites was calculated from UV-Vis diffused reflectance spectra applying Kubelk-a-Munk F(R) function in Tauc method [16, 17]. The optical band gap of composites was increased considerably compared to that of APM, which is significant in solar energy cells. Besides, the role of APM and its synthesized composites in the removal of hexavalent chromium from aqueous solution has also been investigated.

Table VI.1. A preview of PMo_{12} based composites reported in the past decade.

Sl. No.	Composite Composition	Synthesis (method)	Properties/ applications	Refere- nces
1	$H_3PMo_{12}O_{40}$ & Poly vinyl alcohol	Prepared by using layer-by-layer assembly technique to form the multilayer films	Visible light photochromism	[7]
2	$H_3PMo_{12}O_{40}$ & Polyaniline	By stirring solutions of aniline, APS and $H_3PMo_{12}O_{40}$ dissolved/dispersed in DDW together	As electrocatalysts for the reduction of bromates	[8]
3	$H_3PMo_{12}O_{40}$ & Reduced graphene oxide	Reduced graphene oxide was dispersed in DI water. 1% ethylene glycol and an aqueous solution of $H_3PMo_{12}O_{40}.nH_2O$ was added to the rGO and sonicated	Electrochemical oxidation of nitrite ions	[9]
4	$Na_3[PMo_{12}O_{40}]$ & Agarose composite thin film	To Agarose solution in water PMo_{12} was added. After vacuum defoamation process, the mixed solutions were cast on ITO glass substrates, followed by gelating, and drying	Visible light photochromism	[18]
5	Phosphomolybdate	Tetrabutylammonium salts of	Oxidative	[19]

	& Carbon nanomaterial	PMOs were synthesized and it is immobilized on single walled carbon nanotubes	electrocatalysis	
6	APM & polyacrylonitrile	Not reported	Pre-concentration and separation of Rb(I) ion from salt lake brine	[20]
7	APM & polyacrylonitrile	To APM dissolved in DMSO with Tween 80 as surfactant, Pan was added. To get spherical beads, the composite mixture was fed into a syringe with a needle and injected into DW dropwisely	Selective removal of Cesium from water	[21]
8	APM & polyacrylonitrile	20 g of AMP and 0.8 g of Tween 80 were combined with 100ml of DMSO. After stirring the solution for 1 h at 50°C, 8 g of PAN was added and stirred for 5 h at 50°C to obtain composite mixture	Removal of cobalt, strontium and cesium from radioactive laundry wastewater	[22]
9	$H_3PMo_{12}O_{40}$ & Chitosan	To 5 wt% chitosan solution 20% w/v of PMA was added with a cross linking agent	Enhanced thermal stability and mechanical properties	[23]
10	$H_3PMo_{12}O_{40}$ & polyacrylamide	Different solutions of PMA and Polyacrylamide in deionized water and mixed with constant stirring	Photochromic properties	[24]
11	$H_3PMo_{12}O_{40}$ & Chitosan	By drop wise addition under sonication of CTAB in EtOH to an aqueous solution of $H_3PMo_{12}O_{40}$. An equivalent volume of chitosan solution was added under sonication producing the composite	Antimicrobial activity	[25]
12	APM & Poly acrylonitrile	To hot DMSO and Tween 80 APM powder was added with	The effect of gamma irradiation on the ion	[26]

		stirring. PAN was added and stirred for 6 hours. The mixture was sprayed with compressed air into a large excess of deionised water through a confined jet nebuliser	exchange properties of caesium-selective AMP-PAN composites under spent fuel recycling conditions	
13	$H_3PMo_{12}O_{40}$ & Oligomeric ionic liquid	0.3 mmol of oligomeric ionic liquid was dissolved in deionized water and subsequently an aqueous solution of phosphomolybdic acid in 10 ml of H_2O was added to under ultrasonic radiation for 2x15 min to obtain products	Used as heterogeneous catalyst for the oxidation of cyclohexane under solvent free conditions	[27]
14	$H_3PMo_{12}O_{40}$ & Polymethylmatha-crylate (PMMA)	$H_3PMo_{12}O_{40}$ dissolved in ethanol poured to PMMA dissolved in DMF	Photocatalytic property	[28]
15	$[(C_4H_9)_4N]_3$ $[PMo_{12}O_{40}]$ & graphene	Solution-phase reaction method	Advanced cathode for high performance lithium ion batteries	[29]
16	$Cs_3PMo_{12}O_{40}$ & Bi_2O_3	Dissolution-precipitation method	Photocatalytic activity under visible-light irradiation	[30]
17	$[PMo_{12}O_{40}]^{3-}$ & polyamidoamine	Layer by layer electrostatic assembly technique	Electrocatalytic activities regarding methanol oxidation by depositing Pt micro nano clusters on the surface of the composite	[31]

VI.2. Experimental Section

VI.2.1. Synthesis of APM/Polymer composite

The synthesis of composites based on APM *viz.* APM/PAni and APM/PNMAni was carried out as follows:

To a stirring solution of 20 ml ammonium heptamolybdate (0.03 M, Merck, 99%), 10 ml of disodium hydrogen phosphate dihydrate (0.2 N, Aldrich, 99%) in 8 ml conc. HNO_3 was added. 0.5 ml of Aniline/ N-methyl aniline was added in small aliquots to the stirring solution. The contents were stirred for 18 hours and the resultant dark green powder was washed with water. The products thus obtained were dried for 20 hours at 50°C.
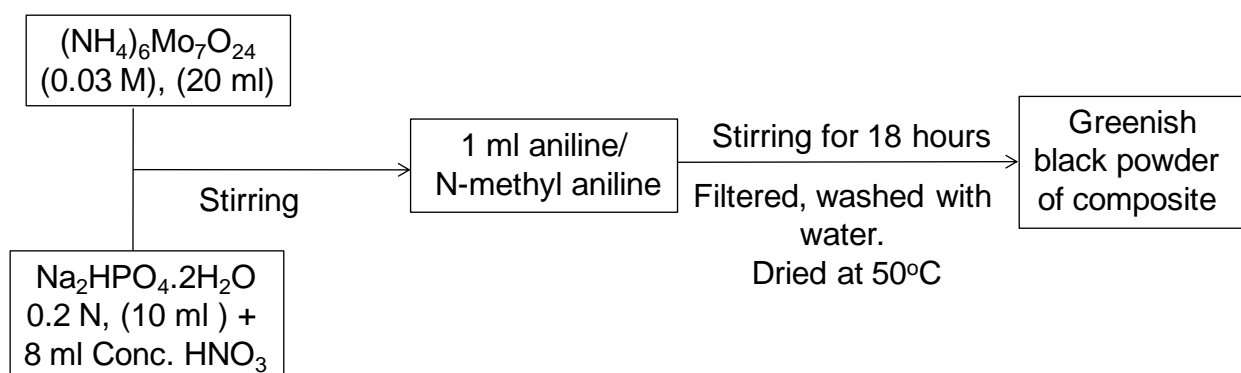
Scheme VI.1. Procedure for the synthesis of APM/PAni and APM/PNMAni.

VI.2.2. Synthesis of Polymers

In order to ascertain the formation of composites; powder X-ray diffraction (PXRD) patterns of composites were compared with those of polymers and APM. The preparation of APM has already been discussed in Chapter V. The methodology employed for the preparation of polymers was similar to that reported in literature by Ganesan *et. al.* [32].

Initially two different solutions were prepared. Solution A consisted of 0.05 mol of aniline/ N-methylaniline in 35 ml of 3 M HCl and solution B was prepared by dissolving 0.05 mol of ammonium persulphate in 50 ml of distilled water. The two solutions were stirred separately for 15 minutes. Then solution A was added to the stirring solution of B drop wise under ice-cold condition. The stirring was continued for 2 hours. The dark green resultant solution was filtered and the product thus obtained was filtered, washed with distilled water and ethanol and dried for 12 hours in oven at 50°C.

VI.3. Characterization

Synthesized APM/PAni and APM/PNMAni composites were characterized using techniques discussed under Section II.2.2 in Chapter II. The presence of Cr(VI) ions was detected with respect to the change in intensity of absorption peaks using UV-Vis spectroscopy (Shimadzu UV-Visible 1800 double beam spectrophotometer).

VI.4. Results and discussion

VI.4.1. Characterization of APM/PAni

The FTIR spectrum of APM/PAni composite showed the presence of bands in the region 1100-550 cm^{-1} which are characteristic of Keggin type heteropoly anions (Figure VI.1a). The peaks at 1066, 970 and 881 cm^{-1} were assigned to γ_{as} (P-O$_a$), γ_{as}(Mo-O$_d$) and γ_{as}(Mo-O$_b$-Mo) respectively [33]. The peaks at 1113 and 807 cm^{-1} were due to the aromatic C-H out-of-plane bending and aromatic C-H in-plane bending vibrations respectively [34]. A well defined peak at 1349 cm^{-1} could be assigned to C=N stretching of secondary amines. Peaks at 1434 and 1533 cm^{-1} were attributed to C=C stretching vibrations of benzenoid ring and

quinonoid ring respectively. The spectrum showed a broad band in the region of 3238–3507 cm^{-1} which is associated with the N-H stretching vibrations of secondary amines [34].

In order to ascertain the formation of composite, PXRD pattern of composite was compared with that of polyaniline and APM. While PXRD of polyaniline showed broad peaks at 2θ values 9°, 14.9°, 20.4°, 25.4°, 27.4° and 29.5° showing an amorphous nature; PXRD pattern of APM was found to be crystalline in nature and it matched well with JCPDS file no. 43-0315 indicating the formation of single-phasic cubic {NH$_4$}$_3$[PMo$_{12}$O$_{40}$].xH$_2$O having lattice constant a = 11.67 Å. On the other hand, PXRD pattern of the composite APM/PAni showed characteristic peaks of APM along with some amorphous nature which confirmed the formation of APM/PAni composite (refer Figure VI.1b). SEM image of the resulting APM/PAni composite (Figure VI.1c) indicated the polydisperse nature of composite particles having irregular morphology. EDAX spectrum (Figure VI.1d) showed the peaks of carbon, nitrogen, phosphorous, molybdenum and oxygen at 0.277(Ka1), 0.392(Ka1), 2.014(Ka1), 2.518(Lβ2) and 0.525(Ka1) respectively (refer Table VI.2)

VI.4.2. Characterization of APM/PNMAni

The FTIR spectrum of PNMAni (Figure VI.2a) showed a band at 2314 cm^{-1} which was attributed to the stretching frequency vibrations of methyl group. The bands representing benzenoid and quinonoid rings appeared at 1500 cm^{-1} and 1576 cm^{-1} in APM/PNMAni composite with appreciable red shift from that of polymer [8] indicating the interaction of PNMAni chains with heteropolyacids. The position of the band at 873 cm^{-1} was attributed to the presence of para-substituted benzene rings ensuring the polymerization of NMAni in

composite [35]. A predominant band at 1304 cm^{-1} was associated with the C-N stretching vibrations of aromatic tertiary amines. Along with the bands of PNMAni, FTIR spectrum of the composite showed the characteristic bands of APM (in the region 1100-700 cm^{-1}) which confirmed the presence of Keggin polyanion in the composite.
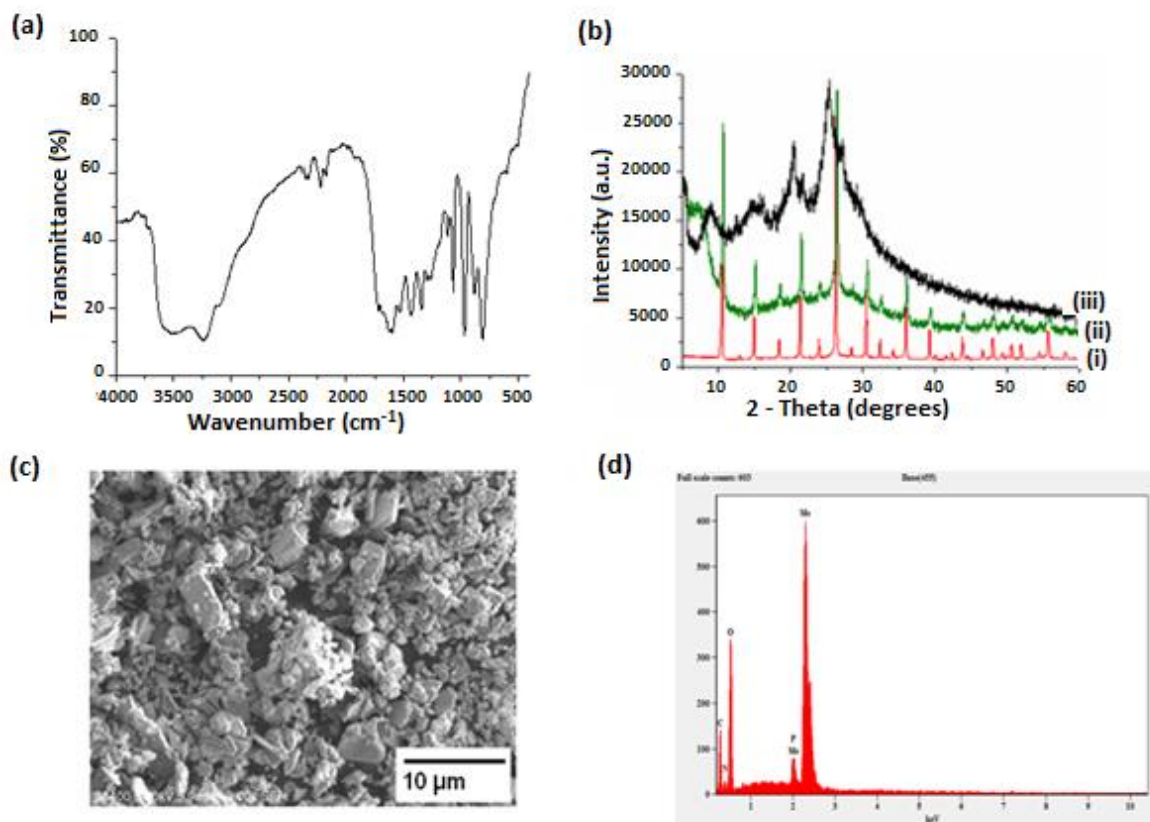
Figure VI.1. (a) FTIR spectrum of APM/PAni composite (b) PXRD pattern of (i) APM (ii) APM/PAni-composite (iii) PAni (c) SEM image and (d) EDAX spectrum of APM/PAni-composite.

PXRD pattern obtained for PNMAni, APM and APM/PNMAni composite are shown in Figure VI.2b. Since PNMAni shows amorphous nature, it does not have long-range atomic order. The PXRD pattern exhibited broad peaks at 2θ angles 10.4°, 18.3° and 23.3°

indicating its low degree of crystallinity. While the PXRD of composite showed an intermediate pattern of APM and PNMAni, with well defined peaks of APM at low intensities and an appreciable broadness of polymer, again confirming the formation of APM/PNMAni composite. SEM image of APM/PNMAni-composite is shown in Figure VI.3c. It showed the presence of polydispersed particles with irregular morphology. EDAX spectrum (Figure VI.2d) showed the peaks of carbon, nitrogen, phosphorous, molybdenum and oxygen at 0.277(Ka1), 0.392(Ka1), 2.014(Ka1), 2.831(Lg3) and 0.525(Ka1) respectively (refer Table VI.3).

Table VI.2. Weight % of elements present in APM/PAni from EDAX.

Element Line	Weight %	Atom %
C K	2.64	4.39
N K	19.76	28.16
O K	48.91	61.02
P K	1.07	0.69
P L	---	---
Mo L	27.62	5.75
Mo M	---	---
Total	100.00	100.00

Table VI. 3. Weight % of elements present in APM/PNMAni composite.

Element Line	Weight %	Atomic %
C K	44.78	61.31
N K	6.84	8.03
O K	26.05	26.78
P K	0.14	0.08
Mo L	22.19	3.80
Total	100.00	100
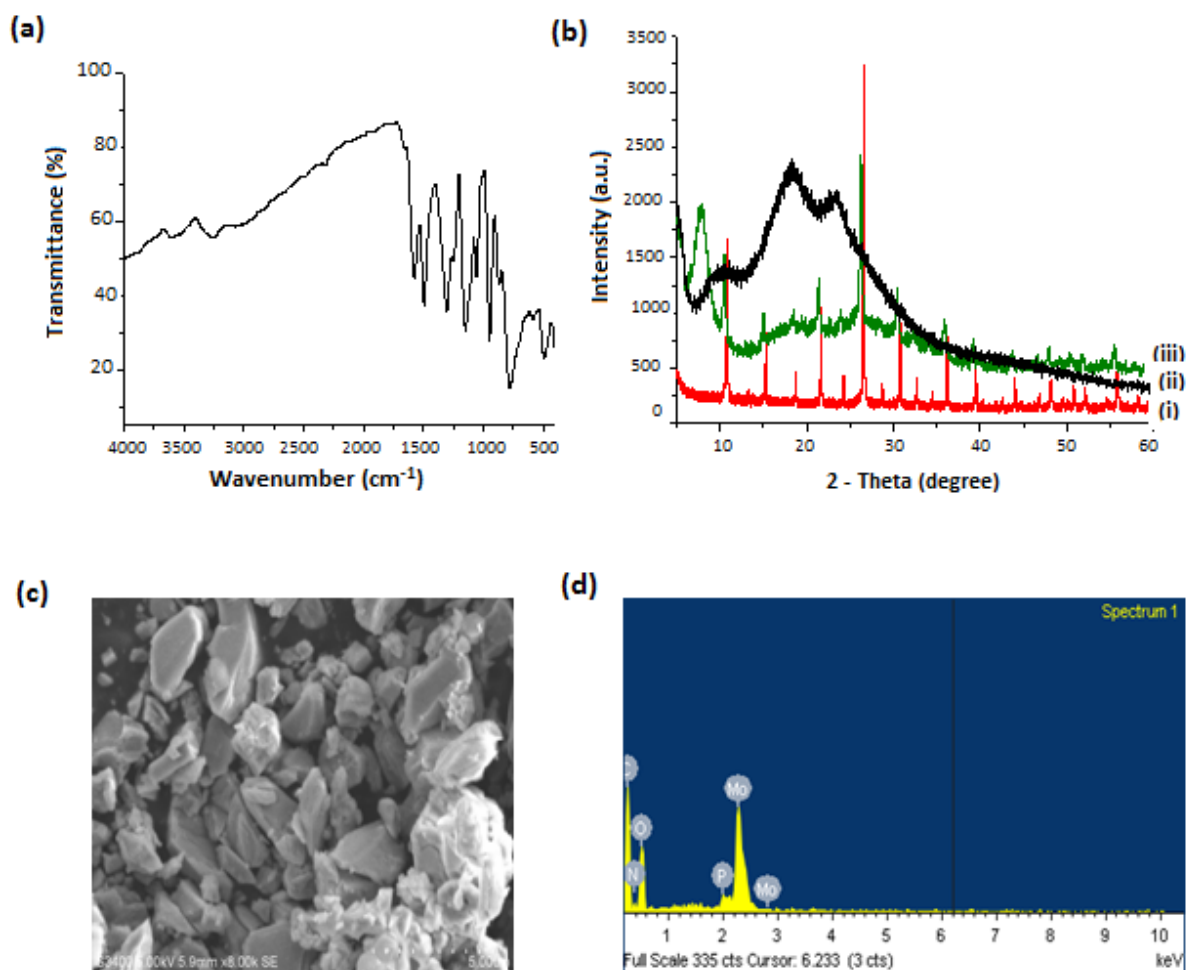
Figure VI.2. (a) FTIR spectrum of APM/PNMAni (b) PXRD pattern of (i) APM (ii) PNMAni and (iii) APM/PNMAni-composite (c) SEM image and (d) EDAX of APM/PNMAni-composite.

VI.5. Electrochemical behavior of composites

The effect of various electrolytes on the performance of composite electrodes was investigated by performing cyclic voltammetry experiments using a glassy carbon electrode (GCE) on which the synthesized APM and composites were coated separately. The electrochemical behavior of the composites in various electrolytes such as H_2SO_4 (0.1 M),

HCl (2 M), KOH (1 M) and $K_4[Fe(CN)_6]$ (1 mM) with a scan rate of 50 mVs^{-1} was investigated. Since PNMAni and PMo$_{12}$ are unstable in basic solutions, desirable results did not obtained when KOH was used as the electrolyte. Among the others, best results were obtained when 1 mM $K_4[Fe(CN)_6]$ in 0.1 M KCl was used as supporting electrolyte. Figure VI.3 represents the cyclic voltammograms (CVs) of Bare GCE, APM, APM/PAni & APM/PNMAni in 1 mM $K_4[Fe(CN)_6]$ with a scan rate of 50 mVs^{-1} by applying potential range of -0.2 to +0.8V.
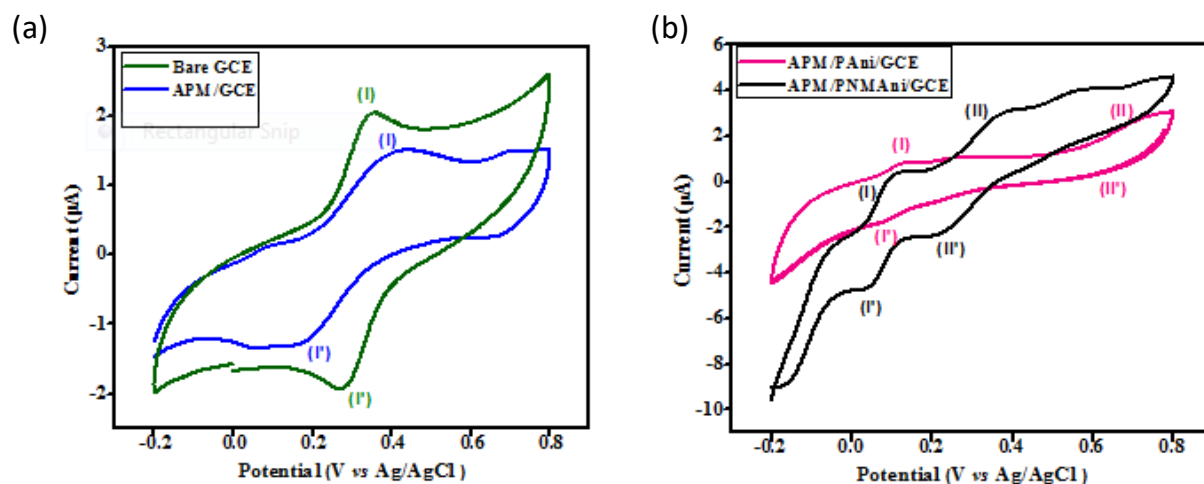
Figure VI.3. (a) CV of bare GCE and APM coated on GCE. (b) CV of APM/PAni and APM/PNMAni coated on GCE.

The small area of current at bare GCE and APM coated GCE represents the less available fast electrons at the electrode-electrolyte interface. The bare GCE gives a redox peak for $K_4[Fe(CN)_6]$ with mean peak potential E*1/2* = (*Epa* + *Epc*)/2 at 0.317 V which can be attributed to Fe^{II}/Fe^{III} [36]. The redox couple obtained for APM at half wave potential 0.281 V could be attributed to Mo^{V}/Mo^{VI} electron process. It is noticeable that the E*1/2* obtained for Strandberg type PMOs were 0.087 and 0.072 V respectively for **1** and **2** described in

184

Chapter II. The different E*1/2* values obtained for Mo^V/Mo^{VI} electron process in {P_2Mo_5} and {PMo_{12}} could be because of the difference in the electron movement on account of different structural environment present in Strandberg and Keggin type PMOs.

The results showed that APM/PNMAni exhibits highest peak current response compared to APM and APM/PAni in the presence of a redox species 1 mM $K_4[Fe(CN)_6]$ in 0.1 M KCl. The redox peaks obtained for APM/PAni and APM/PNMAni at 0.228 V and 0.298 V respectively could be attributed to the Mo^V/Mo^{VI} electron process. The peaks obtained at 0.667 V for APM/PAni and 0.072 V for APM/PNMAni could be due to redox process involved in the polymeric chain of the composite. The appreciable peak shift towards lower potential value could be attributed to the electron donating behavior of methyl groups in poly(N-methyl aniline).

VI.6. Optical band gap energy (E_g) determination applying Kubelk- a–Munk (KeM or F(R)) function in Tauc method.

Optical band gap (E_g) determination was carried out using Tauc method, as discussed in Chapter II, under Section II.3.4.

Plots of F(R) and $(F(R)h\upsilon)^n$ (where n = ½ and 2 for indirect allowed transition and direct allowed transition respectively) versus hυ(eV) for APM, APM/PAni and APM/PNMAni composite are given in Figure VI.4, VI.5 and VI.6 respectively.
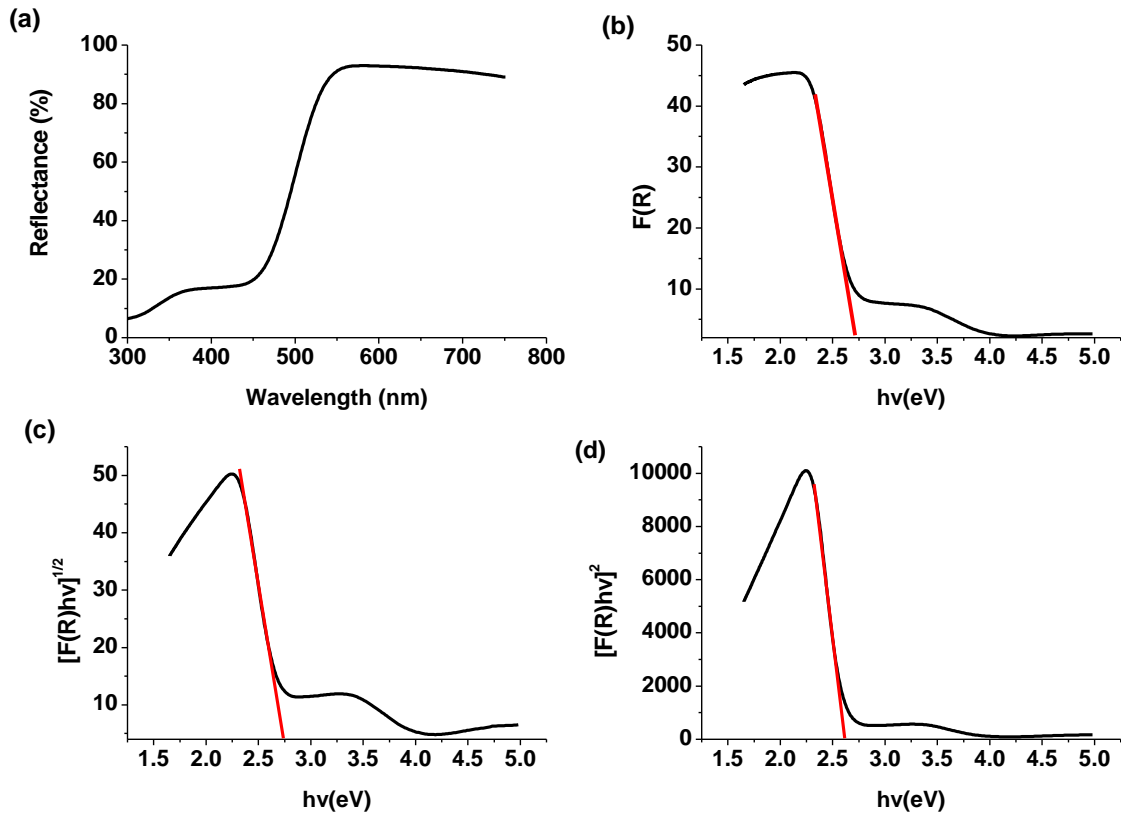
Figure VI.4. Plots of (a) Reflectance versus wavelength (b) F(R) versus hυ(eV), (c) $(F(R)h\upsilon)^{1/2}$ versus hυ(eV) and (d) $(F(R)h\upsilon)^2$ versus hυ(eV) for APM.
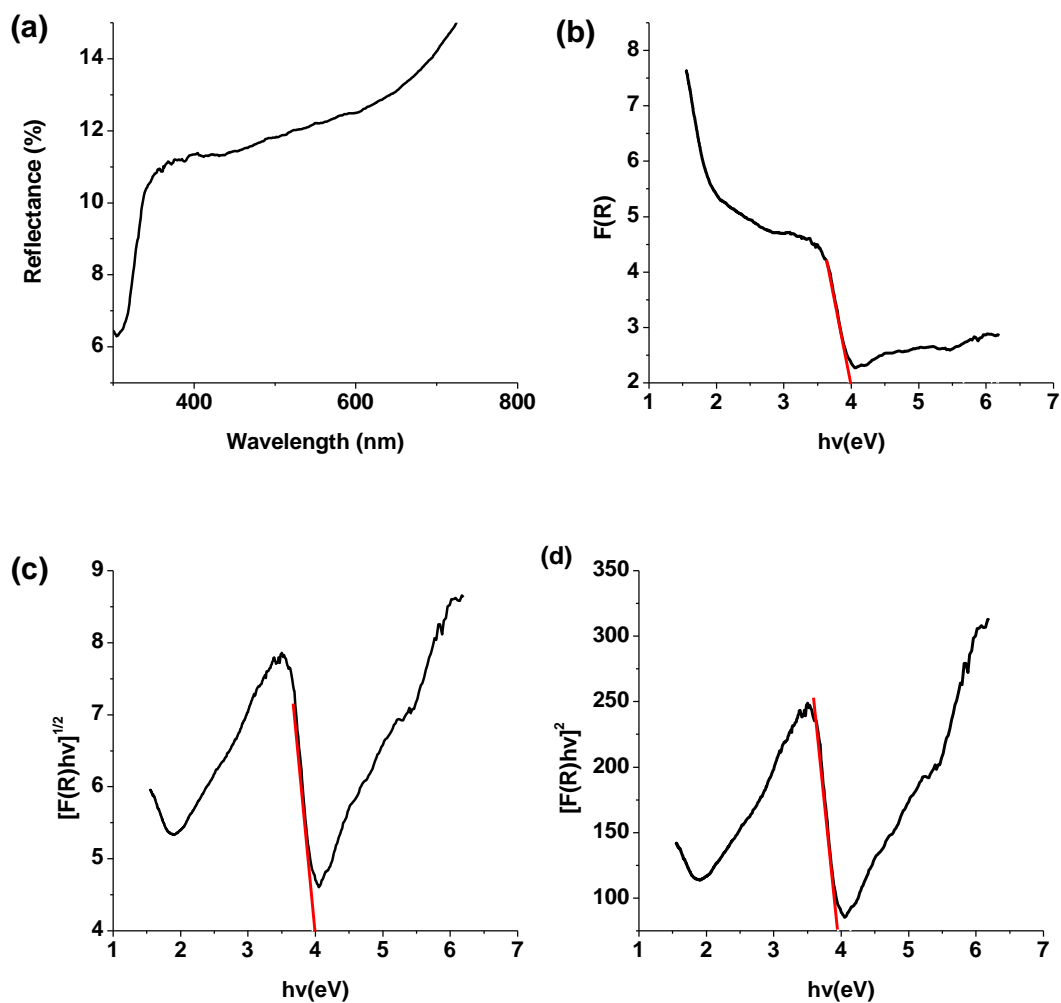
Figure VI.5. Plots of (a) Reflectance versus wavelength (b) F(R) versus hυ(eV), (c) $(F(R)hυ)^{1/2}$ versus hυ(eV) and (d) $(F(R)hυ)^2$ versus hυ(eV) for APM/PAni.
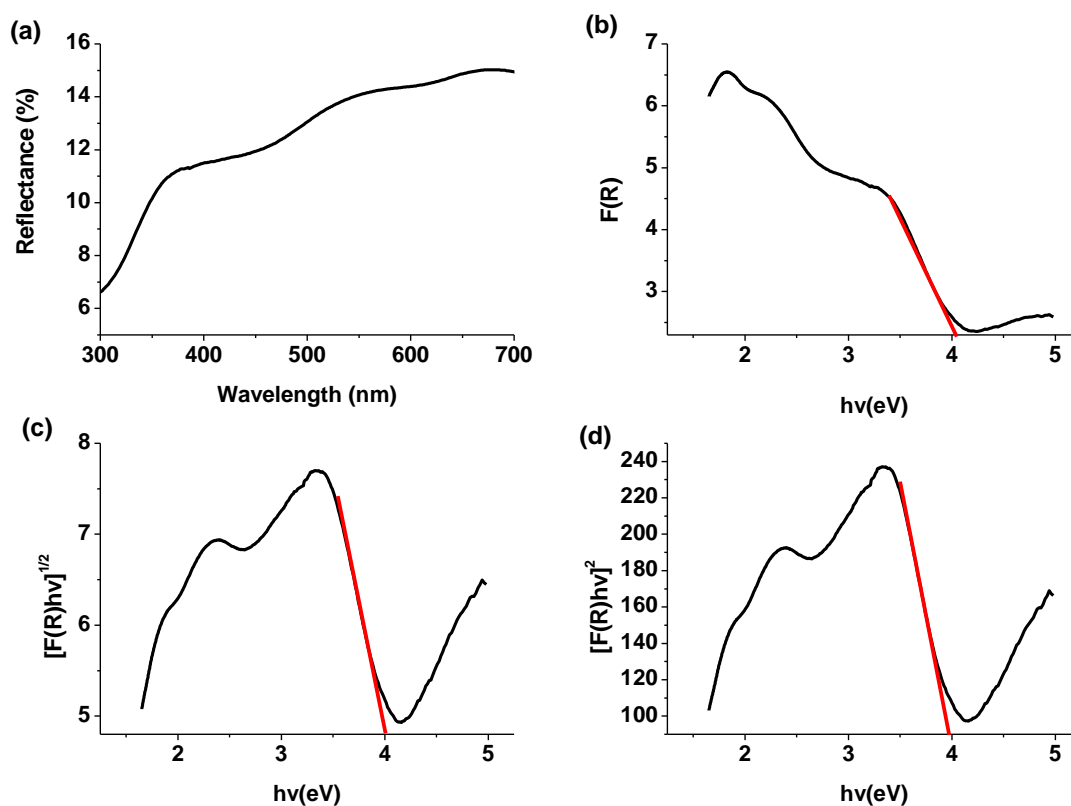
Figure VI.6. Plots of (a) Reflectance versus wavelength (b) F(R) versus hυ(eV), (c) $(F(R)hυ)^{1/2}$ versus hυ(eV) and (d) $(F(R)hυ)^2$ versus hυ(eV) for APM/PNMAni composite.

Table VI.4. Table tabulates the irrespective, allowed indirect and allowed direct band gaps of APM, APM/PAni and APM/PNMAni.

Solids	$[F(R) hυ]^2$ (allowed direct Band gap energy in eV)	$[F(R) hυ]^{1/2}$ (allowed indirect Band gap energy in eV)	F(R) vs hυ (band gap energy Irrespective of direct or indirect in eV)
APM	2.60	2.73	2.71
APM/PAni	3.96	3.97	4.01
APM/PNMAni	3.97	4.03	4.05

The band gap energies of APM and composites calculated from UV-DSR spectra have been tabulated in Table VI.4. In all the three cases, the allowed direct band gap energy showed lowest value. The optical band gaps of composites increased considerably compared to APM. The increase in band gap was probably due to the incorporation of polymer chain in APM. For APM, the corresponding wavelength for allowed direct band gap energy and allowed indirect band gap energy and band gap energy irrespective of direct or indirect are 477, 454 and 457 nm respectively. In the case of APM/PAni as the band energy increased with respect to APM, blue shift observed at 313, 312 and 309 nm respectively. In the case of APM/PNMAni also, the corresponding wavelength was observed at 312, 307 and 306 nm respectively indicating shift towards lower wavelength region compared to APM. The increase in band gap energy provides scope for applications in photonic devices like light emitting diodes and laser diodes [38].

VI.7. Removal of Cr(VI) from aqueous solution

The removal hexavalent chromium was done according to the procedure of United States Environment Protection Agency [39]. The efficiency of the synthesized materials to remove Cr(VI) was determined colorimetrically using UV-Vis spectroscopy. Initially the ability of two components of composite, APM and polymer to remove Cr(VI) from aqueous solution was investigated. It was found that, APM was not a good candidate for this purpose. But PAni and PNMAni polymers could remove hexavalent chromium ions completely from aqueous solution upto nine cycles. In the next step the ability of the synthesized composites to remove Cr(VI) was analyzed. In the preliminary studies, APM/PNMAni showed more

potency; therefore detailed investigation was carried out using APM/PNMAni. The Cr(VI) removal studies were carried out using the following chemicals:

> Stock solution of 50 ppm $K_2Cr_2O_7$ solution was prepared by dissolving 0.014 g of $K_2Cr_2O_7$ in 100 ml deionized water.

> Working standard solution of 2 ppm $K_2Cr_2O_7$ solution was prepared by diluting 4 ml of the above stock solution to 100 ml using deionized water.

> Diphenyl carbazide (DPC) solution was prepared by dissolving 0.05 g of DPC in 10 ml acetone.

> 10 % H_2SO_4

VI.7.1. Procedure for Cr(VI) removal

To 10 ml of 2 ppm $K_2Cr_2O_7$ solution, a definite amount of substance (APM/ polymer / composite) was added and stirred using a magnetic stirrer. The contents of the beaker were centrifuged after 60 minutes. 9.5 ml of the centrifugate was collected and pH was adjusted to 2 ± 0.5 using 10% H_2SO_4. DPC (0.2 ml) was added to develop color and the resultant solution was diluted to 10 ml using deionized water. UV-Vis spectra were recorded in the range 200-800 nm to analyze the presence of Cr(VI). This procedure was repeated in all experiments performed in this chapter.

VI.7.2. Cr(VI) removal studies using the components of composites

The Cr(VI) removal capacity of 0.08 g of APM, PAni and PNMAni for 2 ppm solution of Cr(VI) was investigated at pH 5 ± 0.5 (Figure VI.7). The characteristic peak of Cr(VI) was observed at 542 nm. It was observed that PNMAni was most effective in removing Cr(VI)

from an aqueous solution. Therefore, more studies were carried out using PNMAni to understand the nature and mechanism of the removal of Cr(VI) when polymer is used.
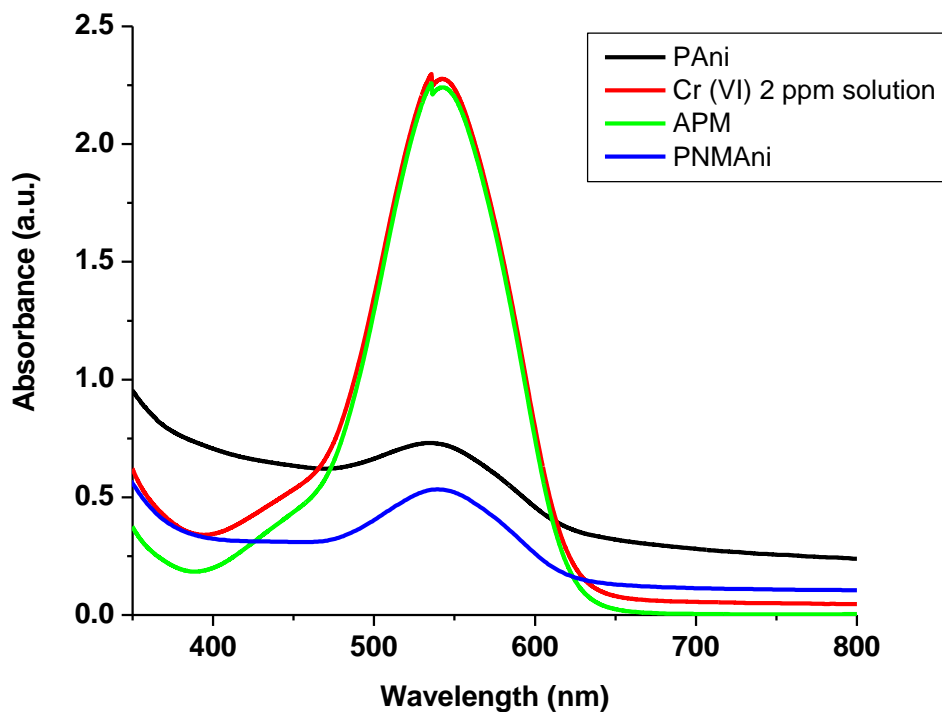
Figure VI.7. The UV-Vis spectra for Cr(VI) removal by PAni, PNMAni and APM; along with 2 ppm Cr(VI) solution.

VI.7.3. Effect of amount of PNMAni

To investigate the effect of amount, different quantities of PNMAni (0.02 g, 0.04 g, 0.06 g, 0.08 g and 0.1 g) was added to 2 ppm solution of Cr(VI) having pH 5±0.5. The above procedure was repeated and the UV-Vis spectra were recorded (refer Figure VI.8). From the UV-Vis data it was concluded that the Cr(VI) removal increases as the amount of polymer increases and maximum removal obtained when 0.1 g of PNMAni was used.
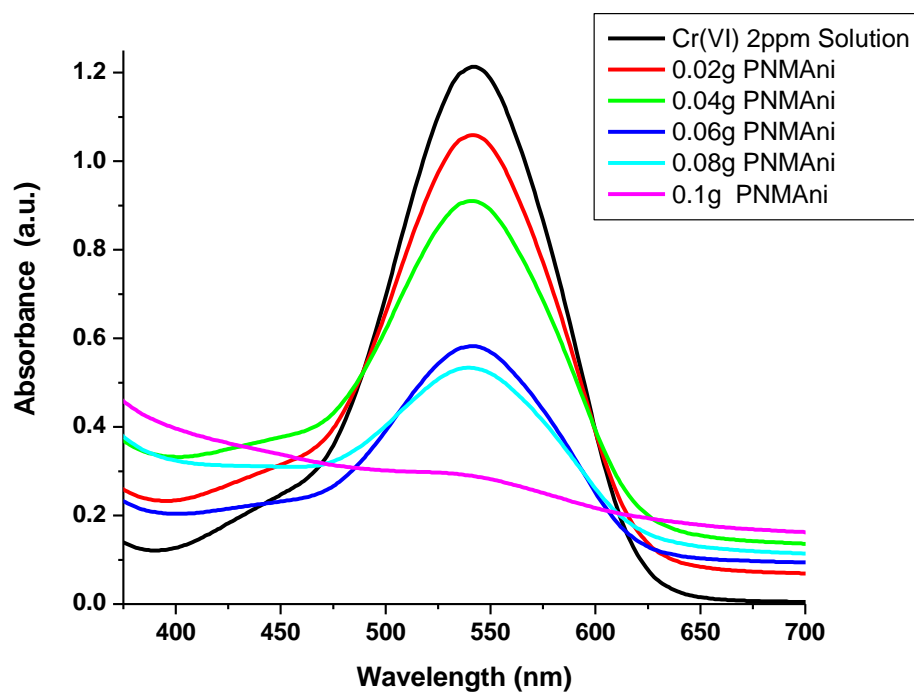
Figure VI.8. The UV-Vis spectra for Cr(VI) removal by PNMAni with varying amount.

VI.7.4. Effect of contact time

To study the effect of contact time between Cr(VI) solution and polymer, 0.1 g of polymer was taken in four different beakers and 10 ml of 2 ppm Cr(VI) solution at pH 5±0.5 was added. The content of first beaker filtered immediately after mixing and considered as zero minutes. The contents of the 2nd, 3rd and 4th beakers were sonicated and filtered at different time intervals i.e. 10 minutes, 20 minutes, 30 minutes and 60 minutes respectively. It was observed that the efficiency of Cr(VI) removal increased when the contact time was increased and maximum removal efficiency was obtained at 60 minutes (refer Figure VI.9).
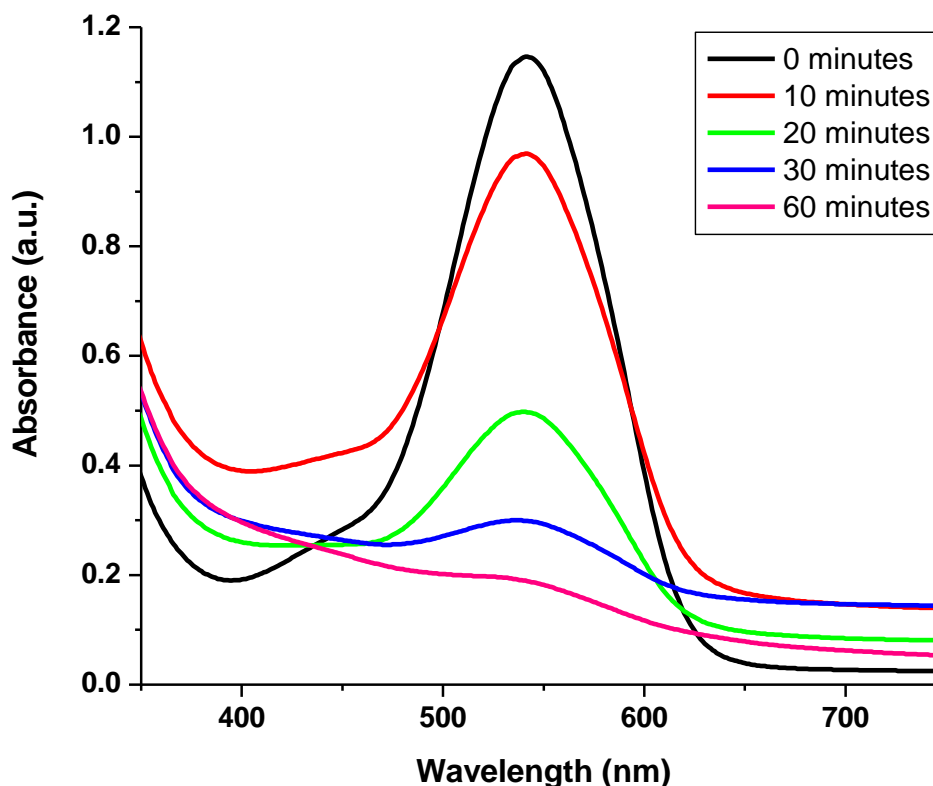
Figure VI.9. The UV-Vis spectra for Cr(VI) removal by PNMAni at different time intervals.

VI.7.5. Cr(VI) removal using APM/PNMAni

APM/PNMAni had selected for Cr(VI) removing studies since it showed good efficiency compared to APM/PAni. In this case, a bluish green coloured solution was obtained after stirring one hour. The content of the beaker was filtered and UV-Vis spectrum of the bluish green solution was recorded. The same procedure was repeated for different pH (pH = 1-5 ±0.5) to understand the effect of pH. The UV-Vis spectrum of this coloured solution exhibited the characteristic absorption peaks of Cr(III) at 430 and 615 nm, indicating the reduction of Cr(VI) to Cr(III) (refer Figure VI.10).
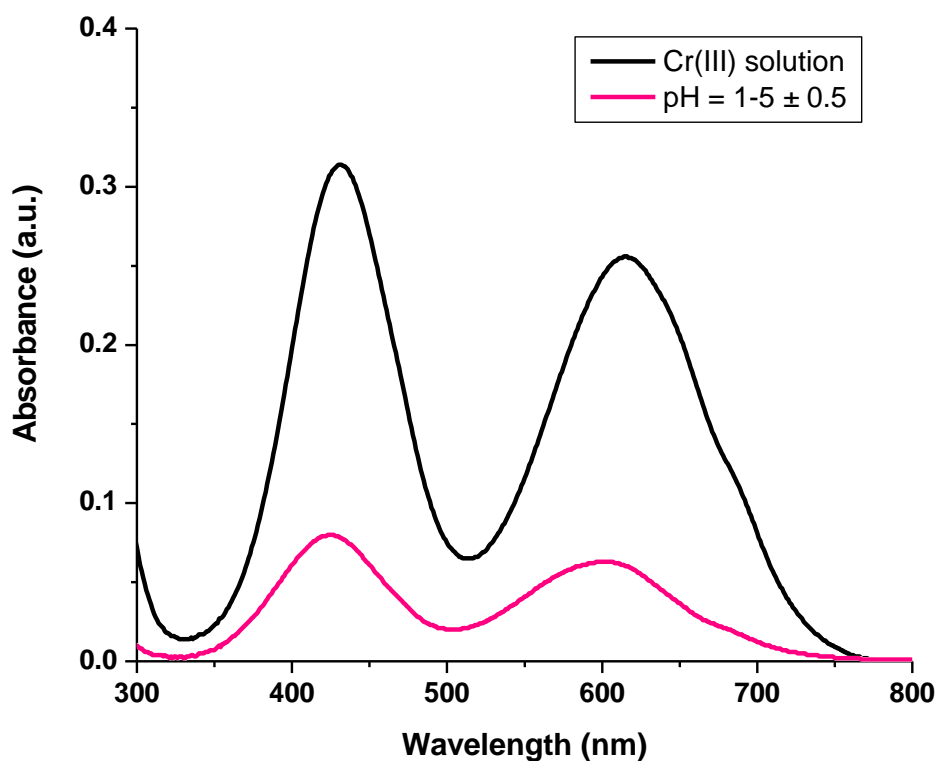
Figure VI.10. The UV-Vis spectra for original Cr(VI) solution and for the solution obtained after adding APM/PNMAni at pH = 1-5 ±0.5.

VI.7.6. Proposed mechanism for Cr(VI) removal

Removal of hexavalent chromium ions has drawn attention of researchers due to its high toxicity and mobility. It is a challenge to remove Cr(VI) ions from industrial waste water. Different materials have been used in the literature for the effective removal of Cr(VI) ions [40-42]. From the above studies it is observed that, Cr(VI) could remove from its 2 ppm aqueous solution with 0.1 g of polymer by one hour of constant stirring. The process of removal could be due to the electrostatic force of attraction between the protonated polymer chain and $Cr_2O_7^{2-}$ anions (as shown in Scheme VI.2).
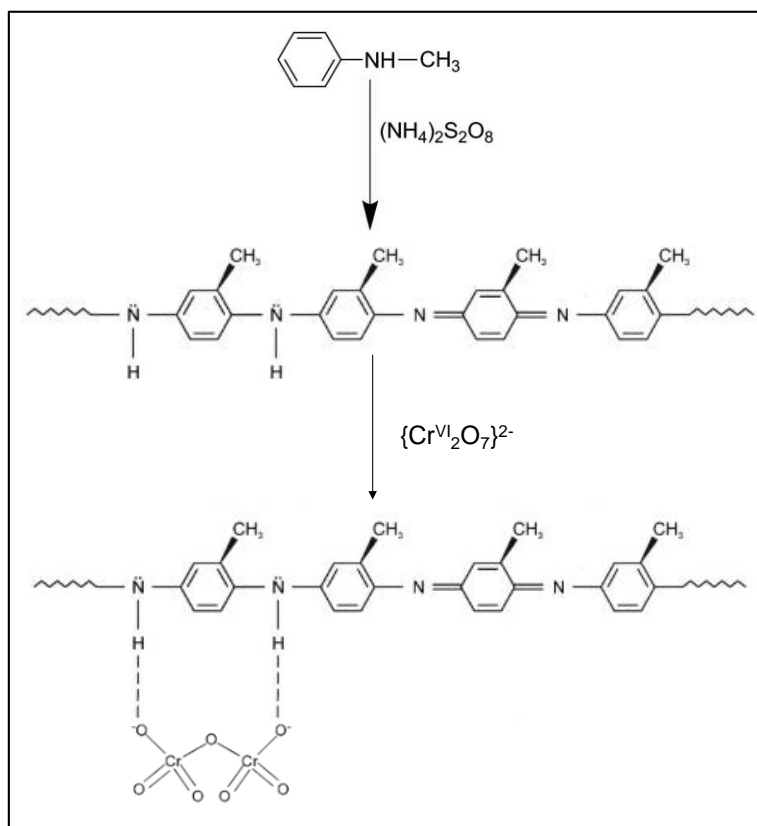
Scheme VI.2. The scheme for the removal of Cr(VI) using poly(N-methylaniline).

On the other hand, the composite acted as a reducing agent for the reduction of toxic Cr(VI) to environmentally benign Cr(III). Earlier Kishore *et. al* [43] have reported the formation of reduced PMo_{12} during the polymerization of aniline using $[H_3PMo_{12}O_{40}]$. The reduced PMo_{12} species generated *in-situ* was utilized for the reduction of metal ions to form metal nanoparticle embedded PAni-PMo_{12} composite. It could be inferred that a similar mechanism was observed herein. Ammonium phosphomolybdate formed in the reaction medium could act as an oxidizing agent and resulted in the polymerization of N-methylaniline, thus forming the composite. The reduced Mo(V) centers in the composite were oxidized to Mo(VI) and in turn reduced Cr(VI) to Cr(III) (refer Scheme VI.3). The CV

results discussed under Section VI.5 also suggested that the redox peaks obtained for APM/PNMAni were corresponding to the one electron transfer.
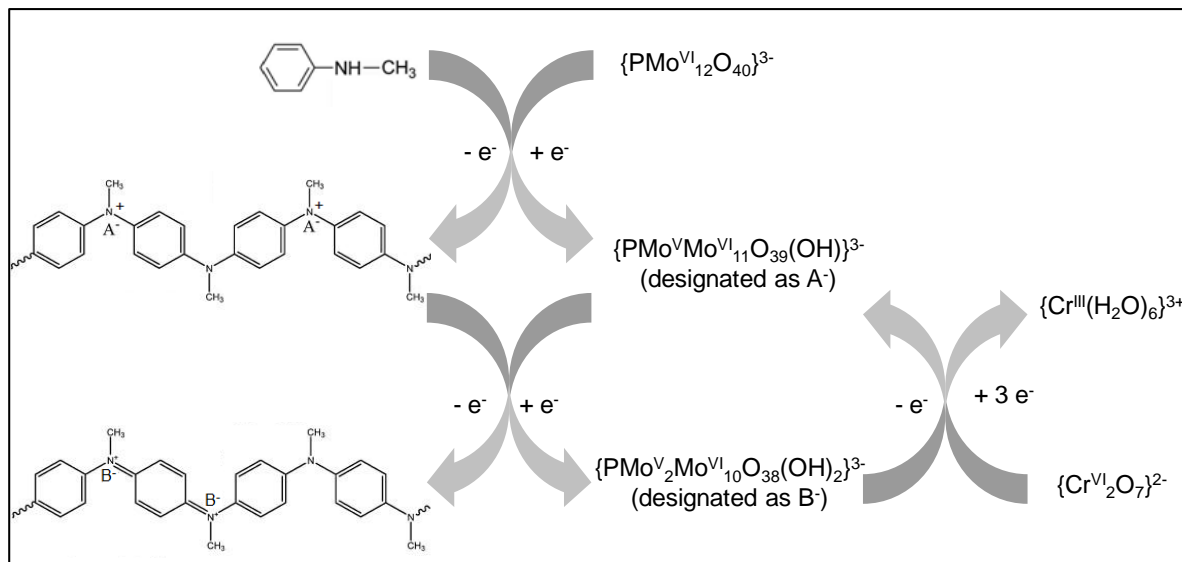
Scheme VI.3. Scheme showing the mechanism for reduction of Cr(VI) to Cr(III) using APM/PNMAni composite.

The reduction of Mo(VI) to Mo(V) during the composite formation was confirmed by recording UV spectrum of the ammonium heptamolybdate solution used for the composite formation and the filtrate collected from the beaker containing the reagents for the composite formation after one hour of stirring (refer Figure VI.11). The broad absorption ~750 nm which is characteristic for the presence of Mo(V) species [43] was obtained for the filtrate collected during composite formation which indicated the reduction of Mo(VI) to Mo(V).
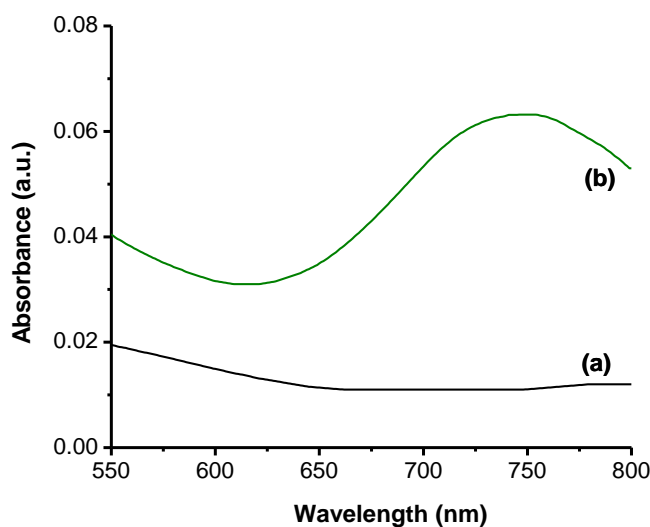
Figure VI.11. UV-Vis spectra of (a) ammonium heptamolybdate solution and (b) filtrate collected during composite formation after stirring one hour.

VI.8. Conclusions

Two polymer composites of APM namely, APM/PAni and APM/PNMAni were synthesized and characterized using FTIR, PXRD and SEM-EDAX. The optical band gap energy of APM and its composites was studied using UV-DRS spectroscopy and it was found that the E_g of the composite materials were higher than that of APM. The electrochemical behavior of APM and its composites was also investigated and APM/PNMAni exhibited highest peak current response as compared to APM and APM/PAni in the presence of a redox species 1 mM $K_4[Fe(CN)_6]$ in 0.1 M KCl indicating its ability to act as a good redox-catalyst. The ability of the synthesized solids to remove toxic Cr(VI) from aqueous medium was investigated. While polymers could removed Cr(VI) via electrostatic interaction between polymeric backbone and dichromate ions; APM/PNMAni could reduce the harmful hexavalent chromium to environmentally benign trivalent chromium species.

197

References

1. Xie, F.; Ren, J.; Liu, W.; Wang. T.; Yuan, J.; Jiang, X.; Zhang, H. *J. Clust. Sci.* **2018**, 29, 1227-1232.

2. Pathan, S.; Patel, A. *Catal. Sci. Technol.* **2014**, 4, 648-656.

3. Ghalebi, H. R.; Aber, S.; Karimi, A. *J. Mol. Catal. A: Chem.* **2016**, 415, 96-103.

4. Xu, J.; Cao, X.; Xia, J.; Gong, S.; Wang, Z.; Lu, L. *Anal. Chim. Acta* **2016**, 934, 44-51.

5. Lu, L.; Xie, Y. *New J. Chem.* **2017**, 41, 335-346.

6. Wang, Z.; Han, Q.; Xia, J.; Xia, L.; Bi, S.; Shi, G.; Zhang, F.; Xia, Y.; Li, Y.; Xia, L. *J. Electroanal. Chem.* **2014**, 726, 107-111.

7. Li, Z. J.; Zhao, W. J.; Shi, Y.; Ying, Z. P.; Feng, W.; Bai, L. *Compos. Interfaces* **2018**, 25, 809-821.

8. Papagianni, G. G.; Stergiou, D. V.; Armatas, G. S.; Kanatzidis, M. G.; Prodromidis, M. I. *Sens. Actuators, B* **2012**, 173, 346-353.

9. Kim, Y.; Shanmugam, S. *ACS Appl. Mater. Interfaces* **2013**, 5, 12197-12204.

10. Wang, Q.; Liu, E.; Zhang, C.; Huang, S.; Cong, Y.; Zhang, Y. *J. Colloid Interface Sci.* **2018**, 516, 304-311.

11. Hou, L.; Zhang, Y.; Ma, Y.; Wang, Y.; Hu, Z.; Gao, Y.; Han, Z. *Inorg. Chem.* **2019**, 58, 16667-16675.

12. Gong, K.; Liu, Y.; Wang, W.; Fang, T.; Zhao, C.; Han. Z.; Zhai, X. *Eur. J. Inorg. Chem.* **2015**, 2015, 5351-5356.

13. Wang, X.; Wang, J.; Geng, Z.; Qian, Z.; Han, Z. *Dalton Trans.* **2017**, 46, 7917-7925.

14. Abu-Zied, B. M.; Farrag, A. A. A.; Asiri, A. M. *Powder Technol.* **2013**, 246, 643-

649.

15. Lento, J.; Harjula, R. *Solvent Extr. Ion Exch*. **1987**, 5, 343-352.

16. Lopez, R.; Gomez, R. *J. Sol-Gel Sci.Technol*. **2012**, 61, 1-7.

17. Reddy, K. M.; Manorama, S. V.; Reddy, A. R. *Mater. Chem. Phys*. **2003**, 78, 239-245.

18. Wang, Z.; Zhang, R.; Ma, Y.; Zheng, L.; Peng, A.; Fu, H.; Yao, J. *J. Mater. Chem*. **2010**, 20, 1107-1111.

19. Fernandes, D. M.; Freire, C. *ChemElectroChem* **2015**, 2, 269-279.

20. Zheng, H.; Liu, Z.; Huang, D.; Wang, S.; Li, B. *ChemistrySelect* **2017**, 2, 7741-7750.

21. Ding, D.; Zhang, Z.; Chen, R.; Cai, T. *J. Hazard. Mater*. **2016**, 324, 753-761.

22. Park, Y.; Lee, Y. C.; Shin, W. S.; Choi, S. J. *Chem. Eng*. *J*. **2010**, 162, 685-695.

23. Bhat, A. H.; Bhat, I. U. H.; Khalil, H. P. S. A. *J. Compos. Mater*. **2010**, 45, 39-49.

24. Chen, J.; Dong, L. L.; Feng, W.; Liu, S. L.; Liu, J.; Yang, F. L. *J. Mol. Struct*. **2013**, 1049, 414-418.

25. Matteis, L. D.; Mitchell, S. G.; Fuente, J. M**. *J. Mater. Chem. B***, **2014**, 2, 7114-7117

26. Holdsworth, A. F.; Eccles, H.; Rowbotham, D.; Bond, G.; Kavi, P. C.; Edge, R. *Separations* **2019**, 6, 1- 9.

27. Sammah, N.; Ghiaci, M. *Ind. Eng. Chem. Res.* **2017**, 56, 10597-10604.

28. Zhang, Z. M.; Li, T. T.; Liu, C. *Appl. Mech. Mater.* **2013**, 395, 415-418.

29. Yang, H.; Xie, Y.; Wang, Y.; Wu, B.; Chen, Y.; Xu, B. *Nano-Structures & Nano-Objects* **2017**, 11, 76-81.

30. Wang, Q.; Liu, E.; Zhang, C.; Huang, S.; Cong, Y.; Zhang, Y. *J. Colloid Interface Sci.* **2018**, 516, 304-311.

31. Li, Z. S.; Lin, S.; Chen, Z. L.; Shi, Y. D.; Huang, X, M. *J. Colloid Interface Sci.* **2012**, 368, 413-419.

32. Ganesan, R.; Gedanken, A. *Nanotechnology* **2008**, 19, 435709.

33. Joseph, J.; Radhakrishnan, R. C.; Johnson, J. K.; Joy, S. P.; Thomas, J. *Mater. Chem. Phys.* **2020**, 242, 122488.

34. Nakamoto K **1978** Infrared and Raman spectra of inorganic and coordination compounds (New York: John Wiley & Sons).

35. Yagan, A.; Pekmez, N. O.; Yildiz, A. *J. Electroanal. Chem.* **2005**, 578, 231-238.

36. Jose, J.; Rajamani, A. R.; Anandaram, S.; Jose, S. P.; Peter, S. C.; Sreeja, P. B. *Appl. Organometal. Chem.* **2019**, 5063.

37. Yogan, A. *Int. J. Electrochem. Sci.* **2019**, 14, 2906-2913.

38. Mukherjee, S.; Maiti, R.; Midya, A.; Das, S.; Ray, S. K. *ACS Photonics* **2015**, 2, 760-768.

39. US EPA (United States Environment Protection Agency), **1992**, Method 7196A, Chromium, Hexavalent (Colorimetric).

40. Shakya, A.; Agarwal, T. *J. Mol. Liq.* **2019**, 293, 111497-111507.

41. Xu, D.; Zhu, K.; Zheng, X.; Xiao, R. *Ind. Eng. Chem. Res.* **2015**, 54, 6836-6844.

42. Xing, J.; Zhu, C.; Chowdhury, I.; Tian, Y.; Du, D.; Lin, Y. *Ind. Eng. Chem. Res.* **2018**, 57, 768-774.

43. Kishore, P. S.; Viswanathan, B.; Varadarajan, T. K. *Nanoscale Res. Lett.* **2008**, 3, 14-20.

CHAPTER VII

Summary and conclusions

PMO based solids represent a unique class of solids by virtue of their structure and properties. There are various factors which affect the formation of these type solids with a particular structure; such as the molar ratio of Mo: metal: ligand, pH and temperature conditions. By varying these conditions structurally diverse PMOs can be formed. Diversification in the size, composition and structure of PMOs has led to significant properties and consequently numerous applications. PMOs exhibit luminescent, unusual magnetic, catalytic and electrochemical properties. On account of these properties they have found applications in various fields including biological and medical fields.

In this present study, we have made an attempt to synthesize novel PMO solids and to explore their properties. The main techniques used were solvent evaporation technique and hydrothermal method. The structural features like supramolecular isomerism, formation of water cluster and porosity have also been illustrated. The non-bonding interactions between the organic cations and the Strandberg anion resulted in the formation of multi-dimensional solids. Comparative studies of the changes in optical band gap energy based on the difference in protonation of the cluster anion and difference in the type of ligands have been done successfully. The electrochemical behaviour of two isomeric ligands based Strandberg type PMOs was investigated by using cyclic voltammetry. Besides Strandberg type solids, a rare Cu based Keggin type solid has been synthesized and characterised. The Keggin type PMO, APM has been synthesized and its dye removal efficiency has been explored. Moreover, two polymer composites of APM were prepared with an account of their properties.

However, the poor solubility and coordinating property of some organic ligands and inefficiency to control pH raise challenges in the engineering of desirable products. Yet,

the possibility of forming a wide range of self-assembled topology attracts the attention

of researchers.